UNIVERSITE BRETAGNE LOIRE

UNIVERSITÉ DE NANTES

Thèse de Doctorat

Camilo ARIAS RUIZ

Mémoire présenté en vue de l'obtention du
grade de Docteur de l'Université de Nantes
sous le sceau de l'Université Bretagne Loire

École doctorale : *EGAAL*

Spécialité : *Sciences de la Terre et de l'environnement*
Unité de recherche : *Laboratoire LPG, UMR CNRS 6112*

Soutenue le 18-12-2017
Thèse N° :

High resolution climate records from modern and last interglacial periods derived from giant clam shells (Tridacnidae) in Sulawesi, Indonesia.

JURY

Président du jury	**Laurent BARILLE,** Professeur, Université de Nantes
Rapporteurs :	**Claire LAZARETH**, Chercheur, Institute de Recherche pour le Développement (IRD) **Laurent CHAUVAUD**, Directeur de Recherche, CNRS Brest
Examinateurs :	**Elisabeth MICHEL,** Chercheur, LSCE Gif-Sur-Yvette **Laurent BARILLE,** Professeur, Université de Nantes
Invité :	**Sri Yudawati CAHYARINI**, Chercheur, Research Center for Geotechnology, Bandung (Indonesia)
Directeur de Thèse :	**Mary ELLIOT**, Professeur, Université de Nantes

UNIVERSITE DE NANTES

ECOLE DOCTORALE EGAAL

THÈSE DE DOCTORAT

Présentée par

Hernan Camilo ARIAS RUIZ

Pour l'obtention du titre de

DOCTEUR DE L'UNIVERSITE DE NANTES

UMR CNRS 6112

Spécialité : Sciences de la Terre et de l'environnement

High resolution climate records from modern and last interglacial periods derived from giant clam shells (Tridacnidae) in Sulawesi, Indonesia.

Travaille dirigé par

Professeur Mary ELLIOT

Jury

Mme Claire LAZARETH	Chercheur IRD, Bondy	Rapportrice
Mr Laurent CHAUVAUD	Chargé de recherche CNRS, Brest	Rapporteur
Mme Elisabeth MICHEL	Chercheur LSCE, Gif-Sur-Yvette	Examinatrice
Mr Laurent BARILLE	Chargé de recherche MMS, Nantes	Examinateur
Mme Sri Yudawati CAHYARINIE	Chercheur LIPI, Indonésie	Invitée

Declaration

This thesis is a presentation of my original research work from 2014 to 2017 and was composed by myself. Wherever contributions of others are involved, every effort is made to indicate this clearly, with due reference to the literature, and acknowledgement of collaborative research and discussions.

This work has not been submitted for any other degree or processional qualification except as specified.

The first results of Chapter III was accepted and published in the journal "Palaeogeography, Palaeoclimatology, Palaeoecology" (Elsevier), with the title: Geochemical fingerprints of climate variation and the extreme La Niña 2010–11 as recorded in a *Tridacna squamosa* shell from Sulawesi, Indonesia.



Hernan Camilo ARIAS RUIZ

Acknowledgements

I firstly thanks my supervisor Mary Elliot for give me the opportunity of participate in this project of paleoceanography and geodynamics in Indonesia, a magic country. I thanks all members of the Indonesian research team, Kevin Pedoja, Laurent Husson, Antoine Bézos, Anne-Morwenn Pastier and Anta-Clarisse Sarr, for the experience in the field, exchanges and contributions in this work. Our mates in Indonesia: Johan Anderssen, Meggi Romadona and Sthéphane Villière for all logistic, guide, funny times and the introduction in the Indonesian culture.

I thanks the entire team of the "Laboratoire de Planétologie et Géodynamique de Nantes". Specially Carola La for her support in mass spectrometry analysis, Laurent Lenta for his help and teaching with thick sections elaboration, all the reparations that we had to do in the micro-drill system an in general all technical help. Marion Rivoal for her help with U-Th series. Mélanie Douarin for her help at the beginning of the PhD in different aspects. To the secretaries of the lab (Marie-Claire Brehier, Stephanie Beaunay and Stephanie Hemery-Filipe) for their help in administration and bureaucracy. The ladies in charge of cleaning the laboratory. Erwan Le Menn and Pierre Gaudin for logistics. Éric Boeuf, Manuel Giraud, Sebastien Guiffan for informatics support.

To all my PhD, technician, ATER and postdoc colleagues of LPG, those who are now everywhere in the world, and for those who follow after me. Anaïs Schmidt, Jassin Petersen, Philipe Terra-Nova, Antoine Ba, Dorine Bouquet, Jihem Jellali, Elsa Cariou, Méric Haugmard, Jonas L'Haridon, Boris Chauviré, Maïwenn Lothodé, Ianis Gaudot, et al…

The internship students who participate in this project: Denovan Chauveau and Khristan Cuny for their help and contributions.

Élisabeth Michel, Fatima Manssouri, Fabien Dewilde, Edwige Ponsbranchu and Lorna Folio from the « Laboratoire des Sciences du Climat et de l'Environnement » (LSCE, Giff-Sur-Yvette), for the help and support in isotopic and Uranium-series chemistry analyses.

Our academic colleagues in Indonesia, Yuda and Imran Oemar for collaboration and exchanges.

Camilo Rojas (rollinga) for all this help in work art.

Special thanks' and gratitude to Lestien family for all their precious help and support in Nantes. Christelle, Mr Remi, Françoise, Vincent and Frederick.

To my daughter, my parents and my sister, my principal source of energy in the universe.

Gracias a la Pachamama y al universo por permitirme terminar este trabajo de investigacion. Un capitulo importante en mi vida profesional.

Para mi hija,
mis padres
y mi hermana.

Contents

Chapitre I. Présentation 17

Chapter I. Research context 18

1.1. Introduction and background 18

1.2. Climate change during the Quaternary 19

1.3. Western Pacific Warm Pool climate change over glacial-Interglacial timescale 22

1.4. ENSO 25

1.5. Paleo reef terraces 27

1.6. Tridacnidae 28

1.6.1. Phylogenetic history 28

1.6.2. Ecology 29

1.6.2. Environmental archive 31

1.5. Statement research 32

Chapitre II. Présentation 37

Chapter II. Study area and methods 38

2.1. The Geological setting and climatology of south east Sulawesi 38

2.1.1. Geologic history 38

2.1.2. Quaternary reef terraces 41

2.1.3. Modern climatic conditions 43

2.2. Field work and sampling 47

2.3. Shell Sample collection 48

2.4. Methodology on shells 49

2.4.1. Scanning for diagenesis 49

2.4.2. Shell thin sections 51

2.4.3. Sclerochronology 52

2.5. Environmental proxies and data 54

2.5.1. Isotopic analyses ($\delta^{18}O$ and $\delta^{13}C$) 54

2.5.2. Trace elements analyses 56

2.5.3. Environmental data 57

2.5.4. Data analysis 58

2.6. Conclusions ... 58
Chapitre III. Présentation ... 65
Chapter III. Geochemical proxy calibration ... 66
3.1. Introduction ... 66
3.2. Environmental signal in *T. squamosa* species ... 68
3.3. Environmental signal in *H. hippopus* species ... 81
3.3.1. Introduction ... 81
3.3.2. Methods ... 82
3.3.3. Results ... 82
3.3.4. Discussion ... 85
3.3.5. Conclusions ... 96
Chapitre IV. Présentation ... 101
Chapter IV. Chronology ... 102
4.1. Introduction ... 102
4.2. Methodology ... 103
4.2.1. Sampling and sample preparation ... 103
4.2.2. The basis of U-series radio-chronology ... 106
4.2.3. U-Th chemistry and ICPQ-MS analysis ... 108
4.2.4. Radiocarbon (^{14}C) ... 110
4.3. Results ... 110
4.3.1. U-series test in a *T. gigas* ... 112
4.3.2. U-series in corals ... 112
4.3.3. Analytical reproducibility ... 118
4.3.4. U-series and ^{14}C ... 119
4.4. Discussion ... 121
4.4.1. The impossibility of use giant clams for U-series ... 121
4.3.2. Defining the criteria for choice reliable ages from U-series ... 123
4.3.3. Regional uplift, dating and sea level consensus ... 126
4.3.4. Final chronology ... 132
4.8. Conclusions ... 133
Chapitre V. Présentation ... 139
Chapter V. Climate reconstructions of past interglacials ... 140
5.1. Introduction ... 140

5.1.1. Mean climate state during T-II/MIS-5 Interglacial 141
5.1.2. MIS-7 143
5.2. Methodology 144
5.2.1 Study areas (description) 144
5.2.2. Sample description 145
5.2.3. Geochemical analyses 148
5.3. Results 149
5.3.1. XRD and bulk/mean isotopic signature ($\delta^{18}O$ and $\delta^{13}C$) 149
5.3.2. Seasonal profiles of stable isotopes ($\delta^{18}O$ and $\delta^{13}C$) 151
5.3.3. Trace elements reconstructions (Mg/Ca, Ba/Ca and Sr/Ca) 153
5.4. Discussion 156
5.4.1. Isotopic comparison between fossil data 156
5.4.2. Seasonally resolved record of past interglacials 158
5.4.3. Trace elements variation 167
5.5. Conclusions 171
Chapter VI. Conclusions and prospects 177
References 183
List of Figures 213
List of Tables 217
Appendix 1. Shell Sample collection 219
Appendix 2. ICP-MS Standards fiability 225
Appendix 3. Trace elements profiles 231
Appendix 4. ^{14}C dating 253
Appendix 5. Growth rate comparison in fossils 257

Chapter I.
Research context

Chapitre I. Présentation

Comprendre l'évolution du climat à travers l'étude des dernières périodes glaciaires et interglaciaires, ainsi que les mécanismes qui génèrent ces changements est un sujet de recherche clé pour la civilisation contemporaine. En effet notre système climatique et en même temps toute la biosphère, connaissent des bouleversements essentiellement liés à la pression anthropique depuis le début de l'industrialisation. Étudier l'histoire récente de la Terre permet d'explorer la variabilité naturelle de notre climat, de mieux estimer l'évolution future et les actions que nous devons prendre pour y remédier. Ces progrès dans la connaissance dépendent de notre capacité à optimiser les apports au bien commun de la recherche scientifique. Dans ce travail, on se propose d'explorer la variabilité climatique à l'échelle saisonnière au cours des 250 derniers milliers d'années. Ces reconstructions climatiques sont obtenues à partir d'archives fossiles, échantillons prélevés dans l'archipel sud-est de Sulawesi en Indonésie, dans une région où des changements thermodynamiques majeurs influent grandement sur la circulation climatique globale.

L'objectif consiste à définir des fenêtres temporelles, à l'échelle saisonnière sur plusieurs années successives. Les études cherchent à comparer les climats sur des périodes interglaciaires analogues à l'actuelle. Pour cela, on utilise une archive fossile qui nous donne cette possibilité d'explorer le climat du passé à une échelle saisonnière sur plusieurs années successives — il s'agit de la famille des bénitiers géants Tridacnidae (Mollusca). Grace à leur longévité, à la déposition de bandes jour-nuit dans la coquille et à leur résistance à la diagenèse (bonne préservation), on peut réaliser différentes analyses géochimiques. On les utilisera comme traceurs de la variabilité environnementale, (ou « proxies ») pendant la période où ces coquilles (aujourd'hui fossiles) se sont formées. De cette façon on peut étudier l'évolution saisonnière de diverses variables climatiques et océanographiques (e. g. la précipitation, la température des eaux de surface), ainsi que les anomalies liées par exemple au phénomène ENSO (de son acronyme en anglais El Niño Southern Oscillation) sur les périodes de temps ciblées. Ces reconstructions paléoclimatiques sont comparables aux informations extraites de bénitiers modernes ; elles permettront de mettre en évidence les similitudes et les différences du système océan-atmosphère entre le passé et le présent, et dessiner ainsi un premier schéma évolutif concernant cette zone d'étude.

Chapter I. Research context

1.1. Introduction and background

Understanding the coupling between surface temperature, atmospheric CO_2 and sea level is critical for assessing future change on a warming planet (Dutton et al., 2015). This can be achieved through studies of the links and feedback processes between mathematical simulations and proxy reconstructions from past geologic periods of the Earth's history. Paleo-climate models take into account the past interactions between atmospheric and ocean circulation and ice sheet dynamics (e.g. Berger et al., 1998; de Boer et al., 2012). Similar climate models are used to assess the consequences of global warming on the Earth's environment (e.g. Friedrich et al., 2016; Kopp et al., 2016). Direct examination of climate and sea level records during past glacial-interglacial cycles from sedimentary and fossil archives include the use of different tools, for example geochemical proxies, organic compounds tracers and taxonomical fossil assemblages.

This PhD focuses on understanding the environmental control on chemical tracers in giant clam shells, and their potential use as proxies of past climate and oceanographic variations derived from fossil shells of the late Pleistocene. We explore a sensitive region to current climate evolution and oscillatory instabilities such as El Niño Southern Oscillation (ENSO): the southeast (SE) Sulawesi (Indonesia). Besides the importance of climate conditions and energy exchange between ocean and atmosphere, this region exhibits an interesting geological architecture to study last Pleistocene environments. On the coast line of SE Sulawesi and surrounding islands the geologic activity, characterized by significant tectonic uplift and erosion, has arranged a terrace sequences complex, or paleo-reefs, built through warm periods (transgressions and posterior highstands) of the Quaternary (Satyana and Purwaningsih, 2011; Pedoja et al., 2014). These paleo-reefs were tropical coral reefs similar to those found today and it is possible to find fossilized material, principally scleractinian corals, and the key for this work, well preserved shells of giant clams (Tridacnidae family, Mollusca).

In marine ecosystems, many invertebrates build an exoskeleton of calcium carbonate ($CaCO_3$) as for example corals, mollusk, foraminifera and some taxa of macro-algae's. In some cases these biogenic structures are secreted in equilibrium with the environments in which they growth (e.g.

Dodd, 1967; Berger, 1981; Grossman and Ku, 1986; Eagle et al., 2013; Fowell et al., 2016). The chemical signature of the environment is preserved in their skeletons, and over the time in the fossil record. Taking into account these parameters is possible to use these fossil structures as paleoenvironmental archives.

In this work, a sclerochronology approach associated with geochemical analyses of modern and fossil Tridacnidae shells are used to derive interannual resolved time series. The chemical proxies used here are: stable oxygen and carbon isotopes and trace elements. This enables to explore past seasonal changes and thereafter compare to modern conditions. Fossil corals are used to date the sequences of fossil reefs in which the fossil material was collected from which climate reconstructions are derived. Corals play an important role of this work because it is not possible to directly date fossil giant clams from the Pleistocene (>50 ka) using U-Th series (Ayling et al., 2017).

The exploration of SE Sulawesi to study different Earth evolution process (geodynamic, morphology and climate-oceanographic aspects) was started in 2012 by a research team from different French universities "L'Institut des Sciences de la Terre" (Grenoble University), "Laboratoire de Morphodynamique continentale et côtière" (Caen University) and "Laboratoire de Planetologie et géodynamique" (Nantes University) where this PhD is enroll. International collaboration was also developed with local researchers from Makassar University (Sulawesi) and the Indonesian Research Center for Geotechnology (Bandung, Java). The present work makes part of this project and aims to respond to aspects of climate and ocean interaction changes during past interglacial periods.

1.2. Climate change during the Quaternary

The Quaternary (Fig. 1.1) has been dominated by sequence of ice ages which provided the theoretical framework to explain successive sea-level changes (Murray-Wallace and Woodroffe, 2014). The onset of Pleistocene is characterized by succession of cold and warm periods, associated to repeated growth and decay of continental based ice sheets at high latitudes (Lambeck et al.,

2002). Constraining the precise timing and magnitude of these oscillations is essential in determining the causes of Quaternary climate change (Potter et al., 2004).

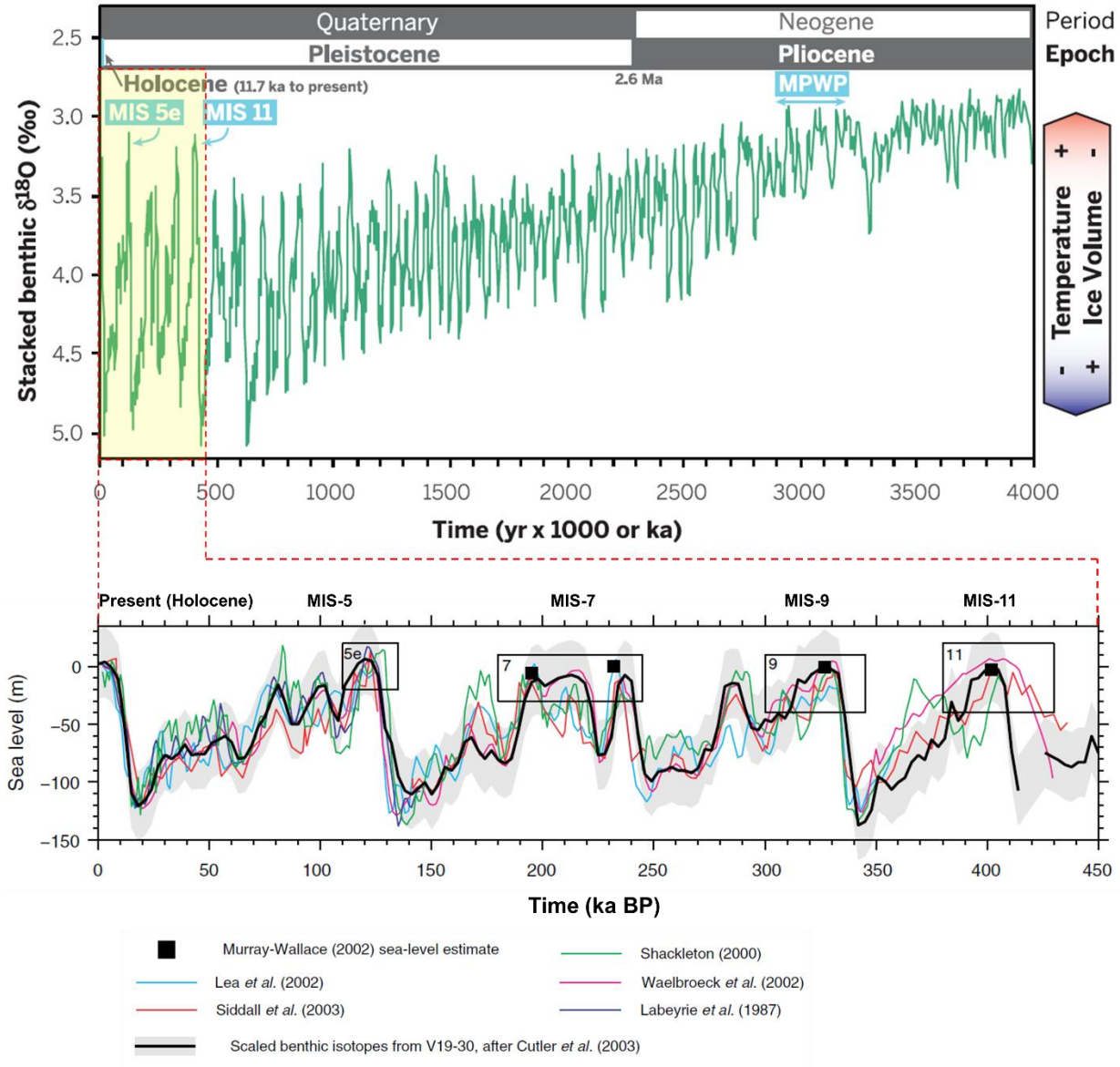

Fig. 1.1. Quaternary evolution. **Up panel:** Stacked benthic $\delta^{18}O$ with time periods discussed in text. **Bottom panel:** Continuous sea-level estimates on the SPECMAP timescale from a variety of sources, together with other sea-level indicators, compared with the benthonic isotope record. Marine isotope stages associated with interglacials are numbered. Figures taken and modified from Dutton et al. (2015) (up panel) and Sidall et al. (2006) (low panel) in The Climate of Past Interglacials encyclopedia (Elsevier, Amsterdam).

Planktonic foraminifera oxygen isotope ($\delta^{18}O$) profiles derived from sediment cores showed a succession of oscillations that were divided by Emiliani (1955) into isotope stages and interpreted

as successive warm and cold climates. Shackleton (1967) provided evidence that these $\delta^{18}O$ profiles were dominated by the effect of changes in the $\delta^{18}O$ composition of the global ocean and therefore implied changes in ice volume as well as temperature. These oscillations were referred to Marine Isotope Stage (MIS 1, 2, etc.) and were used to create a global stratigraphy for paleoceanography research across the Quaternary that are still used today (Shackleton, 2003) (Fig; 1.1).

Reconstructions of past sea-levels provide an estimate of variations in global ice volume and global climate (e.g. Chappell and Shackleton, 1986; Dutton et al., 2015). Several studies have provided estimates of sea level changes during the past Glacial-Interglacial climate oscillations. These studies converge on an average of 120m sea level rise from the last Glacial maxima (20 ka) to the Holocene (Waelbroeck et al., 2002; Schrag et al., 2002) (Fig. 1.1). Estimations of past rates of sea-level rise due to the melting of the continental ice sheets have been estimated and can reach up to 5m per century (Stanford, 2006; Rohling et al., 2008). The geological records of past sea level provide insight into the stability of polar ice sheets in the face of global climate change (Mitrovica et al., 2001; Hay et al., 2014).

However, the rise in sea level associated with ice volume melting is not uniform across the world. In the absence of tectonics, relative sea-level change reflects variations in global ice volume and the response of the Earth in the form of surface deformation and geoid changes, or "Glacio-Hydro-Isostasy" (Cathles, 1975; Lambeck and Nakada 1992). The form of this response to surface loading is dependent on factors including the size, distribution and melting history of the ice and water loads (Potter & Lambeck, 2003).

In this regard, the geological indicators need to be corrected for the perturbations in sea level associated with late Pleistocene glacial cycles (Hay et al., 2014). This process is known as "glacial isostatic adjustment" (GIA) (Lambeck and Nakada, 1992; Raymo et al., 2011; Dutton and Lambeck, 2012; Hay et al., 2014). The GIA correction fixed interglacial ice volumes to present day values, hence, any residual sea-level signals reflect excess melt during the interglacial (Hay et al., 2014). The objective is to obtain a "Eustatic sea level" (ESL) (e.g. Hay et al., 2013). In "eustasy", the solid Earth is assumed to be non-deforming. ESL reflects the uniform redistribution of meltwater after any accommodation space created by retreating (Gomez et al., 2010). The

marine-based accommodation space for meltwater will be largest at the onset of a given interglacial and smallest at the end of the interglacial (Hay et al., 2014).

The mechanisms driving climate and ice-sheet periodicity variation in different mean climate states remain the focus of much research today (Potter et al., 2004; Dutton et al., 2015). The Milankovitch theory describes that global ice volume and climate are dependent on orbital driven seasonal changes, though solar insolation received at high northern latitudes (Milankovitch, 1941; Hays, 1976). With periodicities of 41 ka (obliquity), 23 and 19 ka cycles (precession), 400 and 100 ka cycles (eccentricity). This theory explains gross features of global climate over broad glacial–interglacial cycles but is not able to account for rapid suborbital climate fluctuations, which seem related to internal Earth mechanisms (e. g. Bond and Lotti, 1995). Drew attention for alternative mechanisms to explain short period climate variability (Potter et al., 2004). Additionally, the Milankovitch theory do not predict the 100 ka cycle, which dominated the Middle and Late Pleistocene (Hays, 1976) (Fig. 1.1 down panel). The explanation for the shift from 40 ka (Early Peistocene) to 100 ka still eludes paleo-climatologists.

Tropical climate has been shown to have a strong response to precessional forcing, particularly reflected by changes in the hydrologic cycle (e.g. Clement et al., 2004), and has been hypothesized to have a dominant role on ENSO evolution (Timmermann et al., 2007; Liu et al., 2014).

1.3. Western Pacific Warm Pool climate change over glacial-Interglacial timescale

The Western Pacific Warm Pool (WPWP) is a maritime region in the western Pacific ocean where high sea surface temperatures (>28°C) nourish atmospheric convection and influence tropical climate (Linsley et al., 2010). Previous studies derived from sediment core records from the Maritime Continent (Malesia, Philippines, Indonesia, Papua New Guinea and Northern Australia) provide evidence for changes of precipitation and temperature on Glacial/Interglacial times scales. In one of the longest and most complete sedimentary records sampled in the Indonesian region (Core MD01-2378, last 460 ka in Timor Sea) Kawamura et al. (2006) demonstrated that reduced precipitation (dry conditions) and high primary productivity take place during glacial periods as result of weaker summer (north west) monsoon, whereas enhanced precipitation and reduced productivity are typical of interglacial periods. Kawamura et al. (2006) argued that the better explanation for those variations is the “orbital monsoon hypothesis”,

proposed first by Prell and Kutzbach (1987), in that, precession controls the long-term evolution of Indo-Australian monsoon system: during glacials the amplitude of austral summer insolation at 30°S was low, reducing the wet monsoon, while during interglacials the solar radiation was high (Fig. 1.2).

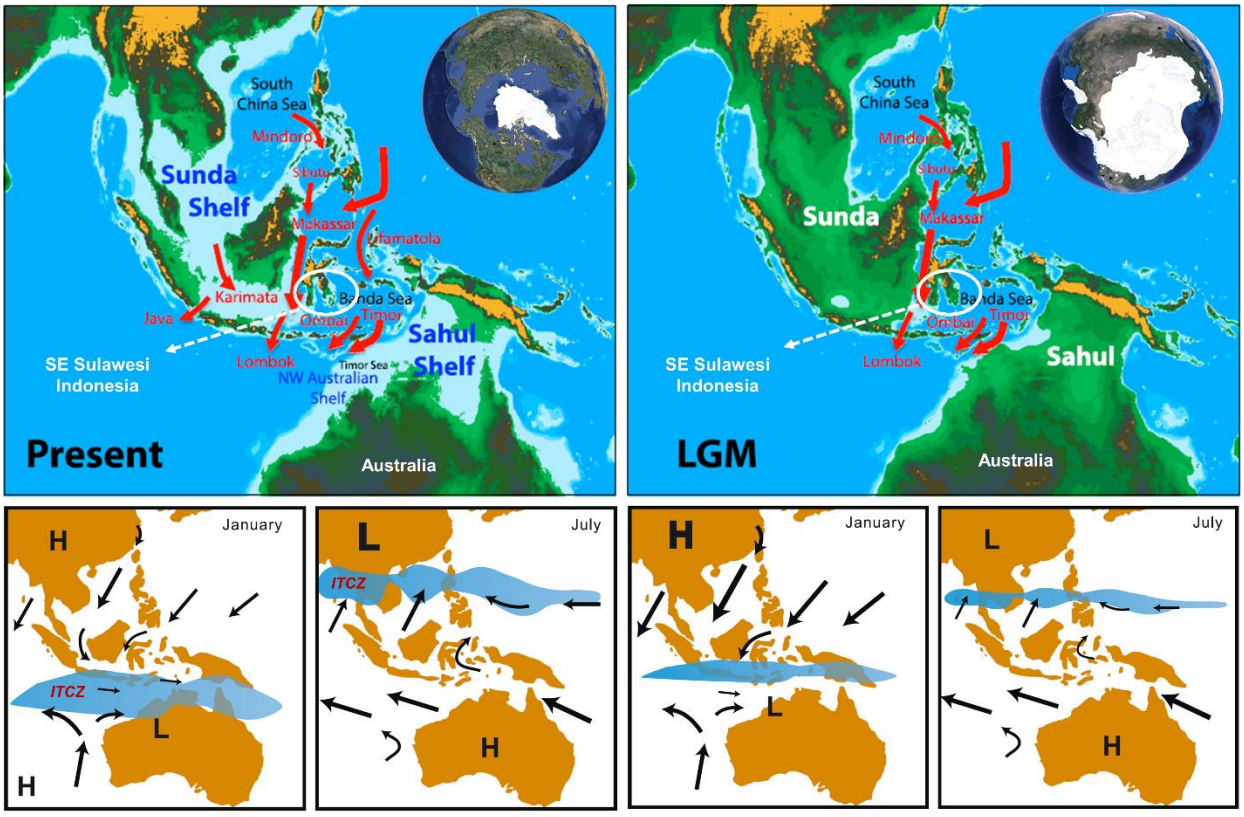

Fig. 1.2. Glacial-Interglacial changes in the WPWP. **Up panel**: Topography and bathymetry of the Maritime Continent and northern latitude in the Present day (left) and in the Last Glacial Maximum (LGM) (right). Red arrows indicate key passages of the Indonesian Throughflow. (Modified from Di Nezio et al., 2016). Ice sheets changes in northern hemisphere from NASA, 2016. **Bottom panel**: the modern (left) and inferred glacial (right) Australasian monsoon system (taken from Xu et al., 2006). **H:** High pressure. **L:** Low pressure. **Arrows:** migration.

In a sediment core located near Timor, Holbourn et al. (2005) showed that all used proxy (chemical indicators) closely tracks changes in paleoproductivity and are also in phase with the precessional band. Other studies on the Indonesian region (e.g. Beaufort et al., 2003; Tachikawa et al., 2011; Dang et al., 2015) also found the precessional influence on oceanograpchic and monsoon dynamics, as well the Intertropical Convergence Zone (ITCZ) shifts between glacial-intergalcials (Fig. 1.2 down panel). The sign of precession in paleoproductivity and upwelling reconstructions was also demonstrated in the east equatorial Pacific (Costa Rica) on the last 140 ka (Ivanova et al.,

2012). Other important factors, such as changes in landmass configuration associated with the glacial/interglacial changes in sea level also played a significant role on precipitation on the Maritime continent and contraction of the WPWP (Denniston et al., 2013; Di Nezio et al., 2016), in reason of important surface shelf exposed and submerged between glacial-interglacial (Fig. 1.2, up panel) modifying circulation parameters.

The climate proxy data from the last glacial period suggest that central Indonesia and Northern Australia were drier than present. This pattern of a dry and reduced WPWP is consistent with large-scale changes of the Walker circulation, with decreased ascending motion (decreased convection) over the Maritime Continent (Di Nezio et al., 2016). Modifications in the glacial state include increased SE monsoon and strength (Jian et al., 2001), position of winter and summer ITCZ closer to the equator with reduced precipitation (De Deckker et al., 2002), and absence of surface water flow from South China Sea into Java Sea because of an exposed Sunda Shelf (Di Nezio et al., 2016). Simulation and proxy record show that the southward shift of the ITCZ in boreal winter (Fig. 1.2, bottom panel) may have been considerably restricted during glacial times (Xu et al., 2006; Jo et al., 2014), and/or the Indo-Australian summer monsoon may have been drier because of cooler Indian Ocean water masses (Xu et al., 2008).

Low sea level in glacials also had an effect on the Indonesian Throughflow (ITF) and water mixing (Xu et al., 2006). In the current interglacial, the ITF transports an annual average ~16 Sv (1 Sv = 106 $m^3.s^{-1}$) of warm and low-salinity water from the WPWP and Indonesian-Malaysian archipelago into the Indian Ocean (Schiller et al., 1998; Gordon et al., 2003).
Müller and Opdyke (2000) demonstrate that paleo-productivity in Timor is inversely proportional to the strength of the ITF. Today on the WPWP the high precipitation creates a surface of low salinity, this layer stabilizes the upper ocean structure, resulting in low primary production in the region (Kawmura et al., 2006). During glacial periods, the reduction or absence of this low salinity cap would have enhanced the upwelling and productivity (Müller and Opdyke, 2000). Xu et al. (2008) proposed that synchronous changes in the SST and ice volume during the last two Terminations (deglaciations) were associated with cooling and freshening of thermocline waters of the ITF.

Indo-Australian hydrological cycle is sensitive to high latitudes. Massive intensification of the monsoon coincided with Southern Hemisphere (Antarctica) warming and intensified greenhouse

forcing over Australia during the atmospheric CO_2 rise at 12.9–10 ka BP (before the present) (Kuhnt et al., 2015). This period concerns the Early Holocene or the beginning of our current interglacial period (Fig. 1.1, up panel). Linsley et al. (2010) found that sea surface temperatures in the Indonesian region were about 0.5 °C higher (between 10 to 7 ka BP) than during pre-industrial times. However a return to dryer conditions occurred between 8.1 and 7.3 ka after the early Holocene runoff and SST maximum. In a core sediment from Flores Sea (Near Sulawesi Island), Muller et al. (2012) demonstrates the sensitivity of the region to climate processes in the Northern Hemisphere. This study indicates strong precipitation at 18-15 ka BP (in agree with Kuhnt et al., 2015) over the region during Heinrich event 1 (Iceberg discharge on Northern Hemisphere), the increase in precipitation is deduced by increased riverine sediment fluxes.

1.4. ENSO

The El Niño Southern Oscillation (ENSO) is an irregular interaction between sea surface temperature (SST) and atmospheric circulation (Bjerknes, 1969), that results in anomalous climatic and oceanographic conditions with catastrophic impacts on ecosystems and human society. The warm phase of the phenomenon is known as El Niño, and its cold phase as that of La Niña (Latif et al., 1998). ENSO is considered the most powerful source of interannual climate variability in the world (Latif and Keenlyside, 2009; Wolter and Timlin, 2011), even if it originates in the tropical Pacific area, it affects global climate circulation (Philander, 1983; D'Arrigo et al., 2006; Latif and Keenlyside, 2009).

Model simulations (Timmermann et al., 1999; Collins, 2000; Liu et al., 2014) and information derived from fossil corals (e.g. Corrège et al., 2000; Tudhope et al., 2001; McGregor and Gagan, 2004) and bivalve mollusks (Driscoll et al., 2014; Carré et al., 2014) confirm that ENSO activity has varied in the past and has increased to become more frequent in the last decades with respect to past centuries and millennia. Although there remain some uncertainties, recent research suggests the direct influence of greenhouse gases in frequency amplifications and unstable oscillation of La Niña (Cai et al., 2015) and El Niño (Cai et al., 2014; Ham et al., 2015).
In the contest of global warming, monitoring climate change in Indonesia becomes relevant because its vulnerability is the highest among Asian countries (Gutman et al., 2000; Measey, 2010).

The Indonesian region presents strong hydrographic changes related to ENSO during the dry season but undergoes weak changes (anomalies) during the wet rainy season (McBride et al., 2003). Several studies show that the ITF is influenced by ENSO, with a strong transport of surface waters and deeper thermocline during La Niña in the Makassar Strait, and a reversed situation during El Niño (Ffield et al., 2000; Sprintall et al., 2009; Feng et al., 2015).

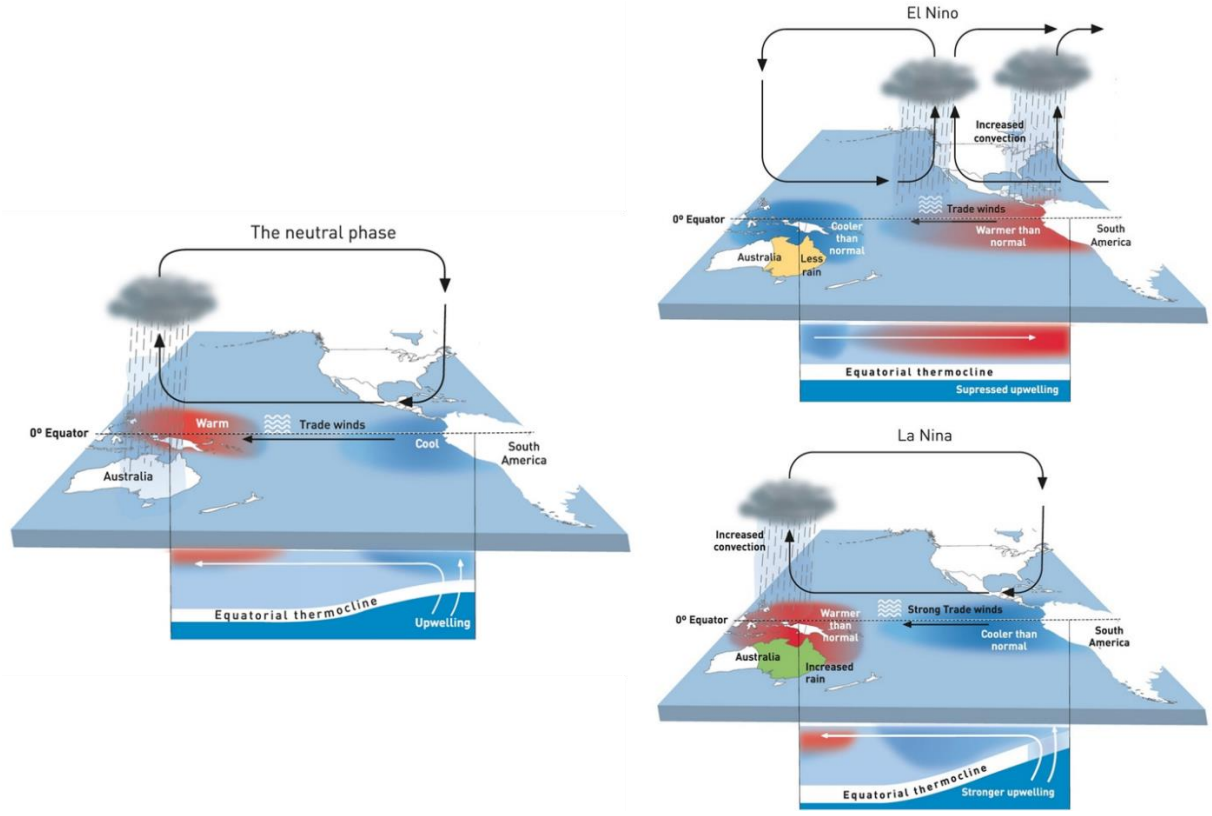

Fig. 1.3. ENSO phases over the Pacific Ocean. Modified from Australian government bureau of meteorology.

In the studied area, during El Niño conditions, SST becomes cooler than normal (Fig. 1.3) due to quickly reinforced easterlies and the significantly decrease of the Walker circulation (Hendon, 2003). As surface pressure and surface divergence increase rainfall activity drops (Nicholls, 1981). During La Niña conditions the opposite situation is observed (Fig. 1.3), convection is increased and SST is warmer than normal resulting in enhanced precipitation (Hendon, 2003; Cai et al., 2015). ENSO activity in Indonesia has become more frequent since the 1960's, the occurrence were 3 years or more between 1910 to 1941, and were around 2-3 years between 1961 à 1990 (Hamada et al., 2002). The influence of ENSO is more important in east than in the west of Indonesia. In south Sulawesi, rainfalls decrease by 46.2 % with respect to mean values, during El

Niño (Hamada et al., 2002). Conversely, during La Niña, rainfall amount increases by 20.8 %. However, on an interannual timescale, dry season anomalies are more spatially coherent and persistent than their wet season counterparts (Haylock and McBride, 2001; Hendon, 2003; As-syakur et al., 2014). The largest absolute monsoon interannual variability occurs at the end of dry season, when the strongest seasonal reversal winds blow across the Austral-Indonesian region (Hendon, 2003). There is a lack of correlation between rainfall and the Southern Oscillation Index (SOI) during wet season, contrarily to dry season (Haylock and McBride, 2001). Hamada et al. (2002) suggested that precipitation mechanism during wet season itself has no significant difference between El Niño and La Niña years.

Based on environmental data used in this PhD, in SE Sulawesi, El Niño event is reflected by SSTs around 0.9 °C colder than normal, and affect mainly the duration of seasons, shorter wet season and longer dry season, decreasing rainfall mean and a light increase of Sea Surface Salinity (SSS). La Niña is typically associated with SST's up to 0.8 °C warmer than normal during the dry season, increased rainfall duration and amount around 50 mm/month, and decreased salinity by 0.4 PSU.

1.5. Paleo reef terraces

Emerged reef terraces on tropical coastal areas are former living coral reefs, which are now sub-aerially exposed (Fig. 1.4) for different reasons: uplift in areas tectonically actives, the glacio-hydro-isostatic readjustments in deglaciations and glaciations, and lithospheric flexure (Cabioch, 2011).

A coral terrace corresponds to a reef flat surface, or a reef platform (Pirazzoli, 2005). Coral reef terraces result from the joint effects of bioconstruction, marine erosion at sea level and subsequent accumulation of the eroded sediments from the living reef (Schwartz, 2005). These terraces are erosional features with regressive encrusting corals, developed upon the transgressive reef (Pedoja et al., submitted). The multiple levels represent episodic and nonlinear uplift, which has occurred repeatedly in the late Quaternary (Pandolfi et al., 1994). The most common fossilized reef morphotypes are fringing reefs (Cabioch, 2011). In the paleo-reef terraces of tropical western Pacific coasts fossil Tridacnidae shells are found.

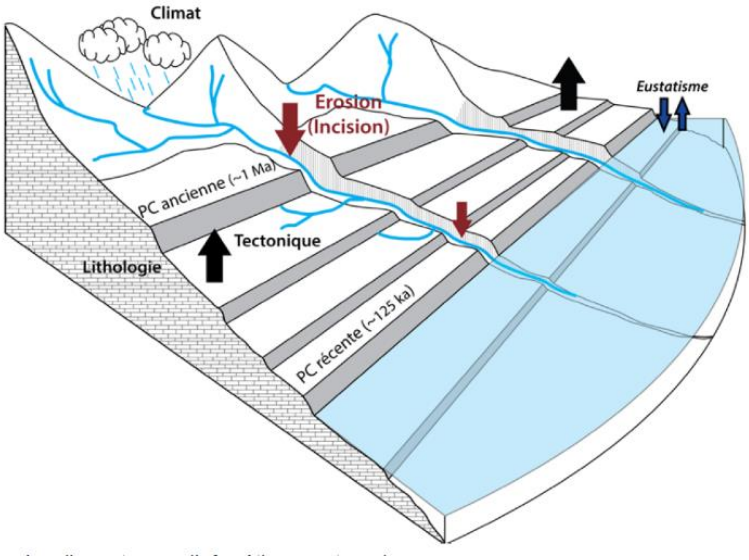

Fig. 1.4. Schematic coastal Paleo-reef sequences. The vast majority of compound paleo-coasts are frequently Middle and Upper Pleistocene. Modified from Pedoja et al. (2014).

1.6. Tridacnidae

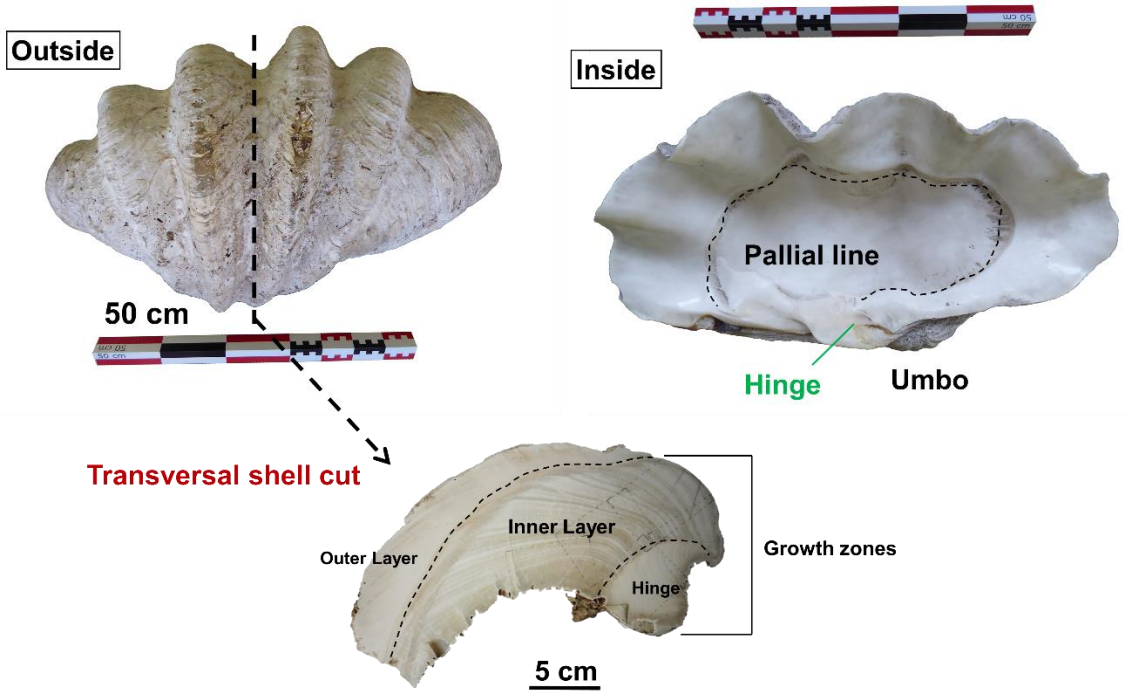

Fig. 1.5. *Tridacna gigas* shell, Tridacnidae family.

1.6.1. Phylogenetic history

Giant clams (family Cardiidae, subfamily Tridacnidae) are the biggest and fastest growing members among the class Bivalvia (Yonge, 1981; Schneider and Foighil, 1999). Tridacnines

appears in the Eocene in the Western Tethys (actual Europe), represented by *Goniocardium*, *Avicularium* and *Byssocardium* (basal extinct genera), and followed by the appearance of *Omanidacna* on the Arabian Peninsula during the Oligocene (Harzhauser et al., 2008). The actual family is composed of two genera. The genera *Hippopus* comprises of two species, *H. hippopus* and *H. porcellanus*. The genera Tridacna comprises ten species regrouped in 2 subgenera: a monophiletic group (*Tridacna* sensu stricto) composed of *T. gigas, T. derasa and T. tevoroa* (Schneider and Foighil, 1999), and *Chametrachea* composed of *T. squamosa, T. crocea, T. maxima, T. rosewateri* (Fig. 1.6), and the most recent species discovered *T. costata, T. noae* and *T. ningaloo.* It is generally accepted that *Byssocardium* was the common ancestor of modern live tridacnines (Stasek 1962; Schneider 1998, Harzhauser et al., 2008). *Hippopus* genera appears in the early Miocene and the rest of *Tridacna* starts to appear from the late Miocene (Harzhauser et al., 2008) (Fig. 1.6).

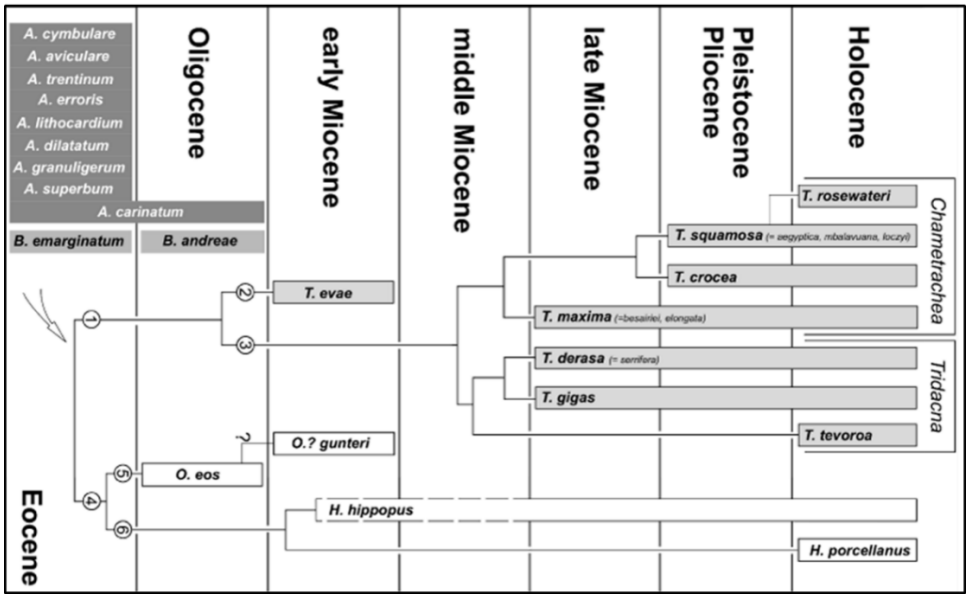

Fig. 1.6. Evolution and stratigraphic description of Tridacnidae family, including extinct genera (Omanidacna, Avicularium and Byssocardium). Numbers on lineages refer to morphological and supposed ecological features that distinguish clades. Modified from Harzhauser et al. (2008).

1.6.2. Ecology

Giant clams are iconic invertebrates that live in shallow coral reef environments (Griffiths and Klumpp, 1996; Hernawan, 2012) and inter-tidal habitats (Munro, 1989). They play important ecological roles as a food source and substrate for epibionts and reef-associated organisms (Neo et

al., 2015). A characteristic feature is the enlarged and brightly coloured mantle, which is packed with symbiotic microalgae. All species host symbiotic photosynthetic dinobiontes (*Gymnodinium spp*. and *Symbiodinium spp.*) (Mangum and Johansen, 1982; Norton et al., 1995; Hirose et al., 2006), for this reason they lives in relatively shallow and clear waters, such as those associated with coral reefs (Klumpp and Lukas, 1994). Tridacnines are mixothrophic organisms (capacity of exploit different ways of nutrition), heterotrophic by typical bivalve filtration and autotrophic with nutrient acquisition by symbiosis, this capacity confers them an unusually high proportion of energy for growth (Klumpp et al., 1992).

As symbiotic corals, Tridacnines are susceptible to stress-induced bleaching (expulsion of their photosynthetic symbiont) associated with increased sea surface temperatures (Norton et al., 1995; Leggat et al., 2003). Tridacnidae family is seriously threated or driven to extinction by the combined effects of overfishing, poaching, habitat degradation and increases in sea surface temperatures (bin Othman et al., 2010; Neo and Todd, 2013).

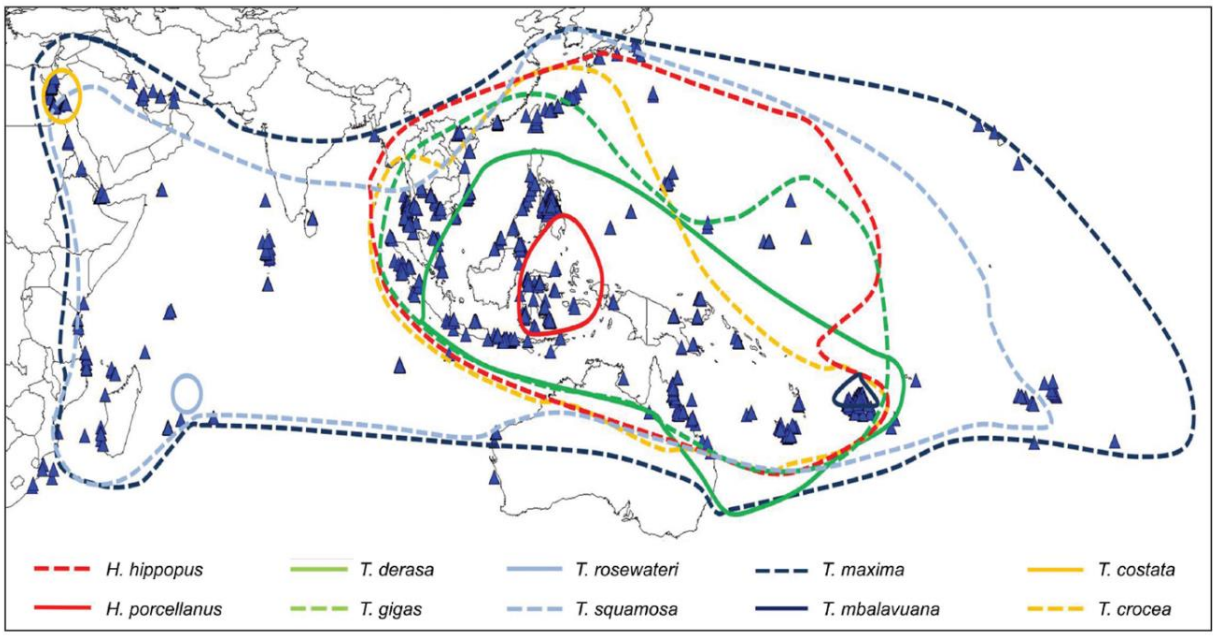

Fig. 1.7. Modern distribution of Tridacnide family among the Indo-Pacific area. The blue triangles represent reef check records without identification species. Taken from bin Othman et al. (2010).

Modern giant clams are present along different regions: French Polynesia, west Pacific, Indian Ocean coasts, South Africa and the Red Sea (Roswater, 1965; bin Othman et al., 2010; Hernawan, 2012). *T. maxima* has the largest distribution, whereas more recently discovered species (*T. costata*,

T. rosewateri, *T. teveroa* and *H. porcellanus*) have the most local distribution (Fig. 1.7). Among all countries where it is possible to find Tridacnines, Indonesia is the region with the highest density and diversity (bin Othman et al., 2010; Hernawan, 2012) (Fig. 1.7).

1.6.2. Environmental archive

The use of giant clams has taken importance in climatic paleo-reconstructions for tree main reasons: 1) the good representation in fossil record from late Quaternary and the actual presence (Fig. 1.6) allows to compare modern and fossil reconstructions, 2) The good preservation of chemical proxies in the massive aragonite shell, 3) Growth characteristics: the longevity (up to 60 years, Watanabe et al., 2004), the shell size and the shell daily growth deposition allow to perform chemical analyses with high resolution, obtaining seasonal interannual records, a fundamental aspect in order to study interannual phenomena as ENSO.

Initial research on modern and fossil Tridanidae shells as environmental archive (Aharon, 1983; Aharon and Chappell, 1986; Jones et al., 1986; Romanek and Grossman, 1989; Pätzold et al., 1991; Watanabe and Oba, 1999) applied stable isotopes of the oxygen and carbon to explore climate reconstruction with seasonal resolution scales. The importance of this archive was then exploited to study paleoclimate and paleoceanography conditions in different periods: Miocene (Batenburg et al., 2011; Warter et al., 2015), Last glacial (60-30ka) and Holocene (past 10ka) (Driscoll et al., 2014), middle Holocene (Watanabe et al., 2004; Sano et al., 2012; Hori et al., 2015), late Holocene (Yan et al., 2015), and interglacial MIS-11 (Ayling et al., 2015). Similar studies focused on anthropogenic impacts on coastal ecosystems using giant clam shells (Madkour, 2005).

These archives provide information on the mean climate and also the interannual variability related in particular to ENSO (Welsh et al., 2011; Driscoll et al., 2014; Ayling et al., 2015; Yan et al., 2016). These studies are mainly based on stable isotope profiles and trace elements proxy have also been measured (e.g. Elliot et al., 2009; Batenburg et al., 2011; Yan et al., 2013; Warter et al., 2015). And finally, Uranium-Thorium analyses with the aim to date the fossil Tridacnae and the reef terraces from which they are extracted (Accordi et al., 2010; Ayling et al., 2017). However, results show they cannot be used for accurate age assessment (Ayling et al., 2017).

1.5. Statement research

The objective of this work is to produce temporal high resolution records on multi-decadal time windows using schlerochronology and geochemical analyses in Tridacnidae fossil shells to interpret past climatic conditions from the last interglacials (MIS-5 and 7) because they are the most recent and analogue periods to current conditions. In order to compare the environmental differences between these periods and provide a first draw of past climate-ocean evolution for the SE Sulawesi.

This document is structured in five chapters. In Chapter II is described the geologic history of SE Sulawesi, the current climatic and oceanographic setting, the field work and sampling in Indonesia and the methodology applied in Tridacnidae shells. In Chapter III are presented the results of geochemical reconstructions on modern shells in order to calibrate and verify the reproducibility of the local environmental conditions using this archive. Chapter IV is consecrated to assess the chronology of this study. As giant clam shells cannot be used for dating through Uranium-series, this chapter is focused on coral dating. In Chapter V the results of fossil shell reconstruction are described, these fossils were dated at the early MIS-5 and the MIS-7. Finally are presented the conclusions, implications and perspectives of this work.

Chapter II.

Study area and methods

Chapitre II. Présentation

La zone étudiée dans ce travail de thèse correspond au Sud Est de l'Ile de Sulawesi (Indonésie) et comprends les archipels de Buton et Tukang Besi. Cette région se trouve à la jonction entre au moins 3 plaques tectoniques : les plaques Eurasienne, Pacifique et Indo-Australienne. La collision de ces trois plaques est toujours active et peut être constatée sur la zone côtière de ces archipels sous la forme d'une succession de paleo-récifs ou dépôts carbonatés émergés, et originaires du Quaternaire. Dans ces terrasses récifales, on trouve des coraux fossiles ainsi que d'autres composants faunistiques fossilisés et préservés, notamment des bénitiers géants (Famille Tridacnidae), l'archive climatique utilisé dans ce travail.

L'Indonésie est divisée aujourd'hui dans trois grandes régions climatiques, à cause de différentes processus climatiques mais aussi grâce à la forte variabilité dans la géographie des îles et le système de courants marines qui traversent cette région. Notre zone d'étude se situe dans une région climatique où les changements saisonniers de précipitation sont très forts. Ce régime est imposé par le mouvement de vents et le passage de la Zone de Convergence Inter-tropicale (ITCZ). Il existe une forte variabilité climatique à l'échelle interannuelle qui est lié à des phénomènes climatiques tels que le phénomène ENSO (El Niño Southern Oscillation). Une forte corrélation entre les variations de précipitations et la température des eaux de surface est aussi caractéristique sans cette zone.

Dans ce chapitre on présente les différents aspects physiques, climatiques et océanographiques de la zone d'étude. Ensuite on décrit comment le matériel fossile a été prélevé et traité au laboratoire. Des observations et des tests sur l'état de préservation du matériel (DRX : diffraction du rayonnement X) ont été effectués, suivis par la préparation des échantillons : dissection et mise en place de la zone interne de croissance de la coquille sous forme de lames minces sur verre. Le point de départ est basé sur la sclérochronologie : l'étude des périodicités des dépôts de croissance, stockées dans des parties dures accrétées ou exosquelettes de divers organismes existants ou éteints (e. g. bivalves). Cette approche permet d'obtenir un modèle de croissance et donc connaitre l'âge des spécimens étudiés.

Dans ce travail, différents types de traceurs chimiques (proxy) sont mesurés afin de reconstruire les conditions environnementales dans lesquelles les coquilles ont été secrétées. Deux techniques ont été utilisées pour extraire l'enregistrement du passé dans ces archives fossiles: le rapport isotopique de l'oxygène ($\delta^{18}O$) et du carbone ($\delta^{13}C$) d'un côté, et de l'autre, la teneur et variation de certains éléments trace par rapport au calcium (Mg/Ca, Sr/Ca et Ba/Ca).

Chapter II. Study area and methods

2.1. The Geological setting and climatology of south east Sulawesi

2.1.1. Geologic history

Indonesia is situated in a tectonically active area related to the presence of several subduction-zones (Gertissr and Keller, 2003). This region offers a unique collection of continental blocks, active and extinct volcanic arcs and associated subduction complexes, old and young ocean basins (Hamilton, 1979; Hall, 2002; Villeneuve et al., 2010). Based on the litho-stratigraphic succession, geological evolution and micro-paleontological information, Villeneuve et al. (2010) describe seven blocks within the three main tectonic plates on the region: the Eurasian (Sundaland), the Indian–Australian and the Pacific–Philippine Sea plate. Sulawesi Island is located at the junction of these plates (Barber and Crow, 2003) (Fig. 2.1). The triple junction is considered a geologic complex because it is situated in a zone of long-term subduction (up to 2000 km wide) and active deformation continues at present with important sutures (Hall and Wilson, 2000).

The tectonic configuration in Sulawesi is the consequence of multiple collision events between continental, ophiolitic and island arc fragments (Silver et al., 1983; Hall, 2002). Palaeomagnetic work supports that Sulawesi is composed of geographically distinct components (Haile, 1978; Sasajima et al., 1980; Ali and Hall, 1995). The island has been divided into several tectonic provinces (Hamilton, 1979): the West Sulawesi plutono-volcanic arc, the Central Sulawesi metamorphic belt, the East Sulawesi ophiolite and the microcontinental blocks of Banggai-Sula and Buton- Tukang Besi, where is placed the study area of this work (Fig. 2.1C).

The stratigraphy of Buton follows from its history as part of Australia-New Guinea continent (pre-rifting sequence), with a detachment (syn-rifting sequence) occurred before the Middle Triassic, posterior movement to its present location (syn-drifting sequence), and collision with SE Sulawesi (syn-orogen and post-orogen sequences) (Audley-Charles et al., 1988; Calvert, 2000). Final separation from Australia occurred in the Late Triassic or Early Jurassic, preceded by a transition from pre-rift to syn-rift sedimentation in the Middle–Late Triassic (Ali and Hall, 1995).

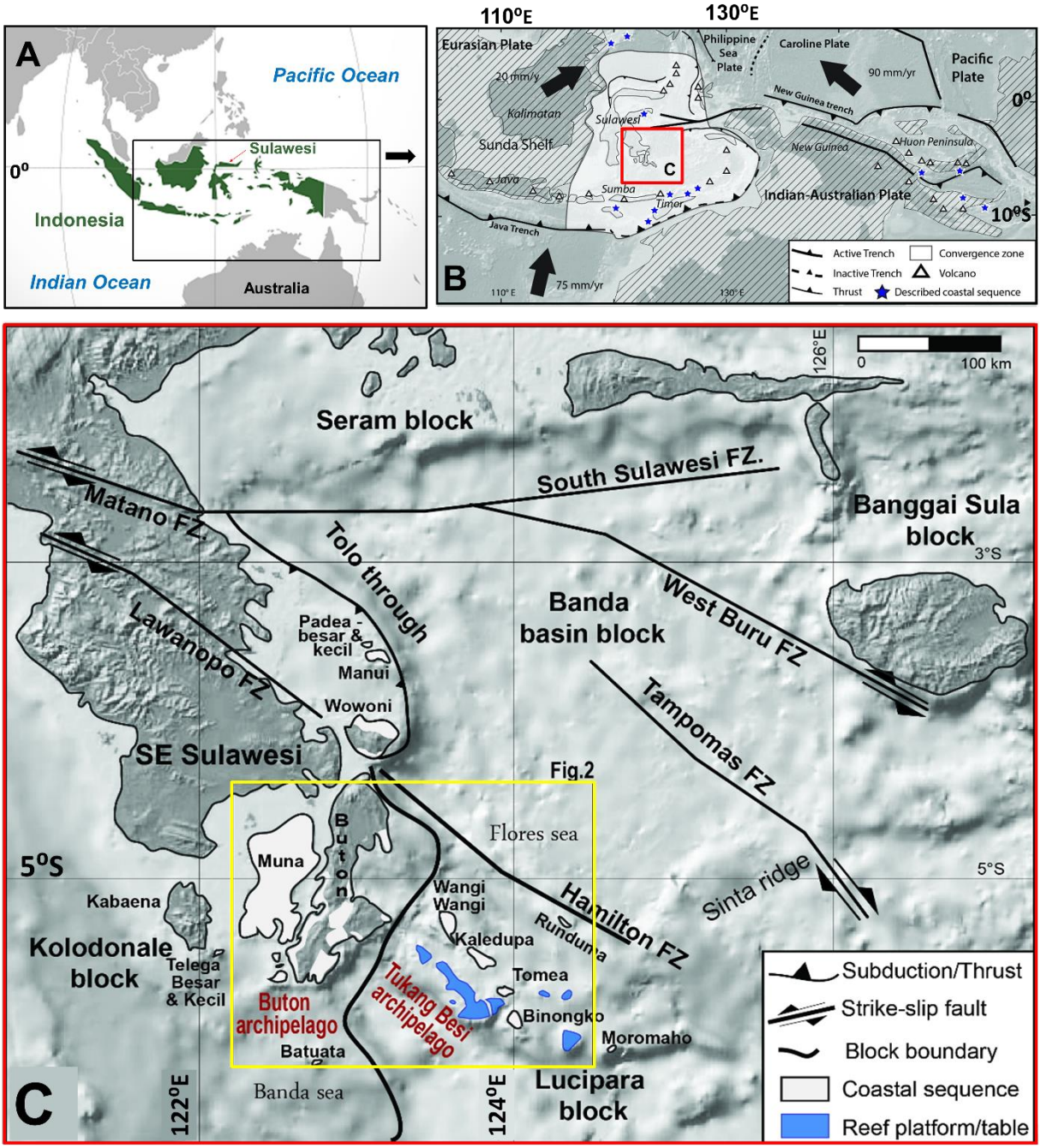

Fig. 2.1. Geological setting of SE Sulawesi. **A)** Geographic Position of Indonesia **B)** Zones of collision between the Eurasian, Indian–Australian and Pacific–Philippine Sea plates Geodynamics and coastal sequences described in the literature (data from Pedoja et al., 2014) **C)** Local tectonic setting and distribution of coral reef sequences (this study). FZ: fault zone. Sequences of marine and coral reefs are present on the following islands of the Buton archipelago: Telega-Kecil, Telaga-Besar, Batuata, Muna, Siumpu, Kadatua, Ular, Buton, Wowoni, Manui, Padea Besar and Padea Kecil and of the Tukang Besi archipelago: Wangi-Wangi, Kambode, Komponaone, Kaledupa, Hoga, Lintea, Tiwolu, Tomea, Runduma, Binongko, Moromaho as well as on the numerous islets nearby the main islands. Modified from Pedoja et al. (submitted).

Australian origin fragments (Buton-Tukang Besi and Banggai-Sula) collided with Eastern Sulawesi in the Neogene. Buton-Tukang Besi micro-continent collided with the SE Arm of Sulawesi/Muna Block from early Miocene until late Miocene (Davidson, 1991; Smith and Silver, 1991). In the Late Miocene, the subduction event was followed by accretion of Buton to Muna/SE Sulawesi (Milsom et al., 2000). Buton and Tukang Besi platform are two separate micro-continents (Fortuin et al., 1990; Davidson, 1991) (Fig. 2.1C). Gravity data suggested that in the east, Buton includes the almost entirely submerged Tukang Besi platform which separated from Buton as a response to post-collision extension (Milsom et al., 2000).

Active deformation throughout Sulawesi continues to the present day, with a continent–continent collision between the Eurasian (Sundaland) margin and fragments of the Australian continental margin (Silver et al, 1983; Villeneuve et al., 2000) (Fig. 2.1B). The junction between subducted oceanic crust and frontal micro-continents broke off and continental parts began to exhume by gravity tectonics, causing collisional uplifts (Audley-Charles et al., 1988). Evidence of deformation related to collision between Sulawesi, Buton-Tukang Besi and Banggai-Sula micro-continents is ongoing as confirmed by the continued uplift of Quaternary reef terraces at the SE coastal lines of Sulawesi and surrounded islands (Satyana and Purwaningsih, 2011; Pedoja et al., 2014; Pedoja et al., submitted).

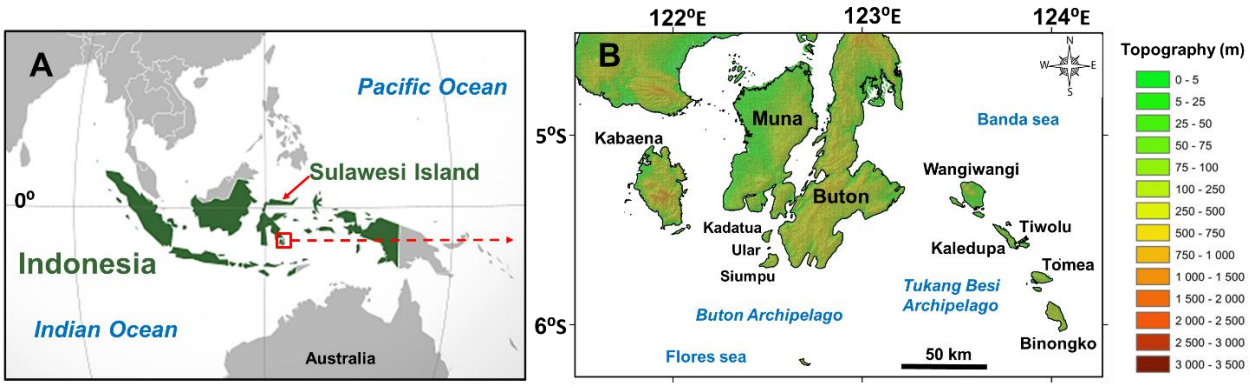

Fig. 2.2. The studied area: SE Sulawesi. **A)** Indonesia geographic position **B)** Zoom on SE Sulawesi

The modern geography of the studied area (Fig. 2.2-B) is surrounded by the Banda and Flores seas where multiple islands cluster in the Buton and Tukang Besi archipelagos. Tukang Besi area is composed of four major islands: Wangi-Wangi, Kaledupa, Tomea, and Binongko, abbreviated as "WaKaToBi isalnds". In Buton archipelago we found the Islands of Buton, Kadatua, Ular and Siumpu (Fig. 2.2-B).

2.1.2. Quaternary reef terraces

The coastal sequences of SE Sulawesi has not been studied in detail. Verbeek (1908) sketched the staircase coastal landscapes of Wangi Wangi and of the Sampolawa Peninsula (SE Buton). Kuenen (1933) analyzed the bathymetry of the Tukang Besi archipelago. Tjia et al. (1974) mentioned a sequence of 14 terraces on Tomea (Tukang Besi Archipelago). Fortuin et al., (1990) described 14 terraces on the Sampolawa Peninsula (SE Buton) and provided a dating of 182 ± 27 ka in SW Buton, in a terrace at 92 m in elevation. Finally, Satyana and Purwaningsih (2011) provided a distribution of the uplifted coasts of Sulawesi that includes brief morphological descriptions of Wangi-Wangi and SE Buton.

The coastal limestone architecture is the result of coral reef growth during high sea levels (transgression and posterior highstands) related to ice-sheets evolution (glacial-interglacial) through Quaternary period (Pedoja et al., 2014), and represent the start point of this work, because these paleo-reefs contain the fossil exoskeletons from marine invertebrates (scleractinian corals and giant clam shells), which are used as chronology indicators and paleo-climatic archives.

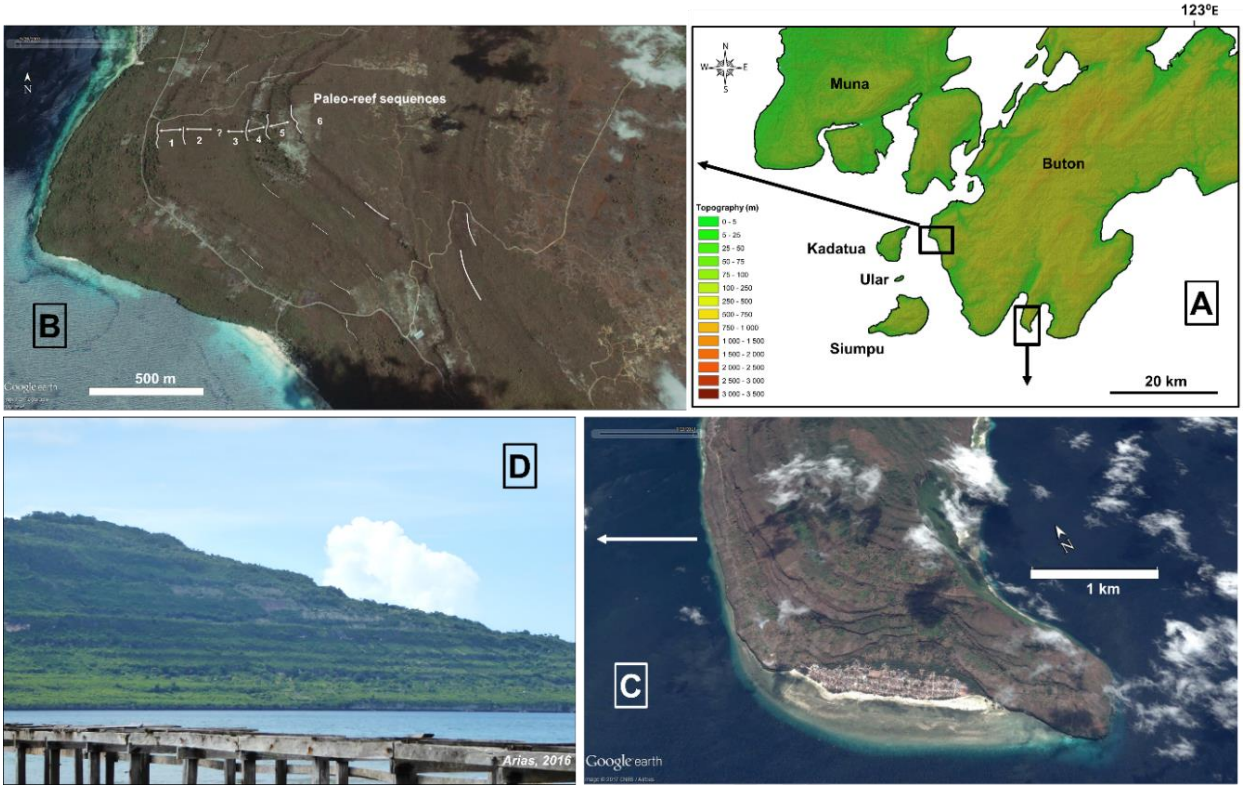

Fig. 2.3. Paleo-reef sequences **A)** SE Sulawesi Islands (Buton archipelago) **B)** Nirwana sequences **C)** Sampolawa Peninsula **D)** Frontal picture of Sampolawa. Images B and C from Google earth, 2017.

In SE Sulawesi. Pedoja et al. (Submitted) described alongshore various interplays between construction (e.g. modern reef crest of fringing reefs), deposition (coastal deposit, sand, coral rubble) and erosion of tropical limestone at sea level (carving of notch and shore platform). The fossil record (Holocene and Pleistocene strandlines) exhibits along-paleo-shore variations of erosional landforms, deposits and construction (Pedoja et al., submitted).

Slow to moderate uplift of SE Sulawesi leads to the formation and preservation of spectacular sequences of strandlines (Satyana and Purwaningsih, 2011) (Fig. 2.3C). Pedoja et al. (submitted) found a mean uplift rate in SE Sulawesi of 0.15 mm/yr, which confirms low uplift when compared with other regions as Huon Peninsula: 1.6 mm/year (McCulloch et al., 1999), or Barbados: 0.5 mm/yr (Radtke and Schellmann, 2006). This low rates in vertical speed can originate polycyclic terraces (e. g. Bard et al. 1990), in which it is possible to find paleo-reef formations from different periods in a same morphologic unity, this phenomenon can be accentuated by erosion. The uplift movement in coastal areas can be also discontinuous due to stepping motions (Pandolfi et al., 1994), with spatial or regional variations in vertical tectonic rates (Radtke and Schellmann, 2006). Numerous topographic features are thus the consequence of episodic coseismic uplift (Ota et al., 1993; Chappell et al., 1996).

The uplift of fossil coral terraces can be observed in the step-like sequence apparent in the landscape (Fig. 2.3-D). The geomorphology and the distribution of Pleistocene reefs suggest that south Buton is currently being uplifted while North Buton is now subsiding (Davidson, 1991). Quaternary uplift in southern Buton is expressed by spectacular flights of coral terraces rising to almost 500 m above sea level (Fig. 2.3). Maximum differential uplift between adjacent fault blocks is approximately 700 meters. Regional Quaternary uplift in south Buton is estimated at 2,500 meters (De Smet et al., 1989).

The Tukang Besi archipelago exhibits a wide array of coral reef morphologies, from platform and table reef, to fringing and barrier reefs (Satyana and Purwaningsih 2011). All islands are totally (e.g. Wangi-Wangi, Binongko) or partially (e.g. Kaledupa) covered by sequences of coral and marine terraces and associated notches with living reefs growing in the surrounding sea (Pedoja et al., submitted). Quaternary uplift of the central ridge is thus been comparable with uplift in southern Buton, but extensive atoll developments point to subsidence of the southern ridge (Satyana and

Purwaningsih, 2011). The morphological and paleoecological comprehension of paleo-reefs, coupled to coral dating give information on vertical motions, past sea-level variations and ocean-climate dynamics evolution over the Late Quaternary (Cabioch, 2011).

The numerous sequences of coral reef terraces in SE Sulawesi offers then an important source of information from fossil archives, relevant to study past climate and oceanographic conditions in this region.

2.1.3. Modern climatic conditions

Indonesia is a large maritime region where island topography and climatic diversity generated a wide array of climatic conditions. Aldrian and Susanto (2003) did a comprehensive study of precipitation and sea surface temperature in this area and recognized three different climatic regions over Indonesia (Fig. 2.4). SE Sulawesi is situated in an area where climate is strongly influenced by a double monsoon cycle: wet northwest (NW) monsoon, from November to Mars, and dry southeast (SE) monsoon from May to September, rainy and dry seasons respectively (Region A in Aldrian and Susanto, 2003).

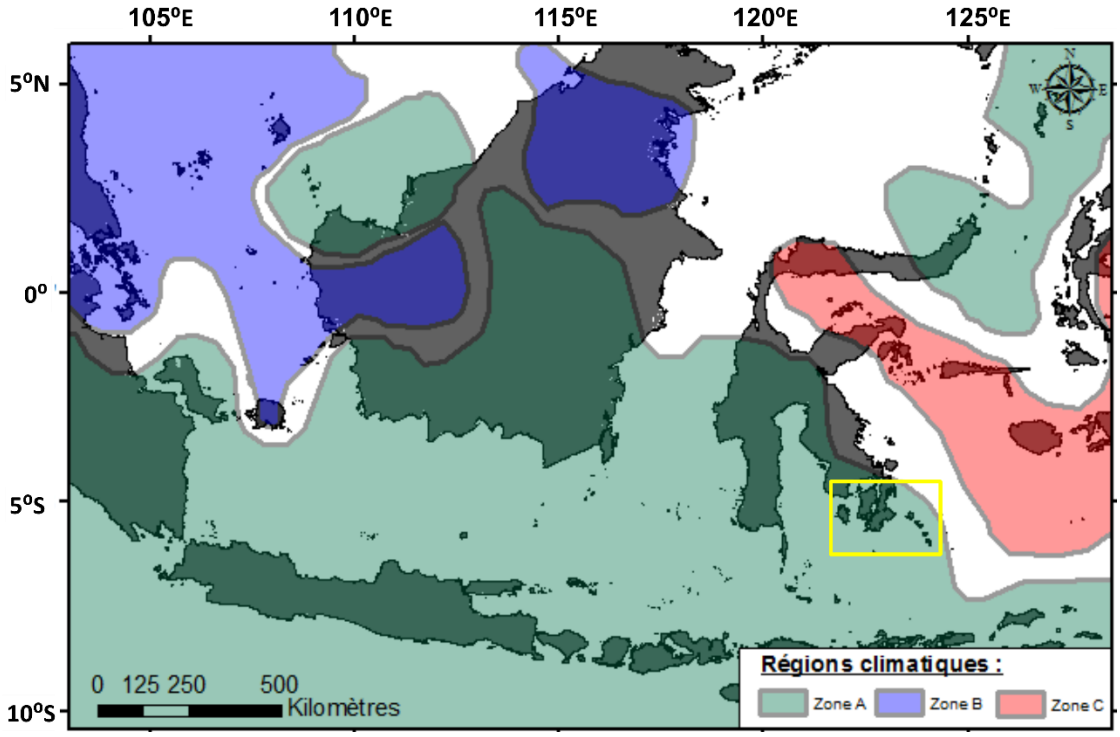

Fig. 2.4. The three climate regions in Indonesia. SE Sulawesi is located in Region A. Modified from Aldrian and Susanto (2003).

Among the tree climatic regions, Region A (Fig. 2.4) presents the largest extremes in the precipitation cycle. During the rainy season it is the wettest region with a precipitation maxima of 320 mm/month, and during the dry season it is the driest region with precipitation minima inferior to 100 mm/month (Aldrian and Susanto, 2003). This rainfall pattern is strongly correlated with SST annual variation (Lau et al., 1997; Susanto et al., 2001; Aldrian and Susanto, 2003). In the studied area from November to May with the NW monsoon, both rainfall and SST are maximum (wet season), and from June to October with the SE monsoon cold SST and rainfall minima (dry season) are registered (Fig. 2.6).

Sulawesi is located in the Western Pacific Warm Pool (WPWP) and is on the path of the Indonesian Troughflow (ITF, Fig.2.5-A), a sea surface current that plays an important role in ocean-climate system because the ITF is a significant component of global thermohaline circulation transporting sea surface waters from the Pacific to the Indian ocean (Schiller et al., 2010; Sprintall et al., 2014).

The WPWP plays a fundamental role in modulating the global climate change on interannual, millennial and orbital timescales (e.g. Godfrey, 1996; Lea et al., 2000; Koutavas et al., 2002; Visser et al., 2003; Medina- Elizalde and Lea, 2005). The high sea surface temperatures (SST $\geq$ 30°C) characteristic of the WPWP (Fig. 2.5) trigger ocean and atmosphere heat exchanges that set the Walker circulation (Kawamura et al., 2006). The location of the convective cell as well as the monsoon regime rely on the southward or northward motion of the Inter-tropical convergence zone (ITCZ) (Schneider et al., 2014) (Fig. 2.6). This "tropical belt of deep convective clouds" (Waliser and Gautier, 1993) is the source of excessive precipitation in the southern hemisphere tropics (Hwang and Frierson, 2013).

The hydrography of the WPWP region is strongly influenced by the semiannually reversed wind regime of the Asian-Australian monsoon and associated seasonal precipitation patterns (Fig. 2.6A-B). The Asian-Australian monsoon is a huge thermal circulation system driven by SST differences between broadly central Asia and Australia (Tapper, 2002; Xu et al., 2006).

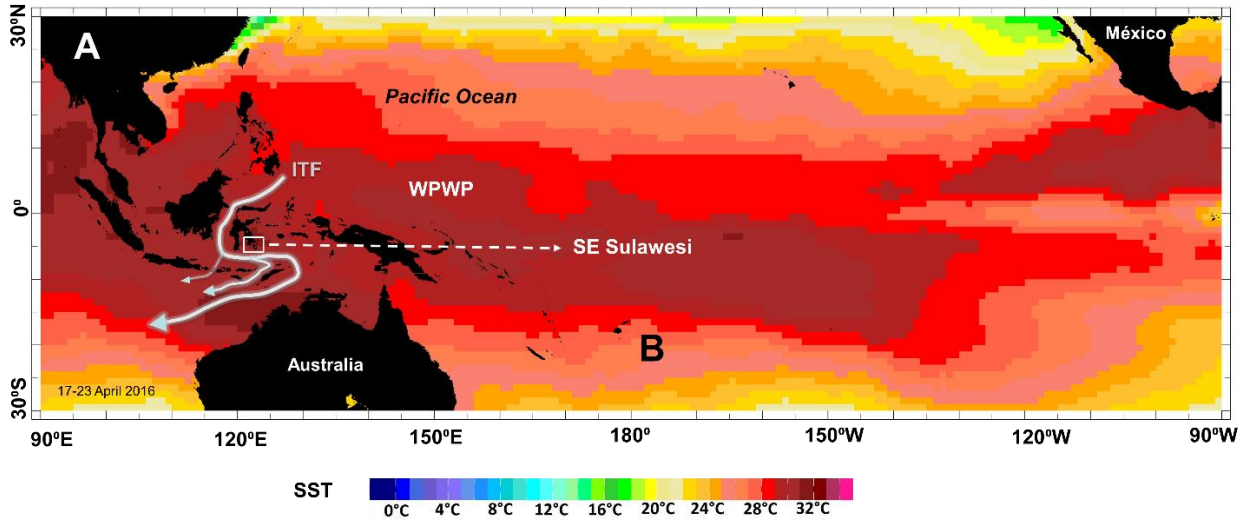

Fig. 2.5. Sea surface temperature (SST) distribution in the western Pacific Ocean. During northwest monsoon period (austral summer), with the position of Indonesia in the Western Pacific Warm Pool (WPWP) and the Indonesian Trough Flow. SST map was downloaded and modified from: http://iridl.ldeo.columbia.edu/SOURCES/.NOAA/.NCEP/.EMC/.CMB/.GLOBAL/.Ren_SmithOIv2/.weekly/.sst/.

Seasonal variation of ITF and SST is also associated with the variations (strength and direction) of monsoon winds (Sprintall et al., 2014). During the dry season (austral winter), south easterlies predominate over Indonesia and drive strong Ekman divergence increasing the ITF, whereas during the wet season (austral summer), warm westerly winds reduce the ITF (Sprintall et al., 2009; Sprintall et al., 2014). Strong westerly winds in the eastern Indian Ocean force equatorial downwelling Kelvin waves that propagate through the Indonesian passage (Susanto et al., 2001), downwelling increases sea level and reduces the flow from Pacific into Indian Ocean (Sprintall et al., 2009). The winds are relatively weak during the monsoon transition of March–April and October–November, as the ITCZ moves alternatively north and south across the region (Tapper, 2002) (Fig. 2.6C-D).

In South Sulawesi a peak in primary productivity is observed in August (dry season), this phytoplankton bloom reflects the persistence of local coastal upwelling, as a result of strong SE monsoon winds between June to August (Habibi et al., 2010). In the surrounding Sulawesi sea of Banda, Gieskes et al. (1990) also reported a peak of productivity in August after upwelling events induced by SE monsoon. These observations are in agreement with the local oceanographic data used here (Fig. 2.6).

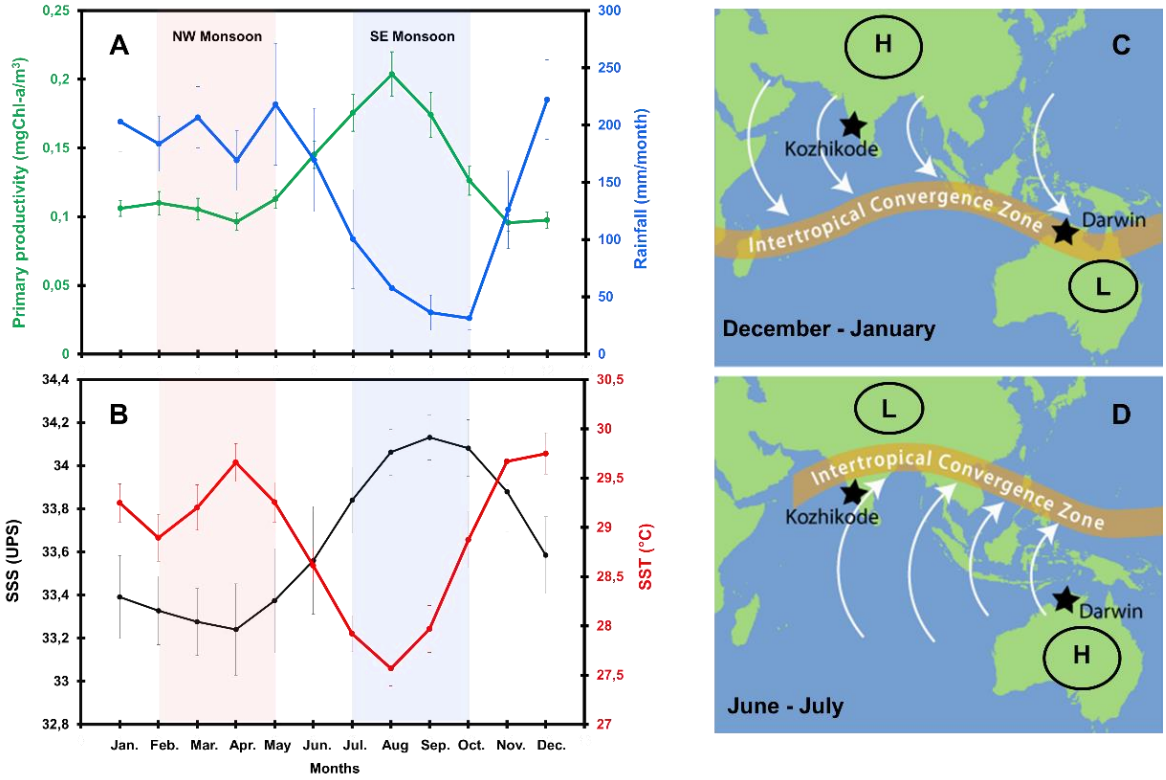

Fig. 2.6. Mean monthly climatological and oceanographic data for south Sulawesi. **A)** Precipitation and primary productivity behavior **B)** Sea surface temperature (SST) and Sea Surface Salinity profiles **C)** ITCZ position in wet season **D)** ITCZ position in dry season. H = High pressure, L= Low pressure. ITCZ migration from: http://monsoon.yale.edu/why-monsoons-happen/.

As described in Chapter I, a low salinity layer in this region plays as a barrier to primary productivity development (Kawamura et al., 2006), nevertheless, during the dry season with the strong southeasterly wind upwelling takes place (Susanto et al., 2001), this event increase the nutrient content in surface waters and therefore phytoplankton blooms are observed. The primary production in this region does not have the same magnitude as in important upwelling systems in the world (e.g. coasts of Chile and Peru) or as during glacial periods in the Indonesian region (e. g. Beaufort et al., 2003; Holbourn et al., 2005), but the phenomenon exists and present a seasonal pattern strongly correlated with SSS (Fig. 2.6-B) and anti-correlated to rainfall (Fig. 2.6-A).

2.2. Field work and sampling

A total of 26 Tridacnidae samples (Table 1.1) were collected from different islands around Buton archipelago (Buton, Muna, Kabaena and and Ular) and Tukand Besi archipelago (Wangi Wangi) (Fig. 2.2-B). From this collection, 3 samples are modern individuals and the other 23 are fossils from late Pleistocene. Modern samples were used to calibrate geochemical proxies and the local environmental conditions that the shells grew in (see calibration, Chapter III), and fossil samples were used for paleoclimate reconstructions (see Chapter V). The ages of fossil corals and shells are described in Chapter IV (Chronology).



Fig. 2.7. Field work, Tridacnidae shell extraction. **A)** Making shell cores with a shaw tool. **B)** Shell excavation, *T. gigas* fossil surrounded by a white dashed circle **C)** Incrusted shell on a paleo-reef **D)** Cut of shells for transport.

As often as possible complete shells were extracted (Fig. 2.7-B). This extraction can sometimes be difficult and requires spades and steel bars. Samples were sectioned in the field when possible (Fig. 2.7-D), given the considerable size and weight of the samples. For small size shells, valves were collected whole. In some cases, it was not possible to extract the specimen, a field drill

(Shaw backpack Drill) was used to extract cores in the inner layer growth part of the shell (Fig. 2.7-A), because it was complicated to extract the entire shell.

Additional material was sampled in Belitung Island (west Indonesia), one modern shell and one fossil from mid-Holocene (^{14}C dating). Belitung is located in a different climatic region (region C in Aldrian and Susanto, 2003, Fig. 2.4), for this reason these samples are just mentioned in this work, but they are the object of a research paper for publication (in prep), as a result of a master degree internship associated with this thesis.

2.3. Shell Sample collection

All samples were identified to lowest taxonomic level as possible. In Table 1.1 general information of sample collection is summarized. Images of complete collection are available in Appendix 1. For all samples, geographic position situation (GPS) and altitude were taken. For the modern shells GPS is approximate, as these were collected in local waste zone. Only clean samples that had been recently deposited were taken as they provide the most accurate date of death (no live Tridacnidae samples were sacrificed for this study). Indications of sampling area was provided by local inhabitants. The modern specimens were collected from modern coral reef areas by local fishermen. The material was extracted through collaboration with the University of Makassar and the Indonesian Institute of Sciences, Research Center for Geotechnology (Bandung, Indonesia).

Table 2.1. Sample information of Tridacnidae shell collection used in this work. The sample collection used in this work is part of a project funded to study the Geodynamics of Sea Level Evolution in Indonesia, for this reason the sample identity code is GSL (acronym), followed of the year (e.g. 2012) and the sample number (e. g. 01): GSL12_01 .

Id Sample	Classification	Type of sample	Location	Altitude (m)	Latitude (°)	Longitude (°)
GSL12_10	*Tridacna sp.*	1 segmented valve	Kadatua Island	20	-5,52696	122,477
GSL12_18	*T. gigas*	1 segmented valve	Nirwana (Buton Island)	19	-5,52249	122,568
GSL12_19	*T. gigas*	1 segmented valve	Nirwana (Buton Island)	19	-5,52249	122,568
GSL12_56	*Tridacna sp.*	1 segmented valve	Muna Island	18	-5,30536	122,642
GSL12_60	*T. gigas*	Core	Muna Island	23	-5,30594	122,642
GSL12_64	*Tridacna sp.*	1 segmented valve	Muna Island	23	-5,30594	122,642
GSL12_78	*T. gigas*	Core	Nirwana (Buton Island)	19	-5,52261	122,568
GSL12_79	*T. gigas*	1 segmented valve	Nirwana (Buton Island)	19	-5,52242	122,568
GSL12_80	*T. gigas*	1 segmented valve	Nirwana (Buton Island)	17	-5,52245	122,568
GSL12_81	*T. gigas*	1 segmented valve	Nirwana (Buton Island)	15	-5,52261	122,568
GSL12_82	*T. gigas*	1 segmented valve	Nirwana (Buton Island)	17	-5,52247	122,568
GSL12_83	*T. gigas*	Core	Nirwana (Buton Island)	19	-5,52235	122,568
GSL13_01	*Tridacna sp.*	1 segmented valve	Buton Island	4	-5,48498	122,564
GSL13_09	*T. gigas*	Core	Lakeba (Buton Island)	8,6	-5,49804	122,559
GSL13_56	*T. gigas*	Core	Wangi-wangi	9	-5,25260	123,552
GSL13_57	*T. gigas*	Core	Lakeba (Buton Island)	4	-5,49800	122,559
GSL13_73	*T. gigas*	Core	Ular Island	0*	-5,59285	122,507
GSL13_75	*T. gigas*	Core	Buton Island	8	-5,48532	122,5635
GSL14_07	*Tridacna sp.*	1 valve	Kadatua South	24	-5,56142	122,503
GSL14_12	*T. gigas*	1 segmented valve	Bahari (Buton Island)	15	-5,68200	122,719
GSL14_15	*Tridacna sp.*	1 segmented valve	Kadatua South	26	-5,56108	122,503
GSL14_19	*T. squamosa*	1 valve	Kabaena Island	modern	-5,23472	121,778
GSL14_20	*H. hippopus*	whole shell	Kadatua South	modern	-5,56479	122,504
GSL14_21	*Tridacna sp.*	1 valve	Ular Island	0*	-5,58982	122,514
GSL14_22	*T. maxima*	1 valve	Ular Island	0*	-5,58982	122,514
GSL14_23	*H. hippopus*	whole shell	Kadatua South	modern	-5,56479	122,504
BEL15_04	*T. squamosa*	1 segmented valve	Belitung Island	5	-2,552075	107,805
BEL16_10	*T. squamosa*	whole shell	Belitung Island	modern	-2,767963	107,530

* Sampled on the recent plataforme, on the swing tidal line

2.4. Methodology on shells

2.4.1. Scanning for diagenesis

The initial step is to check on the quality of sampled material. Screening for diagenesis is performed using X-Ray Diffraction (XRD). Transformation from aragonite to calcite are visible under electron microscopy (SEM images) (Fig. 2.8). XRD measurements provide a percentage of aragonite and calcite. Indeed, recrystallization of the aragonite skeleton into calcite as seen on Fig. 2.8 generates a loss of information, for this reason it is necessary to estimate the % calcite in order

to know if the material can be used for further analyses. A segment of the inner layer area of every sample was reduced to fine powder (with a mechanical grinder). A minimum of 100 mg is needed for XRD. Analyses were performed at the "Institute des Sciences de la Terre" (Isterre), Grenoble and GEOPS laboratory, (Université de Paris Sud, Orsay).

The XRD protocol was as follows: an inner layer fraction was ground, and the resulting slurry freeze/oven-dried to reprecipitate soluble salts before being prepared as a randomly oriented mount. The clay mineralogy was determined on the <2 μm fraction. Following the washing of soluble salts with pure water and the removal of organic matter with H_2O_2, as described by Moore and Reynolds (1997), this fraction was extracted by centrifugation. Oriented mounts were prepared by drying the resulting suspension onto glass slides. Ethylene-glycol (EG) solvation of the slides was achieved by exposing them to EG vapor at 50° C for a minimum of 12h. XRD patterns were recorded with a Bruker D5000/D8 powder diffractometer equipped with a SolXE Si(Li) solid state detector from Baltic Scientific Instruments using CuKα_1+2 radiation. Intensities were recorded at 0.0x° 2-theta step intervals from 20 to 90° (8 s counting time per step) and from 2 to 50° (4 seconds counting time per step) for bulk (and clay) mineralogy determination, respectively.

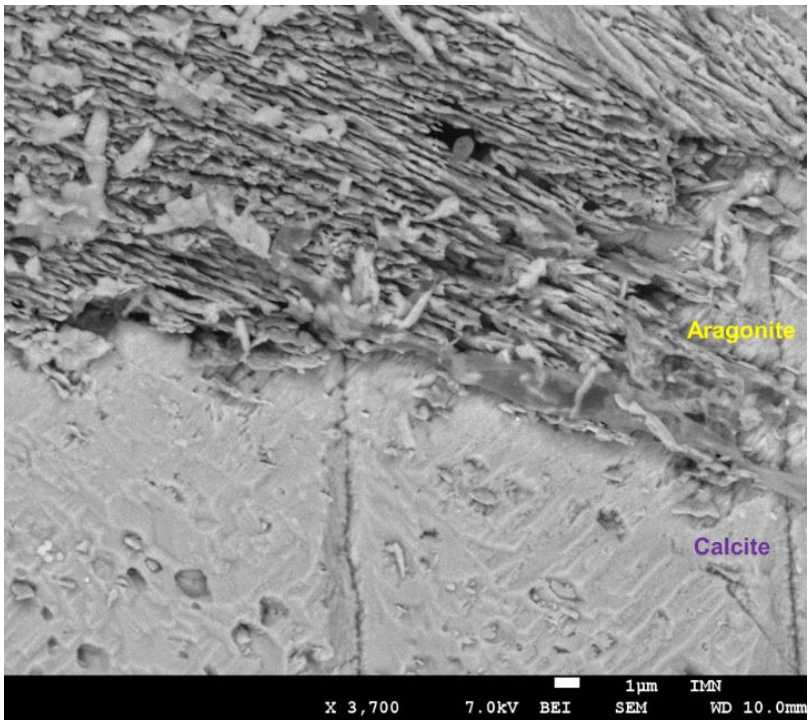

Fig. 2.8. Recrystallization from aragonite (up) into calcite (down). Electronic microscopic picture of a *Tridacna sp.* thick section. Institut Des Matériaux (Université de Nantes).

2.4.2. Shell thin sections

For all samples, a valve was sectioned using a rock saw (Fig. 2.10-A). The transversal cut run from the umbo to the ventral edge of the shell (Fig. 2.9-A). This cut reveals three growth zones: the inner layer and the outer layer separated by the pallial line, and the hinge, close to umbo (Fig. 2.11). The hinge and the inner layer are often well preserved compared to the outer layer which is more affected by bio-erosion and diagenetic processes (Elliot et al., 2009). The inner layer is the best part of the shell to reconstruct seasonal records because it presents highest resolution with respect to hinge zone and better preserved growth increments (Pätzold et al., 1991).

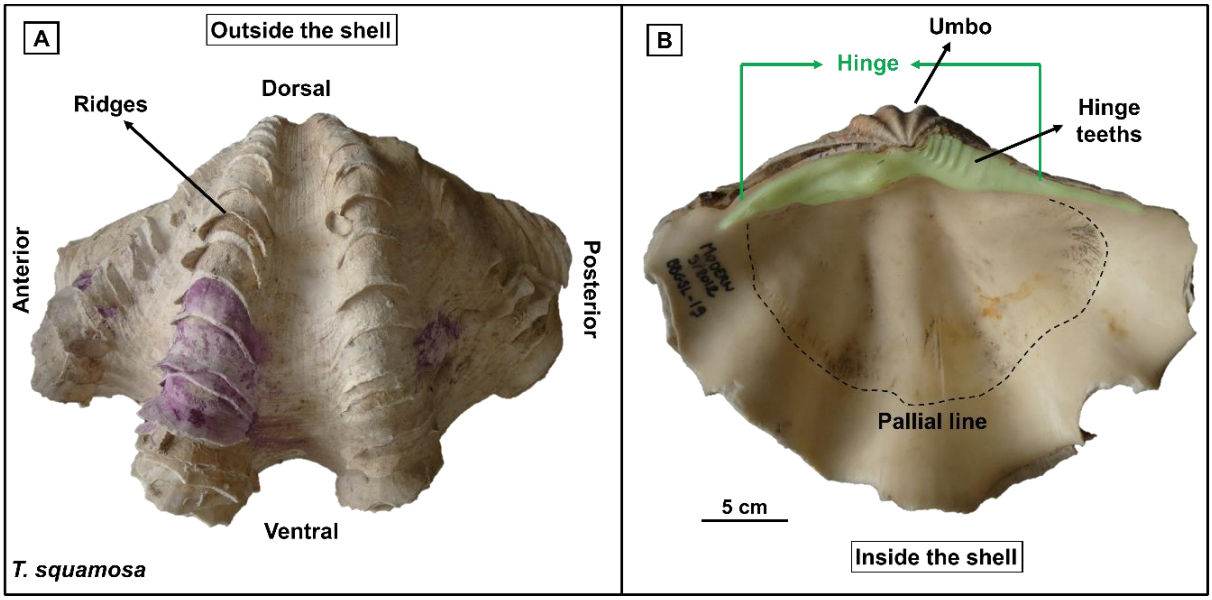

Fig. 2.9. Left valve of a *T. squamosa* specimen (GSL14_19). **A)** Outside part of the shell **B)** Inside part of the shell.

In order to perform sclerochronology and geochemical analysis, thick (1 mm) and thin (~ 30 µm) sections were obtained from the inner layer. Sections were polished to provide better surface uniformity. Optical observations were made on a 30 µm thin section (Fig. 2.10B), whereas a 1 mm thick section (Fig. 2.10-C) was used for laser ablation ICP-MS analysis and carbonate powder micro-sampling.

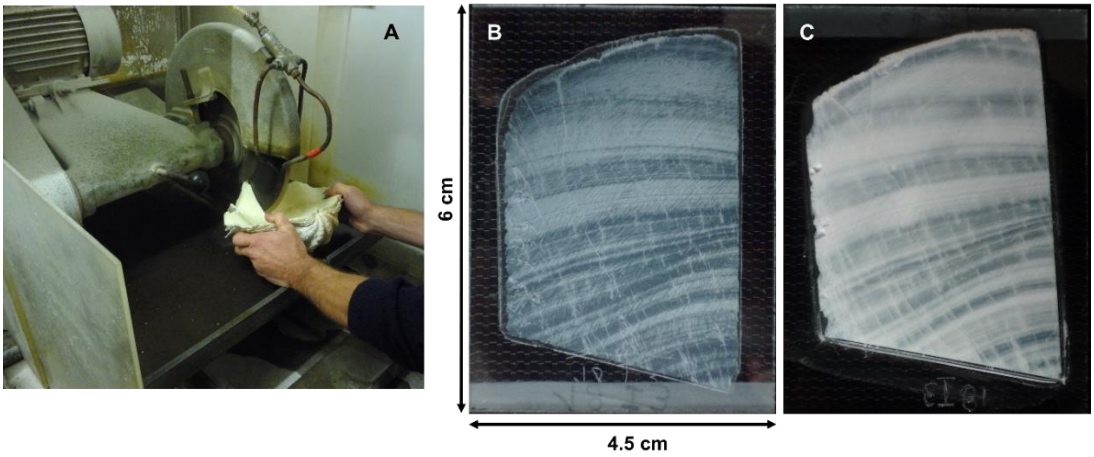

Fig. 2.10. Manufactured shell sections on glass slides. **A)** Rock saw machine **B)** Thin section and **C)** thick section.

For biggest samples such as *T. gigas* species, the inner layer was sectioned in 3 or 4 sections (Fig. 2.11), because there was a size limit in the cell of the laser machine (Fig. 2.13) for trace elements analyses.

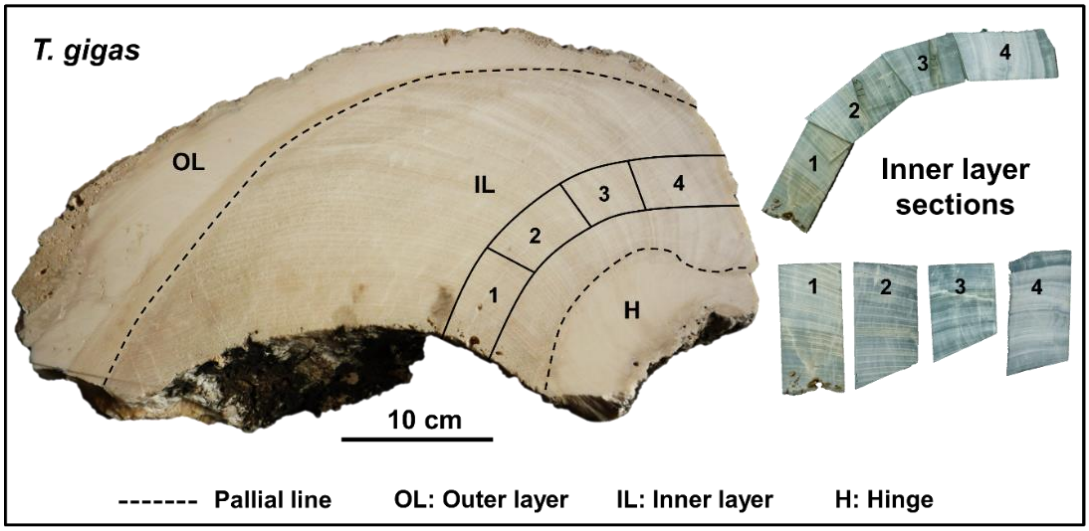

Fig. 2.11. *T. gigas* sectioned shell (sample GSL14_12). In this cut the 3 growth zones of the shell can be appreciated.

2.4.3. Sclerochronology

The term is derived from the Greek words *sklero* (or hard) and *chronos* (time) (Hudson et al., 1976). Sclerochronology is the study of past environmental conditions records stored in accreted hard parts and skeletons of various organisms, corals and bivalves are the most commonly used (Helmle and Dodge, 2011). Bivalve shells record the environmental conditions under which the

organism has grown, and in particular can provide a daily to annually resolved record of how those conditions have changed through the life of the shell (Helmle and Dodge, 2011), thus providing potentially long records of historical variations.

In giant clams, daily increments are visible at 20X microscope magnification (Fig. 2.12-B-C). These growth increments were counted on the inner layer thin sections every millimeter, following the relative chronological order define naturally from the umbo (first calcareous deposits or juvenile growth) to the internal zone (most recent increments adult growth), with an Olympus AX 70 Provi microscope coupled to a camera (Nikon DXM 1200F). The biometric software Lucia (Laboratory Imaging s.r.o., © 2016) was used to measure distances. Given the daily growth increment and its mean thickness defined in several key points of the thin section, it is thus possible to define the growth rate and the age of the organism.

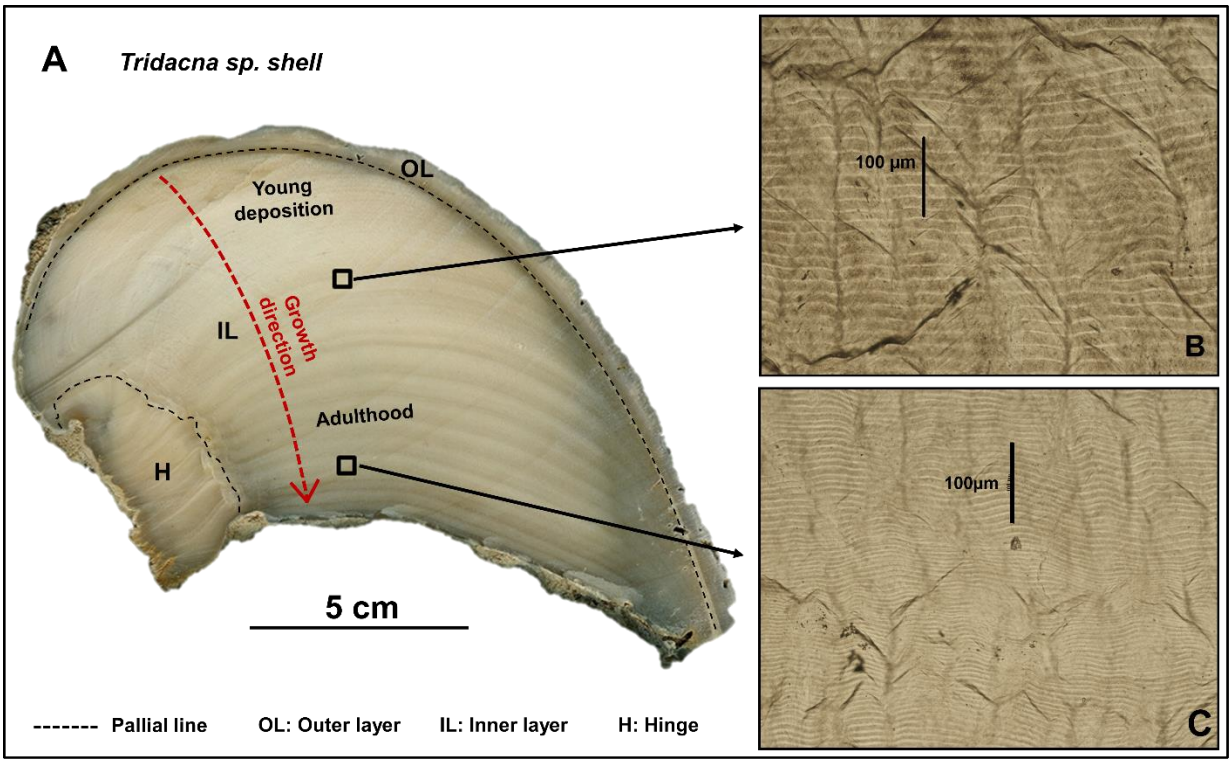

Fig. 2.12. Transversal cut of a giant clam Shell (simple GSL12_64) **A)** Section shell showing the 3 growth zones **B)** daily growth increments in the young part **C)** more packet increments in the adulthood.

Using the growth rate calculated every millimeter in the inner layer is possible to convert distance scale (mm) into time scale (years). For $\delta^{18}O$ micro drill sampling, the distances between

drill sample marks were converted into time, and for trace elements the distance obtained from the shots per second of laser ablation. This first age model based on the growth rate was used as guide, and then, the same techniques of Welsh et al. (2011) and Tynan et al. (2016) were used to assign a chronology. In these techniques it is assumed that the chemical proxies follow the seasonal change of a variable, for example SST for $\delta^{18}O$ and Mg/Ca. This conversion to age enables the comparison of geochemical profiles with temporal records of environmental data.

2.5. Environmental proxies and data

2.5.1. Isotopic analyses ($\delta^{18}O$ and $\delta^{13}C$)

Stable oxygen isotopic composition reflects two factors: water temperatures and the stable isotope composition of sea water ($\delta^{18}O_w$) (e.g. Shackleton, 1987). On long multi-millennial scale the $\delta^{18}Ow$ reflects changes in ice volume with roughly a 0.010 ± 0.001 ‰ m^{-1} (Adkins et al., 2002). There are small differences in paleo-temperature equations but most agree that there is roughly a 0.2 ‰ depletion in carbonate $\delta^{18}O$ for every 1 °C temperature increase for both calcite and aragonite (e.g. O'Neil et al., 1969; Aharon et al., 1991). On short timescales, the $\delta^{18}O_w$ (linearly related to salinity) reflects local changes in precipitation and evaporation balance, as well as river runoff (e. g. LeGrande and Schmidt, 2006; Rohling, 2013). The relationship between $\delta^{18}O_w$ and salinity thus shows a linear relationship that varies from tropical to high latitudes (LeGrande and Schmidt, 2006, Schmidt, 1998). In this work, the Fairbanks et al. (1997) equation is used and shows a +0.27 ‰ increase for every 1 PSU salinity rise.

Micro-sampling was made along inner layer thick sections, following growth increment bands (Fig. 2.12), with the aim to derive a profile with a seasonal resolution. A micro-drill automated system (Micro-Drill New Wave Research, Leica GZ 6) was used to sampling with micron resolution. In this study, due to restriction on the number of samples to be analyzed, carbonate powders were sampled on average every 200 to 400 µm, covering all growth zone. For oxygen isotopic analysis, a minimum powder quantity of 100 µg was processed. The drill micro sampling was performed only in 7 selected samples (Results on Chapter III and V). Bulk isotopic material was measured on all shell collection (Table 1.1) to know the mean isotopic state.

Powder samples were analyzed at "Laboratoire des Sciences du Climat et de l'Environnement" (Gif-Sur-Yvette) using an OPTIMA GV mass spectrometer with an acid bath automatic preparation line. Shell oxygen isotopes values are expressed relative to the isotopic ratio of the carbon dioxide gas derived from the Vienna Pee Dee Belemnite (VPDB) standard in conventional delta notation (δ). Ratios are reported in parts per mille (‰) following equation (1):

$$\delta X\ (‰) = ((R\ sample / R\ standard) - 1) \times 1000 \qquad (1)$$

Where **X** = ^{18}O or ^{13}C; and **R** stands for the heavy/light ratio between the abundances of any two isotopes (e.g., $^{18}O/^{16}O$ or $^{13}C/^{12}C$).

VPDB is defined with respect to the NBS 19 ($\delta^{18}O$ = –2.20 ‰VPDB), limestone standard. The mean external reproducibility (1σ) of carbonate standard is ±0.06 % for $\delta^{18}O$ and ±0.04% for $\delta^{13}C$. Measured NBS18 is –23.2 ± 0.2 % VPDB for $\delta^{18}O$ and 5.0 ± 0.1 % VPDB for $\delta^{13}C$.

Theoretical $\delta^{18}O$ shell values were estimated using the salinity-$\delta^{18}O_{water}$ relationship of Fairbanks et al. (1997) (equation 2) and the $\delta^{18}O_{shell}$-temperature equation (3) of Grossman and Ku (1986) in order to verify the isotopic equilibrium in the studied species.

$$\delta^{18}O_{water}\ (‰) = 0.2673 \times SSS - 9.14 \qquad (2)$$

$$SST\ (°C) = 21.8 - 4.69 \times (\delta^{18}O_{shell} - \delta^{18}O_{water}) \qquad (3)$$

Equation 2 was derived using tropical aragonite mollusk species and the salinity- SSS-$\delta^{18}O_{water}$ relationship of equation 1 was determined for the western tropical Pacific.

To interpret the fossil $\delta^{18}O$ profiles and bulk $\delta^{18}O$, the sea level component is extracted (Chapter V), which is based on accurate age determination of the samples. Chapter IV presents the chronology based primarily on U-Th dating, field observations and information about sea level and coral formation taken from the literature.

2.5.2. Trace elements analyses

Trace element analysis was carried out using a 193nm laser ablation system (Photon Machines, Analyte G2) equipped with an ablation cell (Hel Ex), coupled to a Varian 820 inductively coupled plasma mass spectrometer (LA-ICP-MS) at LPG Nantes laboratory. Thick sections were cleaned in ultrasonic bath of Mili-Q and dried prior to the introduction in the laser ablation cell. Laser ablations was performed in a Helium atmosphere. The ablated material from samples/standards was transported through a Teflon coated tube with flow rate of 1 $L \cdot min^{-1}$ into the Argon plasma, for ionization and subsequent analysis in the mass spectrometer.

The laser beam energy was set at 50 % of its maximum energy, which representing an average fluence of 5.54 J/cm^2 for an 85 µm diameter spot. The repetition rate was set at 10 Hz and the scan speed at 40 µm/s. Data were calibrated against the USGS reference glass material NIST 612 with the preferred values from Jochum et al. (2012). Any laser ablation profile is preceded by a pre-ablation profile (laser energy: 20 % and scan speed: 80 µm/s) to remove any surface contaminant. The NIST 612 was analyzed before and after each sample profile. These repeated analysis ensure the correction of instrumental drift if any. The detection limit (background level intensity plus 3 times its standard deviation) of each element, were all well the signals measured in our sample: Mg/Ca (0.2 mmol/mol), Sr/Ca (0.0004 mmol/mol) and Ba/Ca (0.0001 mmol/mol). The external reproducibility between analytical sessions was estimated over a period of 8 months by repeated measurements of USGS reference glass material NIST 610 (n = 20, over 4 analytical sessions) calibrated against the NIST 612 and yield reproducibility within 3.2 %, 1.6 % and 3.5 % for respectively the Mg/Ca, Sr/Ca and Ba/Ca ratios. We also used MACS-3 to test external reproducibility in the first 3 sessions. The standards concentrations (NIST-610, NIST-612 and MACS-3) measured here were compared with the recommended values of GEOREM ® (geochemical, environmental and biological reference materials) and Jochum et al. (2011), this results are available in Appendix 2.

All laser ablation measurements were made on the 1mm thick section from the inner layer. At least two parallel laser ablation tracks were performed on all samples in order to test the reproducibility of the signal.

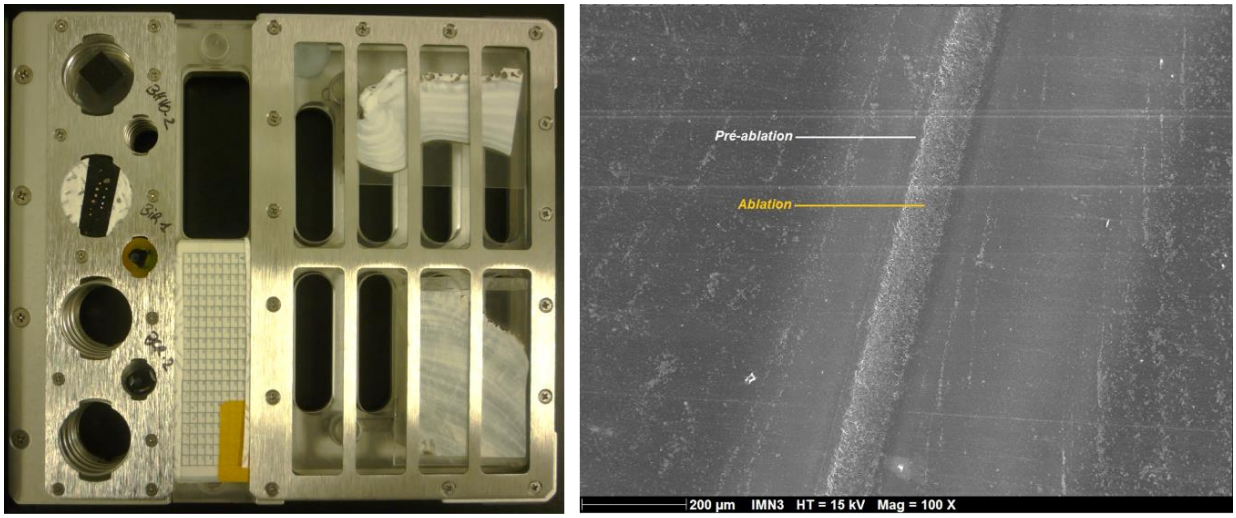

Fig. 2.13. Laser ablation. **Left**: Laser ablation cell (Hel Ex), in this cell only glass slides of the following dimensions can be used: 4.5 x 6 cm or 2.5 x 7.5 cm. **Right:** Laser ablation on a thick section (MEB).

The results from LA-ICP-MS were analyzed in a standard set of programming instructions archive (or macro) with a Visual Basic interface, performed by the informatics service of the LPG laboratory. The element/Ca ratio of the sample is corrected for the drift of the standards, and then the macro carries out the following calculation, aiming at directly transforming the reports from shot per second into ratios in mol/mol:

$$\left[\frac{emt}{Ca_{43}}\right](mmol/mol) = \frac{\left[\frac{emt}{Ca_{43}}\right]_{sample}}{SPS} * \frac{[emt]_{std}/M_{emt}}{[Ca_{43}]_{std}/M_{Ca}} \quad (4)$$

emt = element, M=Molar mass, SPS = Shoots per second

To minimize fine-scale noise, there data were smoothed by aver-aging 15 data points

2.5.3. Environmental data

The environmental data used in this work was downloaded from different databases (IGOSS, NOAA, CHIRPS and NASA). No *in situ* measurements were done. Four variables were used: sea surface temperature (SST) in degrees Celsius, precipitation in millimeter per month, and primary productivity in mg of Chlorophyll-a (Chl-a) per m^{-1}, and sea surface salinity (SSS). Salinity in the

ocean is defined as the grams of salt per 1000 grams of water. One gram of salt per 1000 grams of water is defined as one Practical Salinity Unit (PSU). All data comes from the same geographic area (Buton archipelago), comprised from 4.66°S to 5.33°S of latitude, and from 122.5°E to 123.75°E of longitude.

Data were downloaded respectively from the following sources.

Rainfall	http://iridl.ldeo.columbia.edu/SOURCES/.UCSB/.CHIRPS/.v1p8/.monthly/.global/.precipitation/
Productivity	http://giovani.sci.gsfc.nasa.gov/giovanni
Temperature	http://iridl.ldeo.columbia.edu/SOURCES/.IGOSS/.nmc/.Reyn_SmithOIv2/.monthly/.ssta
Salinity	http://iridl.ldeo.columbia.edu/SOURCES/.NOAA/.NCEP/.EMC/.CMB/.GODAS/.monthly/.BelowSeaLevel/.SALTY
Multivariate ENSO Index (MEI)	http://www.esrl.noaa.gov/psd/enso/mei/table.html

2.5.4. Data analysis

When different data was compared, normal distribution was tested with Shapiro-Wilk. Pearson (parametric) or Spearman (nonparametric) were used to know the correlation coefficient between the interested variables. To compare geochemical analyses with monthly environmental data, trace elements and isotopic records were resampled with a monthly scale using the software AnalySeries (Paillard et al., 1996), following similar conventional methods (e.g. Welsh et al., Driscoll et al. Tynan et al., 2016). Statistical tests were performed with the software PAST (Paleontological Statistics) 3.15, a software package for paleontological (stratigraphy and time series) data analysis (Hammer et al., 2001).

2.6. Conclusions

This work has used the combination of stable isotope measurements ($\delta^{18}O$ and $\delta^{13}C$) and trace elements (mainly Sr/Ca, Mg/Ca and Ba/Ca) measured on modern and fossil specimen. The age of the samples (number of years of growth) is defined by counting the daily bands which are visible

under an optical microscope and processed. The results derived from the modern specimens are presented in Chapter 3 which is a calibration study of modern samples from the study area. The fossil sample results will be presented in Chapter V following the chronology Chapter IV, in which The U/Th methods used to date each study site will be detailed.

Chapter III.
Geochemical proxy calibration

Chapitre III. Présentation

Dans ce chapitre, sont décrits les résultats obtenus dans l'étape de calibration qui consiste à tester la reproductibilité du signal environnemental, à partir de traceurs chimiques (proxys), mesurés sur des bénitiers contemporains. Deux espèces ont été utilisés : *Tridacana squamosa* et *Hippopus hippopus*, échantillonnées à la fois dans les iles de Kabaena et celles de Kadatua. Ce chapitre se subdivise en deux sections. La première partie est consacrée à la calibration de l'espèce *T. squamosa*. Ce bénitier a vécu et enregistré les conditions et la variabilité environnementale pendant 6 années, de 2006 à 2012. Des profils d'isotopes stables ($\delta^{18}O$ et $\delta^{13}C$) ont été obtenus sur la zone interne de croissance de la coquille. Sur la même partie de la coquille, des profils d'ablations laser ont été aussi obtenus afin d'étudier les variations temporelles des rapports en éléments trace : Mg/Ca, Sr/Ca et Ba/Ca. Les mesures isotopiques ($\delta^{18}O$) dans cette coquille confirment un fractionnement à l'équilibre, avec une influence très marquée du régime des pluies lors de la mousson d'été dans cette région (du sud-est de l'île Sulawesi). Les résultats concernant le rapport Mg/Ca et Sr/Ca se caractérisent par des variations saisonnières qui reflètent les températures des eaux de surface, avec une corrélation plus forte pour le Mg/Ca. La variabilité du rapport Ba/Ca semble principalement enregistrer l'apport en nutriment associé à deux sources : d'une part l'« upwelling » côtier avec une augmentation de la productivité et d'autre part le ruissellement continental quand les précipitations deviennent plus fortes. Des anomalies de tous les traceurs sont associées au phénomène climatique de La Niña en 2010.

La deuxième partie porte sur la calibration de l'espèce *H. hippopus*. La stratégie a été de comparer 2 spécimens contemporains de cette espèce, collectés le même jour sur le même site. Les résultats montrent une reproductibilité entre les profils du $\delta^{18}O$, du $\delta^{13}C$ et de Mg/Ca, mais pas pour le Sr/Ca et le Ba/Ca. Un des *H. hippopus* a enregistré aussi les anomalies environnementales associées à l'évènement de La Niña 2010.

Finalement, une comparaison inter-spécimen a porté sur la différence des résultats entre *T. squamosa* et *H. hippopus*. La variation saisonnière moyenne entre le $\delta^{18}O$ et $\delta^{13}C$ est la même pour les deux espèces, alors que le $\delta^{18}O$ chez *H. hippopus* présente des valeurs $\delta^{18}O$ en moyenne 0.2 ‰ inférieure — ce qui correspond à une différence de température moyenne de 1° C. Cette différence est attribuée à une différenciation d'habitat de ces espèces : pour *H. hippopus* dans la zone intertidale et pour *T. squamosa* dans la zone infralittorale. Avec le Mg/Ca on trouve le même signal de variation saisonnière mais avec des concentrations plus élevées pour *H. hippopus*.

Chapter III. Geochemical proxy calibration

3.1. Introduction

This chapter provides results derived from the shells of two Tridacnidae species (*Tridacna squamosa* and *Hippopus hippopus*) collected in Kabaena and Kadatua islands (Fig. 3.1). The largest species of the giant clam family (*T. gigas*) is useful for its size and longevity, however, it is currently threated in reason of over fishing and habitat degradation (Neo et al., 2015). So we cannot sacrifice a specimen to do a calibration study of this species. For this reason, we used species that can be found throughout the Indonesian area (see Fig. 1.6 in Chapter I, bin Othman et al., 2010). The status for *T. squamosa* and *H. hippopus* is "lower risk/conservation dependent" (Neo et al., 2015), so we focus on those species.

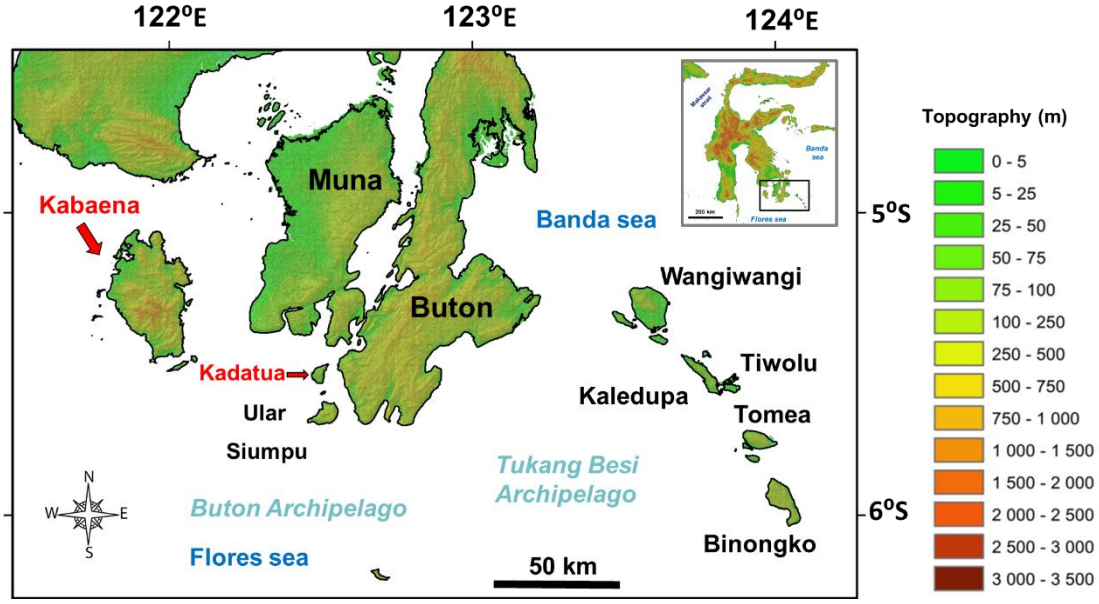

Fig. 3.1. Sampling locations. The samples used in this chapter comes from reef areas of Kabaena and Kadatua Islands.

Calibrations between modern samples and oceanographic data is vital for the interpretation of isotopic proxy record (LeGrande and Schmidt, 2006). Regarding shell trace element analyses, conflicting results are regularly obtained and element incorporation has been shown to be strongly influenced by physiological and taxonomic factors (Freitas et al., 2005; Carré et al., 2006). Important differences have also been reported between field and laboratory conditions (Gillikin et al., 2006) or in a geographic context for the same species in different hydrodynamic localities (e.g.

Lazareth et al., 2003; Tynan et al., 2016). For these reasons, target species have to be tested to provide a reliable bio-indicator of the local hydrographic context, in order to use it in environmental (paleo) reconstructions.

Previous studies of Tridacnidae shells for environmental applications suggest that different species of this family precipitate their aragonite shells at, or close to, the oxygen isotopic ($\delta^{18}O$) equilibrium in sea water, reflecting the combined effects of regional SST and water $\delta^{18}O_w$ (Aharon and Chappell, 1986; Watanabe et al., 2004; Welsh et al., 2011). In modern and fossil *T. gigas* (Welsh et al., 2011; Batenburg et al., 2011; Driscoll et al., 2014; Warter et al., 2015) it was confirmed the potential to reconstruct seasonally resolved climatic series and past ENSO anomalies. The latest advances in trace element analyses of giant clams show how ultra-high resolution can be achieved reflecting the daily light cycle (Sano et al., 2012; Hori et al., 2015) and tidal cycles (Warter and Müller, 2017).

The objective of this chapter consists in testing the local environmental reproducibility using geochemical tracers and their reliability as ENSO proxies in modern shells, a fundamental step to provide benchmark modern records, against which shells of fossil specimens will be compared (see Chapter V). These modern specimens are used to evaluate if shell $\delta^{18}O$, $\delta^{13}C$ and trace elements profiles (Mg/Ca, Sr/Ca and Ba/Ca) reliably reflect local environmental changes and verify if taxonomical, biological and geographical factors affect the shell's geochemistry. The aim is to test how the local changes in water temperature and salinity driven by changes in the monsoon-precipitation budget influence the $\delta^{18}O$ signal in the *T. squamosa* shell. Trace element analysis was performed to study the temperature dependence on shell Mg/Ca and Sr/Ca, as well as the relation between nutrient availability/productivity and shell Ba/Ca. Finally, this work provides evidence of environmental anomalies inferred from the geochemical signal (in all used tracers) during 2010. The 2010/11 La Niña was one of the strongest ENSO cold event in the past decades generating multiple impacts in oceanic and climatic conditions throughout the tropical and subtropical area of the Pacific Ocean (Nicholls, 2011; Boening et al., 2012; Hendon et al., 2014) and therefore provides an excellent setting to benchmark the relationships between ENSO anomalies and shell proxy data.

This chapter is divided in two sections. The first part presents the calibration study of *T. squamosa* (Arias-Ruiz et al., 2017). The second section provides an intra-species comparison between 2 *H. hippopus* individuals, and finally, the results from *T. squamosa* are compared to *H. hippopus* ones to test the inter-species reproducibility.

3.2. Environmental signal in *T. squamosa* species

Palaeogeography, Palaeoclimatology, Palaeoecology 487 (2017) 216–228

Contents lists available at ScienceDirect

Palaeogeography, Palaeoclimatology, Palaeoecology

journal homepage: www.elsevier.com/locate/palaeo

Geochemical fingerprints of climate variation and the extreme La Niña 2010–11 as recorded in a *Tridacna squamosa* shell from Sulawesi, Indonesia

Camilo Arias-Ruiz[a,*], Mary Elliot[a], Antoine Bézos[a], Kevin Pedoja[b], Laurent Husson[c], Sri Yudawati Cahyarini[e], Elsa Cariou[a], Elisabeth Michel[d], Carole La[a], Fatima Manssouri[d]

[a] Laboratoire de Planétologie et Géodynamique UMR 6112, 44300 Nantes, France
[b] CNRS, UMR 6143 M2C, F-14000 Caen, France
[c] ISTerre, Université de Grenoble Alpes, F-38014 Grenoble, France
[d] LSCE/IPSL, Laboratoire CNRS-CEA-UVSQ, 91198 Gif-sur-Yvette, France
[e] Indonesian Institute of Sciences (LIPI), Research Centre for Geotechnology, Sangkuriang, Bandung 40135, Indonesia

ARTICLE INFO

Keywords:
Tridacna squamosa
$\delta^{18}O$
Trace elements
Southeast Sulawesi
ENSO anomalies

ABSTRACT

We used a *Tridacna squamosa* (Tridacnidae, Bivalvia) shell that lived between 2006 and 2012 to reconstruct environmental conditions in South East Sulawesi (Indonesia). We focused mainly on estimating the influence of temperature and rainfall on the shell geochemistry, as well as ENSO anomalies. Comparison of the measured and theoretical $\delta^{18}O$ values show clear seasonal variations and confirms that this species secretes its shell at isotopic equilibrium. The $\delta^{18}O$ in *T. squamosa* shows how the increased rainfall associated with monsoon precipitations in this area influences the $\delta^{18}O$ shell signal during the rainy season, the correlation between shell $\delta^{18}O$ and SST ($r^2 = 0.62$) decrease in warm/wet seasons (SST > 28.5 °C). Shell Mg/Ca profiles presents better correlation with SST ($r^2 = 0.8$) than Sr/Ca profiles ($r^2 = 0.52$). Shell Ba/Ca ratio increases during each dry season when primary productivity is maximum. Secondary Ba/Ca peaks also occur during the certain wet seasons and appear associated with abnormal enhanced runoff. Shell $\delta^{13}C$ co-varies with primary productivity and salinity, with highest $\delta^{13}C$ values occurring during the dry seasons. During 2010–11, abnormal values were detected in all geochemical proxies as result of the strong La Niña event. This calibration study demonstrates the ability of *T. squamosa* shells to accurately reflect present day environmental processes with seasonal resolutions and to define the local signature of hydrological changes associated with ENSO.

1. Introduction

Sulawesi Island (Fig. 1) is located in a region characterized by major ocean-atmosphere energy exchange on seasonal and inter-annual timescales (Sprintall et al., 2014). Indonesia is a sensitive region to the current climate change because its extensive shorelines make it most vulnerable to global warming (Measey, 2010). Model simulations (Timmermann et al., 1999; Liu et al., 2014) and data derived from fossil corals (Corrège et al., 2000; Tudhope et al., 2001; McGregor and Gagan, 2004) and bivalves (Welsh et al., 2011; Driscoll et al., 2014) confirms that El Niño Southern Oscillation (ENSO) activity has increased to become more frequent in the recent decades with respect to past centuries and millennia. ENSO is considered the most powerful source of inter-annual climate variability in the world (Latif and Keenlyside, 2009). This phenomenon is originated in the tropical Pacific area, and consists of an unusual interaction between sea surface temperature (SST) and atmospheric circulation (Philander, 1983), that result in anomalous climatic and oceanographic conditions. In our study area cold SST anomalies/reduced rainfall are related to El Niño events and the warm SST anomalies/increased rainfall are related to La Niña events (Hendon, 2003; McBride et al., 2003), whereas it is the inverse in the eastern Pacific. Furthermore, the Indonesian region undergoes strong hydrographic changes related to ENSO during the dry season but undergoes weak changes (anomalies) during the wet rainy season (McBride et al., 2003). On an interannual timescale, dry season anomalies are more spatially coherent and persistent than their wet season counterparts (Haylock and McBride, 2001; Hendon, 2003; Assyakur et al., 2014). The largest absolute monsoon interannual variability occurs at the end of the dry season, when the strongest seasonal reversal winds blow across the Austral-Indonesian region (Hendon, 2003). There is a lack correlation between rainfall and the Southern Oscillation Index (SOI) during the wet season, contrary to the dry season (Haylock and McBride, 2001). Hamada et al. (2002) suggested that the precipitation mechanism during the wet season itself is not

* Corresponding author at: Laboratoire de Planétologie et Géodynamique UMR 6112, 2 rue de la Houssinière, 44300 Nantes, France.
E-mail address: hernan.arias-ruiz@univ-nantes.fr (C. Arias-Ruiz).

http://dx.doi.org/10.1016/j.palaeo.2017.08.037
Received 7 April 2017; Received in revised form 21 August 2017; Accepted 27 August 2017
Available online 31 August 2017
0031-0182/ © 2017 Elsevier B.V. All rights reserved.

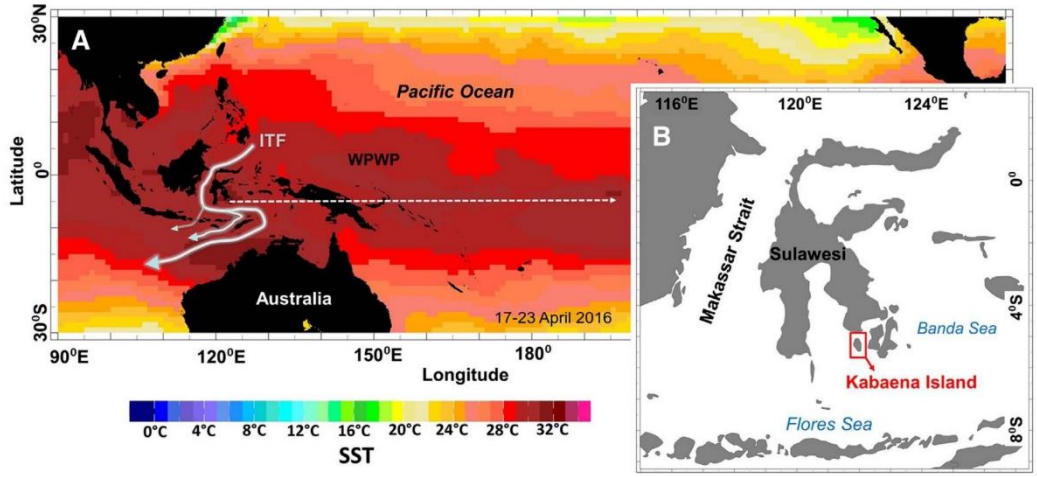

Fig. 1. Map of general study area A) Sea surface temperature (SST) distribution in the western Pacific Ocean at northwest monsoon period (austral summer), and the convergence of the Western Pacific Warm Pool (WPWP) and the Indonesian Trough Flow (ITF) in Sulawesi B) Position of the sampling area: Kabaena Island. SST map was downloaded and modified from: http://iridl.ldeo.columbia.edu/SOURCES/.NOAA/.NCEP/.EMC/.CMB/.GLOBAL/.Ren_SmithOIv2/.weekly/.sst/.

significantly different between El Niño and La Niña years.

Several studies show that the Indonesian trough flow (ITF) (Fig. 1A) is also influenced by ENSO, with a strong transport of surface waters and deeper thermocline during La Niña in the Makassar Strait, and a reversed situation during El Niño (Ffield et al., 2000; Sprintall et al., 2009; Feng et al., 2015). ENSO activity in Indonesia has become more frequent since the 1960s, and its influence is more important in the east than in the west (Hamada et al., 2002).

The use of long-lived organisms like giant clams (Tridacnidae family) has been considered as an accurate tool reconstructing climate conditions, because the shells of these species preserve regular daily growth increments during their life-spans of several decades, up to 60 years (Watanabe et al., 2004). Tridacnidae are the largest bivalves in the world and live in shallow coral reef environments (Hernawan, 2012) and intertidal habitats (Munro, 1989). According to the fossil record, giant clams first appear in the early Miocene (Harzhauser et al., 2008) and are still present today in the Indo-Pacific region, South Africa and the Red Sea (Rosewater, 1965; bin Othman et al., 2010; Hernawan, 2012).

Previous studies using Tridacnidae shells suggest that different species of this family precipitate their aragonite shells at, or close to, the oxygen isotopic ($\delta^{18}O$) equilibrium in sea water, reflecting the combined effects of regional SST and water $\delta^{18}O_w$ (Aharon and Chappell, 1986; Watanabe et al., 2004; Welsh et al., 2011). In modern and fossil *Tridacna gigas*, previous works (Welsh et al., 2011; Batenburg et al., 2011; Driscoll et al., 2014; Warter et al., 2015) confirmed that they could be reliably used to reconstruct seasonally resolved climatic series and past ENSO anomalies.

The variation of trace element concentrations (such as Sr/Ca, Mg/Ca or Ba/Ca) in bivalve shells has been studied, because they potentially could provide additional information on environmental changes in marine ecosystems (Freitas et al., 2005; Higuera-Ruiz and Elorza, 2009). The latest advances in spatially resolved analyses of trace elements in giant clams, shows how ultra-high resolution can be achieved reflecting the daily light cycle (Sano et al., 2012; Hori et al., 2015) and tidal cycles (Warter and Müller, 2017).

Here, we investigated the environmental control on stable isotope composition and trace element incorporation in a modern *T. squamosa* shell from SE Sulawesi (Fig. 1B). We used this modern specimen to test if shell $\delta^{18}O$, $\delta^{13}C$ and trace elements (Mg/Ca, Sr/Ca and Ba/Ca) reliably reflect local environmental changes. We inspect how the local changes in water temperature and salinity driven by changes in the monsoon-precipitation budget influence the $\delta^{18}O$ signal in the *T. squamosa* shell. Additional trace elements analyses were performed to study the temperature dependence (Mg/Ca and Sr/Ca), as well as the relation to local coastal upwelling and continental run-off (Ba/Ca). Finally, we focus on environmental anomalies inferred from the geochemical signal (in all proxies) during 2010. The 2010/11 La Niña was one of the strongest cold ENSO event in the past decades generating multiple impacts in oceanic and climatic conditions throughout the tropical and subtropical area of the Pacific Ocean (Nicholls, 2011; Boening et al., 2012; Hendon et al., 2014), and therefore provides an excellent setting to benchmark the relationships between ENSO anomalies and proxies.

2. Local setting

Indonesia is a large insular region where topographic and climatic diversity generate a wide array of conditions. Aldrian and Susanto (2003) recognized three different climatic regions. The Sulawesi Island (Fig. 1B) is situated in an area, where climate is strongly influenced by a double monsoon cycle: the wet northwest (NW) monsoon, from November to Mars, and the dry southeast (SE) monsoon from May to September, the rainy and dry seasons respectively (Fig. 2) (Region A in Aldrian and Susanto, 2003). Among the three climatic regions, our area of study (Region A) has the largest extremes in the precipitation cycle. During the rainy season, it is the wettest region, but it is the direst region in dry season (Aldrian and Susanto, 2003). This rainfall pattern is strongly correlated with annual variations in SST (Lau et al., 1997; Aldrian and Susanto, 2003). From November to May with the NW monsoon (the wet season), both rainfall and SST are maximum, and from June to October with the SE monsoon (the dry season) SST and rainfall minima are registered (Fig. 2).

Sulawesi is located in the Western Pacific Warm Pool (WPWP) and is on the path of the ITF (Fig. 1A), a significant component of global thermohaline circulation linking sea surface waters from the Pacific and Indian oceans (Schiller et al., 2010; Sprintall et al., 2014). The high temperatures of the WPWP (Fig. 1A) trigger ocean and atmosphere heat exchange that drives the Walker circulation (Kawamura et al., 2006). The location of the convective cell as well as the monsoon regime are dominated by the south or north motion of the Inter-Tropical Convergence Zone (ITCZ) (Schneider et al., 2014). This “tropical belt of

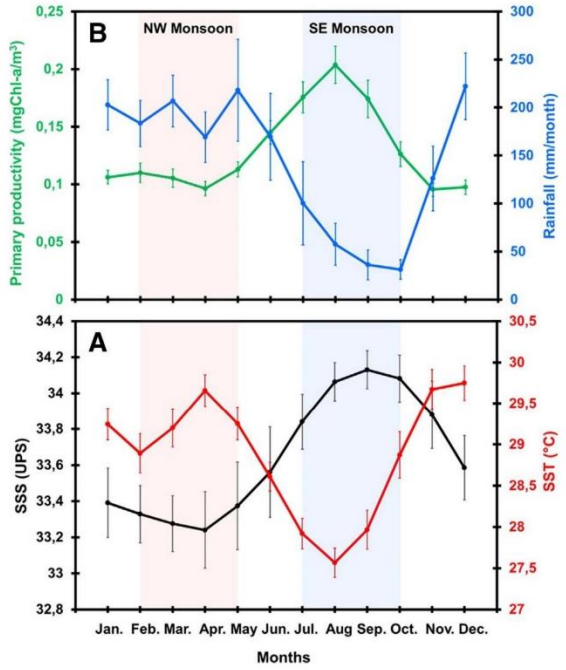

Fig. 2. Mean monthly climatological and oceanographic data for south Sulawesi A) Precipitation and primary productivity B) Sea surface temperature (SST) and Sea Surface Salinity profiles. Rainfall, productivity, SST and SSS were respectively downloaded respectively from: http://iridl.ldeo.columbia.edu/SOURCES/.UCSB/.CHIRPS/.v1p8/.monthly/.global/.precipitation/,http://giovanni.sci.gsfc.nasa.gov/giovanni/,http://iridl.ldeo.columbia.edu/SOURCES/.IGOSS/.nmc/.Reyn_SmithOIv2/.monthly/.ssta,http://iridl.ldeo.columbia.edu/SOURCES/.NOAA/.NCEP/.EMC/.CMB/.GODAS/.monthly/.BelowSeaLevel/.SALTY/.http://www.esrl.noaa.gov/psd/enso/mei/table.html.

deep convective clouds" (Waliser and Gautier, 1993) is the source of excessive precipitation in the southern hemisphere tropics (Hwang and Frierson, 2013).

Seasonal variations in the ITF and SST are associated with the behavior of monsoon winds (Sprintall et al., 2014). During the dry season (austral winter), south easterly winds are dominant over Indonesia and drive strong Ekman divergence increasing the ITF, whereas during the wet season (austral summer), warm westerly winds serve to directly reduce the ITF (Sprintall et al., 2009; Sprintall et al., 2014). Strong westerly winds in the eastern Indian Ocean force equatorial downwelling Kelvin waves that propagate through the Indonesian passage; this increases sea level and reduces the flow from the Pacific into Indian Ocean (Sprintall et al., 2009). In South Sulawesi, a peak in primary productivity is observed in August (the dry season), this phytoplankton bloom reflects the persistence of local coastal upwelling, a result of strong SE monsoon winds between June to August (Habibi et al., 2010). In the surrounding Sulawesi sea of Banda, Gieskes et al. (1990) also reported a peak of productivity in August after upwelling events induced by SE monsoon. These observations are in agreement with the local oceanographic data used here (Fig. 2).

3. Methodology

3.1. Sample description

The left valve of a modern *T. squamosa* shell (sample code: GSL14_19, Fig. 3A) was collected off coral reef area in Kabaena Island (Fig. 1B) by local fishermen in early 2012. The *T. squamosa* species is characterized by prominent scales or ridges arranged regularly on radial fold, the ridges being larger and spaced more widely than for *T. maxima* (Hernawan, 2012). From this characteristic comes its common name: fluted clam or scaly clam (Neo and Todd, 2013). The shell is solid and thick; equivalve, inflated and longer than high, with lengths up to 40 cm (Hernawan, 2012). No alteration in shell composition was found. X-Ray Diffraction (XRD) analyses were performed to know if any alteration was produced, for that we used a bulk inner layer part of the shell.

3.2. Sample preparation

The shell valve was sectioned using a rock saw. The transversal cut run from the umbo to the ventral edge of the shell (Fig. 3A) along the growth direction from the dorsal to ventral margins. This cut reveals three growth zones (Fig. 3B): the inner layer and the outer layer separated by the pallial line, and the hinge, close to the umbo. The hinge and the inner layer are often well preserved compared to the outer layer which is more affected by bio-erosion and diagenetic processes (Elliot et al., 2009). The inner layer is the best part of the shell to use to reconstruct seasonal records, because it has the best preserved area of the shell and higher resolution of growth increments compared to hinge area (Pätzold et al., 1991).

In order to perform sclerochronological and geochemical analysis, thick and thin sections were obtained from the same inner layer sample (Fig. 3C). Sections were polished to provide better surface uniformity. Microscopic observations (daily growth increments) were made on a 30 μm thick thin section, whereas a 1 mm thick thin section was used for laser ablation ICP-MS analysis and carbonate powder micro-sampling.

3.3. Building the shell chronology

In the studied *T. squamosa* shell, daily increments are visible at 20 × microscope magnification (Fig. 3D). These growth increments were counted on the inner layer thin section every millimeter, following the relative chronological order defined naturally from the umbo (first calcareous deposits or juvenile growth) to the internal zone (most recent increments or adult growth), with an Olympus AX 70 Provi microscope coupled to a camera (Nikon DXM 1200F). The biometric software Lucia (Laboratory Imaging s.r.o., ©, 2016) was used to measure distances. Given the daily growth increment and its mean thickness defined at several key points in the thin section, it is thus possible to define the growth rate and the age of the organism.

Using the growth rate measured every millimeter from the inner layer, it is possible to convert geochemical profiles measured as a function of distance scale (mm) into time scale (years). We use this initial age model based on the growth rate as a guide, and then small adjustments within the uncertainty of the initial age model can be applied to assign a final time chronology, this approach is similar to previous work (Driscoll et al., 2014; Welsh et al., 2011; Tynan et al., 2017). The final age model makes it possible to compare geochemical profiles with temporal records of environmental data.

3.4. Isotopic analysis ($\delta^{18}O$-$\delta^{13}C$)

Micro-sampling was performed along the same inner layer thick section, following growth increments (Fig. 3C). With a micro-drill automated system (Micro-Drill New Wave Research, Leica GZ 6) controlled by computer. Carbonate powders weighing a minimum of 100 μg were sampled on average every 200 to 400 μm, covering all of the growth zone.

Powder samples were analyzed at "Laboratoire des Sciences du Climat et de l'Environnement" (Gif-Sur-Yvette) using an OPTIMA GV mass spectrometer with an acid bath automatic preparation line. Shell oxygen isotope values are expressed relative to the isotopic ratio of the carbon dioxide gas derived from the Vienna Pee Dee Belemnite (VPDB)

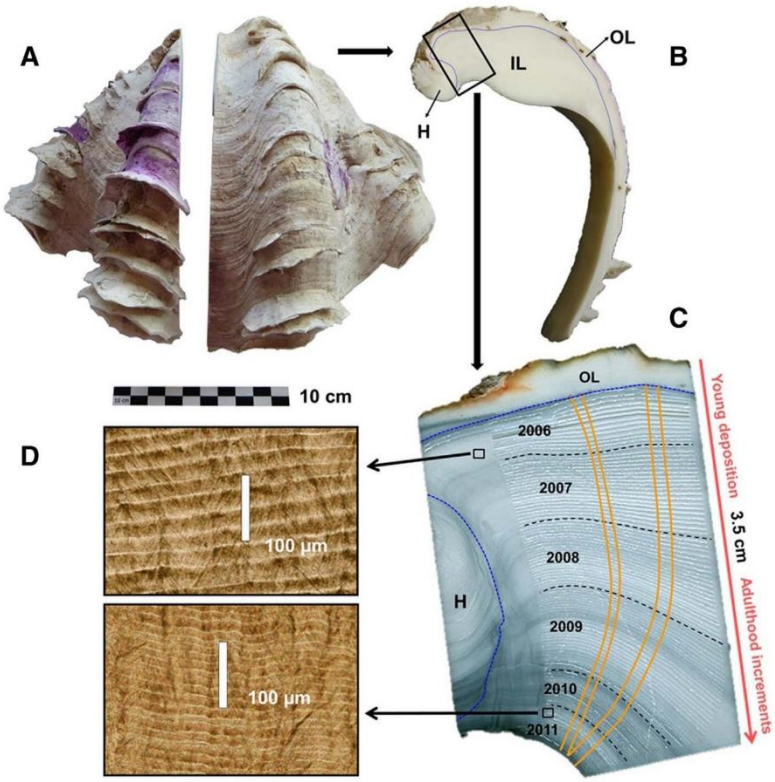

Fig. 3. A) Sectioned *T. squamosa* shell from umbo to ventral margins B) Section shell showing the shell growth zones: the inner layer (IL), the outer layer (OL) and the hinge (H) C) 1 mm thick section from the IL with the micro-drill marks of $\delta^{18}O$ powder sampling, the life time period of the clam (dash line division) and the 4-laser ablation tracks D) Pictures obtained using optic microscopy (20 ×) of daily growth increments. Pallial line in blue. (For interpretation of the references to color in this figure legend, the reader is referred to the web version of this article.)

standard in conventional delta notation (δ). Ratios are reported in ‰. VPDB is defined with respect to the NBS 19 ($\delta^{18}O = -2.20$‰VPDB), limestone standard. The mean external reproducibility (1σ) of carbonate standard is ± 0.06% for $\delta^{18}O$ and ± 0.04% for $\delta^{13}C$. Measured NBS18 is −23.2 ± 0.2% VPDB for $\delta^{18}O$ and 5.0 ± 0.1% VPDB for $\delta^{13}C$.

3.5. Trace element analysis

Trace element analysis was carried out using a 193 nm laser ablation system (Photon Machines, Analyte G2) equipped with a large volume ablation cell (Hel Ex), coupled to a Varian 820 inductively coupled plasma mass spectrometer at LPG Nantes laboratory. The thick section was cleaned in ultrasonic bath of Milli-Q water and dried prior its introduction in the laser ablation cell.

The laser beam energy was set at 50% of its maximum energy, which representing an average fluence of 5.54 J/cm^2 for an 85 µm diameter spot. The repetition rate was set at 10 Hz and the scan speed at 40 µm/s. Data were calibrated against the USGS reference glass material NIST 612 with the preferred values from Jochum et al. (2012). Any laser ablation profile is preceded by a pre-ablation profile (laser energy: 20% and scan speed: 80 µm/s) to remove any surface contaminant. The NIST 612 was analyzed before and after each sample profile. These repeated calibration analyses allow correction of any instrumental drift. The detection limit (background level intensity plus 3 times its standard deviation) of each element, were all well below the signals measured in our sample: Mg/Ca (0.022 mmol/mol), Sr/Ca (0.001 mmol/mol) and Ba/Ca (0.0001 mmol/mol). The external reproducibility of standards between analytical sessions was estimated over a period of 8 months by repeated measurements of USGS reference glass material NIST 610 (n = 20, over 4 analytical sessions) calibrated against the NIST 612 and yield reproducibility within 3.2%, 1.6% and 3.5% for respectively the Mg/Ca, Sr/Ca and Ba/Ca ratios.

The sample reproducibility was estimated by conducting four parallel laser ablation tracks (Fig. 3C) performed on the same drilled area (before drilling) to obtain a mean value on this area.

3.6. Data processing and statistical analyses

For test the normal distribution, the Shapiro-Wilk test was used, and then, Pearson (parametric) or Spearman (nonparametric) was used to find the correlation coefficient between the variables of interest. In order to compare our geochemical analyses with monthly environmental data, trace elements and isotopic records were resampled to a monthly scale using the software AnalySeries (Paillard et al., 1996), as used for other studies in Sclerochronology (e.g. Tynan et al., 2017). Statistical tests were performed with PAST (Paleontological Statistics) 3.15, a software package for paleontological (stratigraphy and time series) data analysis (Hammer et al., 2001).

Statistical tests were performed with PAST (Paleontological Statistics) 3.15, a software package for paleontological (stratigraphy and time series) data analysis (Hammer et al., 2001).

4. Results

4.1. Sclerochronology

No alteration in shell composition was found. XRD analyses reveals 99.14% of aragonite composition for the inner layer in the *T. squamosa* shell (GSL14_19).

To determine the accuracy of the model age, growth increments were counted eight times along the same section, in different zones of

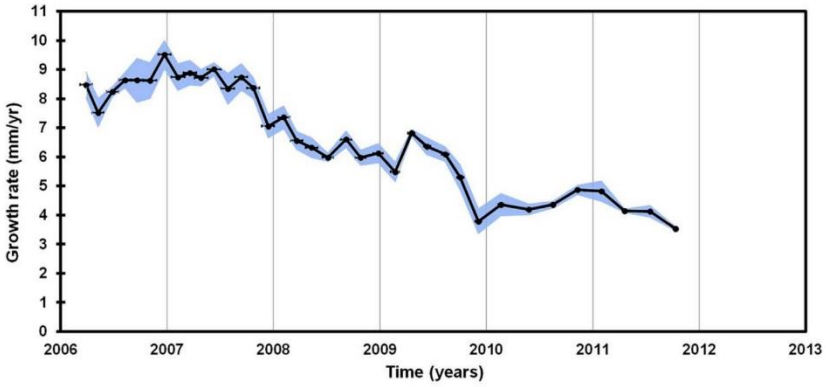

Fig. 4. Growth rate model derived from counting 8 times the growth increments in the same area where geochemical analyses were performed. Standard deviation is illustrated for growth rate (bleu shaded area) in the studied section as for the age model.

the section. We were able to compare 8 independently derived age models. The mean growth model is presented in Fig. 4, with the respective standard deviations, for time and for growth rate.

Given the daily growth increments of *T. squamosa* shell, the age of this shell was estimated to have a life-span of around 5.7 ± 0.08 years (n = 8), from 2006 to the end of 2011 (Figs. 3C and 4). As for other giant clams (Jones et al., 1986; Welsh et al., 2011) and in general for mollusks (e.g. Schöne et al., 2002), the growth rate decreases over time, here with an average of 8 ± 0.8 mm/year in the first two years (juvenile phase of growth), 6 ± 0.9 mm/year in the following two years, and 4 ± 0.5 mm/year at last two years of life (Fig. 4). Daily growth increments become tightly packed as the shell ages especially in last two years (Fig. 3C-D). The mean thickness of a daily growth increment was estimated to be 23 ± 2 μm in the first two years (2006 and 2007), 16 ± 2 μm in the following years (2008–9) and 12 ± 1 μm in the last two years.

The annual growth thickness also decreases with time (Fig. 3C), and it is possible to differentiate the seasonal change on the shell section using transmitted light, as described by Pätzold et al. (1991) in *T. gigas*. Each year is comprised of a dark/light couple of increments: a dark or more transparent increment (high light attenuation) corresponds to the wet season, deposited during the highest temperatures of the year, and the light increment (low light attenuation) corresponds to the dry season, with the lowest annual temperatures. This pattern is more clearly visible during periods of high growth (> 6 mm/year) between 2007 and 2009 (Fig. 3C).

For sampling using the micro-drill the maximum temporal resolution can reach a week per sample during the juvenile growth period, and 2 weeks during the adult period of growth. The laser ablation spot is 85 μm corresponding to a resolution of 3 days resolution during the juvenile growth period and weekly during the adult period of growth. These are sufficient resolution to detect seasonal changes.

4.2. Stable isotope records ($\delta^{18}O$ and $\delta^{13}C$)

The $\delta^{18}O$ values of *T. squamosa* (Fig. 5B) range from −2.11‰ (min) to −1.01 (max) with a mean value of −1.5‰ (n = 104). The $\delta^{18}O$ profile shows approximately 6 seasonal cycles, which is in agreement with the estimated age obtained by counting the daily growth increments.

More negative $\delta^{18}O$ values are observed for the more transparent/dark growth layers, which correspond to warm temperatures, while less negative $\delta^{18}O$ values are observed for the light growth layers, associated with low temperatures (Fig. 5A). Although the record is short, we clearly observe anomalously more negative $\delta^{18}O$ values during the dry seasons of 2009 and 2010 (Fig. 5B).

Predicted/theoretical $\delta^{18}O$ shell values were estimated using the SSS-$\delta^{18}O_w$ relationship of Fairbanks et al. (1997) (Eq. (1)) and the $\delta^{18}O_{shell}$-temperature Eq. (2) of Grossman and Ku (1986) in order to verify the isotopic equilibrium of this species.

$$\delta^{18}O_{water}\ (‰) = 0.2673 \times SS - 9.14 \quad (1)$$

$$SST\ (^{\circ}C) = 21.8 - 4.69 \times (\delta^{18}O_{shell} - \delta^{18}O_{water}) \quad (2)$$

Eq. (2) was derived using tropical aragonite mollusk species, and the salinity-$\delta^{18}O_w$ relationship of Eq. (1) was determined for the western tropical Pacific.

Theoretical and measured $\delta^{18}O$ records (Fig. 5B) match perfectly, which confirms that *T. squamosa* precipitates its shell in isotopic equilibrium.

The $\delta^{13}C$ recorded in this *T. squamosa* shell ranges from 1.03‰ (min) to 1.64‰ (max) with a mean value of 1.37‰. As for $\delta^{18}O$, the $\delta^{13}C$ profile resolves approximately 6 years of seasonal variation (Fig. 5C). High values of $\delta^{13}C$ occur during the dry seasons around 1.5‰, and the lowest values during wet seasons around 1.16‰. Between 2010 and 2011, the dry season have abnormally high $\delta^{13}C$ values relative to previous years, and during the wet season (in the same year) have the lowest shell $\delta^{13}C$ values for this profile.

4.3. Trace elements (Mg/Ca, Sr/Ca and Ba/Ca)

Four independent laser tracks were measured on the same sample inner layer area to check for reproducibility (Fig. 3C). Each profile was converted into age scale and compared, as length of ablations was different, Analyseries software was used to set all ablations on the same scale.

The mean Mg/Ca ratio derived from these 4 parallel laser tracks ranges from 0.48 to 0.95 mmol/mol with a mean value of 0.67. There is a good reproducibility between laser tracks (mean standard deviation = 0.08 mmol/mol). The mean profile present well-defined seasonal variations with higher values (around 0.90 mmol/mol) during summers and lower values (around 0.55 mmol/mol) during winters (Fig. 6B). In contrast to $\delta^{18}O$ profile, the Mg/Ca profile exhibits a double peak during warm periods. No temporal trend is observed in the seasonal amplitude (ontogenic influence) of the Mg/Ca ratio. The 2010 cold/dry season shows abnormally higher Mg/Ca ratios at around 0.63 mmol/mol relative to the previous dry seasons (~0.48 mmol/mol).

The mean Sr/Ca ratios range from 1.48 to 1.85 mmol/mol with mean value of 1.64 ± 0.08 mmol/mol (n = 4 ablations). The Sr/Ca profile resembles that of Mg/Ca, with well-defined seasonal variations (Fig. 6C), higher Sr/Ca values (1.65–1.85 mmol/mol) are recorded in summer compared to in winter (1.50–1.60 mmol/mol). As for the Mg/Ca profile, the double Sr/Ca peak is observed during the warm/wet summer periods, and during 2010 a higher Sr/Ca value is observed,

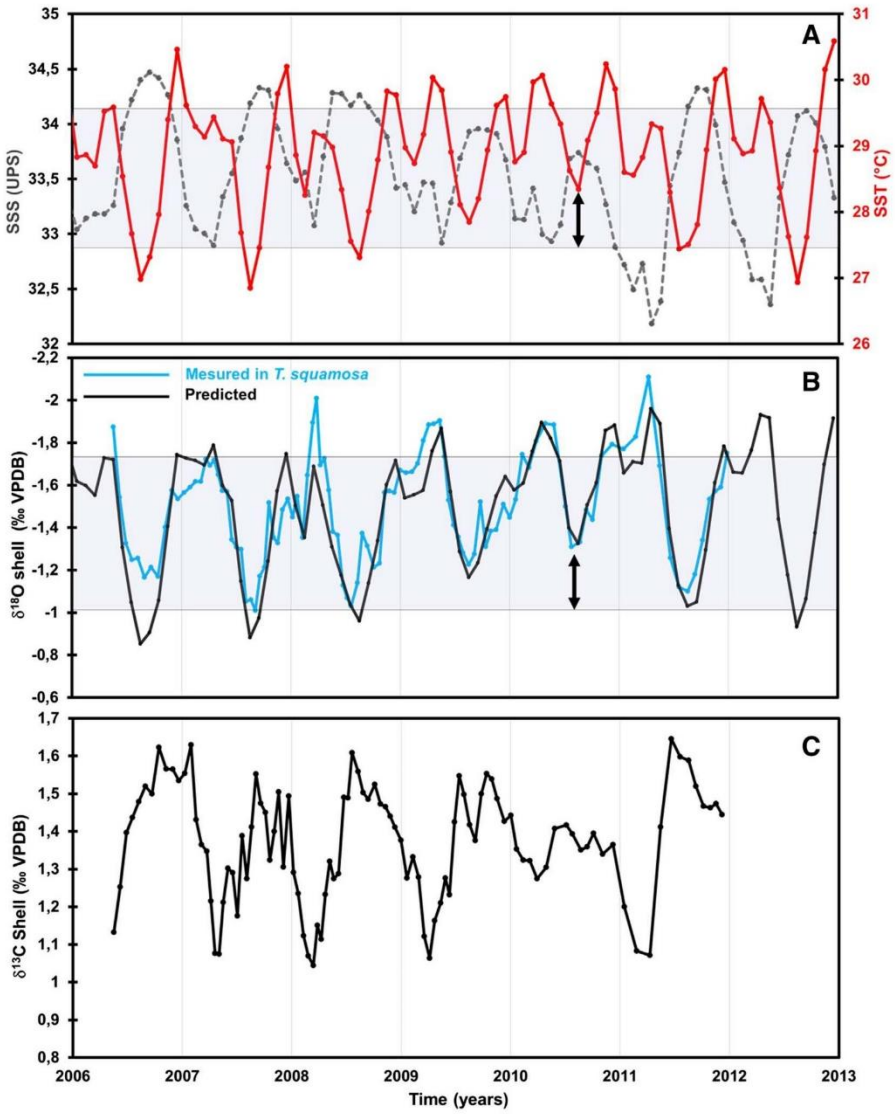

Fig. 5. Isotopic and environmental profiles A) SST and SSS profiles B) Comparison of the *T. squamosa* $\delta^{18}O$ record (blue line) and the predicted record (black line) C) *T. squamosa* $\delta^{13}C$ profile. Shaded boxes in panels A and B indicate the monthly mean range for SST and $\delta^{18}O$ in the last 30 years, respectively. Arrows highlight the 2010 shell $\delta^{18}O$ and SST anomalies. (For interpretation of the references to color in this figure legend, the reader is referred to the web version of this article.)

1.64 mmol/mol relative to values recorded in previous dry seasons (~1.49 mmol/mol).

Measured Ba/Ca values range from around 0.4 to 7.0 μmol/mol, with a mean value of 1.62 ± 0.7 μmol/mol (n = 4 ablations). The Ba/Ca profile (Fig. 7D) has a different behavior compared to that of Sr/Ca and Mg/Ca profiles. The low background signal (~0.4 μmol/mol) is punctuated by unevenly distributed, yet annual, sharp Ba/Ca peaks (Fig. 7D) of ~5 μmol/mol. These peaks present an estimated average duration of around one month, except to the peak of 2010 which presents more than two months. Most of the peaks in Ba/Ca profile occur during the dry season, when productivity and salinity are at their maxima (Fig. 7C) and rainfall at a minimum (Fig. 7B). Nevertheless, some peaks appear during the wet season when the situation is the opposite (NW monsoon). In 2010, the Ba/Ca record has a strong peak and the signal remains higher than background until 2011.

5. Discussion

Calibrations between modern samples and oceanographic data are vital for the interpretation of isotopic proxy record (LeGrande and Schmidt, 2006). Regarding shell trace element analyses, conflicting results are regularly obtained and element incorporation seem to be strongly influenced by physiological and taxonomic factors (Freitas et al., 2005; Carré et al., 2006). Important differences have also been reported between field and laboratory conditions (Gillikin et al., 2006), or in a geographic context for the same species in different hydrodynamic localities (e.g. Lazareth et al., 2003; Tynan et al., 2017). For these reasons, target species have to be tested to provide a reliable bio-

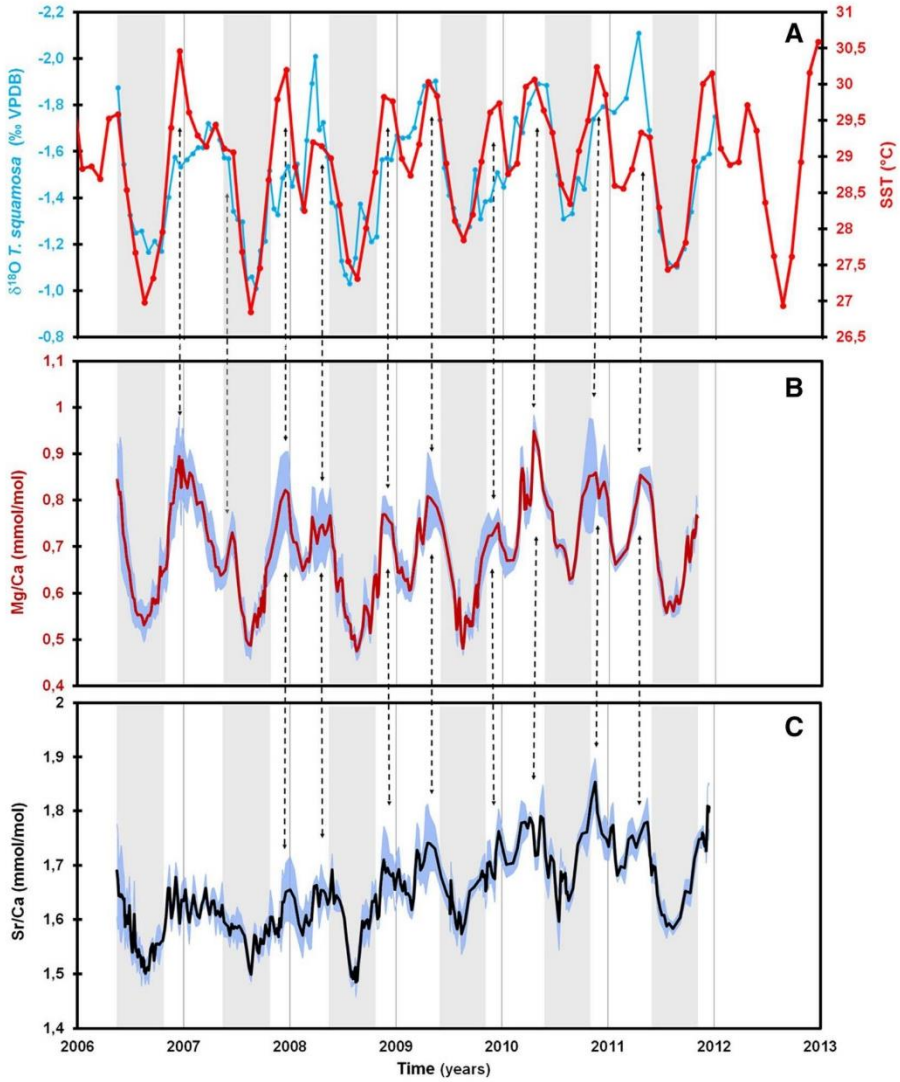

Fig. 6. Geochemical profiles from *T. squamosa* and SST record A) SST and *T. squamosa* $\delta^{18}O$ record B) Mg/Ca profile C) Sr/Ca profile. Dry season is highlighted by the grey-shaded rectangles. Dash lines highlight the co-variation between summer double peak in SST and trace elements.

indicator of the local hydrographic context to be used in environmental (paleo) reconstructions.

5.1. Environmental controls on *T. squamosa* $\delta^{18}O$

The comparison of measured and predicted shell $\delta^{18}O$ profiles (Fig. 5B) with SST (Fig. 5A) confirm the annual cycle of dry and wet season (Fig. 2) described by Aldrian and Susanto (2003) in controlling $\delta^{18}O$ values in this area. The $\delta^{18}O$ signal follows seasonal SST and SSS variations, where more negative values correlate to warm SST during the wet season (NW monsoon), when salinity is at its minimum (Fig. 5A). More positive $\delta^{18}O$ values occur during the dry season (SE monsoon), in which precipitation decreases as the ITCZ moves north and strong southeast winds induce Ekman upwelling of cold water (Hendon, 2003) and increased salinity.

A double peak in the SST is observed during the warm/wet summer season that track the seasonal path of the ITCZ in the area (Fig. 5A). This feature is not observed in the predicted and measured *T. squamosa* $\delta^{18}O$ record. The $\delta^{18}O$ composition reflects a combination of SST variation and water $\delta^{18}O$ associated with salinity variation (Delaygue et al., 2001). Rainfalls are normally depleted in ^{18}O (Dansgaard, 1964) and Indonesia is a region with an excess in precipitation, more important than in other tropical regions of the world (Hwang and Frierson, 2013). The $\delta^{18}O$ water input influence the shell $\delta^{18}O$ signal in summer when precipitation is maximum. This isotopic signature of rainfall is known as the rainfall *amount effect* (Dansgaard, 1964; Moore et al., 2014), and has been described for the WPWP (Conroy et al., 2016) and regions where seasonal variations in rainfall are more frequent or intense, increasing the light oxygen in isotopic signal (Moreno et al., 2014). This phenomenon is maintained when precipitations are more important than evaporation (Moore et al., 2014). The rainfall *amount effect* seems to be the reason why double SST warm peak is

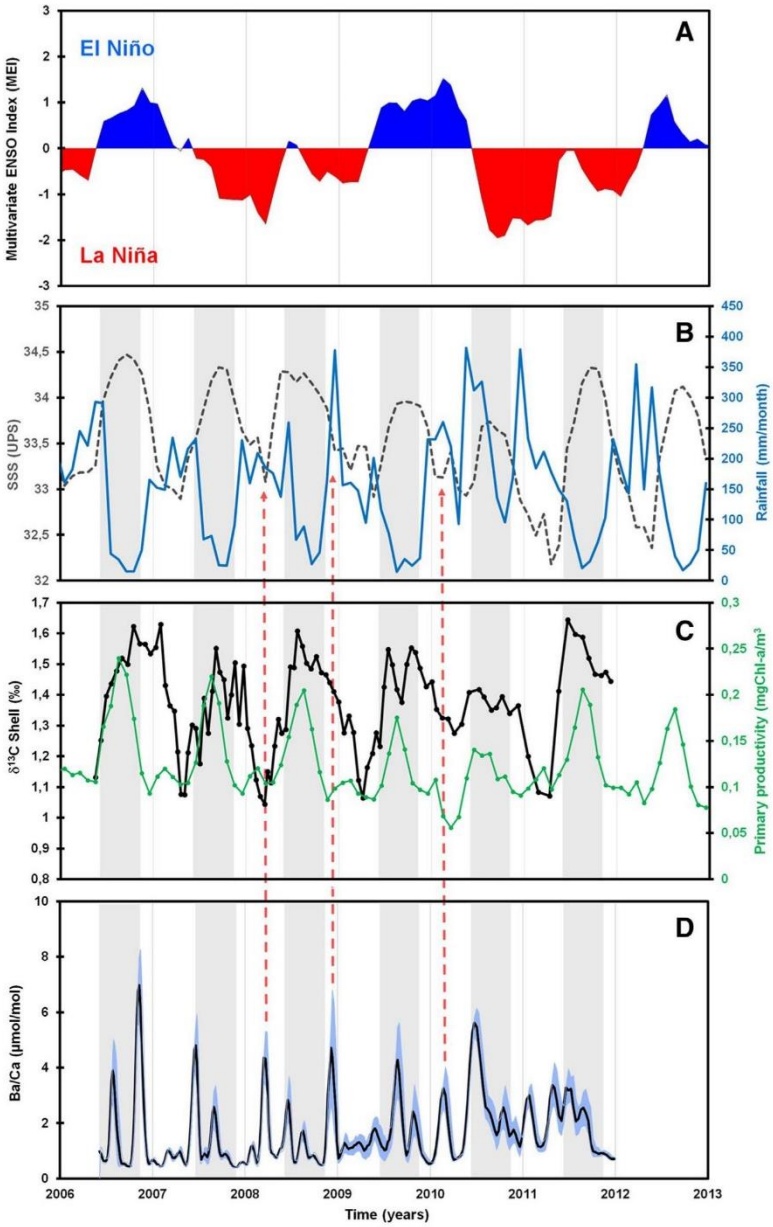

Fig. 7. Geochemical profiles from *T. squamosa* and local hydrographic record A) Multivariate Enso Index, La Niña is a warm anomaly in Indonesia for this reason is graphically presented in red and El Niño (cold anomaly) in blue B) Rainfall and salinity C) $\delta^{13}C$ and primary productivity D) Ba/Ca record. Dash lines highlight the Ba/Ca peaks related only to rainfall in La Niña years. Multivariate ENSO Index (MEI) data downloaded from: http://www.esrl.noaa.gov/psd/enso/mei/table.html. (For interpretation of the references to color in this figure legend, the reader is referred to the web version of this article.)

masked on shell $\delta^{18}O$ signal, and consequently confirm the important local precipitation.

In order to quantify more precisely the different factors that control shell $\delta^{18}O$ composition, predicted $\delta^{18}O$ profiles (Fig. 8) were calculated with only the variation of SST (constant salinity) (Fig. 8B), and a profile with only the variation of salinity (constant SST) (Fig. 8B) using the same Eqs. (1) and (2). According to the information in Table 1, the mean range of $\delta^{18}O$ signal in 30 years (0.7‰) must be composed of 71.4% from temperature contribution (0.5‰), and 28.6% from salinity contribution (0.2‰).

Linear regression in Fig. 9A illustrates how correlation between $\delta^{18}O$ from *T. squamosa* and SST decrease when temperatures exceeds 28.5 °C (wet season), correlation coefficient (r) was of 0.72 (R^2 = 0.62). These results confirm that salinity variation is an important component in the shell $\delta^{18}O$ of *T. squamosa* in SE Sulawesi during the NW monsoon.

5.2. The temperature control on T. squamosa Mg/Ca and Sr/Ca

The relation between trace elements (Mg/Ca and Sr/Ca) and SST were explored with the aim of providing independent information to separate the temperature/rainfall effects of the isotopic record. Previous studies in bivalves point to a primordial biological control on bivalve shell Mg/Ca and Sr/Ca incorporation (e. g. Gillikin et al., 2005;

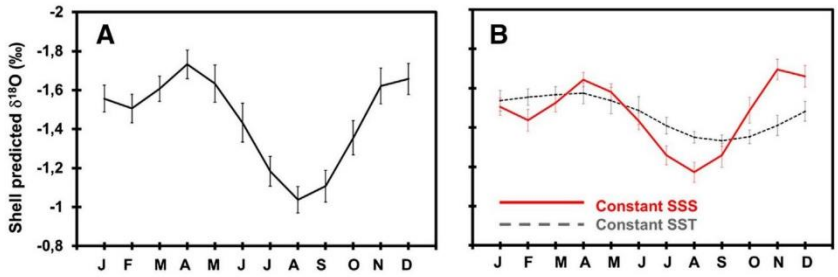

Fig. 8. Predicted mean seasonal $\delta^{18}O$ profiles A) Mean seasonal $\delta^{18}O$ profile calculated from the last 30-years variation of SST and SSS (Eqs. (1) and (2)) B) Comparison between the mean expected $\delta^{18}O$ record without the effect of salinity (red line) and without the effect of temperature (dashed line). (For interpretation of the references to color in this figure legend, the reader is referred to the web version of this article.)

Table 1
Mean interannual $\delta^{18}O$ isotopic composition calculated in the last 30 years, using constant salinity and constant SST to separate contributions.

	Mean	σ	Max	Min	Range	Composition (%)
30 yr $\delta^{18}O$	− 1.45	0.16	− 1.04	− 1.73	0.7	100
30 yr $\delta^{18}O$ (SSS constant)	− 1.47	0.10	− 1.17	− 1.70	0.5	71.4
30 yr $\delta^{18}O$ (SST constant)	− 1.47	0.09	− 1.33	− 1.57	0.2	28.6

Carré et al., 2006; Poulain et al., 2015). A shift in element incorporation associated with changes in growth patterns has been observed in bivalves. For some species (e.g. *Mercenaria campechiensis* and *Crassostrea virginica*), during the adult phase of growth, SST and Mg/Ca are strongly correlated (Surge and Lohmann, 2008). While for others species (e.g. *Pinna nobilis* and *Mytilus edulis*) there is a significant relationship only during the juvenile phase of growth (Freitas et al., 2005; Wanamaker et al., 2008).

In Tridacnidae family, growth appears to have an effect on Mg/Ca ratio. In *T. gigas*, a constant increase of Mg/Ca is observed, displaying a progressive increase of Mg/Ca with age (Elliot et al., 2009; Warter et al., 2015). Although this ontogenic development influence element incorporation, seasonal oscillations for Mg/Ca have been reported in all shell growth zones of *T. gigas*, reflecting a temperature control at seasonal level (Elliot et al., 2009), with higher Mg/Ca values related to warm SST and negative $\delta^{18}O$ also reported for *T. gigas* samples from the Indonesian region (Batenburg et al., 2011; Warter and Müller, 2017). The ontogenic increase of Mg/Ca in *T. squamosa* is not observed here (Fig. 6B), however this may be explained by its short life span (6 years). A modern *T. squamosa* sample from Malaysia was studied by Batenburg et al. (2011), but the authors did not find any relation between trace elements (Mg/Ca, Sr/Ca, Ba/Ca) and $\delta^{18}O$.

In this study, Mg/Ca and Sr/Ca profiles of *T. squamosa* compare well with the seasonal SST variations from 2006 to 2012 (Fig. 6). These trace elements not only have a good quality match between them, but a negative correlation with $\delta^{18}O$ (Fig. 6A), high values of Mg/Ca and Sr/Ca are associated with negative $\delta^{18}O$ (warm SST), and low Mg/Ca and Sr/Ca values with more positive $\delta^{18}O$ ratios (cold SST). In the same region, the co-variation between Mg/Ca and Sr/Ca has been reported in a Miocene *T. gigas* from Java (Batenburg et al., 2011) and in two late Miocene *Tridacna* sp. fossils from Borneo (Warter et al., 2015). This correlation is not systematically observed in other modern *T. gigas* from various localities around the Indo Pacific region (Elliot et al., 2009) illustrating a potential site effect.

Contrary to $\delta^{18}O$ profile, the double warm peak of SST has equivalent peaks in Mg/Ca and Sr/Ca record during the warm/wet seasons (Fig. 6A-B). Correlation analyses between Mg/Ca and SST (Fig. 9B-C) is higher ($r^2 = 0.80$) than for Sr/Ca ($r^2 = 0.52$). Other studies in giant clams found no significant relationship between Sr/Ca and SST (Elliot et al., 2009, Batenburg et al., 2011; Warter et al., 2015). Generally, in bivalves, Sr/Ca has been attributed mainly to biological

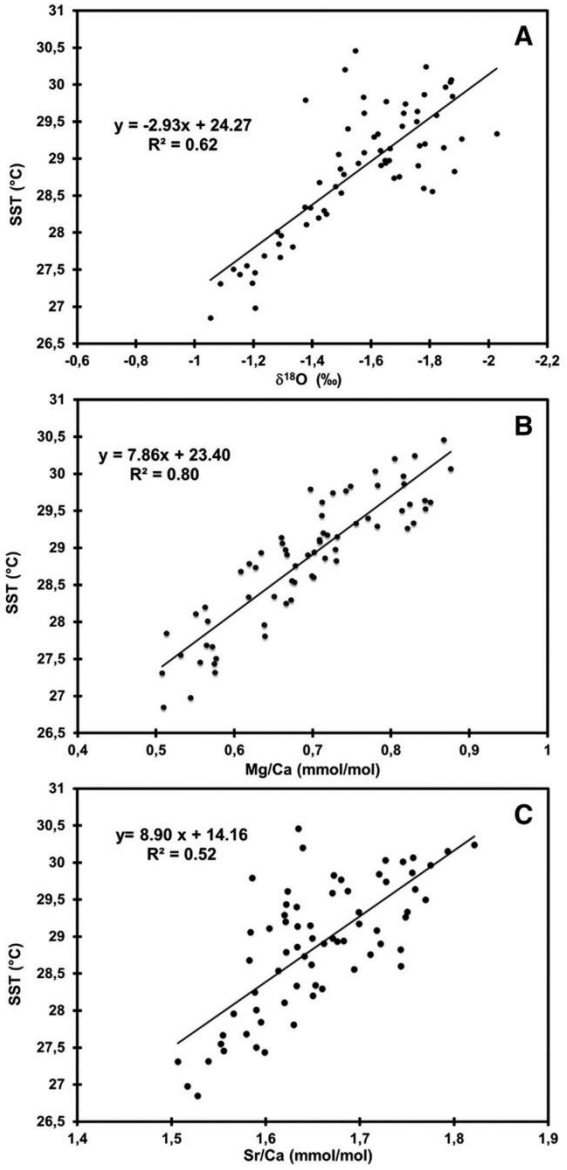

Fig. 9. Linear regression between proxies and SST A) Correlation between *T. squamosa* $\delta^{18}O$ and SST B) Correlation between Mg/Ca and SST C) Correlation between Mg/Ca and SST.

factors (e. g. Gillikin et al., 2005; Carré et al., 2006; Poulain et al., 2015).

These results contrast markedly with the measurements of Sr/Ca in corals that reflect more consistently variations of water temperatures (e.g. Corrège et al., 2000). However, Sano et al. (2012) found no correlation between Sr/Ca and SST in a *T. derasa* specimen, but with light day cycle. Yan et al. (2013) reported a strong anti-correlation between Sr/Ca and SST in a *T. gigas* from the South China Sea, and more recently, Yan et al. (2015) used the resulting Sr/Ca equation to reconstruct SST from a Holocene *T. gigas*.

The latest advances in ultra-high resolution (daily resolved series) demonstrated that environmental rhythms drive the daily incorporation of trace elements in giant clams, reflecting the diurnal light cycle (Sano et al., 2012), and a strong daily co-variation (tidal changes) between Ba/Ca, Mg/Ca and Sr/Ca (Warter and Müller, 2017), and thus, provide important evidence for the use of these tracers in fossil Tridacnae shells.

The taxonomic factor reflects in some cases a metabolic influence for uptake the same element that, other bivalves precipitate in their shell through incorporation dependent only on external conditions. The results presented here suggest that SST has a primary influence for Mg/Ca incorporation (Fig. 9B), more than any other parameter, and more important than in Sr/Ca. However, it is necessary to understand the biological mechanisms behind the uptake and deposition in the aragonite structure of target species in giant clam family, to evaluate the precise quantitative potential of these tracers.

5.3. Productivity and runoff controls on T. squamosa Ba/Ca

Mechanisms invoked to explain Ba/Ca peaks in biogenic carbonates consist of an increased consumption of Ba-rich particles (phytoplankton), an ambient enrichment in seawater Ba by riverine supply and continental runoff (Hatch et al., 2012) or by local upwelling. The Ba/Ca ratio in *T. gigas* shells (Elliot et al., 2009) as in other bivalves (Vander Putten et al., 2000; Lazareth et al., 2003; Thébault et al., 2009, Hatch et al., 2012, Poulain et al., 2015) have been reported as a potential proxy for primary productivity, upwelling or estuarine salinity. Although this relationship is frequently observed it has been questioned (Gillikin et al., 2006, 2008) and further studies are required to assess more precisely the link between shell Ba/Ca and environmental factors. The timing of Ba/Ca peaks is compared with primary productivity (Chlorophyll-a concentration), rainfall, salinity and shell $\delta^{13}C$ (Fig. 7). The occurrence of Ba/Ca in both seasons suggests that several processes control the incorporation of this element in *T. squamosa*.

$\delta^{13}C$ variation is also compared with environmental parameters (Fig. 7) because an interesting covariation is observed with Chl-a concentration and salinity (Fig. 7C-B). Only during 2010, $\delta^{13}C$ appears anti correlated to Chl-a, during the wet 2010 season, shell $\delta^{13}C$ increases while Chl-a undergoes an abnormal decrease below the background mean ($\sim$1.1 mg/m^3). Nevertheless, the covariation with salinity remains the same throughout the record. Batenburg et al. (2011) measured also $\delta^{13}C$ in a modern *T. squamosa* and found some covariance with $\delta^{18}O$, but no interpretations were proposed. Using *T. maxima* specimens, Jones et al. (1986) and Romanek et al. (1987) found variations in $\delta^{13}C$ but with no systematic pattern, and suggest that $\delta^{13}C$ is influenced by CO_2 resulting from metabolic activity of symbiotic microalgae.

The Ba/Ca profile of *T. squamosa* show peaks associated with high SSS and high productivity, and these Ba peaks probably reflect the increases in vertical mixing bringing nutrients into the surface waters. In south Sulawesi, a strong correlation between SSS and productivity is observed during the studied period (Fig. 7B-C) and in an interannual mean (30 years, Fig. 2), the phytoplankton blooms in this area has been described to be one of the most important in Indonesia due to important wind-driven coastal upwelling activity in dry season (Habibi et al., 2010). During wet seasons, high rainfall reduces the SSS, and productivity is also low, due to poor light attenuation and strong turbidity in the water column, determinant parameters for phytoplankton development (Cloern et al., 2014).

We propose that the Ba/Ca peaks that occur during the dry season reflect the increase in primary productivity as a result of coastal upwelling in South Sulawesi. However, the Ba/Ca profile shows other peaks during the wet seasons in 2008, 2009 and 2010 (Fig. 7C dashed lines) that we interpreted as related rainfall and Ba-rich waters from continental runoff as seen in corals (e. g. Sinclair and McCulloch, 2004). More importantly, these Ba/Ca peaks occur during specific rainy seasons of La Niña years, according to the Multivariate ENSO Index (MEI) (Fig. 7A).

Although there is an apparent relationship between shell Ba/Ca incorporation and marine primary productivity, the relationship is not simple. There is no apparent clear relationship between the amplitude of the Ba/Ca peaks (dry seasons of 2008 and 2011) and the amplitude of the seasonal increases in chlorophyll. Some peaks are less prominent ($\sim$3 μmol/mol) than others ($\sim$5 μmol/mol) during the dry season Ba peaks. Secondly there is more structure in the Ba record which frequently shows a double peak during the dry season and there is no corresponding double peak in the Chlorophyll data. One explanation could be that the chlorophyll data used in this study represents a regional mean gridded value (Giovanni, NASA's Earth Science Data Systems) whereas the shell Ba/Ca could reflect more local micro-environmental variations of productivity which is agreement with the patchiness of phytoplankton blooms frequently observed. For this reason, we consider that further analyses with in situ measurements of primary productivity are essential to better understand the relationship between in situ primary productivity, satellite imagery of chlorophyll and shell Ba/Ca.

5.4. The extreme La Niña 2010–2011 recorded

The 2010–11 La Niña was the strongest cold ENSO phase over the past decades (Fig. 10A) with a historic decrease in global mean sea level (Boening et al., 2012), excess in regional precipitation (Boening et al., 2012; Hendon et al., 2014) and important modifications in the ITF transport (Feng et al., 2015). During the dry season of 2010, the *T. squamosa* $\delta^{18}O$ record shows strongly negative values explained by higher than normal SSTs and excess precipitation (Fig. 10C-D) associated with the strong 2010–11 La Niña event (Fig. 10A). SST anomaly in 2010 was 0.84 °C warmer than mean interannual value during the dry season (Fig. 5A, Table 2).

The La Niña anomaly in the $\delta^{18}O$ of *T. squamosa* shows a difference of 0.28‰ relative to the calculated 30 year interannual mean for the dry season (Table. 2). If SST is responsible of 71.4% for the whole $\delta^{18}O$ composition, then, the isotopic anomaly in the shell related only to temperature is 0.19‰ or 0.9 °C. This result is in agreement with the difference found in SST data (0.84 °C) and the difference when SST is calculated from $\delta^{18}O$ *T. squamosa* using Eq. (2) (0.86 °C) (Table 2).

As in the $\delta^{18}O$ profile, abnormal Mg/Ca and Sr/Ca values are observed during the dry season of 2010. Ba/Ca values are also higher than normal in 2010, a prominent peak of Ba/Ca starts in the middle of 2010 and values do not return to normal background signal until the end of 2011 (Fig. 7D). This increase in Ba/Ca is related to the high precipitation of 2010 and the persistence of La Niña into 2011 (Fig. 7D-A). Feng et al. (2015) describe the influence of the long-lived 2010–2012 La Niña and identify oceanographic connections: the low-salinity anomalies in the Indo-Australian Basin were mainly driven by anomalous precipitation in the region and the ITF freshwater advection, affecting areas outside the tropical Pacific as for example the 30% volume transport increase of the Leeuwin Current (western Australia) during the evolution of the 2010–2011.

For all proxies measured here, abnormal values occur during the dry season, this is the same situation for environmental data (SST, SSS, rainfall and productivity). Different studies in the area, show that anomalies in local hydrography related to ENSO are more evident and

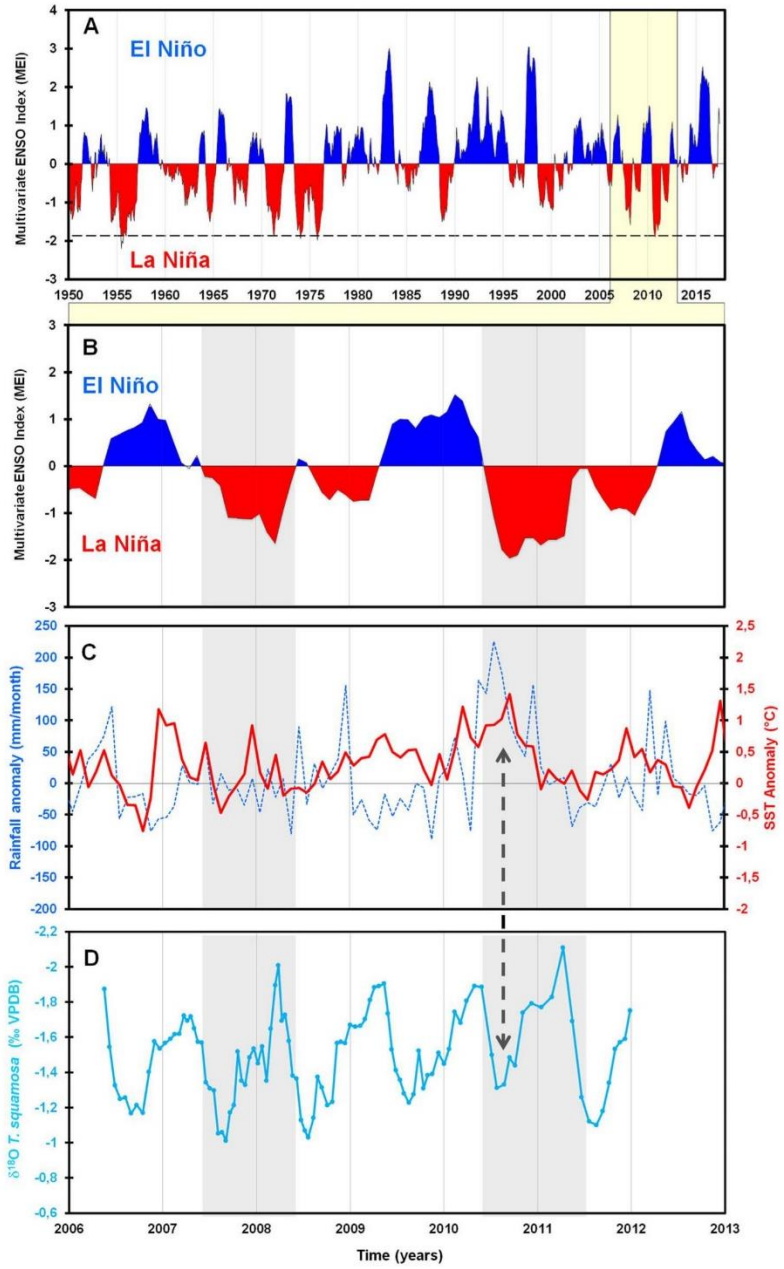

Fig. 10. ENSO anomalies A) MEI index in the last 65 years B) zoom between the studied period (2006–2012) on the MEI index C) Temperature and Rainfall anomaly D) $\delta^{18}O$ record of *T. squamosa*. The La Niña 2007 and 2010 are highlighting with a shaded rectangle.

coherent in time and space during the dry season (Haylock and McBride, 2001; Hamada et al., 2002; Hendon, 2003). Even in 2009 the $\delta^{18}O$ record start to present abnormal values during the dry season as is also observed in SST and SSS (Fig. 5A-B). These observations strengthen the interpretation that the modern *T. squamosa* has recorded the 2010–11 La Niña event.

In the studied period (2006–2012) another La Niña occurred in 2007–8 (Fig. 10B) but with a lower magnitude, shorter duration, and no significant rainfall anomaly is appreciated in this period (Fig. 10C). Only between 2010 and 2011 important rainfall and SST anomalies take place at the same time (Fig. 10C). This anomaly marked a record in La Niña history (Nicholls, 2011; Boening et al., 2012; Hendon et al., 2014) and illustrates the relation with $\delta^{18}O$ *T. squamosa* in which only the strong anomaly is recorded in abnormally ratio as result of strong oceanographic and climatic perturbations (Fig. 10C-D). Before the anomaly of 2010–11, the most recent strongest La Niña events were those from 1988 and 1975 (Wolter and Timlin, 2011) (Fig. 10A). Similarly, the Sr/Ca and Mg/Ca records do not show anomalies during the 2007–8 La Niña (Fig. 10B-C). Only the Ba/Ca profile shows a peak during the wet season which we interpret as an increase in rainfall and

Table 2
El Niño and La Niña anomalies in dry season for SST, $\delta^{18}O$, rainfall and salinity for a strong ENSO events. Arrows represent a decrease or increase in respect to mean values.

	From environmental data set			*T. squamosa* shell
	El Niño 1997	La Niña 1998	La Niña 2010	La Niña 2010
SST (°C)	0.9°↓	0.85°↑	0.84°↑	0.86°↑[a]
$\delta^{18}O$ (‰)	0.2↑[a]	0.2↓[a]	0.3↓[a]	0.28↓
Rainfall (mm/month)	[b]	[b]	141.1↑	
Salinity (PSU)	[b]	[b]	0.47↓	

[a] Values from equations.
[b] No significance difference.

runoff.

To conclude, SE Sulawesi appears to be an interesting area to study interannual variation and seasonal sensibility in ocean-atmosphere in response to the current reinforced ENSO and ITF activity (Cai et al., 2015; Sprintall et al., 2014). Using the approach of multi proxy comparison we assessed information on the amplitude and timing of past conditions and their respective anomalies. $\delta^{18}O$ and Mg/Ca tracing the seasonality and recording SST anomalies, and Ba/Ca peaks allow to determine if the Ba/Ca increase was the result of upwelling (productivity) and/or enhanced precipitation. Likewise, $\delta^{13}C$ seems to reproduce SSS, productivity variation and increases of nutrient inflows.

6. Conclusions

The geochemical profiles derived from a modern shell of the *T. squamosa* species from SE Sulawesi provides a coherent answer to climatic, oceanographic variability and ENSO events. In well-preserved shells, it is possible to assess a calendar time using the growth increments or internal chronometer. The $\delta^{18}O$ profile derived from this sample records seasonal changes in SST and SSS, as the extreme La Niña of 2010–11. This ENSO event is characterized by abnormally warm SST's during dry season, and strong rainfalls on the tropical western Pacific area. A good correlation between $\delta^{18}O$ and trace elements profiles was found. However, contrary to $\delta^{18}O$ which present an important salinity signature (strong rainfall influence), trace elements (Mg/Ca and Sr/Ca) appear to reproduce with more fidelity the SST variations and show for example the double SST peak during the warm season.

The evolution of *T. squamosa* through ontogeny seems to have less influence on the Mg/Ca incorporation than previously observed in other Tridacnidae species, and principal temperature dependence for Mg/Ca ($r^2 = 0.8$) is observed. For shell Sr/Ca, the relation is less clear ($r^2 = 0.52$).

The analysis of Ba/Ca shows that high values are derived from both changes in upwelling (during the dry season) and changes in runoff during periods of high rainfall of the NW monsoon. These abnormal Ba/Ca peaks occur mainly during La Niña events which are associated with higher than normal rainfalls. $\delta^{13}C$ seems also to reflect changes in primary productivity and/or salinity, but is also influenced when other carbon source or input, as for example the enhanced continental inflows.

The geochemical information derived from this *T. squamosa* shell provides a benchmark for other environmental (paleo) reconstructions in the area. In SE Sulawesi, numerous sequences of coral reef terraces (i.e. emerged Pleistocene reef) (Pedoja et al., 2014) offer an important source of information from fossil archives, relevant to the study of the evolution of climate and oceanographic conditions in this region.

Acknowledgments

This research was funded thanks to the INSU-LEFE-IMAGO, CNRS PICS program CLODINE (Franco-Indonesian collaboration program), PACMEDY program, additional funding from the ANR JCJC GiSeLE 601 01 (geodynamics of sea level evolution) program. We are grateful to our colleagues in Indonesia, Sri Yudawati Cahyarini (Indonesian Institute of Sciences LIPI, Research Center for Geotechnology) and Imran Oemar (Makassar University) for their collaboration and assistance while in the field in Indonesia. Special thanks to Johan Andersen for all the logistics on the field. This manuscript has greatly benefited from critical revision and very helpful comments by Viola Warter and Paul Butler. Finally, we thank the LSCE laboratory for their services in isotopic analysis.

Appendix A. Supplementary data

Supplementary data associated with this article can be found in the online version, at http://dx.doi.org/10.1016/j.palaeo.2017.08.037. These data include the Google map of the most important areas described in this article.

References

Aharon, P., Chappell, J., 1986. Oxygen isotopes, sea level changes and the temperature history of a coral reef environment in New Guinea over the last 10^5 years. Palaeogeogr. Palaeoclimatol. Palaeoecol. 56, 337–379.
Aldrian, E., Susanto, R., 2003. Identification of three dominant rainfall regions within Indonesia and their relationship to sea surface temperature. Int. J. Climatol. 23, 1435–1452.
As-syakur, A.R., Adnyana, I.-W.S., Mahendra, M.S., Arthana, I.-W., Merit, I.-N., Kasa, I.-W., Ekayanti, N.W., Nuarsa, I.-W., Sunarta, I.-N., 2014. Observation of spatial patterns on the rainfall response to ENSO and IOD over Indonesia using TRMM Multisatellite Precipitation Analysis (TMPA). Int. J. Climatol. http://dx.doi.org/10.1002/joc.3939.
Batenburg, S.J., Reichart, G.-J., Jilbert, T., Janse, M., Wesselingh, F.P., Renema, W., 2011. Interannual climate variability in the Miocene: high resolution trace element and stable isotope ratios in giant clams. Palaeogeogr. Palaeoclimatol. Palaeoecol. 306 (1–2), 75–81.
Boening, C., Willis, J.K., Landerer, F.W., Nerem, R.S., Fasullo, J., 2012. The 2011 La Niña: so strong, the oceans fell. Geophys. Res. Lett. 39, L19602.
Cai, W., Wang, G., Santoso, A., McPhaden, M., Wu, L., Jin, F., Timmermann, A., Collins, M., Vecchi, G., Lengaigne, M., England, M., Dommenget, D., Takahashi, K., Guilyardi, E., 2015. Increased frequency of extreme La Niña events under greenhouse warming. Nat. Clim. Chang. 5 (2), 132–137.
Carré, M., Bentaleb, I., Bruguier, O., Ordinola, E., Barrett, N., Fontugne, M., 2006. Calcification rate influence on trace element concentrations in aragonitic bivalve shells: evidences and mechanisms. Geochim. Cosmochim. Acta 70, 4906–4920.
Cloern, J., Foster, S., Kleckner, A., 2014. Phytoplankton primary production in the world's estuarine-coastal ecosystems. Biogeosciences 11, 2477–2501.
Conroy, J., Noone, D., Cobb, K., Moerman, J., Konecky, B., 2016. Paired stable isotopologues in precipitation and vapor: a case study of the amount effect within western tropical Pacific storms. J. Geophys. Res. Atmos. 121, 3290–3303.
Corrège, T., Delcroix, T., Récy, J., Beck, W., Cabioch, G., Le Cornec, F., 2000. Evidence for stronger El Niño-Southern Oscillation (ENSO) events in a Mid-Holocene massive coral. Paleoceanography 15, 465–470.
Dansgaard, W., 1964. Stable isotopes in precipitation. Tellus 16, 436–468.
Delaygue, G., Bard, E., Rollion, C., Jouzel, J., Stiévenard, M., Duplessy, J., Ganssen, G., 2001. Oxygen isotope/salinity relationship in the northern Indian Ocean. J. Geophys. Res. Oceans 106, 4565–4574.
Driscoll, R., Elliot, M., Russon, T., Welsh, K., Yokoyama, Y., Tudhope, A., 2014. ENSO reconstructions over the past 60 ka using giant clams (*Tridacna* sp.) from Papua New Guinea. Geophys. Res. Lett. 41 (19), 6819–6825.
Elliot, M., Welsh, K., Chilcott, C., McCulloch, M., Chappell, J., Ayling, B., 2009. Profiles of trace elements and stable isotopes derived from giant long-lived *Tridacna gigas* bivalves: potential applications in paleoclimate studies. Palaeogeogr. Palaeoclimatol. Palaeoecol. 280 (1–2), 132–142.
Fairbanks, R., Evans, M., Rubenstone, J., Mortlock, R., Broad, K., Moore, M., Charles, C., 1997. Evaluating climate indices and their geochemical proxies measured in corals. Coral Reefs 16, 93–100.
Feng, M., Benthuysen, J., Zhang, N., Slawinski, D., 2015. Freshening anomalies in the Indonesian throughflow and impacts on the Leeuwin Current during 2010–2011. Geophys. Res. Lett. 42, 8555–8562.
Ffield, A., Vranes, K., Gordon, A., Dwi Susanto, R., Garzoli, S., 2000. Temperature variability within Makassar Strait. Geophys. Res. Lett. 27, 237–240.
Freitas, P., Clarke, L., Kennedy, H., Richardson, C.A., Abrantes, F., 2005. Mg/Ca, Sr/Ca and stable-isotope ($\delta^{18}O$ and $\delta^{13}C$) ratio profiles from the fan mussel *Pinna nobilis*: seasonal records and temperature relationships. Geochem. Geophys. Geosyst. 6 (4), Q04D14. http://dx.doi.org/10.1029/2004GC000872.
Gieskes, W., Kraay, G., Nontji, A., Setiapermana, D., Sutomo, 1990. Monsoonal differences in primary production in the eastern Banda Sea (Indonesia). Neth. J. Sea Res.

25 (4), 473–483.
Gillikin, D., Lorrain, A., Navez, J., Taylor, J., André, L., Keppens, E., Baeyens, W., Dehairs, F., 2005. Strong biological controls on Sr/Ca ratios in aragonitic marine bivalve shells. Geochem. Geophys. Geosyst. 6, Q05009. http://dx.doi.org/10.1029/2004GC000874.
Gillikin, D., Dehairs, F., Lorrain, A., Steenmans, D., Baeyens, W., André, L., 2006. Barium uptake into the shells of the common mussel (*Mytilus edulis*) and the potential for estuarine paleo-chemistry reconstruction. Geochim. Cosmochim. Acta 70, 395–407.
Gillikin, D.P., Lorrain, A., Paulet, Y.-M., André, L., Dehairs, F., 2008. Synchronous barium peaks in high-resolution profiles of calcite and aragonite marine bivalve shells. Geo-Mar. Lett. 28, 351–358.
Grossman, E.L., Ku, T.-L., 1986. Oxygen and carbon isotope fractionation in biogenic aragonite: temperature effects. Chem. Geol. Isot. Geosci. Sect. 59, 59–74.
Habibi, A., Setiawan, R.Y., Zuhdy, A.Y., 2010. Wind-driven coastal upwelling along south of Sulawesi island. Indones. J. Mar. Sci. 15 (2), 113–118.
Hamada, J., Yamanaka, M.D., Matsumoto, J., Fukao, S., Winarso, P.A., Sribimawati, T., 2002. Spatial and temporal variations of the rainy season over Indonesia and their link to ENSO. J. Meteorol. Soc. Jpn. 80 (2), 285–310.
Hammer, Ø., Harper, D.A.T., Ryan, P.D., 2001. PAST: Paleontological Statistics Software Package for Education and Data Analysis. Palaeontol. Electron. 4 (1), 9.
Harzhauser, M., Mandic, O., Piller, W.E., Reuther, M., Kroh, A., 2008. Tracing back the origin of the Indo-Pacific mollusc fauna: basal *Tridacninae* from the Oligocene and Miocene of the Sultanate of Oman. Palaeontology 51 (1), 199–213.
Hatch, M.B.A., Schellenberg, S.A., Carter, M.L., 2012. Ba/Ca variations in the modern intertidal bean clam *Donax gouldii*: an upwelling proxy? Palaeogeogr. Palaeoclimatol. Palaeoecol. 373, 98–107.
Haylock, M., McBride, J., 2001. Spatial coherence and predictability of indonesian wet season rainfall. J. Clim. 14, 3882–3887.
Hendon, H., 2003. Indonesian rainfall variability: impacts of ENSO and local air-sea interaction. J. Clim. 16 (11), 1775–1790.
Hendon, H., Lim, E., Arblaster, J., Anderson, D., 2014. Causes and predictability of the record wet east Australian spring 2010. Clim. Dyn. 42, 1155–1174.
Hernawan, U., 2012. Taxonomy of Indonesian giant clams (Cardiidae, Tridacninae). Biodiversitas 13 (3), 118–123.
Higuera-Ruiz, R., Elorza, J., 2009. Biometric, microstructural, and high-resolution trace element studies in *Crassostrea gigas* of Cantabria (Bay of Biscay, Spain): anthropogenic and seasonal influence. Estuar. Coast. Shelf Sci. 82, 201–213.
Hori, M., Sano, Y., Ishida, A., Takahata, N., Shirai, K., Watanabe, T., 2015. Middle Holocene daily light cycle reconstructed from the strontium/calcium ratios of a fossil giant clam shell. Sci Rep 5.
Hwang, Y.-T., Frierson, D.M.W., 2013. Link between the double-Intertropical Convergence Zone problem and cloud biases over the Southern Ocean. Proc. Natl. Acad. Sci. U. S. A. 110 (13), 4935–4940.
Jochum, K.P., Scholz, D., Stoll, B., Weis, U., Wilson, S.A., Yang, Q., Schwalb, A., Börner, N., Jacob, D.E., Andreae, M.O., 2012. Accurate trace element analysis of speleothems and biogenic calcium carbonates by LA-ICP-MS. Chem. Geol. 318, 31–44.
Jones, D., Williams, D., Romanek, C., 1986. Life history of symbiont-bearing giant clams from stable isotope profiles. Science 231, 46–48.
Kawamura, H., Holbourn, A., Kuhnt, W., 2006. Climate variability and land–ocean interactions in the Indo Pacific Warm Pool: a 460-ka palynological and organic geochemical record from the Timor Sea. Mar. Micropaleontol. 59, 1–14.
Latif, M., Keenlyside, N.S., 2009. El Niño/Southern Oscillation response to global warming. Proc. Natl. Acad. Sci. U. S. A. 106 (49), 20578–20583.
Lau, K., Wu, H., Bony, S., 1997. The role of large-scale atmospheric circulation in the relationship between tropical convection and sea surface temperature. J. Clim. 10, 381–392.
Lazareth, C., Putten, E., André, L., Dehairs, F., 2003. High-resolution trace element profiles in shells of the mangrove bivalve *Isognomon ephippium*: a record of environmental spatio-temporal variations? Estuar. Coast. Shelf Sci. 57, 1103–1114.
LeGrande, A., Schmidt, G., 2006. Global gridded data set of the oxygen isotopic composition in seawater. Geophys. Res. Lett. 33.
Liu, Z., Lu, Z., Wen, X., Otto-Bliesner, B.L., Timmermann, A., Cobb, K.M., 2014. Evolution and forcing mechanisms of El Niño over the past 21,000 years. Nature 515, 550–553.
Lucia software, Laboratory Imaging s.r.o., ©, 2016. http://www.lucia.cz/.
McBride, J., Haylock, M., Nicholls, N., 2003. Relationships between the maritime continent heat source and the El Niño–Southern Oscillation phenomenon. J. Clim. 16, 2905–2914.
McGregor, H.V., Gagan, M.K., 2004. Western Pacific coral $\delta^{18}O$ records of anomalous Holocene variability in the El Niño-Southern Oscillation. Geophys. Res. Lett. 31, L11204.
Measey, M., 2010. Indonesia: a vulnerable country in the face of climate change. Global Majority E-Journal 1 (1), 31–45.
Moore, M., Kuang, Z., Blossey, P., 2014. A moisture budget perspective of the amount effect. Geophys. Res. Lett. 41, 1329–1335.
Moreno, A., Sancho, C., Bartolomé, M., Oliva-Urcia, B., Delgado-Huertas, A., Estrela, M., Corell, D., López-Moreno, J., Cacho, I., 2014. Climate controls on rainfall isotopes and their effects on cave drip water and speleothem growth: the case of Molinos cave (Teruel, NE Spain). Clim. Dyn. 43, 221–241.
Munro, J.L., 1989. Fisheries for giant clams (Tridacnidae: Bivalvia) and prospects for stock enhancement. In: Caddy, J.F. (Ed.), Marine Invertebrate Fisheries: Their Assessment and Management. John Wiley and Sons Inc., New York, pp. 541–558.
Neo, M.L., Todd, P.A., 2013. Conservation status reassessment of giant clams (Mollusca: Bivalvia: Tridacninae) in Singapore. Nat. Singapore 6, 125–133.
Nicholls, N., 2011. What caused the eastern Australia heavy rains and floods of 2010/11? Bull. Aust. Meteorol. Oceanogr. Soc. 24, 33–34.
bin Othman, A.S., Goh, G.H.S., Todd, P.A., 2010. The distribution and status of giant clams (family Tridacnidae) – a short review. Raffles Bull. Zool. 58, 103–111.
Paillard, D., Laberyrie, L., Yiou, P., 1996. Macintosh program performs time-series analysis. Eos. Trans. AGU 77, 39.
Pätzold, J., Heinrichs, J.P., Wolschendorf, K., Wefer, G., 1991. Correlation of stable oxygen isotope temperature record with light attenuation profiles in reef-dwelling *Tridacna* shells. Coral Reefs 10, 65–69.
Pedoja, K., Husson, L., Johnson, M., Melnick, D., Witt, C., Pochat, S., Nexer, M., Delcaillau, B., Pinegina, T., Poprawski, Y., Authemayou, C., Elliot, M., Regard, V., Garestier, F., 2014. Coastal staircase sequences reflecting sea-level oscillations and tectonic uplift during the Quaternary and Neogene. Earth Sci. Rev. 132, 13–38.
Philander, S.G.H., 1983. El Niño Southern Oscillation phenomena. Nature 302, 295–301.
Poulain, C., Gillikin, D., Thébault, J., Munaron, J., Bohn, M., Robert, R., Paulet, Y., Lorrain, A., 2015. An evaluation of Mg/Ca, Sr/Ca, and Ba/Ca ratios as environmental proxies in aragonite bivalve shells. Chem. Geol. 396, 42–50.
Romanek, C.S., Jones, D.S., Williams, D.F., Krantz, D.E., Radtke, R., 1987. Stable isotopic investigation of physiological and environmental changes recorded in shell carbonate from the giant clam *Tridacna maxima*. Mar. Biol. 94, 385–393.
Rosewater, J., 1965. The family Tridacnidae in the Indo-Pacific. Indo-Pacific Mollusca 1, 347–396.
Sano, Y., Kobayashi, S., Shirai, K., Takahata, N., Matsumoto, K., Watanabe, T., Sowa, K., Iwai, K., 2012. Past daily light cycle recorded in the strontium/calcium ratios of giant clam shells. Nat. Commun. 3, 761.
Schiller, A., Wijffels, S., Sprintall, J., Molcard, R., Oke, P., 2010. Pathways of intraseasonal variability in the Indonesian Throughflow region. Dyn. Atmos. Oceans 50, 174–200.
Schneider, T., Bischoff, T., Haug, G.H., 2014. Migrations and dynamics of the intertropical convergence zone. Nature 513, 45–53.
Schöne, B., Lega, J.W., Flessa, K., Goodwin, D., Dettman, D., 2002. Reconstructing daily temperatures from growth rates of the intertidal bivalve mollusk Chione cortezi (northern Gulf of California, Mexico). Palaeogeogr. Palaeoclimatol. Palaeoecol. 184, 131–146.
Sinclair, D., Mcculloch, M., 2004. Corals record low mobile barium concentrations in the Burdekin River during the 1974 flood: evidence for limited Ba supply to rivers? Palaeogeogr. Palaeoclimatol. Palaeoecol. 214, 155–174.
Sprintall, J., Wijffels, S., Molcard, R., Jaya, I., 2009. Direct estimates of the Indonesian Throughflow entering the Indian Ocean: 2004–2006. J. Geophys. Res. 114.
Sprintall, J., Gordon, A., Koch-Larrouy, A., Lee, T., Potemra, J., Pujiana, K., Wijffels, S., 2014. The Indonesian seas and their role in the coupled ocean–climate system. Nat. Geosci. 7, 487–492.
Surge, D., Lohmann, K., 2008. Evaluating Mg/Ca ratios as a temperature proxy in the estuarine oyster, *Crassostrea virginica*. J. Geophys. Res. 113 (G02001), 2156–2202.
Thébault, J., Chauvaud, L., L'Helguen, S., Clavier, J., Barats, A., Jacquet, S., Pécheyran, C., Amouroux, D., 2009. Barium and molybdenum records in bivalve shells: geochemical proxies for phytoplankton dynamics in coastal environments? Limnol. Oceanogr. 54, 1002–1014.
Timmermann, A., Latif, M., Bacher, A., Oberhuber, J., Roeckner, E., 1999. Increased El Niño frequency in a climate model forced by future greenhouse warming. Nature 398, 694–696.
Tudhope, A., Chilcott, C., McCulloch, M., Cook, E., Chappell, J., Ellam, R., Lea, D., Lough, J., Shimmield, G., 2001. Variability in the El Niño Southern Oscillation through a glacial-interglacial cycle. Science 291, 1511–1517.
Tynan, S., Opdyke, B., Walczak, M., Eggins, S., Dutton, A., 2017. Assessment of Mg/Ca in *Saccostrea glomerata* (the Sydney rock oyster) shell as a potential temperature record. Palaeogeogr. Palaeoclimatol. Palaeoecol. 484, 79–88.
Vander Putten, E., Dehairs, F., Keppens, E., Baeyens, W., 2000. High resolution distribution of trace elements in the calcite shell layer of modern *Mytilus edulis*: environmental and biological controls. Geochim. Cosmochim. Acta 64 (6), 997–1011.
Waliser, D., Gautier, C., 1993. A satellite-derived climatology of the ITCZ. J. Clim. 6, 2162–2174.
Wanamaker, A., Kreutz, K., Wilson, T., Borns, H., Introne, D., Feindel, S., 2008. Experimentally determined Mg/Ca and Sr/Ca ratios in juvenile bivalve calcite for *Mytilus edulis*: implications for paleotemperature reconstructions. Geo-Mar. Lett. 28, 359–368.
Warter, V., Müller, W., 2017. Daily growth and tidal rhythms in Miocene and modern giant clams revealed via ultra-high resolution LA-ICPMS analysis — a novel methodological approach towards improved sclerochemistry. Palaeogeogr. Palaeoclimatol. Palaeoecol. 362–375.
Warter, V., Müller, W., Wesselingh, F.P., Todd, J.A., Renema, W., 2015. Late Miocene seasonal to sub-decadal climate variability in the Indo-West Pacific (East Kalimantan, Indonesia) preserved in giant clams. Palaios 30, 66–82.
Watanabe, T., Suzuki, A., Kawahata, H., Kan, H., Ogawa, S., 2004. A 60-year isotopic record from a mid-Holocene fossil giant clam (*Tridacna gigas*) in the Ryukyu Islands: physiological and paleoclimatic implications. Palaeogeogr. Palaeoclimatol. Palaeoecol. 212, 343–354.
Welsh, K., Elliot, M., Tudhope, A., Ayling, B., Chappell, J., 2011. Giant bivalves (*Tridacna gigas*) as recorders of ENSO variability. Earth Planet. Sci. Lett. 307 (3–4), 266–270.
Wolter, K., Timlin, M.S., 2011. El Niño/Southern Oscillation behaviour since 1871 as diagnosed in an extended multivariate ENSO index (MEI.ext). Int. J. Climatol. 31, 1074–1087.
Yan, H., Shao, D., Wang, Y., Sun, L., 2013. Sr/Ca profile of long-lived *Tridacna gigas* bivalves from South China Sea: a new high-resolution SST proxy. Geochim. Cosmochim. Acta 112, 52–65.
Yan, H., Sun, L., Shao, D., Wang, Y., 2015. Seawater temperature seasonality in the South China Sea during the late Holocene derived from high-resolution Sr/Ca ratios of *Tridacna gigas*. Quat. Res. 83, 298–306.

3.3. Environmental signal in *H. hippopus* species

3.3.1. Introduction

According to the fossil record (Harzhauser et al., 2008) and molecular phylogeny (Schneider and Foighil, 1999), *H. hippopus* is the oldest species of Tridacnidae family (living species), this species appears around 18 million of years (Ma) before present (BP) in the Early Miocene. *H. hippopus* is easily distinguished from the other giant clams by the presence of irregular semi-tubular spines and numerous riblets on the principal ribs and interstices (Hernawan, 2012) (Fig. 3.2).

H. hippopus lives in sandy zones of coral reefs down in shallow waters to a depth of 6 m (Seeto et al., 2012). Maximum abundance of this species is in the shallow well light intertidal reef flats (Griffiths & Klumpp, 1996). As a consequence *H. hippopus* has been characterized as a "reef-top" species (Adams et al., 1999), which underlines its exposure at low tide (Thomas, 2007). Youn individuals of *H. hippopus* are attached by their byssus to the substrate but adults are unattached (Rosewater, 1965). This habitat makes it easier to collect this species than other giant clams who are heavier and live deeper in the water column (Thomas, 2007). Adult *H. hippopus* individuals have low absolute photosynthetic rates relative to other giant clams, because a low-weight-specific zooxanthellae population in this species (Griffiths & Klumpp, 1996).

Daily growth increments in *H. hippopus* species was described by Watanabe and Oba (1999) and Aubert et al. (2009), demonstrating the use for high resolution in time series reconstructions. These studies focused on the stable isotope ($\delta^{18}O$) profiles derived from modern specimen collected in New Caledonia and in Japan. In this chapter, stable isotopes and trace element profiles derived from 2 modern *H hippopus* (intra-species comparison) are compared. Secondly, results presented here offer the rare and unique possibility to compare geochemical profiles derived from both modern *H. hippopus* and *T. squamosa* collected in the same area (inter-species comparison). So this study provides new and original information about application of proxies in *H. Hippopus*.

3.3.2. Methods

Two modern specimens of *H. hippopus* were collected recently dead on the same day in March 2014. These samples were obtained from local fishermen from south Kabaena Island (Fig. 3.1). The shells of *H. hippopus* correspond to GSL14_20 (Fig. 3.2A$_1$) and GSL14_23 (Fig. 3.2A$_2$). The same methodology approach used in *T. squamosa* (GSL14_19, see previous section) was performed for these *H. hippopus* shells.

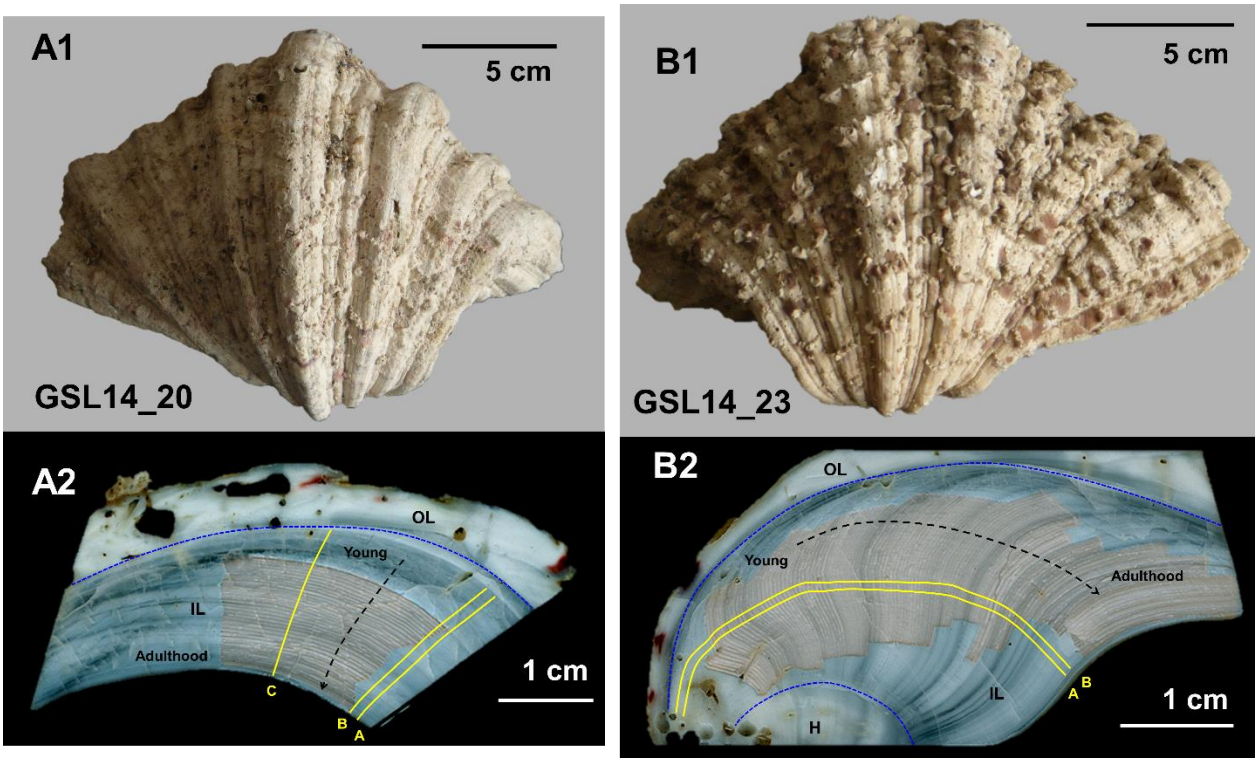

Fig. 3.2. *H. hippopus* shells **A1)** GSL14_20 sample **A2)** Thick section with micro-drill sampling marks **B1)** GSL14_23 sample **B2)** Thick section with micro-drill sampling marks. Micro-drill marks highlighted with a red shadow, black dash arrows indicated the growth direction from young depositions to old (more recent) deposition. Yellow lines indicates the laser ablation tracks for each sample. Pallial line in blue. OL: Outer Layer. IL: Inner Layer.

3.3.3. Results

3.3.3.1. Growth rates

The growth model and the age of these samples were determined as for sample GSL14_19 (*T. squamosa*) by counting the daily growth increments. The information derived from growth rate

measurements provides an age of ~ 2 years for GSL14_20, and ~ 4 years for GSL14_23. In GSL14_23 the growth rate does not vary significantly during the lifetime: 8.5 ± 1.6 mm/yr in the first year and 8.9 ± 1.2 mm/yr during the second year, 10.3 ± 1.5 mm/yr in the third year and 11.3 ± 3 mm/yr in the last year. In GSL14_20 the result is quite similar, during the two years of life the growth rate is respectively: 9.7 ± 0.9 mm/yr and 9.7 ± 1.7 mm/yr.

3.3.3.2. Stable isotope records ($\delta^{18}O$ and $\delta^{13}C$)

The $\delta^{18}O$ values of GSL14_23 (Fig. 3.3A) range from -2.2 to -1.14 ‰ with a mean value of -1.70 ‰ (n = 113), $\delta^{13}C$ values range from 0.92 to 1.67 ‰ with a mean of 1.28 ‰ (Fig. 3.3B). The $\delta^{18}O$ and $\delta^{13}C$ profile shows around 4 seasonal cycles confirming the estimated age obtained through the growth model.

The $\delta^{18}O$ values of GSL14_20 $\delta^{18}O$ range from -2.2 to -1.3 ‰ with a mean of -1.8 ‰ (n = 36), for this sample one year and a half has been reconstructed (Fig. 3.3, orange profile). This period is common for both samples (GSL14_20 and GSL14_23).

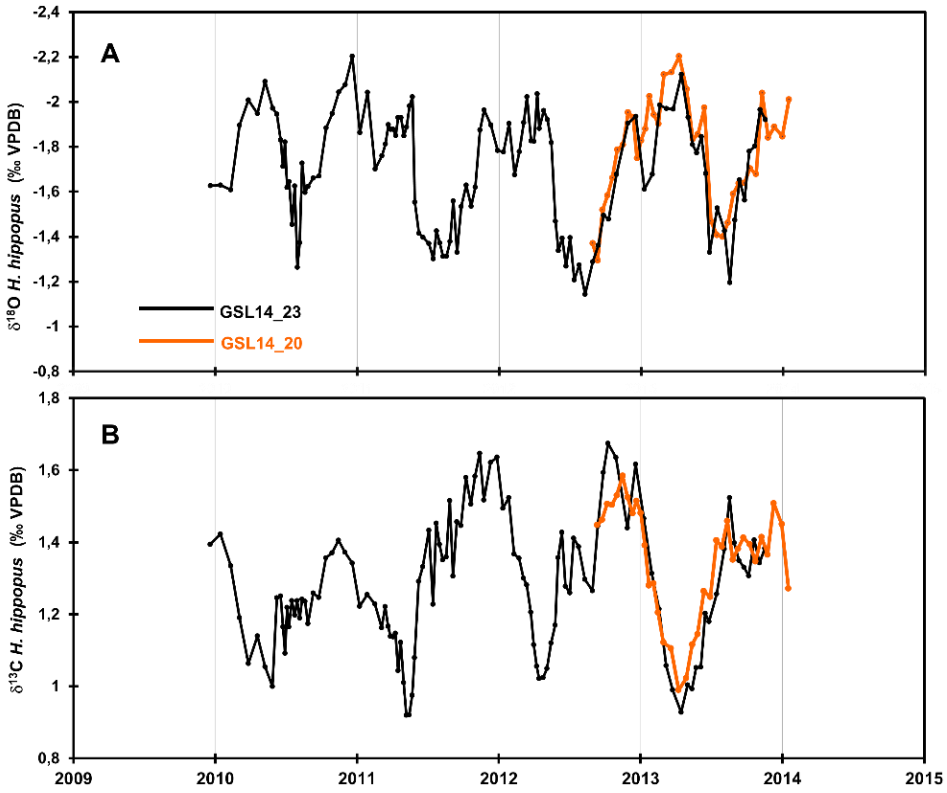

Fig. 3.3. Isotopic results from *H. hippopus* shells **A)** $\delta^{18}O$ profiles **B)** $\delta^{13}C$ profiles.

3.3.3.3. Trace elements (Mg/Ca, Sr/Ca and Ba/Ca)

The same laser ablation conditions used in *T. squamosa* were conducted for *H. hippopus* shells. For GSL14_20 sample, three parallel laser ablation profiles were measured (Fig. 3.2A$_2$), while in GSL14_23, two laser ablation profiles were measured (Fig. 3.2B$_2$).

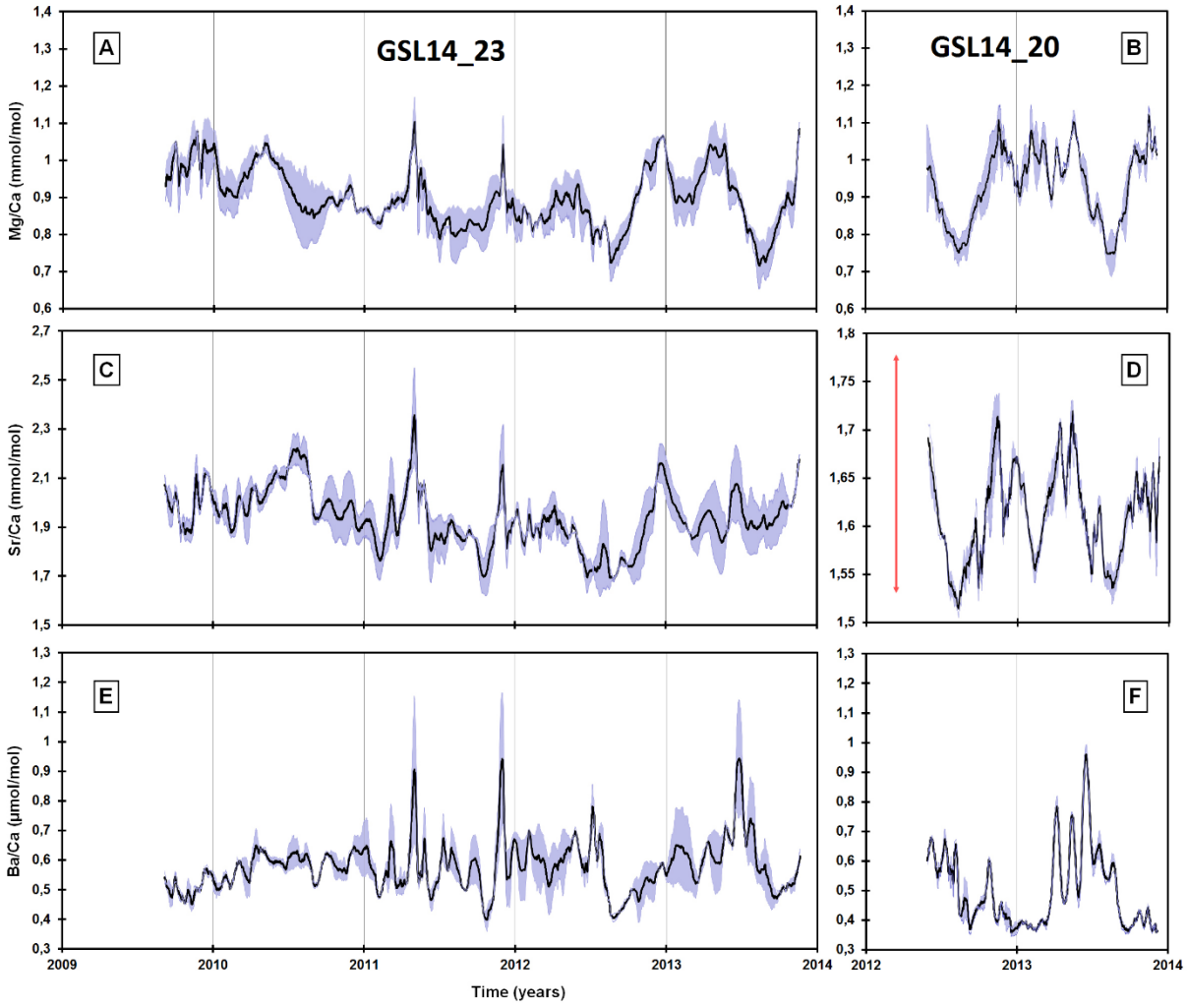

Fig. 3.4. Trace elements comparison in *H. Hippopus* samples. Mg/Ca profiles for **A)** GSL14_23 and **B)** GSL14_20. Sr/Ca profiles for **C)** GSL14_23 and **D)** GSL14_20. Ba/Ca Profiles for **E)** GSL14_23 and **F)** GSL14_20. Red arrows highlighted different scale in Sr/Ca between GSL14_23 and GSL14_20. Blue shadow represents the standard deviation.

In GSL14_23 sample, Mg/Ca ranges from 0.72 to 1.10 mmol/mol with a mean value of 0.91 ± 0.07 mmol/mol (n = 2 tracks) (Fig. 3.4-A); Sr/Ca ranges from 1.68 to 2.36 mmol/mol with a

mean value of 1.96 ± 0.1 mmol/mol (Fig. 3.4-C); and Ba/Ca ranges from 0.4 to 0.94 µmol/mol with a mean value of 0.58 ± 0.07 µmol/mol (Fig. 3.4-E). For GSL14_23, the 2 tracks of laser ablation are plotted to illustrate intra-shell variability found for this sample.

In GSL14_20 sample, Mg/Ca ranges from 0.75 to 1.21 mmol/mol with a mean value of 0.95 ± 0.08 mmol/mol (n = 3 tracks) (Fig. 3.4-B); Sr/Ca ranges from 1.51 to 1.72 mmol/mol with a mean value of 1.62 ± 0.02 mmol/mol (Fig. 3.4-D); and Ba/Ca ranges from 0.36 to 0.96 µmol/mol with a mean value of 0.51 ± 0.03 µmol/mol (Fig. 3.4-F).

3.3.4. Discussion

3.3.4.1. Intra-species reproducibility of $\delta^{18}O$ and $\delta^{13}C$ (H. hippopus)

The T-Student test was applied on the isotopic records ($\delta^{18}O$ and $\delta^{13}C$) of GLS14_23 and GLS14_20 over the common period of life (Fig. 3.3). No statistical difference was found ($p = 0.25$) and confirms the reproducibility of the isotopic ratios between 2 individuals of the same species (*H. hippopus*) in the studied area.

The $\delta^{18}O$ profile of GLS14_23 was compared with SST (Fig. 3.5). As observed for GSL14_19 (*T. squamosa*), more negative $\delta^{18}O$ values are observed in warm/wet seasons, while more positive $\delta^{18}O$ values are associated to colder/dry seasons. The double SST peak observed in the hydrographic data is also observed in the *H. hippopus* $\delta^{18}O$ profile.

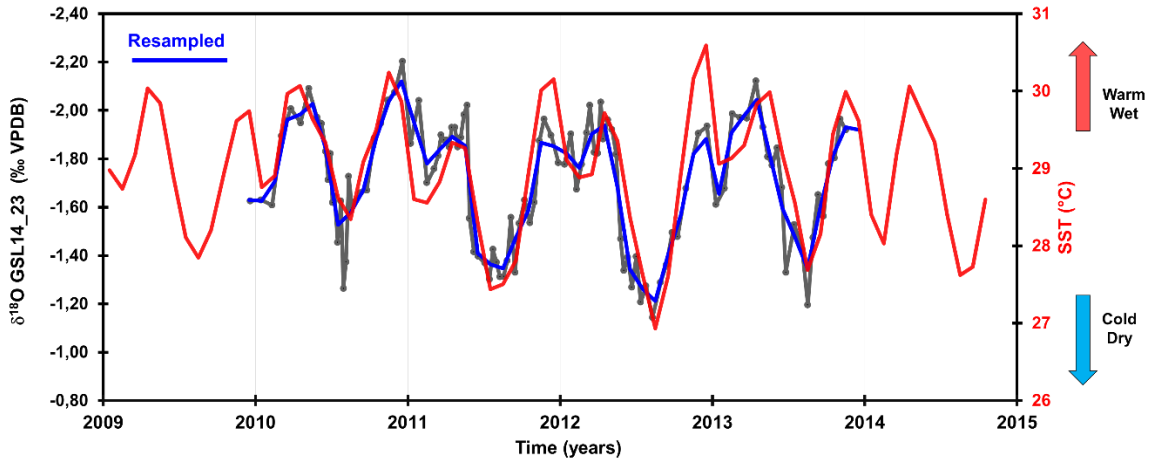

Fig. 3.5. $\delta^{18}O$ profile of GLS14_23 sample compared to SST. Blue line represents a monthly $\delta^{18}O$ resampled profile.

The resampled mean monthly $\delta^{18}O$ profile of *H. hippopus* (GSL14_23) also presents abnormally negative values, around -1,6‰ associated with the 2010 cold/dry season (see Fig. 3.5), as observed in the *T. squamosa* section. This warmer event is the response of local surface hydrography to the La Niña event of 2010-11 and suggests that *H. hippopus* species also record SST and precipitation anomalies in SE Sulawesi related to the ENSO events.

3.3.4.2. Intra-species reproducibility of trace elements (H. hippopus)

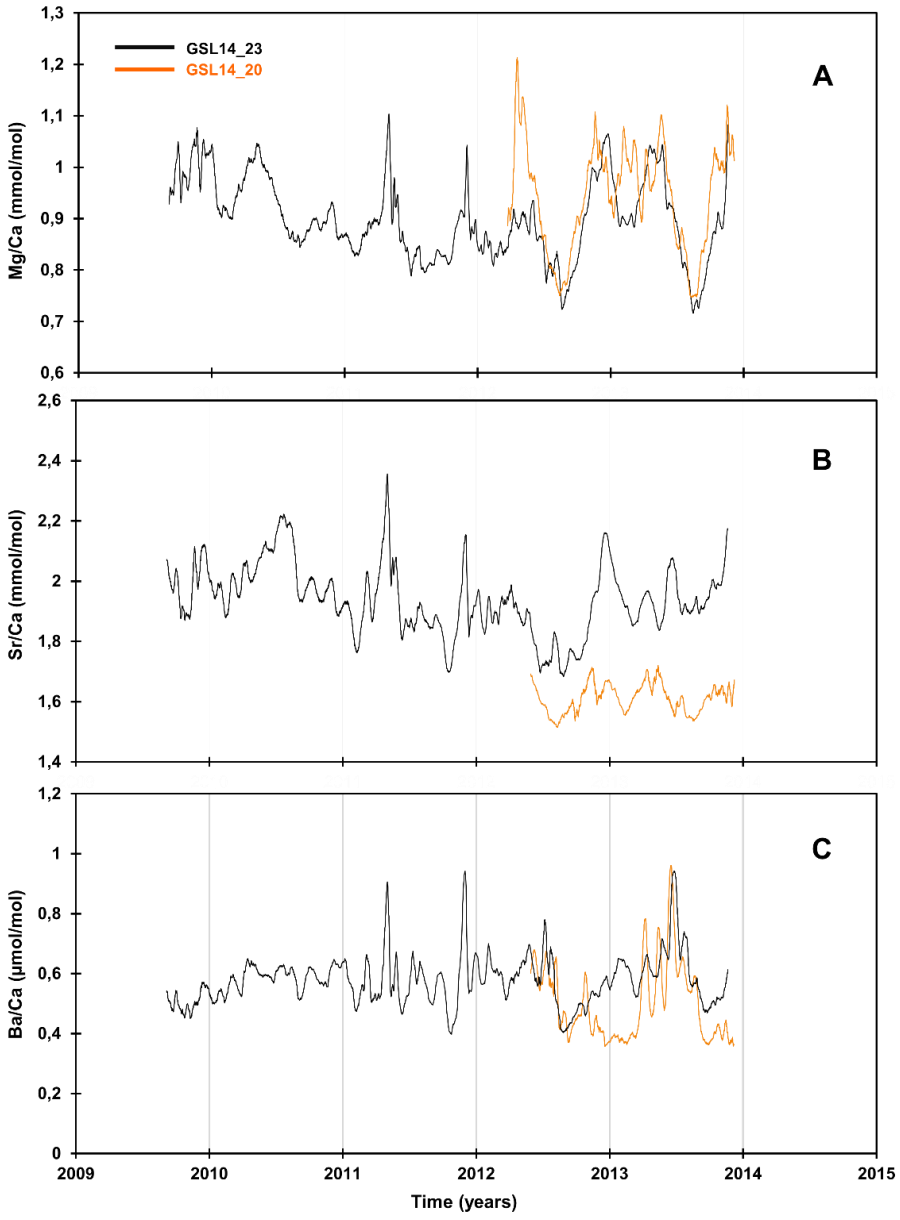

Fig. 3.6. Intra-species comparison for trace elements (*H. Hippopus* samples GSL14_20 and GSL14_23). **A)** Mg/Ca profiles for **B)** Sr/Ca profiles **C)** Ba/Ca profiles.

When comparing the trace element profiles of GSL14_20 with the counterpart period (2012-2014) in GSL14_23, only Mg/Ca presents similar pattern in seasonal variation (Fig. 3.6-A) and the same mean ratio, which means a good reproducibility between these individuals.

For Sr/Ca, GSL14_20 presents a clear signal of seasonal variation with the double peak of summer (Fig. 3.6-B), however the concentration is lower than GSL14_23 (Fig. 3.6-B) with a difference between means of 0.3 mmol/mol. As discussed in *T. squamosa* section, Sr/Ca presents more variability in giant clams (e. g. Elliot et al., 2009; Warter et al., 2009).

For Ba/Ca the same mean concentration was found (0.5 µmol/mol), similar pattern is appreciated in both individuals for the end of 2013 (Fig. 3.6-C) however GSL14_23 presents more internal variability (Fig. 3.6-C).

Fig. 3.4 illustrates larger standard deviations for GSL14_23 trace elements than GSL14_20. For GSL14_20 no significant differences were found between the 3 laser ablations in the shell for any trace element ratio as observed is standard deviations (Fig. 3.4-B-D-E).

3.3.4.3. Inter-species growth rate comparison (H. hippopus vs T. squamosa)

Similar growth rates are observed in both *H. hippopus* specimen, which are significantly higher than growth rates of *T. squamosa* (Fig. 3.7). The minimum rates in *H. hippopus* are equivalent to the highest rates of *T. squamosa* (~ 8 mm/year), this values are also higher than the mean growth of *T. gigas* (Aharon et al., 1991; Elliot et al., 2009).

Klump and Griffiths (1994) studied the relationship between nutrition requirements (from symbiosis and heterotrophic consumption), the metabolism and growth in four Tridacnidae species (*T. gigas*, *T. crocea*, *T. squamosa* and *H. hippopus*). This research revealed that *H. hippopus* allocated the highest proportion of carbon expenditure to growth (30 to 90 %), up to half of which was used for shell growth. *T. gigas* and *T. squamosa* both put 20 to 40% of carbon into growth, compared with only 10 to 20% in *T. crocea*. These authors also found that *H. hippopus* had a highest growth rates (0.10 to 0.21 mm/day) than *T. squamosa* (0.05 to 0.14 mm/day) and *T. crocea* (0.01 to 0.05 mm/day) in agreement with the findings of this study.

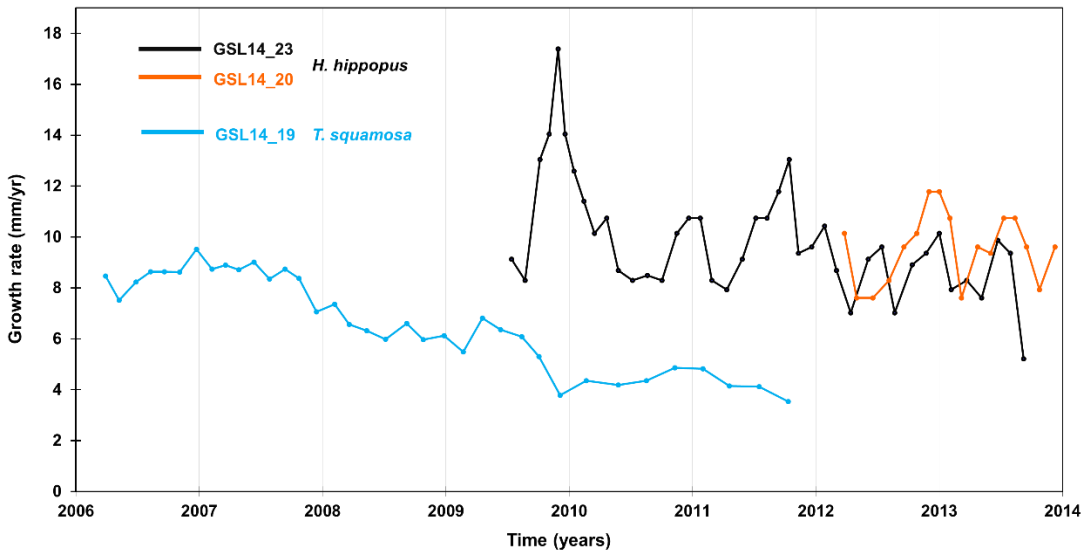

Fig. 3.7. Inter-species growth rate comparison. Between *H. hippopus* samples (GSL14_23 and GSL14_20) and *T. squamosa* (GSL14_19).

In other studies from different regions growth rates from *H. hippopus* species were also estimated with different results from this study. For example Aubert et al. (2009) reported a mean thickness of daily increments with a range of 1.1 to 53.3 µm with a mean value of 13.2 ± 7 µm, in a *H. hippopus* from New Caledonia. In Watanabe and Oba (1999) the thickness ranged from 10 to 70 µm with a mean ~37 µm in a *H. hippopus* from Japan. Here, in GSL14_20 the mean thickness in the 2 years of life is 26.2 ± 3.8 µm ranged from 20.8 to 32.26 µm; and in GSL14_23 the mean thickness in the 4 years of life is 27.1 ± 6 µm ranged from 14.2 to 47.2 µm. In this samples from SE Sulawesi, the growth rate have a narrower range in respect to the samples used in Watanabe and Oba (1999) and Aubert et al. (2009). These differences could be a related to mean SST seasonal amplitude, with higher amplitudes in SST and growth rates in higher latitudes (Japan and New Caledonia) compared to tropical results from SE Sulawesi. Translating information of these studies in mm/yr we obtained a mean of 4.8 mm/yr in the specimen from New Caledonia, 13.5 mm/yr in Japan, compared to 9.7 ± 0.2 mm/yr for SE Sulawesi samples of *H. hippopus*, which confirm that growth rate is dependent on local (SST) conditions.

3.3.4.4. Inter-species comparison of $\delta^{18}O$ and $\delta^{13}C$ profiles

In order to test inter-species reproducibility of stable isotopes, the data from GSL14_23 (*H. hippopus*) and GSL14_19 (*T. squamosa*) is compared (Fig. 3.8-A). Growth rates and age estimates results shows that these specimens both lived and recorded the period from 2010 to 2012. In both species, seasonal cycles of the $\delta^{18}O$ profiles are observed (Fig. 3.8-A), and in both profiles anomalous negative $\delta^{18}O$ values are associated with the 2010 La Niña event.

The $\delta^{13}C$ profiles also show seasonal variations in both species (Fig. 3.8-B), highest $\delta^{13}C$ values occur during the dry seasons and lowest values in wet seasons. During the dry season of 2010 lowest values of $\delta^{13}C$ (compared with other years) are recorded in both species. However, for *T. squamosa* record, $\delta^{13}C$ in wet season of 2010 registered higher than normal values, whereas *H. hippopus* did not recorded abnormal ratios in $\delta^{13}C$ for this season in 2010 (Fig. 3.8-B).

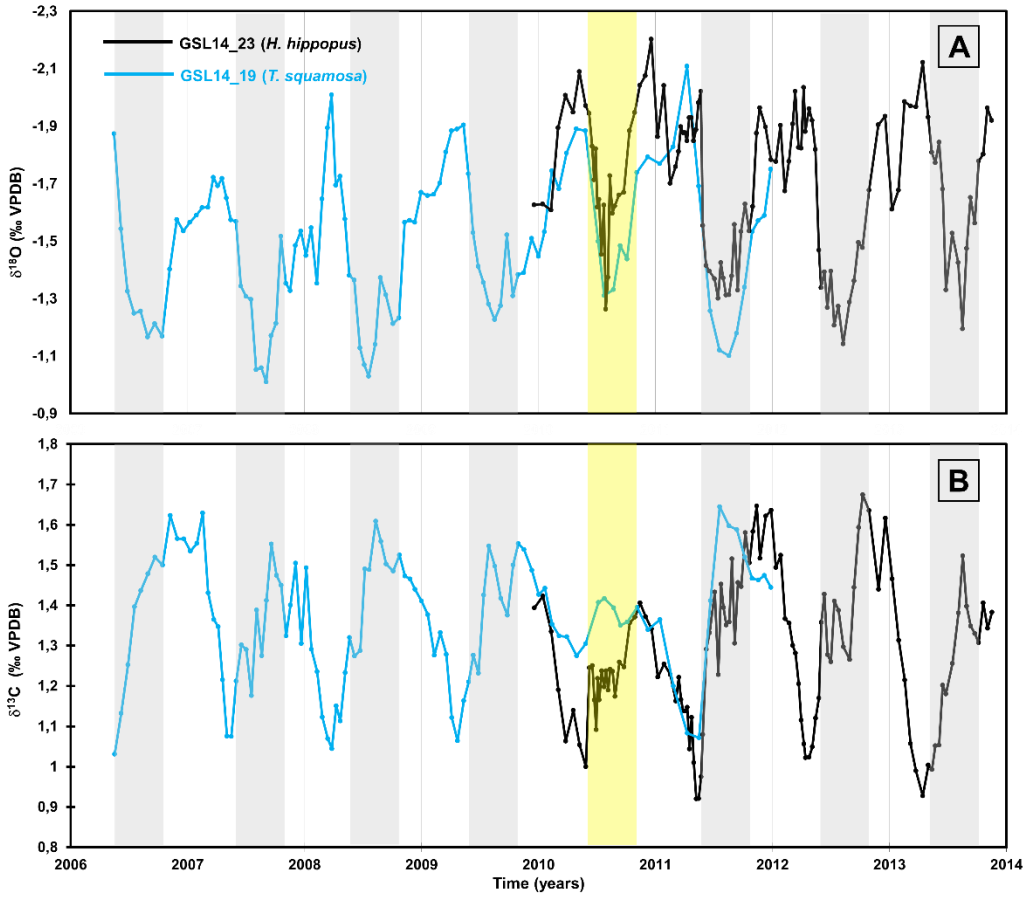

Fig. 3.8. Isotopic inter-species comparison **A)** $\delta^{18}O$ comparison **B)** $\delta^{13}C$ comparison. *T. squamosa* in blue (GSL14_19) and *H. hippopus* in black (GSL14_23). Shaded grey bars highlight the dry season. Yellow bar highlight the La Niña event.

During the period 2010 to 2012 (in common for both species), *H. hippopus* $\delta^{18}O$ are on average 0.2 ‰ higher than *T. squamosa* $\delta^{18}O$ (Fig. 3.8A). Mean monthly $\delta^{18}O$ values were estimated and compared with the calculated (theoretical) mean monthly $\delta^{18}O$ for the last 30 years (Fig. 3.9-A). Theoretical $\delta^{18}O$ was calculated using the SST record from 5m of depth (IGOSS database), equations are described in the *T. squamosa* section (3.2). The comparison between *T. squamosa* $\delta^{18}O$ and the theoretical mean $\delta^{18}O$ shows no statistic differences (T-student, P = 0.46) but *H. hippopus* presents significant differences of around 0.26 ‰ (T-student, P = 0.0065).

Both Aubert et al. (2009) and Watanabe and Oba (1999) demonstrated that *H. hippopus* calcifies in isotopic equilibrium with the surrounding sea water and present strong correlation with SST (r^2 = 0.88). The difference in mean $\delta^{18}O$ values (0.2 ‰) between these species is thus not associated to isotopic disequilibrium. The isotopic difference is equivalent to 1°C of temperature. One possible explanation is that this equivalent 1°C could reflect different depth habitat and mean temperature which decreases with depth.

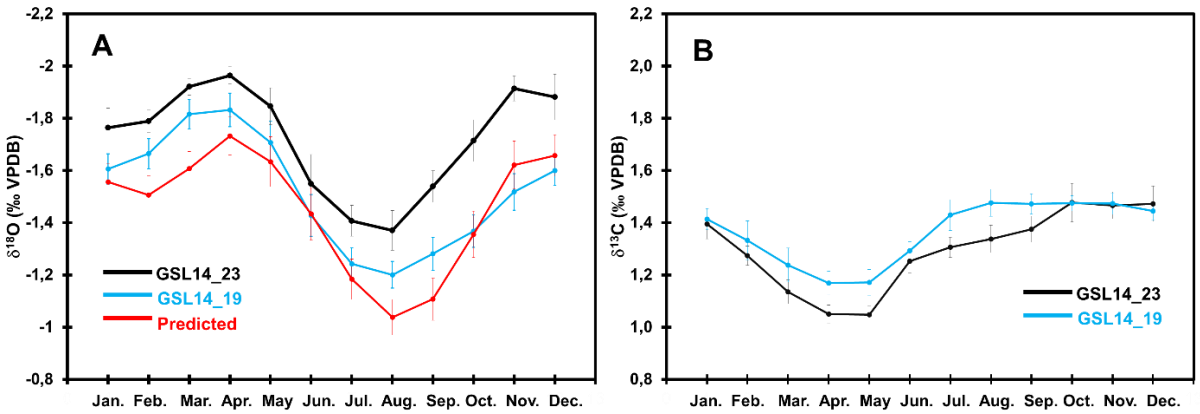

Fig. 3.9. Interannual mean comparisons **A)** $\delta^{18}O$ comparison **B)** $\delta^{13}C$ comparison. *T. squamosa* in blue (GSL14_19) and *H. hippopus* in black (GSL14_23). Red line is the isotopic mean from the last 30 years.

Unfortunately, no *in situ* measures of SST are available for this study and it was not possible to obtain specific information of SST at different depths from data bases in a remote area. Nevertheless, ecologic observations support the hypothesis of habitat differentiation from $\delta^{18}O$ ratios in these species. *H. hippopus* present a wide range of habitats, sandy atoll lagoon floors or exposed intertidal habitats (Munro, 1989) and live not attached by a byssus to the substrate

(Hernawan, 2012). *T. squamosa* could be found in the littoral but also in shallow water to a depth of 20 m, live not embedded into a coral boulder attached by the byssus to the substrate (Hernawan, 2012). Yonge (1982) describes that *H. hippopus* lives free in the juvenile phase (not attached) and the final habitat is on the lee of reefs, frequently on sand. Some observations in Palau Islands and Australia found that *H. hippopus* prefers warm temperatures to spawn (Jameson, 1976). Intertidal reef flats in nearshore areas are the characteristic habitat of both *H. hippopus* and *T. crocea*, whereas *T. gigas* and *T. squamosa* are more common subtidal (5 to 15 m) on offshore reefs (Klump and Griffiths, 1994).

The hypothesis presented here to explain the 0.2 ‰ $\delta^{18}O$ offset between *H. hippopus* and *T. squamosa* consists in different habitat for each species, and consequently different conditions of temperature. With *H. hippopus* inhabits preferentially intertidal zones and *T. squamosa* in deeper zones (sub littoral) (Fig. 3.10).

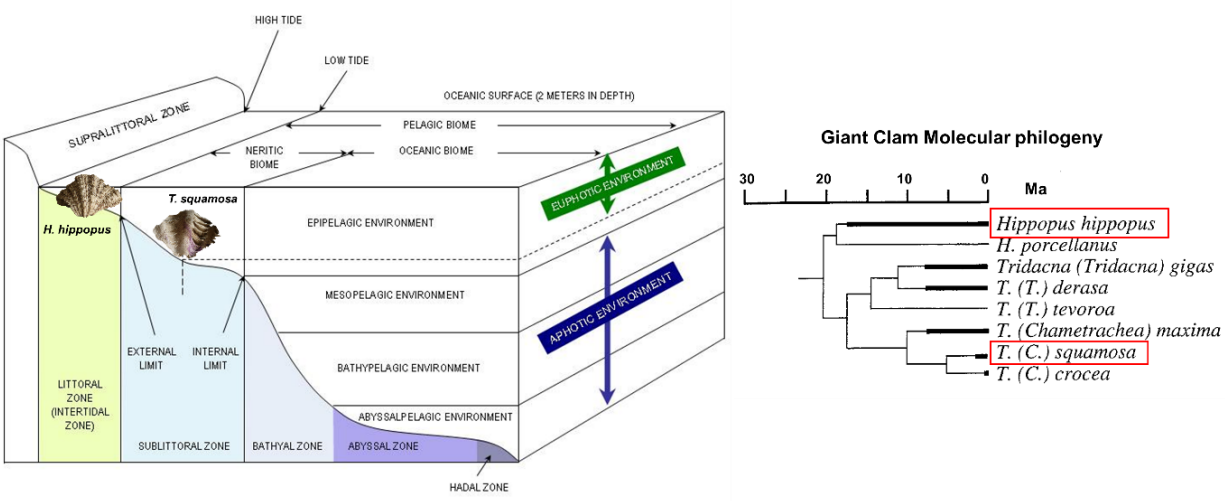

Fig. 3.10. Habitat differentiation **Left:** diagram littoral occupation for each species. **Right:** the molecular phylogeny of Giant Clams (Cardiidae: Tridacninae) with the known stratigraphic record of living species of *Hippopus* and *Tridacna*. Timescale in millions of years before present (Ma). Stratigraphic ranges of species are indicated by heavy horizontal lines. Molecular phylogeny from Schneider and Foighil (1999).

Both species present the same mean seasonal amplitude which is comparable to the mean theoretical seasonality derived from the past 30 years of hydrographic data (Table 3.1). In GSL14_20, seasonality is slightly higher compared to other means, but this record represents less

than two years of variation. This result set the mean seasonality range of today, which will help us to study seasonal variation in fossils

The comparison of mean monthly $\delta^{13}C$ of *T. squamosa* and *H. hippopus* (Fig. 3.9-B) shows only small difference around 0.06 ‰ without statistical difference (T-student, P = 0.25). The seasonality of *H. hippopus* $\delta^{13}C$ is similar to *T. squamosa*: high $\delta^{13}C$ during the dry/cold season and low $\delta^{13}C$ during wet/warm season (Fig. 3.8-B), which means that potentially the same processes control shell ^{13}C composition in both species.

Table 3.1. Seasonal range comparison between all modern sells and expected record from data set.

Sample	Time recorded (yr)	$\delta^{18}O$ seasonal range (‰)
Data set	30	0.69 ± 0.2
GSL14_19 (*T. squamosa*)	6	0.63 ± 0.2
GSL14_20 (*H. hippopus*)	1,8	0.74 ± 0.03
GSL14_23 (*H. hippopus*)	4	0.59 ± 0.2

The explanation for shell ^{13}C variations are numerous and include changes in sources of food to changes in the $\delta^{13}C$ of water in which the bivalves grew. For example, Nerot et al. (2012) shows how $\delta^{13}C$ values (in muscle tissues) of different epifaunal scallops decrease far below the expected depth reduction in benthic primary production, suggesting that $\delta^{13}C$ not only track primary productivity utilization, but other sources. Bivalves use nutrients from a large variety of particulate material, including phytoplankton, zooplankton, bacteria, re-suspended benthic microalgae and detritus from different sources (e. g. Kreeger and Newell, 1996; Kach and Ward 2008). In trophic ecology, $\delta\ ^{13}C$ signature is used to identify the source(s) of carbon exploited by an organism (Vander Zanden and Rasmussen, 1999). Riera and Richard (1997) demonstrated that when freshwater inflow discharge increase, the oyster *Crassotrea gigas* preferentially feeding on the increasing contribution of terrestrial organic matter, enriched in ^{13}C. Surge and Lohmann (2008) found that $\delta^{13}C$ reflects mixing relationship between salinity and dissolved inorganic carbon (DIC) for *Crassostrea virginica*, and temperature only has a minor effect on $\delta^{13}C$, in consequence they conclude that it serves as a proxy for salinity.

In other giant bivalve (the oyster *Hyotissa hyotis*) Titschack et al. (2010) interpreted the $\delta^{13}C$ signal to reflect changes in the respiration rate, which increase during periods of enhanced

planktonic food supply. In *T. maxima*, $\delta^{13}C$ was also interpreted as an increase in metabolism but from symbiotic microalgae (Jones et al., 1986; Romanek et al., 1987).

The $\delta^{13}C$ signal in bivalve shells is controlled by the $\delta^{13}C$ of the DIC in the extra pallial fluid (EPF) which precipitated the shell (Kirby 2000). At the same time, the $\delta^{13}C$ composition of the EPF is controlled by the $\delta^{13}C$ of the ambient seawater, carbonate ion effects, pH, food sources, growth and changes in the metabolic rate (Romanek et al. 1992; McConnaughey and Gillikin, 2008; Lartaud et al. 2010). All these processes vary in strength and time, and then, complicate the interpretation of $\delta^{13}C$ in bivalve shells (Lorrain et al. 2004; Titschack et al., 2010).

In our local context there is a correlation between shell ^{13}C and primary productivity which is also correlated with salinity. These changes in salinity could be associated with other carbon inputs from important discharges from local rivers into the coastal areas. Although the common results in two Tridacnidae species (*H. hippopus* and *T. squamosa*) argue for $\delta^{13}C$ as potential proxy of primary productivity and salinity in this area, further *in situ* analyses (including metabolic tests) must be conducted in order to verify these interpretations.

3.3.4.5. Inter-species comparison of trace element profiles

H. hippopus Mg/Ca values are higher (on average 0.3 mmol/mol) than *T. squamosa* Mg/Ca (Fig. 3.11A). During 2010 anomalous signal was also recorded for *H. hippopus* and could be related to anomalous SST of La Niña. The double peak related to SST is also observed in Mg/Ca of *H. hippopus*, as in *T. squamosa*. However in Mg/Ca record of *H. hippopus*, the double peak appears more detailed in the last two years (2012-2014).

The fact that Mg/Ca values are ~0.3 mmol/mol higher in *H. hippopus* individuals could reflect warmer temperatures. This would be in agreement with the hypothesis of deeper habitat. In *T. squamosa* strong correlation was found between Mg/Ca and SST ($r^2 = 0.8$). The resulting formula from *T. squamosa* calibration (Fig. 9-B, p.p. 74) was tested to calculate SST derived from *H. hippopus* Mg/Ca.

SST was calculated using the Mg/Ca from *H. hippopus* individuals (GSL14_23 and GSL14_20) and compared with the SST data used in *T. squamosa* calibration. The results are presented in Fig. 3.12. Mean SST from Mg/Ca calculation of *H. hippopus* is 30.2 ± 0.5 °C, with a difference of 1.18 °C (warmer) in respect to SST data (Fig. 3.12).

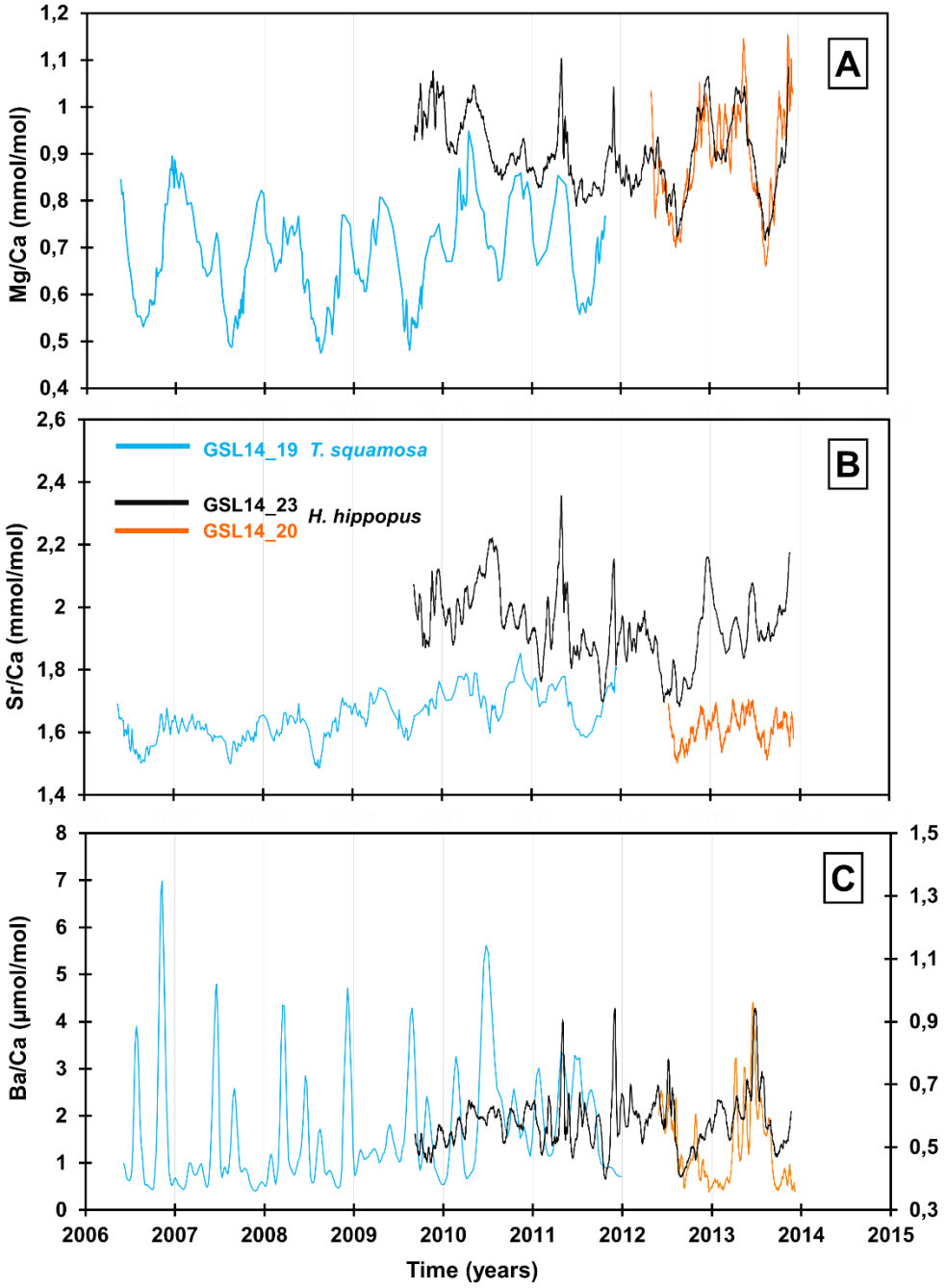

Fig. 3.11. Inter-species comparison for trace elements. *T. squamosa* (GSL14_19, in blue) and *H. hippopus* individuals (GSL14_23 and GSL14_20) **A)** Mg/Ca profiles **B)** Sr/Ca profiles **C)** Ba/Ca profiles. Note that Ba/Ca profiles of *H. hippopus* are plotted in a different axis of *T. squamosa* profile (blue) in reason of inferior concentrations.

From SST estimations from Mg/Ca (Fig. 3.12) it is possible to confirm the $\delta^{18}O$ differences, and then support the habitat/temperature differentiation between *H. hippopus* and *T. squamosa* (Fig. 3.10).

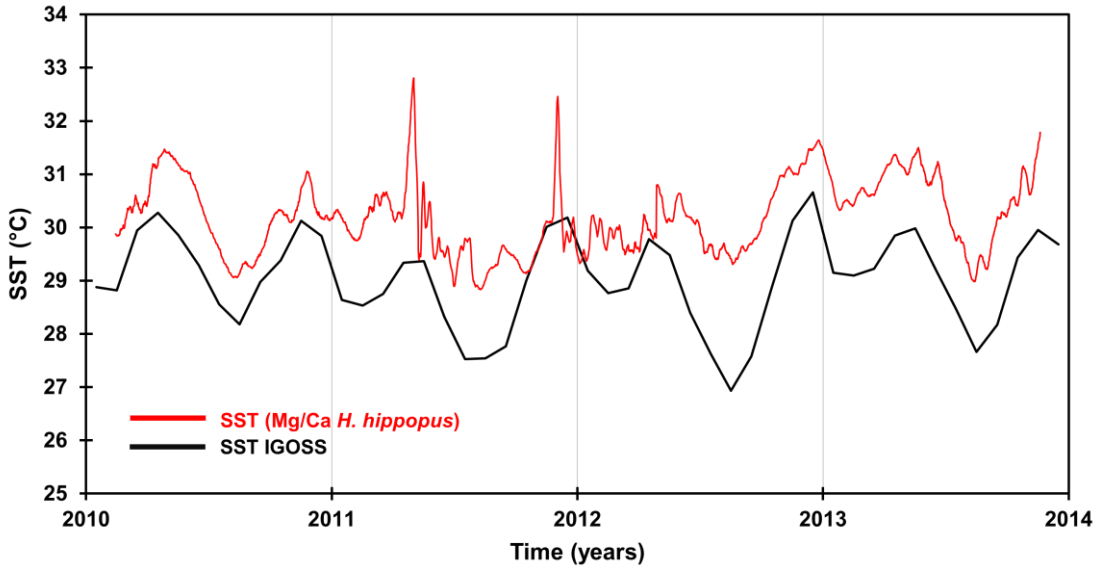

Fig. 3.12. SST derived from Mg/Ca ratios in *H. hippopus* using the equation calibrated for *T. squamosa* (SST= 7.86 * Mg/Ca + 23.4, r = 0.80).

From Sr/Ca ratios, heterogeneous results were obtained for intra-species as well inter-species comparisons. In *H. hippopus* GSL14_23, Sr/Ca values are higher than *T. squamosa* (Fig. 3.11B), whereas *H. hippopus* GSL14_20 have similar values to those of *T. squamosa* (Fig. 3.11B). As discussed before Sr/Ca presents more variability in general in bivalves and in Tridacnidae family.

The average *H. hippopus* Ba/Ca concentrations are similar between them but, when compared to *T. squamosa*, Ba/Ca values are significantly lower (Fig. 3.11C). Peak *H. hippopus* Ba/Ca reach values around 1.2 µmol/mol, whereas in *T. squamosa*, peaks Ba/Ca values are around 5 µmol/mol (Fig. 3.11C). If Ba/Ca is not reproducible between this two species it could reflects taxonomic factors, or geographic factors, however in none of the islands (Kabaena and Kadatua) there are important river mouths. Other possibility, as in $\delta^{18}O$, a difference in depth (habitat) could be involved, with different rates of primary productivity in function of littoral zone, if Ba/Ca mainly reflects productivity. *In situ* measurements will be necessary to clarify these taxonomic differences.

3.3.5. Conclusions

The intra-species comparison conducted in the two samples of modern *H. hippopus* demonstrated the good reproducibility of stable isotopes ($\delta^{13}C$ and $\delta^{18}O$) profiles. However for trace elements some differences are identified. Only Mg/Ca seems to be reproducible between two specimens. Sr/Ca in *H. hippopus* show heterogeneous distribution, with higher concentrations in one specimen. For Ba/Ca same concentrations were found but different pattern in variation, however it could be related to more intra-shell variability for one specimen (GSL14_23).

The principal result from the inter-species comparison between *H. hippopus* and *T. squamosa* is a habitat/temperature difference confirmed by both $\delta^{18}O$ and Mg/Ca shell measurements. Mg/Ca values recorded by *H. hippopus* are higher and could reflect warmer temperatures than *T. squamosa*. Such a hypothesis is in agreement with the habitat of this species that inhabits mainly shallow intertidal areas, while *T. squamosa* are found in deeper/colder subtidal settings. This result shows how ecological information could influence paleo-environmental reconstructions. Results derived from the $\delta^{13}C$ measurements argued for more investigation in this species. The good reproducibility found as in intra-species level as well in inter-species comparison is promising and excludes significant biological processes which would probably differ between specimens. $\delta^{13}C$ variation presents the same saionality that salinity and/or productivity, for this reason is hipothetise the control of these variables in $\delta^{13}C$ adquisition in Tridacnidae shells for SE Sulawesi.

A possible relationship between shell $\delta^{13}C$ and salinity and/or productivity is observed.

Further research particularly on the biology is required to understand the environmental controls on shell chemical composition for Tridacnidae family.

Chapter IV.
Chronology

Chapitre IV. Présentation

La datation des fossiles est très certainement le paramètre le plus fondamental à étudier pour permettre la reconstruction des paléoclimats. Cette information indexe correctement la période géologique, mais fournit aussi des indications précieuses sur la dynamique des changements climatiques — plus précisément sur la vitesse de ces changements. Des datations précises sur des archives climatiques prélevées dans différentes régions du monde, permettent d'établir des liens entre les modifications environnementales. Ainsi il devient possible d'étudier les mécanismes et les processus qui sont à l'origine des modifications climatiques (e. g. les variations orbitales).

Sur des carbonates biogéniques, ou exosquelettes des invertébrés marins de moins de 50 milliers d'années, la datation par Carbone 14 (^{14}C) est la technique la plus utilisée. On recourt à cette méthode aussi bien sur les squelettes de coraux, comme les coquilles de mollusques, que sur les foraminifères. Par contre pour des fossiles plus âgés (plus de 50 milliers d'années) on s'adresse habituellement à la chaine de désintégration de l'Uranium. Malheureusement, cette méthode est inapplicable sur les coquilles de bivalves. La stratégie poursuivie dans ce travail a donc été de dater des coraux échantillonnés à proximité des bénitiers fossiles (Tridacnidae) — c'est-à-dire prélevés sur une même terrasse comme cela a été fait dans d'autres études (Welsh, 2008; Driscoll et al., 2014). Mais contrairement à ce qui ressort des études précédentes, nos calculs montrent une vitesse d'élévation plus lente (de l'ordre de 0.1-0.2 mm/yr) sur la zone étudiée. Le point de départ pour l'U-Th repose donc sur un travail d'échantillonnages et d'observations sur le terrain. De plus, il est important d'avoir un très grande nombre de datations, sur chaque zone d'études, pour assurer de rendre compte au mieux des différents phénomènes géologiques comme la présence de terrasses polycycliques, avec des récifs de différentes périodes sur une même unité. Ce phénomène peut être accentué à cause de l'érosion, et entrainer de confusions.

Ce chapitre décrit le cadre chronologique pour les fossiles étudiés. Il est montré que le résultat d'un âge en système fermé (en équilibre par rapport à l'évolution de l'Uranium dans l'eau de mer) n'est pas tout le temps garanti, malgré les méthodes physico-chimiques ici utilisées pour détecter l'altération et/ou la diagenèse du matériel fossile. Finalement il s'agit de trouver un consensus tenant compte des âges U-Th, du taux d'élévation régionale, de l'altitude et des meilleures estimations de niveau marin lors les périodes étudiées, afin de construire le cadre de recherche le plus cohérent possible.

Chapter IV. Chronology

4.1. Introduction

A fundamental parameter in paleoclimate reconstruction is the accurate determination of the timing of past climate changes, this information provides the phasing of change, and then allows to establish potential links between climate in different regions over the world and between climate change and forcing mechanisms (Hendersson, 2006; Scholz and Hoffmann, 2008). The SE Sulawesi sequences are merely described and no chronologic framework has yet been proposed, first dating results in this region are described in Pedoja et al. (submitted).

The objective in this work was to explore the past 200-300 ka with a specific focus on interglacial periods. Two techniques were used for dating different reef terraces in SE Sulawesi and Belitung Island (West Indonesia): radiocarbon (^{14}C) applied directly on shells and corals, and Uranium-Thorium (U-Th) on corals. The shells of marine bivalves generally exhibit an open system behavior for U-Th (e.g. Kaufman et al., 1996). U-series dating of each material is associated with specific uncertainties. Mollusk shells and foraminifera take up and exchange U after deposition violating the basic closed-system assumption of U-series dating (Scholz and Hoffmann, 2008). Although some research has tried to date Tridacnidae shells using U-Th methods (e.g. Accordi et al., 2010), here we found the heterogeneus results (open system behavior) in a *T. gigas* fossil from Buton Island, in agreement with Ayling et al. (2017). Hence, the chronology is based on U-series dating of coral samples collected close to the Tridacnidae samples.

U-series methods in Pleistocene coral reefs and speleothems however have been accurately and precisely used (e. g. Bard et al., 2002; Andersen et al., 2008). These materials are widely used because they provide the most reliable and precise ages for samples younger than 600 ka (thousands of years) using U-series disequilibrium methods (Chen et al., 1981; Andersen et al., 2008; Scholz and Hoffmann, 2008) and are largely used in sea level and paleoclimate reconstruction over the Quaternary (e.g. Henderson, 2002; McCulloch and Mortimer, 2008; Dutton et al., 2015).

The age of samples collected from Holocene reef were directly assessed by ^{14}C method in shells and corals, but in samples from older/higher Pleistocene terraces, U-Th dates were derived only from fossil corals sampled close to fossil shells.

In this chapter, the results from of U-series and ^{14}C dating used to assign a chronology to fossil Tridacnidae samples are presented. The different geologic parameters influencing the actual reef terraces architecture and the implications to interpret the chronology of events is described. A consensus is made between dating results, samples altitude relative to modern sea level, regional uplift (Pedoja et al., submitted) and best sea level evolution constraints from different records, in order to establish coherent paleo sea level at which the studied reefs were built.

4.2. Methodology

4.2.1. Sampling and sample preparation

Fossil coral samples were collected from two zones in Indonesia (Fig. 4.1-A), Belitung Island (West) and SE Sulawesi (Fig. 4.1-B), as close as possible to fossil Tridacnidae shells.

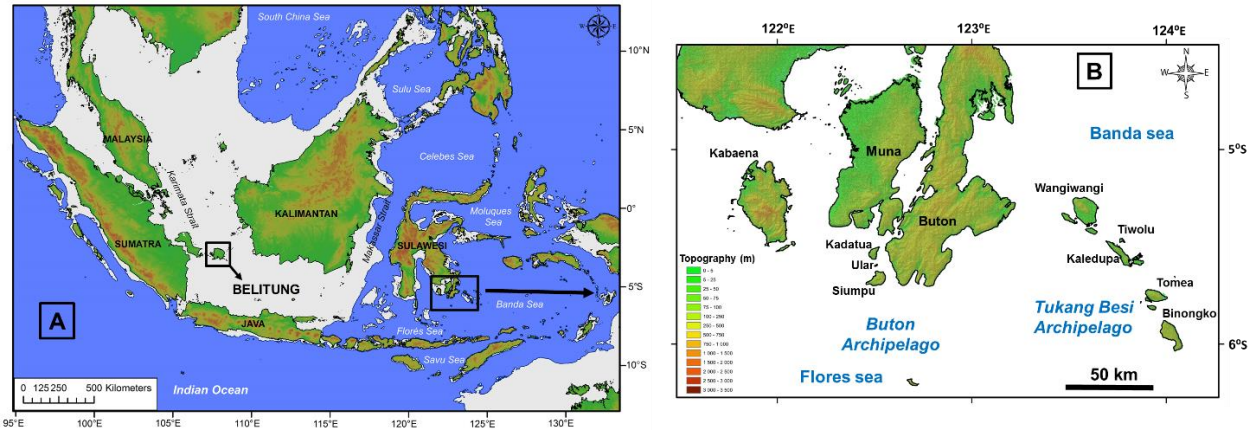

Fig. 4.1. Map of Indonesia **A)** Sampling areas highlighted with black rectangles: Belitung and SE Sulawesi, white areas represent the continental shelf (-200 m isobaths) **B)** Zoom on SE Sulawesi.

A field drill (Shaw backpack Drill, Fig. 4.2A) was used to collect coral core samples (Fig. 4.2C). Due to weathering rates and high precipitation, pristine samples were difficult to find in some key locations. In Nirwana site for example, samples had to be re-collected during the field trip in 2016 to obtain sufficient well-preserved corals for U/Th dating. Sampling can be hampered

by vegetation which grows fast in the tropics as shown on Fig. 4.3, taken a few years interval. This rich vegetation covers the outcrop and makes sampling more difficult.



Fig. 4.2. Drilling on a paleo coral reef terrace from Buton Island **A)** Shaw tool machine **B)** Drill hole **C)** Coral core.

In laboratory the first step was to screen the samples for digenesis and select the best preserved material for dating. Two techniques were used: petrography observations in thin coral sections (Fig. 4.4) and X-ray Ray Diffraction (XRD) to estimate the aragonite/calcite content (Table 4.1).

For coral thin sections (Fig. 4.4) we proceeded as for the shell sections (Chapter II, p.p. 51). The only difference was to fill the pores of the coral with resin because the skeleton is not massive like bivalve shells. To filling porosity, a vacuum chamber was used. This is a delicate procedure as the material could be disintegrated in the manufacturing process.

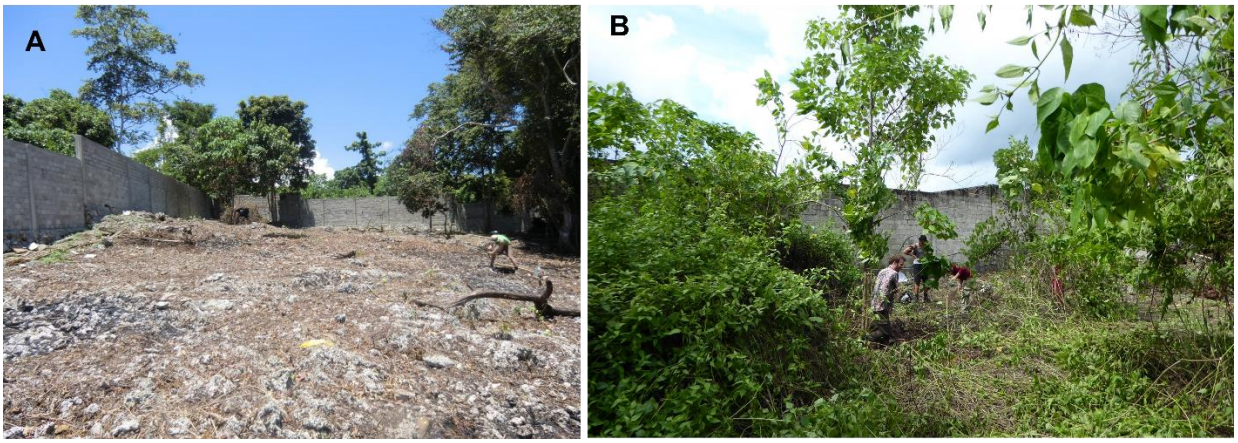

Fig. 4.3. Studied Reef terrace in Nirwana locality (Buton Island) **A)** Exposed carbonate formation **B)** The same place completely covered by vegetation few years later.

After observations using a polarized light microscopy, target corals (without visible/petrographic alteration) were mechanically cleaned with a Dremel tool and reduced to pieces. These fragments of the coral skeleton were secondly cleaned in Milli-Q water and leached in 0.1 N bi-distilled HCL for 15 to 20 minutes in an ultrasonic bath. This leaching procedure does not alter the samples neither affect the results of dating, and ensure the complete removal of organic particles. Finally, the cleaned coral fragments were reduced to powder using an agate mortar. Carbonate powders were sent to GEOPS laboratory (Université Paris Sud, Orsay) for XRD analysis to quantify the extent of calcite recrystallization if any. For XRD methodology we proceeded as in shells, cleaning and reducing material into fine powder (for details refers to Chapter II, p.p. 49). The samples selected for U-Th had a minimum of 2% calcite. These samples were treated at the U-Th platform of the LSCE laboratory (Gif-Sur-Yvette).

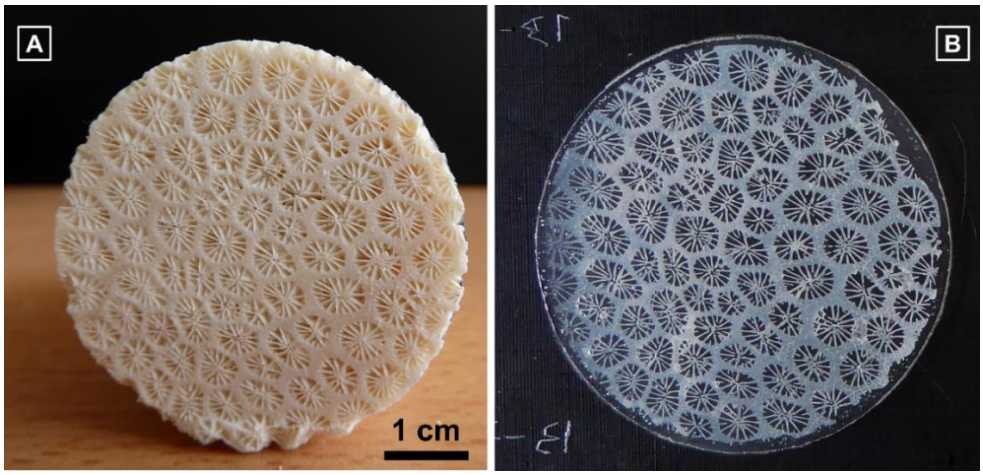

Fig. 4.4. Transversal cut of coral sample GSL13_74 **A)** Core sample **B)** Thin section (40 µm).

4.2.2. The basis of U-series radio-chronology

The U-series isotope decay chain is based on the decay of ^{238}U ($t_{1/2}$~4.5x 10^9 a) (Fig. 4.5) to stable ^{206}Pb via intermediate daughters: ^{234}U ($t_{1/2}$ ~245 ka) and ^{230}Th ($t_{1/2}$ ~75 ka) (Edwards, 1986). The half-lives of parents are much longer than those of their daughters in the decay chain. In an undisturbed system the daughter nuclides naturally reach a state of radioactive or secular equilibrium with the parent nuclide after several millions of years (Jaffey et al. 1971; Holden 1990; Stirling and Andersen, 2009). In nuclear physics, secular equilibrium is achieve when the production rate of a radioactive isotope is equal to its decay rate (IUPAC, 2014).

A variety of studies showed that the U/Ca ratio of scleractinian corals is controlled by the absolute U concentration of seawater (Cross & Cross, 1983; Min et al., 1995; Shen and Dunbar 1995; Swart & Hubbard 1982). Isotope fractionation between ^{234}U and ^{238}U does not occur during coral growth (Cobb et al., 2003), which is demonstrated by the good agreement of the average $\delta^{234}U$ value measured on modern corals with the seawater value (i.e. 146.6 ± 1.4 ‰, Delanghe et al., 2002). Molar $^{232}Th/^{238}U$ values of young corals are slightly lower than seawater values (Chen et al., 1986). This research shows that U and Th are not significantly fractionated during aragonite formation and are incorporated into coral skeletons in their proportions with respect to seawater. Consequently, the low ($^{230}Th/^{238}U$) activity ratio in seawater leads to close to zero initial ($^{230}Th/^{238}U$) activity ratio in corals, the basic premise for U-series dating (Edwards et al., 1986; Scholz and Hoffmann, 2008).

However, natural processes can disrupt the state of isotopic equilibrium, the return to equilibrium then allows quantification of time and, thus, dating of the timing of chemical or physical fractionation (Bourdon et al. 2003), which is the key of the U-series disequilibrium dating methods (Scholz and Hoffmann, 2008). In the case of corals the disequilibrium start when no more skeleton deposition occurred, i.e. the death of the polyp coral.

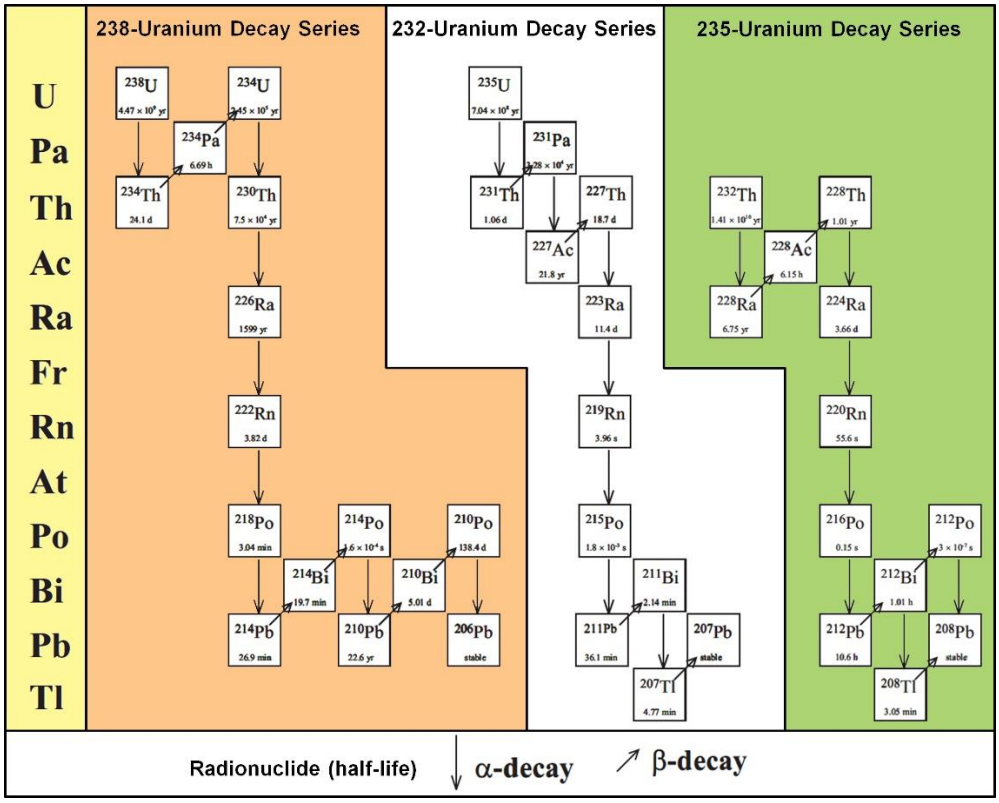

Fig. 4.5. Schematic drawing of the ^{238}U, ^{235}U and ^{232}Th decay chains. The half-lives of the nuclides are indicated in the boxes. In this methodology we used the ^{238}U decay chain series (in red). Modified from Scholz and Hoffmann (2008).

A state of disequilibrium in the ^{238}U decay chain can result from elemental fractionation of Th from U or from isotope fractionation between ^{234}U and ^{238}U (Scholz and Mangini, 2007) (Fig. 4.5). The fractionation of ^{234}U and ^{238}U ($\delta^{234}U$) is produced by the α-recoil effect. An α-decay (e.g. decay of ^{238}U) results in the emission of a He nucleus with finite kinetic energy (Scholz and Hoffmann, 2008).

The $\delta^{234}U$ seawater composition has remained constant in the last 500 ka (Henderson, 2002; Esat and Yokoyama, 2006). Shifts in $\delta^{234}U$ seawater occurred at times of major sea level (glacial-interglacial) transitions (Esat and Yokoyama, 2006; Robinson et al., 2004), but during periods of high sea level (interglacials) seawater $\delta^{234}U$ should have been in the range of 146 ± 10 ‰ (Henderson, 2002). If coral was not altered the initial $\delta^{234}U$ (calculated) must be in this range.

4.2.3. U-Th chemistry and ICPQ-MS analysis

A total of 17 samples were analyzed, following the protocol of Douville et al. (2010). A quantity of ~ 400 mg of coral powder was weighted for every sample and a spike solution (mixture of ^{229}Th, ^{233}U and ^{236}U) was added. Carbonate matrix was dissolved in 11N HCl at 100˚C, and then, target elements were precipitated following the next steps: addition of Fe (iron) solution (plus 1 hour warm-up), addition of NH_4OH (plus 30 min. warm-up), centrifugation and finally elimination of the supernatant. The fractions of Th and U were separated using the UTEVA column chemistry method from Douville et al. (2010). The concentrations of ^{238}U, ^{232}Th and U-Th isotopic compositions for U-series disequilibrium dating were measured on the Inducted coupled quadrupole mass spectrometer (ICPQ-MS) Thermo Fisher Scientific X series II at the LSCE laboratory as described in Douville et al. (2010) and Pons-Branchu et al. (2014). Two additional replicate samples were measured in a high resolution multicollector ICP-MS Neptune.

The results from mass spectrometry were analyzed in a standard set of programming instructions archive (or macro) of the LSCE laboratory, for calculated the different isotope ratios and finally the age of samples.

The activity of isotopes within a decay chain is described by a system of differential equations. The (^{234}U/^{238}U) activity are expressed in delta notation (δ^{234}U), representing the permil (parts per thousand) deviation away from secular equilibrium:

$$\delta^{234}\mathrm{U}(‰) = \left\{ \left(\frac{^{234}\mathrm{U}/^{238}\mathrm{U}_{\mathrm{sample}}}{^{234}\mathrm{U}/^{238}\mathrm{U}_{\mathrm{sec.eq.}}} \right) - 1 \right\} \times 10^3 \qquad (1)$$

Where $(^{234}\mathrm{U}/^{238}\mathrm{U})_{\mathrm{sample}}$ is the measured atomic ratio and $(^{234}\mathrm{U}/^{238}\mathrm{U})_{\mathrm{sec.eq.}}$ is the atomic ratio at secular equilibrium.

If decay system remains closed after deposition or coral death (not gain or loss of U and Th) and half-live of ^{238}U is much longer than ^{234}U and ^{230}Th, the activity of (^{234}U/^{238}U) and (^{230}Th/^{238}U) is described by equations (2) and (3):

$$\left(\frac{^{234}U}{^{238}U}\right)(t) = \left(\left(\frac{^{234}U}{^{238}U}\right)_{init.} - 1\right) e^{-\lambda_{234}\, t} + 1 \qquad (2)$$

$$\left(\frac{^{230}Th}{^{238}U}\right)(t) = (1 - e^{-\lambda_{230}\, t}) + \left(\left(\frac{^{234}U}{^{238}U}\right)(t) - 1\right)\frac{\lambda_{230}}{\lambda_{230} - \lambda_{234}}(1 - e^{-(\lambda_{230} - \lambda_{234})\, t}) \qquad (3)$$

Where $(^{234}U/^{238}U)_{init.}$ is the initial activity ratio, and the λ are the decay constants for ^{230}Th and ^{234}U. The values of these constants are λ_{230} = 9.1577 × 10-6 a-1 and λ_{234} = 2.8263 × 10-6 a-1 (Cheng et al. 2000).

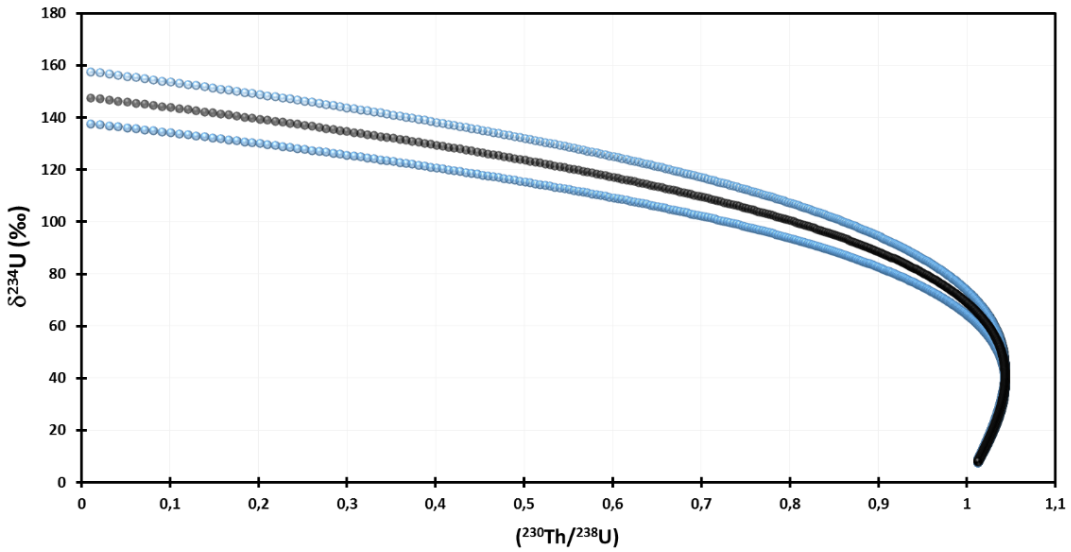

Fig. 4.6. Seawater evolution curve ($^{234}U/^{238}U$ vs. $^{230}Th/^{238}U$ diagram), which describes the closed-system evolution of a coral with the $(^{234}U/^{238}U)_{initial}$ ratio of modern seawater. The blue lines denote the range of ± 10‰ corresponding to the strict reliability criterion. Values from Thompson et al. (2003).

To visualize the temporal development of the activity ratios and illustrate the open or closed system behavior, the sea water relation of $\delta^{234}U$ vs. $(^{230}Th/^{238}U)$ is plotted on a diagram evolution (Fig. 4.6) and compared to every result from corals. In Fig. 4.6, the solid black line shows the seawater evolution curve, which describes the closed-system evolution of a coral with the initial $^{234}U/^{238}U$ ratio of modern seawater. It is assumed that the $^{234}U/^{238}U$ ratio of seawater has not significantly changed during the last 500 ka (Henderson, 2002), and has been similar to the modern seawater value, in particular for interglacial periods (Scholz and Hoffmann, 2008).

4.2.4. Radiocarbon (^{14}C)

The samples for ^{14}C dating were only mechanically cleaned with a Dremel tool to remove detrital material, and reduced in pieces. The fragments samples were analyzed by the research team of the "Laboratoire de Mesure du Carbone 14" (LMC 14 - Saclay, France). For technical details of ^{14}C methodology, refers to Dumoulin et al. (2017), in carbonates section.

Radiocarbon dating measurements produce ages in "radiocarbon years", here it was used the CalPal Program (Calpal-online) to converts ^{14}C dates into calendar years. This calibration process is needed because the atmospheric $^{14}C/^{12}C$ ratio (key element in radiocarbon dating) has not been constant historically (Taylor, 1987).

4.3. Results

The most part of U-Th information were produced in this work but we used also some results (samples from 2012, GSL12 corals) from Pedoja et al. (submitted). This paper focus on geomorphology of emerged reef terraces in SE Sulawesi and produced the first U-Th dating for this region.

The general information of coral samples and the XRD results in percentage of aragonite content are presented in Table 4.1. In Fig. 4.7, is presented the principal areas (red squares) of SE Sulawesi, in which were possible to sampled clam and coral fossils in the same terrace, and obtain age results.

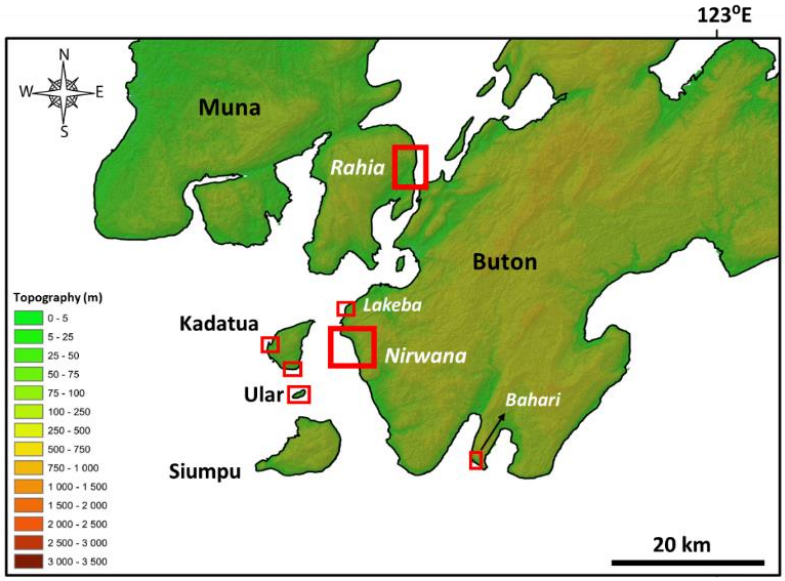

Fig. 4.7. SE Sulawesi map. Red rectangles indicate the principal dated areas in function of Tridacnidae shells and U-series results from corals sampled around. The areas: Nirwana, Lakeba and Bahari (Buton Island), Rahia village (Muna Island), Ular Island, Kadatua (south village and west coast).

Table 4.1. Fossil coral samples information. Locality, latitude/longitude, altitude and XRD results. These samples have been used to derive a chronology for the study area and to assign an age to the fossil Tridacnidae samples.

ID. Coral	Locality	Latitude (°)	Longitude (°)	Altitude (m)	Aragonite (%)
GSL12_15	Nirwana (Buton Island)	-5.52244	122.56789	20	80
GSL12_16	Nirwana (Buton Island)	-5.52244	122.56789	20	35
GSL12_17	Nirwana (Buton Island)	-5.52244	122.56789	20	*
GSL12_61	Muna Island	-5.30591	122.64223	23	15
GSL12_66	Muna Island	-5.30629	122.64218	20	*
GSL12_67	Muna Island	-5.30629	122.64218	20	85
GSL12_68	Muna Island	-5.30629	122.64218	20	80.4
GSL12_36	Bahari (Buton Island)	-5.68190	122.71900	23	99
GSL12_9	Kadatua Island	-5.52692	122.47700	20	97.5
GSL12_11	Kadatua Island	-5.52692	122.47700	20	97.5
GSL14_05	Kadatua Island	-5.56142	122.50260	26	98
GSL14_06	Kadatua Island	-5.56142	122.50260	26	98
GSL13_10	Lakeba (Buton Island)	-5.49804	122.55945	6	100
GSL13_11	Lakeba (Buton Island)	-5.49804	122.55945	6	79
GSL13_59	Lakeba (Buton Island)	-5.48498	122.56364	4	97
GSL13_60	Lakeba (Buton Island)	-5.48498	122.56364	11	94
GSL13_74	Ular Island	-5.59285	122.50700	0-0.2	100
GSL14_13	Ular Island	-5.59250	122.50750	0	98
GSL14_14	Ular Island	-5.59250	122.50750	0	95
GSL16_48	Ular Island	-5.59823	122.50937	0	100
GSL16_50	Ular Island	-5.59926	122.50747	0	100
GSL16_51	Ular Island	-5.59267	122.50799	0	95
GSL16_53	Ular Island	-5.59270	122.50795	0	100
GSL16_58	Ular Island	-5.59292	122.50708	0	100
GSL16_03	Nirwana (Buton Island)	-5.52258	122.56775	16.9	100
GSL16_04	Nirwana (Buton Island)	-5.52255	122.56777	15	100
GSL16_06	Nirwana (Buton Island)	-5.52257	122.56767	17	90
GSL16_61	Nirwana (Buton Island)	-5.52256	122.56769	17.9	90
GSL16_62	Nirwana (Buton Island)	-5.52262	122.56772	18.5	100
GSL16_63	Nirwana (Buton Island)	-5.52262	122.56768	17.3	65
GSL16_64	Nirwana (Buton Island)	-5.52250	122.56788	21.1	90
GSL16_65 A	Nirwana (Buton Island)	-5.52252	122.56788	21.1	80
GSL16_65 B	Nirwana (Buton Island)	-5.52252	122.56788	21.1	15
GSL16_67	Nirwana (Buton Island)	-5.52250	122.56788	21.1	20
GSL16_68	Nirwana (Buton Island)	-5.52250	122.56788	21.1	80
GSL16_70	Nirwana (Buton Island)	-5.52242	122.56775	19.8	55
BEL16_04	Belitung Island	-2.55954	107.80168	4	100
BEL16_05	Belitung Island	-2.55954	107.80168	4	100
BEL16_08	Belitung Island	-2.56688	107.80134	10	100

* Not measured

In Table 4.2 is presented the general information and XRD results of bivalve samples used for ^{14}C dating, only one sample was tested in U-series (GSL14_12).

Table 4.2. Fossil Shells information of marine Bivalve used for U-Th test and ^{14}C dating in this study.

ID. Sample	Locality	Classification	Latitude (°)	Longitude (°)	Altitude (m)	Aragonite (%)
GSL14_12	Bahari (Buton Island)	*T. gigas*	-5.68200	122.71910	15	99
GSL16_44	Ular Island	*Tridacna sp.*	-5.58957	122.51357	0	100
GSL16_59	Ular Island	*Tridacna sp.*	-5.59280	122.50757	0	100
BEL15_3A	Belitung Island	Veneridae (Bivalve)	-2.55942	107.01531	6	15
BEL15_04	Belitung Island	*T. squamosa*	-2.55208	107.80454	5	100

4.3.1. U-series test in a *T. gigas*

The Tridacnidae sample GSL14_12 (*T. gigas*) was used to test the reliability of giant clam shells for U-Th dating. Two subsamples (A and B) from the inner layer growth part of the shell were analyzed, obtaining two different age results (Table. 4.3).

Table 4.3. U-Th test results from GSL14_12 shell (Bahari, Buton Island).

Id. Sample	^{238}U	^{232}Th (ppb)	($^{230}Th/^{232}Th$)	$\delta^{234}Ui$ (‰)	$^{230}Th/^{238}U$	Age BP (ka)	$\delta^{234}Um$ (‰)
GSL14_12 A	0,01000	0,0072	2359.7 ± 12	107.33 ± 2	0.57	77 ± 0.8	133.44 ±3.3
GSL14_12 B	0,00400	0,0071	42 ± 7	110.98 ± 3	0.26	29.2 ± 7	120.55 ± 37.1

The important difference in the age results between two subsamples from the same growth zone reflecting a clear open system evolution of this shell. Even if the aragonite content was 99 % (Table 2). Uranium content are also very low (Table 4.3).

4.3.2. U-series in corals

After petrography observations to detect altered textures on thin sections and XRD analyses on coral powders, only some samples were selected (Table 4.3) to perform U-series analyses. The principal criteria was the recrystallization (% of calcite), which means a loss of Uranium and then, possible biases in age calculus. However we used also some corals with an aragonite content <98 %, because we had not enough material for some areas as Muna.

Table 4.4. U-series results from selected corals to assign a chronology situation in fossil shells.

ID. Coral Sample	^{238}U (ppm)	^{232}Th (ppb)	(^{230}Th/^{232}Th)	δ^{234}Ui (‰)	^{230}Th/^{238}U	Age (ka BP)		δ^{234}Um (‰)	Corrected ages**
						Closed system	Open system		
GSL12_15	2.3	0,23	24545.6 ± 237	146.1 ± 10	0,80		135.3 ± 3	99.6 ± 6	
GSL12_17	2.3	0,27	22573.6 ± 141	171.8 ± 7	0,84		149.1 ± 3	112.7 ± 4	140 ± 5
GSL16_03	2.1	0,25	20469.9 ± 192	129 ± 6	0,77		133.4 ± 3	88.5 ± 4	
GSL16_04	2.6	0,22	28837.6 ± 279	134.9 ± 6	0,80	136.5 ± 3		91.7 ± 4	
GSL16_04 *	5.3	0,48	28222.1 ± 108	150.2 ± 1	0,80	132.6 ± 1		103.3 ± 1	
GSL16_62	2.3	1,40	4186.3 ± 46	164.1 ± 6	0,80		143.3 ± 4	109.4 ± 4	
GSL16_62 *	4.6	3,16	3992.3 ± 101	173.3 ± 3	0,82		141.9 ± 7	116.1 ± 1	
GSL12_36	2.6	0,35	16467.1 ± 299	151.5 ± 9	0,72		112.7 ± 4	110.1 ± 6.5	
GSL12_68	2.2	0,39	16907.3 ± 253	152.7 ± 17	0,95		223.3 ± 15	81.2 ± 9	
GSL12_9	2.1	0,47	13813.1 ± 263	168.5 ± 22	0,98		246.9 ± 26	83.8 ± 11	232.8 ± 23
GSL12_11	2.2	0,40	16503.4 ± 281	176.2 ± 21	1,00		248 ± 22	87.4 ± 10	230.5 ± 21
GSL14_05	5.6	0,36	45160.1 ± 884	161.5 ± 61	0,93		212.7 ± 40	88.5 ± 33	
GSL14_06	5.1	0,48	31390.4 ± 403	180.3 ± 16	0,98		228.9 ± 16	94.4 ± 8	
GSL14_08	5,3	0,61	20597,53 ± 303	147,7 ± 13	0,80	131,8 ± 9		101,8 ± 9	
GSL14_09	7,8	0,63	29627,2 ± 377	147 ± 9	0,80	129,8 ± 6		101,9 ± 6	
GSL13_74	4.9	0,20	68047.8 ± 893	121.1 ± 14	0,90		193 ± 11	70.2 ± 8	
GSL14_13	5.8	0,31	52202.5 ± 631	154.9 ± 11	0,90	184.7 ± 8		91.9 ± 6	
GSL16_48	4,00	0,25	3191.4 ± 50	118.3 ± 2	0,07		7 ± 0.1	116 ± 2	
GSL16_53	2.4	0,09	71382.5 ± 605	116.1 ± 5	0,88		184.2 ± 5	69 ± 3	
GSL16_50	2.3	0,53	11983.5 ± 83	122.3 ± 7	0,89		188.5 ± 5	71.8 ± 4	
GSL13_10	5.1	0,26	53714.1 ± 698	153.7 ± 11	0,88	170.3 ± 7		94.9 ± 7	

* Replicate samples analyzed in a high resolution multicollecteur mass spectrometer (Neptune)
** Thompson et al. (2003) model

The principal area for dating was a place in Nirwana (Fig. 4.7, zoom in Fig. 4.8). From 5 selected corals (GSL12_15, GSL12_17, GSL16_03, GSL16_04 and GSL16_62) we obtained only one result (GSL16_04) in a straight closed system. From this sample we obtained two ages (replicate in different spectrometers): 132.6 ± 1.1 and 136.5 ± 3.3 ka BP (Table 4.4). This period correspond to the limit between Termination II (deglaciation) and the beginning of the last interglacial period, Marine Isotopic Stage 5 (MIS 5). However the other samples (open system) present close results: 133 and 135 ka. So we calculated a mean age for these samples: 133.7 ± 3 ka.

.

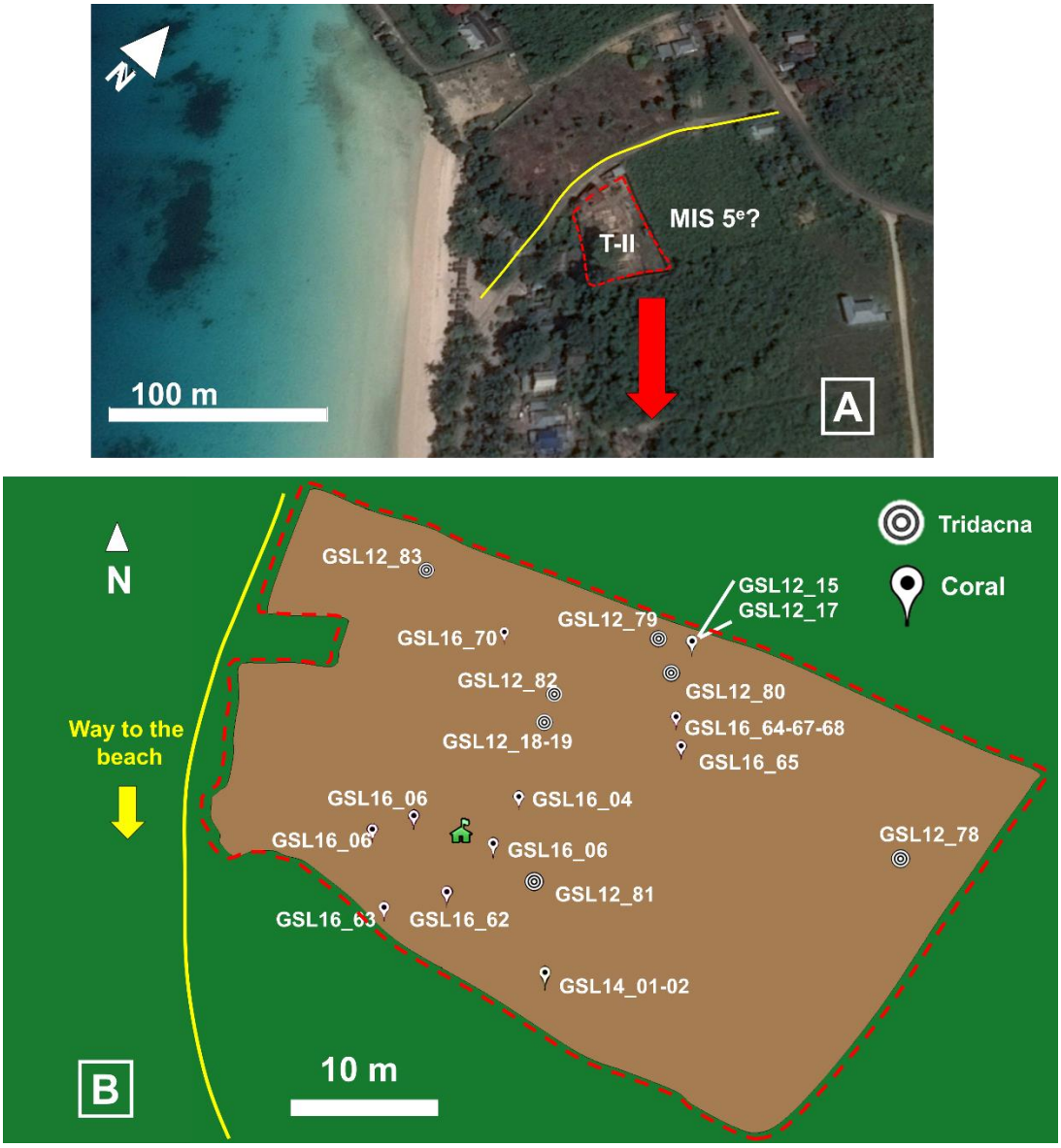

Fig. 4.8. Nirwana studied zone **A)** The specific sampling area are bordered in dashed lines **B)** Zoom of sampling area (Johan's Garden). Yellow line is a local way. This zone is dated from Termination II. Upper-next area perhaps belongs to MIS 5e. Modified from Google earth images (2017).

In the Bahari sector (Sampolawa Peninsula, Fig. 4.7, zoom in Fig. 4.9) one coral (GSL12_36) near from a fossil shell (GSL14_12) has an age of 112.7 ± 4 ka at 23 m above sea level. This age is at the end of the sea level highstand MIS 5e. Despite a 99 % aragonite content, this sample exhibit an open system result. The GSL14_12 sample is the Tridacnidae fossil used in U-Th test, but as we showed the result of this shell is not reliable, neither in agreement with the dating of GSL12_36 coral sample (Table 4.4).



Fig. 4.9. Bahari village (Sampolawa Peninsula, Buton Island). Modified from Google earth images (2017).

From the Rahia village (Muna Island) we obtained a coral dated at 223.35 ± 15.6 ka BP (GSL12_68) at 20 m, which corresponds to the penultimate interglacial MIS 7 (Fig. 4.7, zoom in Fig. 4.10), in the same area we sampled also two fossil shells. However this coral present two inconvenients. Firstly, this sample only has an 80% of aragonite content and secondly, the age is associated with a large uncertainty (15.6 ka). This age uncertainty propagates into an uncertainty in sea level associated with this samples as the age corresponds to a complex period including a reversal sea level, this will be discussed later. This coral is the only reference for two Tridancidae shells collected nearby (GSL12_60 and GSL12_64) (Fig. 4.10).

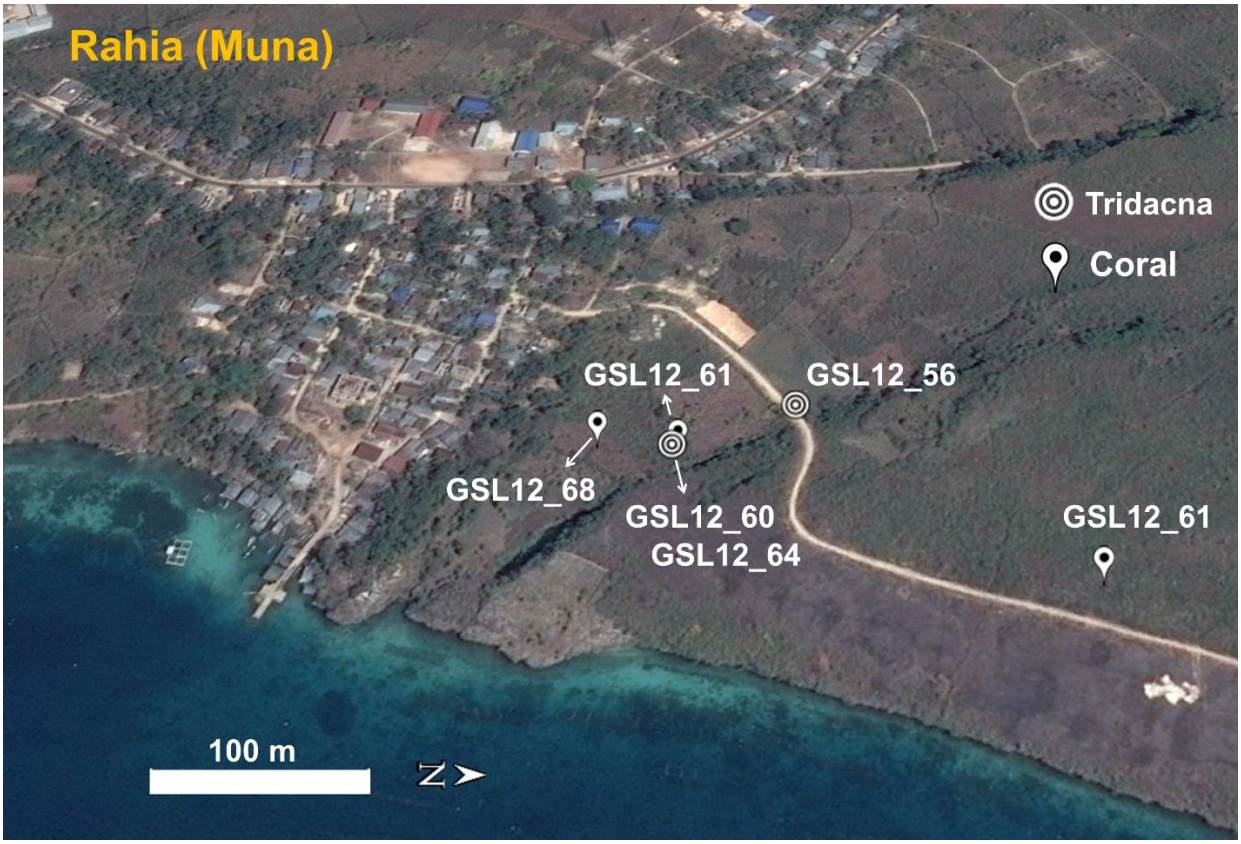

Fig. 4.10. Rahia village, Muna Island. Modified from Google earth images (2017).

On the west side of Kadatua Island (Fig. 4.7, zoom in Fig. 4.11) we have two corals (GSL12_09 and GSL12_11) close to a Tridacnidae shell (GSL12_10), the ages are respectively: 232.8 ± 23.8 and 230.5 ± 21.2 ka (Table 4.4). Take into account the uncertainty, these samples comes from MIS 8 or MIS 7, with more possibility for this last one, because MIS 8 was a glacial period.

In the south village (south Kadatua, Fig. 4.11) one fossil shell (GSL14_07) are near of two coral samples (GSL14_05 and GSL14_06), with ages of 212.7 ± 40.2 and 229 ± 16 ka respectively. Again this corals exhibit an open system for U-series, despite 98 % of aragonite content. Another coral in this zone (GSL14_16) is dated at 123.34 ± 5.1 ka (MIS 5e), however the most close fossil shell (GSL14_15) was sampled at 70 m of distance and the dating result are also in open system, with 100% of aragonite content. The coral samples GSL14_08 and GSL14_09 were found in closed-system, but no fossil clams are close to these corals.

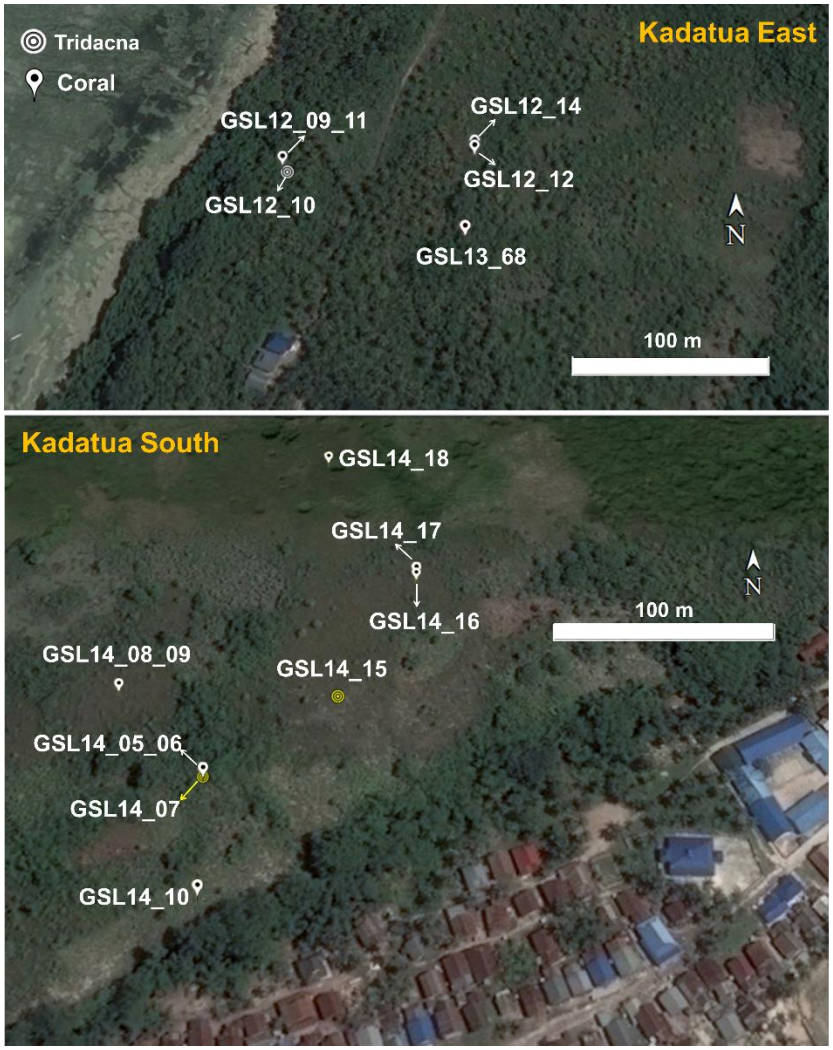

Fig. 4.11. Kadatua samples. From the south village of the island and the east side. Modified from Google earth images (2017).

On Ular Island (Fig. 4.7, zoon in Fig. 4.12) 4 corals were dated with U-Th (GSL14_13, GSL13_74, GSL16_53 and GSL16_50), of which two were replicated in ^{14}C (GSL16_53 and GSL16_50). Additional coral (GSL16_48) and two Tridacnines (GSL16_44 and GSL16_59) were dated using ^{14}C.

For U-Th, only GSL14_13 presents a closed system result (98% of aragonite), the age is 187.1 ± 9.4 ka. Nevertheless the other corals (open system) have ages around the same period: 194.73 ± 7.3, 184.2 ± 5.6 and 188.50 ± 5.6 ka. The period is the end of MIS 7 or MIS 6e interstadial.

These age results (MIS 6/MIS 7) were unexpected because corals were sampled in a platform at at present day sea level (0 m).

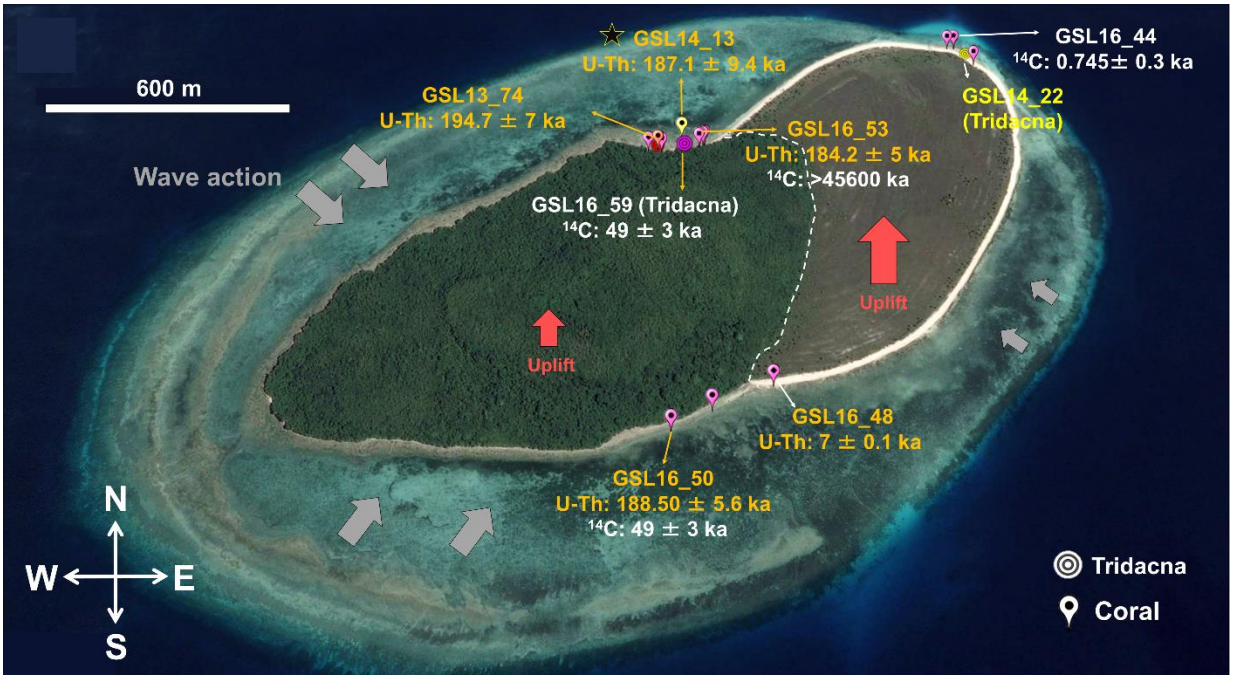

Fig. 4.12. Ular Island dating map. U-Th dating in orange and ^{14}C dating in white. Arrows indicate the intensity of the wave action and uplift rate. Modified from Google earth images (2017).

4.3.3. Analytical reproducibility

In every U-series dating session of the Indonesian project, one coral sample (GSL12_14) was used as control for the reproducibility of the method from 2012 to 2016. The results are presented in Table 4.5 and Fig. 4.13. From 5 different sessions we conclude a good reproducibility of the method over the time, with an age for this sample around 136 ka (Table 4.5). However, in two sessions (2013 and December 2016) different results were obtained, with older ages and open-system behavior. It can be explained because in these sessions we used different fractions of the same coral, obtaining slightly different ages (Table 4.5). These results could reveals differences in micro-structural skeleton (e.g. Tomiak et al., 2016; Obert et al., 2016) or the fact of sampling multiple fractions from a same coral head.

Table 4.5. Control sample (GSL12_14) results from different analytical sessions.

Id. Sample (year)	^{238}U	^{232}Th (ppb)	($^{230}Th/^{232}Th$)	$\delta^{234}Ui$ (‰)	$^{230}Th/^{238}U$	Age BP (ka)	$\delta^{234}Um$ (‰)
GSL12_14 (2012)	2,20	0,22	24346.3 ± 269	99.64 ± 5	0.8	136.1 ± 3.3	146.4 ± 7
GSL12_14 (2013)	2,26	0,23	24466.1 ± 202	98.51 ± 7.5	0.8	136.9 ± 4.1	145.06 ± 11
GSL12_14 (2014)*	2,32	0,38	15769.02 ± 237	104.46 ± 10.9	0.8	150.1 ± 6.7	159.6 ± 16
GSL12_14 (2016 Jan.)	5,48	0,29	44988.9 ± 658	95.46 ± 12.7	0.8	136.2 ± 7.	140.3 ± 18
GSL12_14 (2016 Dec.)*	2,34	0,14	42153.6 ± 393	85.61 ± 3.6	0.8	141.4 ± 3.5	127.7 ± 5

* Different fraction from the same coral

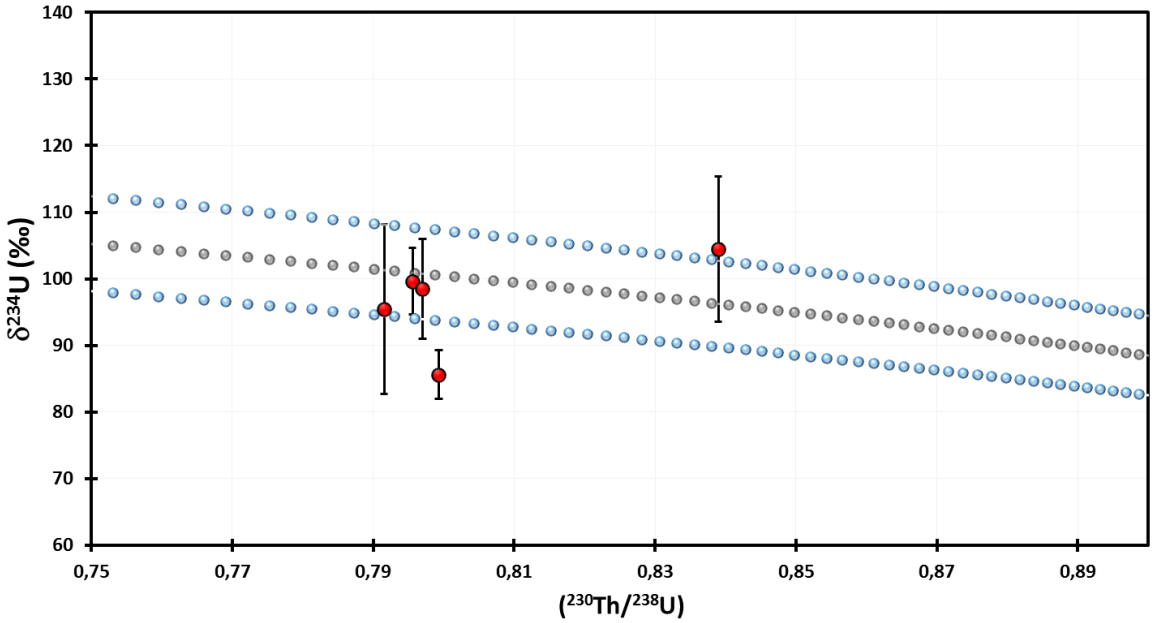

Fig. 4.13. Control sample (GSL12_14) results in different analytical sessions (years).

In a second reproducibility test, we replicated two coral samples (GSL16_62 and GSL16_04) and compare the results using two different spectrometers: ICPQ-MS and MC-ICP-MS. The MC-ICP-MS equipment is a high resolution multicollecteur mass spectrometer (Neptune). With the Neptune we obtained slightly younger ages than in the Quadrupole spectrometer in both samples. At the same time higher concentrations of ^{238}U and ^{232}Th. The replicated samples comes from Nirwana, and support the Transgression-II age.

U-series dating by ICP-QMS can display greater analytical uncertainty when compared to conventional TIMS or MC-ICP-MS measurements. However, the error bars obtained by ICP-QMS still allow to identify open and closed-system behaviours and to discriminate different isotopic stages. With the two methods close results were obtained (Table 4.4). Douville et al. (2010) shows that the accuracy of ICP-QMS U-series ages are equals to that obtained by MC-ICP-MS.

4.3.4. U-series and ^{14}C

Finally it was tested the reproducibility between U-series and ^{14}C dating in samples from Ular and Belitung islands (Table 4.6). In Belitung Island (West Indonesia) two corals (BEL16_05 and BEL16_08) were used for U-Th and ^{14}C. For U-Th only BEL16_08 was found in closed-system, and the counterpart result in ^{14}C give the same age (6 ka) at Middle Holocene (Table 4.6).

BEL16_05 present open system but the age (7.3 ka) is not far from the counterpart ^{14}C dating (6.7 ka). The ^{14}C results from bivalves give also the same period (Mid-Holocene). Belitung results are exploited in a paleoclimate reconstruction work (in prep) and in a geodynamic model simulation (Sarr et al., submitted), both research associated in the same project of this PhD. Complementary results of ^{14}C dating in Appendix 4.

Table 4.6. Comparison between U-Th and ^{14}C ages from Ular and Belitung Islands.

ID. sample	Locality	Altitude (m)	U-Th Age (ka)	^{14}C Age (Ka) calibrated	Period
GSL13_74	Ular West	0	193 ± 11.1 *		
GSL14_13	Ular West	0	184.7 ± 9		
GSL16_53	Ular West	0	184.2 ± 5 *	49.5 **	MIS 6e
GSL16_50	Ular West	0	188.5 ± 5.6 *	>45.6 **	Interstadial
GSL16_59 Δ	Ular West	0		49.3 **	
GSL16_44 Δ	Ular East	0		0.7 ± 0.06	Late Holocene
BEL15_04 Δ	Belitung Island	6		6.3 ± 0.09	
BEL15_03A Δ	Belitung Island	5		7.4 ± 0.06	
BEL16_04	Belitung Island	4	5 ± 0.13 *		Mid. Holocene
BEL16_05	Belitung Island	4	7.3 ± 0.28 *	6.7 ± 0.05	
BEL16_08	Belitung Island	10	6.8 ± 0.13	6.5 ± 0.08	

* Open system Δ = Tridacnidae/Bivalve shell

** Understimated, on the detection limit of radicarbon technique (50 Ka)

Concerning Ular Island heterogeneous results were obtained (Table 4.6). In the west side of the Island (Fig. 4.12), two corals (GSL16_50 and GSL16_53) were used for both dating technics, and two Tridacnine shells (GSL16_44 and GSL16_59) in ^{14}C. From these 4 dating results (^{14}C), three were found in the detection limit of radiocarbon technic (~50 ka). The responsible researcher of the LMC-14 laboratory conclude that these results are not reliable because they are on the detection limit of the method, and consequently must be considered as older than 50 ka, which means Pleistocene origins. The counterpart U-series dating for these corals were found at 184 and 188 ka BP (Table 4.6), with open-system for both samples. However other coral (GSL14_13) from the same platform (Fig. 4.12) was dated at 184.7 ka and was found in closed-system. Although GSL16_50 and GSL16_53 are in open system, the ages are the same of closed-system sample GSL14_13. The period corresponds to the interstadial (incomplete deglaciation) MIS 6e.

All these samples were expected to come from the Holocene because they were sampled at sea level (~0 m) in west side of the Island, but the U-series age is supported by the underestimation of ^{14}C. This result reveals interesting process besides modern architecture of paleo reefs in the area, because in the east side of Ular, Late Holocene dating was also obtained at sea level from ^{14}C, in a Tridacnidae sample (Table 4.6).

4.4. Discussion

U-series radio-chronology is a delicate and exhaustive technique. A large amount of samples are needed to detect reliable ages and avoid over/under estimations. In a same terrace (level) multiple ages can be found, polycyclic terraces (e.g. Bard et al., 1996) as result of erosion and/or tectonics. Second, the effort and methodic sampling is important because not all corals will meet the requirements for U-series closed system evolution. Here we discuss this features and the final scenarios that we can interpret using dating, actual altitude of pale-reefs, uplift rates and sea level (SL).

4.4.1. The impossibility of use giant clams for U-series

Giant clams have a dense structure skeleton, usually better preserved than fossil corals and then, keeping intact the geochemical information from the past (e.g. Driscoll et al., 2014; Warter et al., 2015; Ayling et al., 2015). However, unlike corals, mollusks do not incorporate appreciable quantity of Uranium into their skeleton during growth, modern specimens commonly contain less than 100 parts-per-billion (ppb) (Kaufman et al., 1971; Kaufman et al., 1996). Furthermore, fossil mollusks often exhibit greater uranium concentrations than in living individuals, indicating post-mortem uptake of uranium and hence open-system behavior e.g. (Ayling et al., 2017).

The U/Th ages derived from a fossil *T. gigas* sample (GSL14_12) are very heterogeneous. The shell subsamples (GSL14_12A and B) has a very low concentration in uranium (Table 4.3), then very weak signals are obtained and the error on the measurement of ^{230}Th could be greater than the value given by the spectrometer. Both subsamples exhibit a clear open system behavior, out from the equilibrium with sea water (Fig. 4.14).

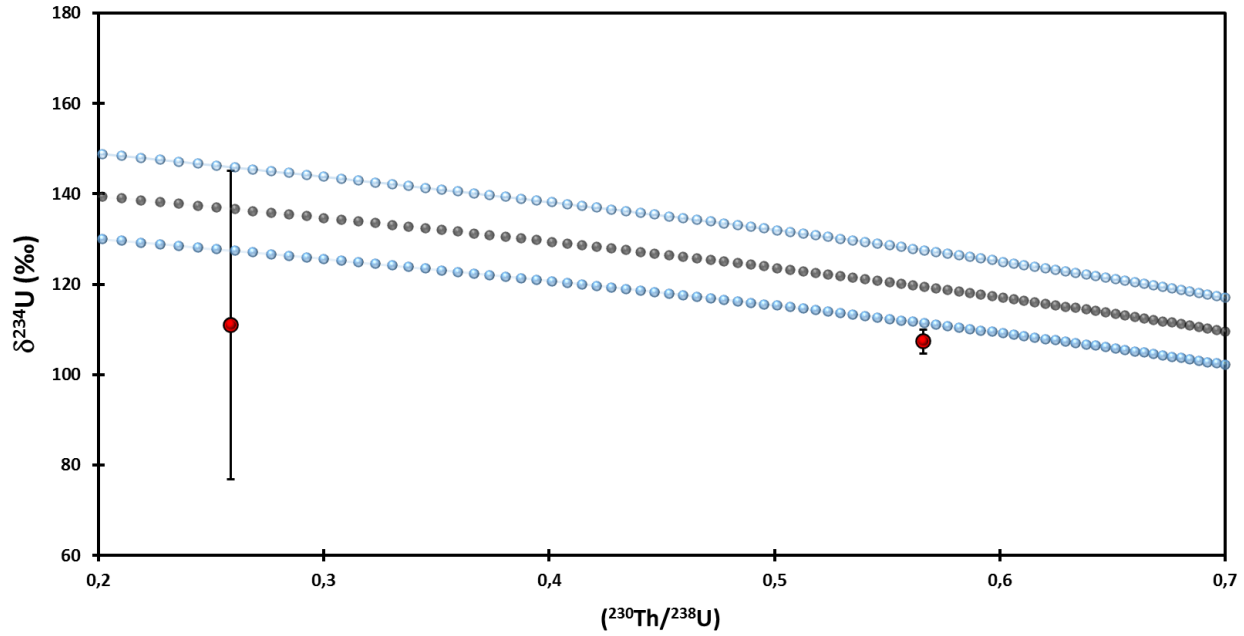

Fig. 4.14. *T. gigas* U-Th test. Red filled symbols represent bulk material samples.

Ayling et al. (2017) conducted a detailed U-Th study using *T. gigas* fossils from Huon Peninsula (Papua New-Guniea), comparing different individuals and shell growth zones. The authors infer that Tridacnaidae shells have experienced multi-stage uptake with varying uranium sources with one or more loss events that do not allow the application of existing open system models (e.g. Thompson et al., 2003; Villemant and Feuillet, 2003; Scholz et al., 2004). The inner zone in all fossil shells from Huon Peninsula contains negligible uranium (<0.01 ppm), as we found in our test for GSL14_12 *T. gigas*. Ayling et al. (2017) found zonal differences in U concentration, attributed to crystallographic differences between the growth zones.

Uranium uptake and loss can affect time-integrated uranium distributions and are difficult to constrain. For this raison Ayling et al. (2017) conclude that fossil Tridacnidae cannot provide independent geochronological control using either closed or open-system U-series dating techniques.

The inconsistent results from U-Th in fossil *T. gigas* (Fig. 4.13) are in agreement with the studies referenced before in giant clams as in general in mollusks. The high uncertainty in U-series from Tridacnidae fossils and the impossibility to correct the ages with the developed models, lead

to the conclusion that given the current research state to a limitation and/or impossibility to use giant clams for U-Th dating. As a result, in this study we focus only on corals for U-series.

.

4.3.2. Defining the criteria for choice reliable ages from U-series

Reliable closed-system U-series ages can be obtained from well preserved corals, but only some samples actually satisfy the criteria for preservation and closed-system U-series dating (when compared Table 1 and Table 4), and then, few corals help us to reference the age of Tridacnidae shells.

The U-series calculus have three main assumptions: 1) initial thorium concentrations are zero ($^{230}Th/^{238}U_{init.} = 0$), 2) no significant ^{238}U decay has occurred over the period of interest, 3) any changes in isotopic ratios are a consequence of decay and ingrowth. If it is the case for a given sample, the measurement of ($^{234}U/^{238}U$) and ($^{230}Th/^{238}U$) allows the calculation of the time since the death of the coral (Cheng et al., 2000; Henderson, 2002).

In Table 4.4 are summarized the U-series results from selected corals to establish a chronology situation for Tridacnidae shells. From 21 coral samples, only 5 are in closed-system with sea water and have a content of aragonite >98%. Because corals incorporate ^{234}U and ^{238}U in the same ratio/equilibrium of modern seawater, the initial coral ($^{234}U/^{238}U$) (calculated in equation 2) should agree with modern seawater ($^{234}U/^{238}U$). Hence, a significant deviation of the initial $\delta^{234}U$ (in corals) from the seawater value in Fig. 4.14, indicates open-system behavior and the ^{230}Th/U-age has not be considered as reliable. For this reason corals off the equilibrium with sea water (145 ± 10 ‰) must be considered as open system. The sea water reference is the first discrimination index for open-system.

Fossil corals often contain excess initial ^{234}U relative to generally accepted seawater values (146 ± 10 ‰) indicating isotopic enrichment in ^{234}U (or depletion in ^{238}U) after their initial equilibrium with seawater (Banner et al., 1991; Bard et al., 1991).

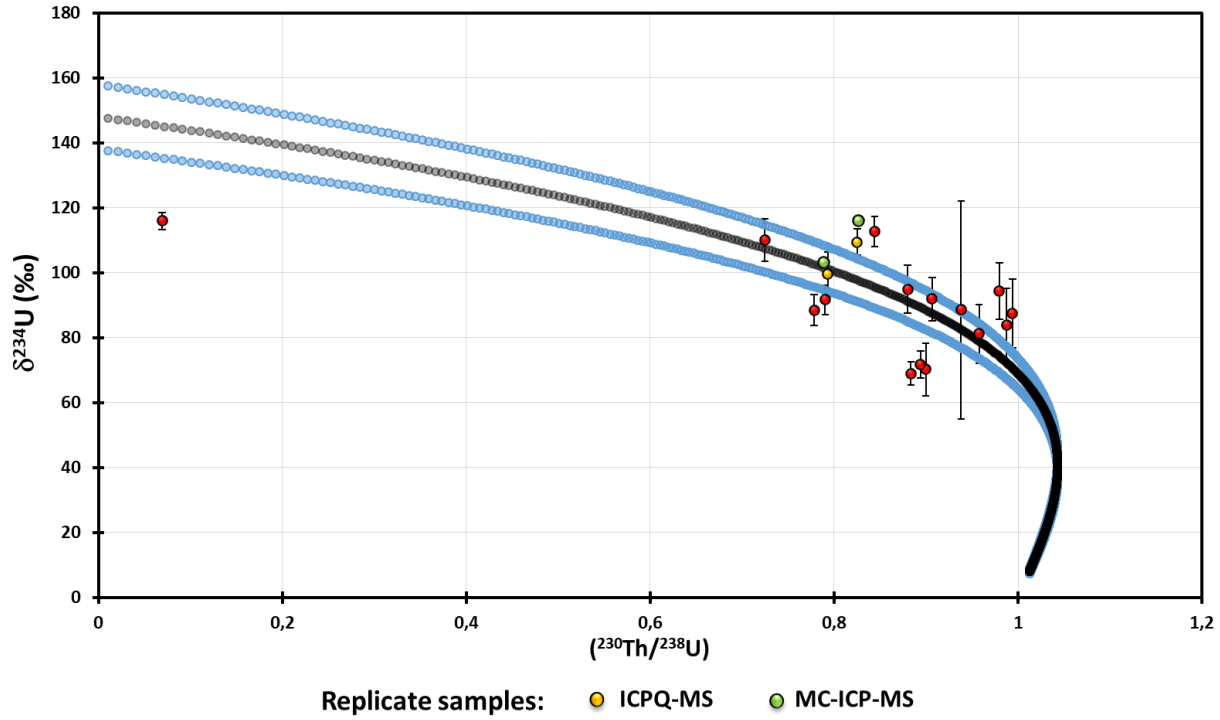

Fig. 4.15. U-series results from selected corals. Green circles represent replicate samples (GSL16_04 and GSL16_62) analyzed in a high resolution multi-collector mass spectrometer (Neptune).

The ^{232}Th excess is another index for open-system behavior. Elevated ^{232}Th is also related to post-depositional contamination from detrital sources and therefore, considered as an indicator for open-system evolution (Scholz and Hoffmann, 2008). ^{232}Th concentrations higher than 1 ppb indicate Thorium detrital contamination (Stirling et al. 1998). The only sample with a content higher than 1 ppb was GSL16_62 (Table 4.4).

The low ^{232}Th contents together with high (^{230}Th/^{232}Th) activities ratios argue for the absence of significant detrital contamination. These samples display initial δ^{234}U values that agree with the range in modern ocean water values, which indicates isotopic evolution in a closed system (Table 4.4, Fig. 4.15).

Several open-system U-series dating models have been proposed to correct the uranium-series isotope mobilisation in fossil corals as a result of α-recoil processes (Thompson et al., 2003; Villemant and Feuillet, 2003; Scholz et al., 2004). Here is tested the model of Thompson et al. (2003) in some samples (Table 4.4). This model corrects the data for ^{234}U and ^{230}Th excess related to α-recoil process. The model turns out to be the best performing model to reasonably correct

anomalous shift in U-series, given consistent results with reliable closed-system ages from the same reef unit.

We have actually only 5 samples that check all criteria (Table 4.4) with only 3 near to Tridacnidae fossils. But here it is also considered using open-system ages because in some cases, open-system results reflects the same age of closed-system corals for a same sampled area (e.g. Nirwana and Ular west). In some studies, reliable sea-level reconstructions and suborbital events are reconstructed from open-system corals (e.g. Thompson and Goldstein, 2005).

A relevant observation during the dating process was to obtain open system evolution from ~100 % aragonite corals (Table 4). The requisite in calcite content for reliable U-series is maximum 2% (Stirling et al., 1998; Sholz and Hoffmann, 2008). The fact that even samples, which are apparently pristine according to mineralogical criteria, show elevated initial $\delta^{234}U$ (Table 4) suggests that the isotopic system is more sensitive to post-depositional changes than any petrographic or general geochemical parameter (Chen et al., 1991; Zhu et al., 1993). Therefore, the premise of closed-system behaviour is not generally warranted for fossil reef corals, and the accuracy of the ages is more limited due to the isotopic anomalies than analytical precision (Bard et al., 1990; Stirling et al., 1995). Potter et al. (2004) demonstrated that "there is no clear correspondence between petrographic textures and U-Th results in subtly altered corals", and recommended to analyze a large number of samples for each study site (or terrace in our case) to avoid the risk of over interpreting isolated age samples. The mechanisms and effects of diagenetic alteration on U-series ages are not yet completely understood and current screening approaches are unable to identify all altered samples (Potter et al., 2004; Tomiak et al., 2016; Obert et al., 2016).

Tomiak et al. (2016) found that skeletal micro-architecture plays an important role in diagenesis and U-Th dating and recommended selective sampling of low porosity skeleton to obtain the most reliable U-series ages. These authors also used an organic geochemistry method as alternative tool to date Pleistocene samples that have suffered heavy dissolution and are unsuitable for U-series analyses. The technique is the amino acid racemization (ACR), and it can be used also as tool for diagenetic screening prior to any U-analyses. ^{231}Pa (protactinium) dating has also been used to evaluate the reliability of U-series ages (Cheng et al., 1998; Gallup et al., 2002). Pirazzoli

et al. (1991) found that recrystallization have only a limited effect on electron spin resonance (ESR) dating results from 60 % aragonite corals of Sumba Island (Indonesia).

To summarize the findings of this work, minor secondary aragonite and calcite overgrowth cannot reliably identify U-series open-system behavior (Hamelin et al., 1991; Bar-Matthews et al., 1993; Stirling et al., 1998; Scholz and Hoffmann, 2008). Supplementary methods such as ACR and/or ^{231}Pa should be taken into account to identify unaltered samples for U-Th in future works. In this study, it is demonstrated that further efforts in sampling are necessary with only three rigorous closed-system ages.

4.3.3. Regional uplift, dating and sea level consensus

Before any local interpretation from past climate and ocean conditions inferred from $\delta^{18}O$, it is needed to determine the SL during the studied periods relative to the present day, in order to correct the fossil $\delta^{18}O$ signal for global ice volume (Chapter V). To constrain SL in past periods, three main parameters were used: dating results, uplift regional rate and the altitude (relative to sea level) in which fossil samples were found. These results are contrasted to the best SL constraints available in the literature for the studied periods, to find the most coherent scenarios of SL evolution.

In Fig. 4.16 are plotted the age results derived from study, with complementary close-system ages from Pedoja et al. (submitted) obtained around different places in SE Sulawesi. The ages are compared to a composite model of sea level evolution (Fig. 4.16). These results show that the paleo-reefs we sampled were mainly constructed during interstadial and transgression (sea level rising) periods. In Huon Peninsula, Stein et al. (1993) also reported a major reef building event, dated at ~134–135 ka during Termination II.

Another key factor in reef construction is the geometry in which coral reef is built. As slope increases less space will be available for coral growth. Consequently when sea level reaches the maximum (highstand), there is less accommodation space for reefs to build. A second consequence of high slope in platform geometry is observed during regression (drop sea level/transition to a

glaciation). These periods are associated with more important erosion of most recently deposited corals (interglacial reef): regressive facies (Pedoja et al., submitted). The direct consequence of this architecture of emerged terraces (for some areas) is to find more abundant coral fossils during transgression times than highstands (more eroded).

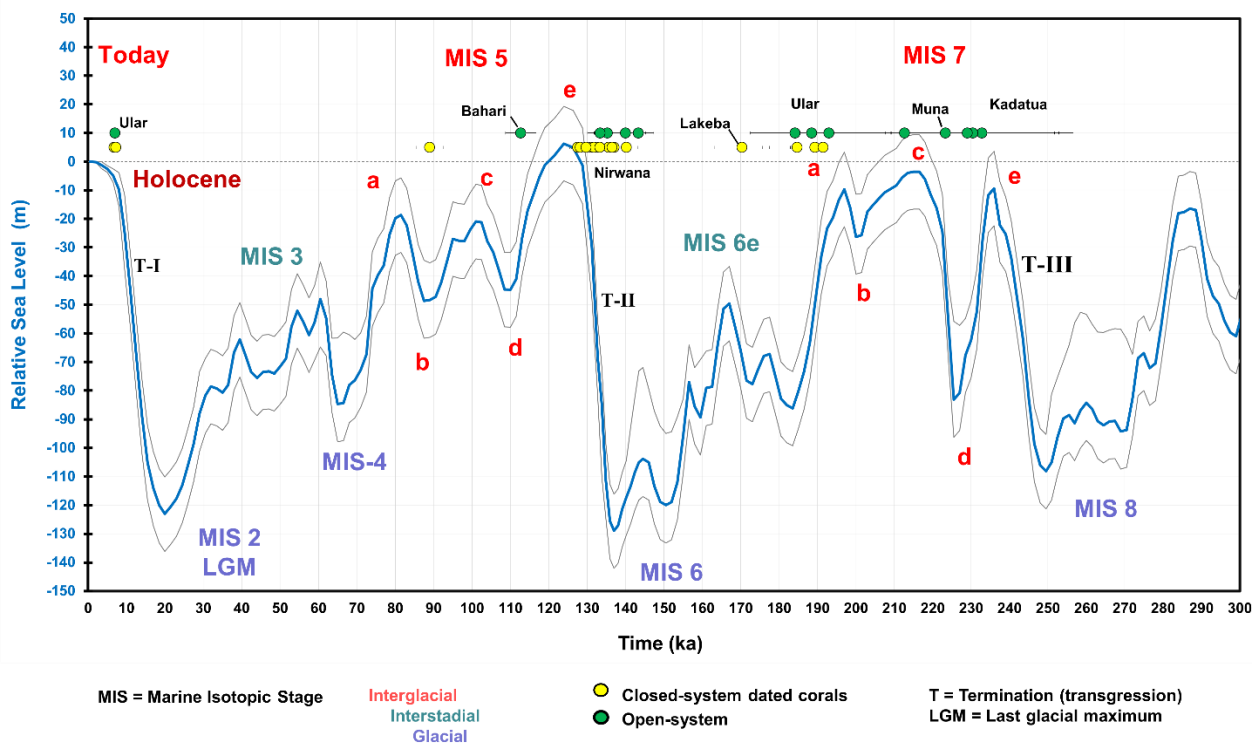

Fig. 4.16. U-Th dating results relative to the last glacial-interglacial periods over the past 300 ka. Closed-system results include information from Pedoja et al. (submitted). Composite sea level evolution model modified from Waelbroeck et al. (2002).

The principal chosen areas for climate reconstructions was Nirwana (Buton) and Rahia (Muna). Nirwana in reason of number of corals dated with a mean age between the Termination II and the beginning of the last interglacial (MIS 5), and the presence of Tridacnidae fossils. And Rahia because the age (even in open system) corresponds to the penultimate interglacial (MIS 7).

The mean age for Nirwana was found at 133 ± 3 ka with a mean altitude of 16 m. Pedoja et al. (submitted) assessed the mean regional uplift in Buton Archipelago at 0.15 mm/yr. The SL during which that fossil reef grew can be estimated using the mean age of the fossil terrace, the actual altitude and the uplift rate. It can be expressed as:

$$SL = age(ka) * uplift\ (mm/yr) - H$$

The age by uplift rate is equal to the total vertical rise over time, and the difference with actual altitude (H) is the paleo SL relative to the present. Using the regional uplift of Buton archipelago the paleo SL obtained for Nirwana is 4.9 ± 0.5 m below sea level. The local uplift rate of Nirwana was also calculated using model simulations in other research of the same project, the results (not published, Pastier et al., in prep) give a best fit of 0.15 mm/yr.

Regarding the SL reconstructions around the world for the concerned period (~ 133 ka) a large variety of results are found (Table 4.7). The problem to assign a SL is based on the fact that every site in the world recorded different SL for the same period. Several reasons explain these SL differences, age uncertainty is an important element, secondly because the rise in sea level is associated with ice volume melting which is not uniform across the world (Hay et al., 2014). Ice melting and associated rise in sea level is accompanied of local geodynamic process or "glacio-isostatic-adjustments" (GIA) (Lambeck and Nakada, 1992; Raymo et al., 2011). The fingerprints of the GIA are then reflected in differential SL reconstructions and must be corrected to obtain a "eustatic sea level" (ESL, Raymo et al., 2011) (refers to Chapter I).

Table 4.7. Sea level reconstruction for MIS 5e and TII from different sites around the world.

Time (Ka BP)	RSL (m)	Study	Location
133	-60	Lambeck and Nakada, 1992	Bermuda and Caribbean Islands
135	-10	Stirling et al., 1998	Western Asutralia
133	-5		
130	0		
125	3 ± 2		
130 ± 2	-60	McCulloch et al., 1999; Esat et al., 1999	Huon Peninsula, Papua New Guinea
125	3±2		
135 ± 0.8	18 ± 3	Gallup et al., 2002	Barbados (Caribbean)
133	-50	Sidall et al., 2006	Red Sea
133	-70	Thomas et al., 2009	Tahiti
135	-50		
133	-30	Stap et al., 2014	Model simultaion
125	6		
133	-30	Waelbroeck et al., 2002	Composite SL profile
125	6		
133	-80	Bates et al., 2014	Composite SL profile
125 ± 2	6		
133	-6	Dutton et al., 2015	Seychelles islands (Indian Ocean)
125	0		
133	-7	Dutton and Lambeck, 2012	Composite model including ESL
133	0	Hearty et al., 2007	Composite model
125	2		

For the near sites from ice sheet formation, GIA effects become more important than far-field sites (tropical latitudes) (Lambeck and Nakada, 1992; Hay et al., 2014). For example, studied coral reefs from Florida, Bermuda Islands, Bahamas and Barbados are exposed to GIA effects from the massive Laurentide ice sheet (McCulloch and Esat, 2000). During the Holocene, SL in the western Atlantic was purely transgressive, whereas in the Indo-Pacific it was slightly higher than the present, before drop as a result of an equatorial syphoning effect in far-field sites (Mitrovica and Peltier, 1991).

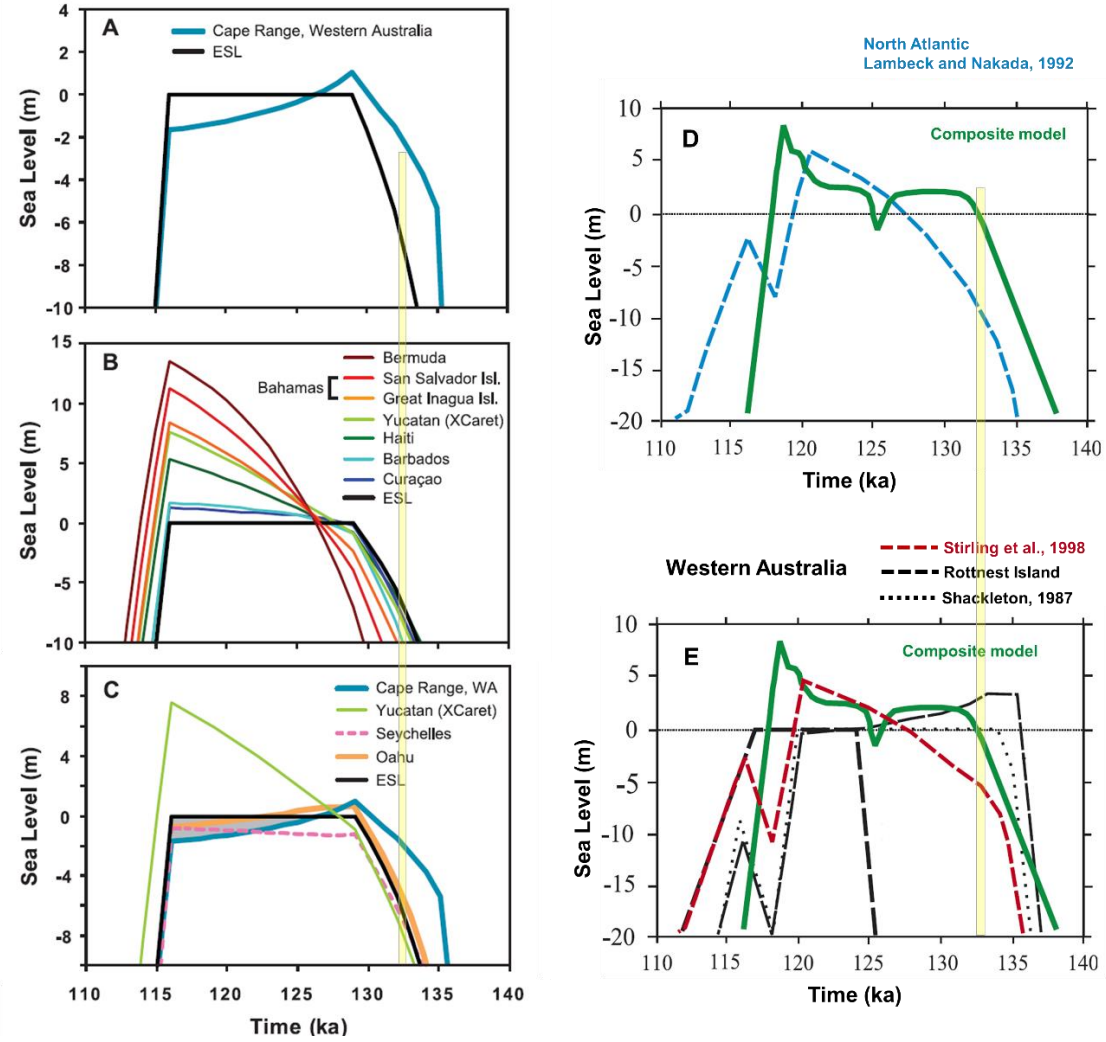

Fig. 4.17. Relative Sea Level (RSL) during the LIG for **A)** Cape Range, Western Australia, **B)** several sites across the Caribbean-Atlantic region, **C)** several disparate sites display the differences in timing and magnitude of RSL (colored lines) compared with ESL (heavy black line). ESL is set equal to zero (present sea level) for the duration of the LIG in this forward model in all cases except. Taken from Dutton and Lambeck (2012). **D)** Predicted glacio- hydro-isostatic sea-level effects during MIS 5e from far-field Western Australia (Shackleton, 1987; Stirling et al., 1995, 1998) **E)** North Atlantic (Lambeck and Nakada, 1992). Modified from from Hearty et al. (2007). Yellow bar is the reference age of Nirwana from this study.

Taking into account the relative low uplift rates of for Nirwana and in general for SE Sulawesi terraces, we consider more appropriated to use SL from stable platforms. The best indicators of the relative sea levels are the sites that present a stable continental margins such as Western Australia (McCulloch and Esat, 2000; O'Leary et al., 2013) and the Seychelles (Dutton et al., 2014). So the best options to correct SL from the fossil records are those of Western Australia (Stirling et al., 1998), the ESL calculated from a variety of sites of Dutton and Lambeck (2012) (Fig. 4.17 A-C), and the SL from composite model of Hearty et al. (2007) (Fig. 4.17 D-E).

In Sterling et al. (1998) the SL at 133ka is 5m below SL. The composite model of Hearty et al (2007) 133 are at the same SL than today. And using the best constraint of time and SL for the last interglacial (Dutton and Lambeck, 2012) found an ESL at 133 around 6m. The model evolution of SL in Nirwana is illustrated in Fig. 4.18.

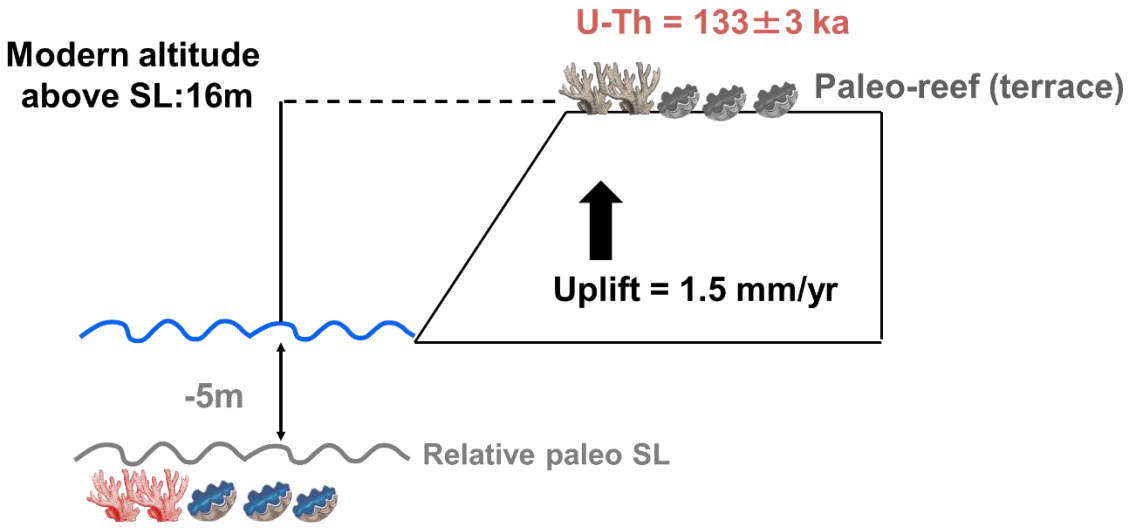

Fig. 4.18. Simplified model for SL evolution in Nirwana zone. Based on U-series dating, modern paleo-reef altitude and regional uplift. This terrace was formed in the end of Termination II and the beginning of MIS 5.

In Rahia site, (Muna Island, Fig. 4.7 and Fig. 4.10) an age of 223 ± 15 ka was found at 20 m above sea level. This age indicates MIS 7c or 7e formation for this reef, MIS 7d is not possible because it was a reversal sea level, which drops to 50 or 70 m below SL depending on the record (Fig. 4.19). Using the mean uplift rate (0.15 mm/yr) from Pedoja et al. (submitted) the paleo-SL in Rahia was 13.4 ± 3 m below modern SL. If we use the max uplift rate in the area (0.3 mm/yr) paleo-SL would has been 46.9 m, which is not possible.

Less information is available about the penultimate interglacial MIS 7, however the literature set maximum SL of MIS 7 highstands (a, c and e) at 9 m below SL. The min SL for MIS 7 was set from submerged speleothems sampled Argentarola cave (Italy) at 20 m below SL (Bard et al., 2002). Using this same record, with complementary U-series dating, Dutton et al. (2009) provide actually the best timing constrain for MIS 7.

Taking into account the uncertainty on the calculated age (± 15 ka) for Rahia, the paleo-reef must have grown between 15.3 and 11.2 m below SL, with more probability (based in reef ecological parameters: light/depth) for shallowest SL. Which is in the uncertainty for the high stands from Bard et al. (2002) and Dutton et al. (2009).

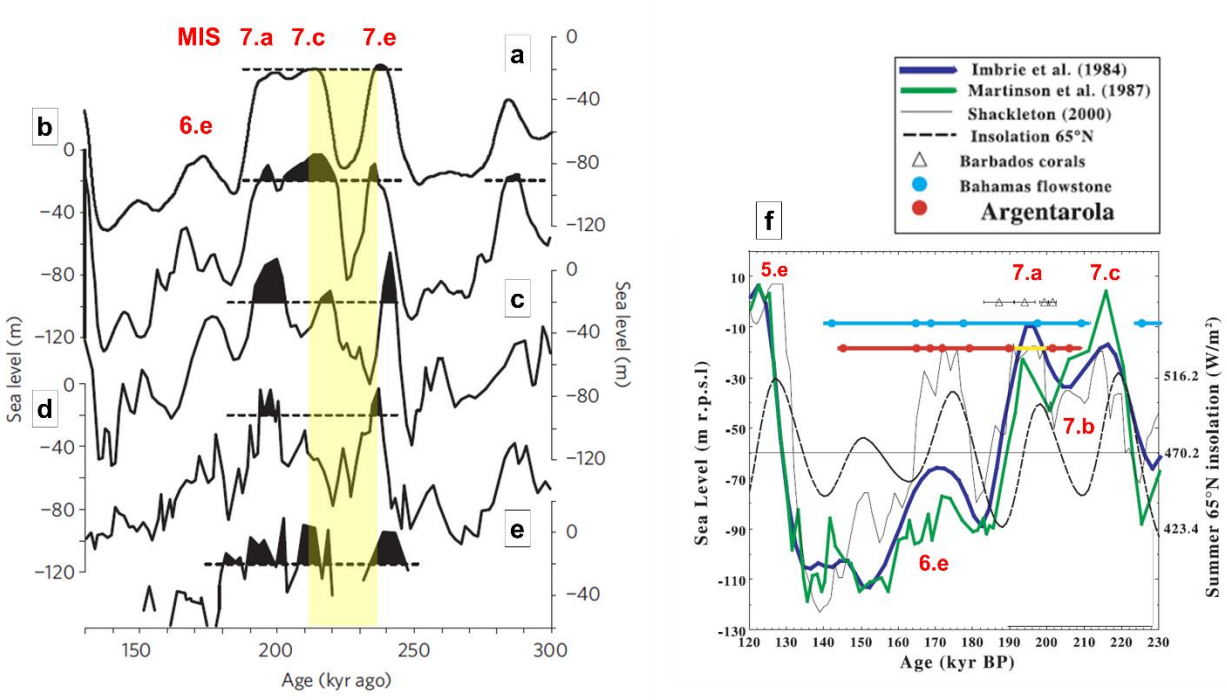

Fig. 4.19. RSL during the penultimate interglacial (MIS 7) for **A)** Model driven by benthic oxygen isotope ($\delta^{18}O$) stack (Bintanja et al., 2005) **B)** Sea-level curve based on benthic $\delta^{18}O$ data and ice-volume model (Waelbroeck et al., 2002) **C)** Reconstructions on the basis of sea water $\delta^{18}O$ calculated from paired Mg/Ca and $\delta^{18}O$ measurements on planktonic foraminifera (Lea et al., 2002) **D)** Reconstruction of Red Sea sea water $\delta^{18}O$ (Siddall et al., 2003) **E)** Reconstruction derived from open-system U–T ages of corals (Thompson and Goldstein, 2005). Shading indicates periods of time for which sea level rises above -20m (dashed lines), the approximate depth of Argentarola Cave speleothems. Modified from Dutton et al. (2009). **F)** Different Sea-level records during the penultimate glacial cycle from Bard et al., 2002. Yellow bar is the reference age of Rahia (Buton) from this study.

Applying the same assumptions, relative SL was also determined for the other areas (Lakeba, Bahari, Ular and Kadatua). In Lakeba, paleo-SL is estimated at 20 ± 7 m below SL, for this zone the age given a MIS 6e interstadial, SL in this period from Shackleton (2000) and Bard et al. (2002) present a maximum around 20 m below SL (Fig. 4.19-f). In Bahari (Buton): -5 ± 1 m, here was found an age at the end of MIS 5e, drop in SL, in Dutton and Lambeck (2012) SL at 115 ka is around -8 m, the age of the dated coral is 112.7 ± 4 ka. In Kadatua west: 14.7 ± 3m, and for Kadatua south: 7 ± 4m, in both places the ages correspond to MIS 7. Finally, in Ular west, also MIS 6e: -18.5 ± 1 m.

The case of Ular Island illustrates key features that are extended to the rest of the studied area. Heterogeneous results were found with MIS 6 reef formations in the west of the Island and Holocene ages in the east, both platforms at modern sea level. The fact that different periods or MIS are found in the same area demonstrated the effects of erosion process and/or low uplift rate to differentiate emerged morphological units or terraces (e. g. Bard et al., 1996). The age distribution and morphology in Ular suggest that it rises faster to the east than to the west and the max Holocene is perched out of the water to the east (Fig. 4.12). Maybe the max Holocene is released to the west by more aggressive waves (Fig. 4.12). Ular is a perfect example of polycyclic reef.

4.3.4. Final chronology

In Table 4.8. is synthetized the information for assigning a chronology in the Tridacnidae fossils. In total, actually 16 fossil clams are referenced. In Chapter V, seasonal reconstructions are described for 4 samples, two from Nirwana (Buton) and two from Rahia (Muna).

Using relative SL in every area, the $\delta^{18}O$ signal from fossil shells are corrected to interpreted mean temperature differences (Chapter V), but only in the fossil clams who were collected close to the dated corals (Table 4.8).

Table 4.8. Final chronology. Correspondence between U-Th/^{14}C dating and concerned or near Tridacnidae samples. Closed system ages in bleu.

ID. sample	Locality	Altitude	U-Th Age (ka)		^{14}C Age (Ka)	Period	Near/Concerned Tridacnines (ID)
			Quadrupole	Neptune			
GSL12_15	Nirwana (Buton Island)	19	135.3 ± 3.5 **			Termination II early MIS 5	GSL 12_18, GSL12_19
GSL12_17		19	140 ± 5.2 *				GSL 12_78, GSL12_79
GSL16_03		16.9	133.4 ± 3.3 **				GSL 12_80, GSL12_81
GSL16_04		15	136.5 ± 3.3	132.6 ± 1.1			GSL 12_82, GSL12_83
GSL16_62		18.5	143.3 ± 4 **	142 ± 7.3 **			
GSL12_36	Bahari (Buton Island)	23	112.7 ± 4 **			MIS 5d	GSL14_12
GSL12_68	Rahia (Muna Island)	20	223.3 ± 15.6 **			MIS 7c or e	GSL 12_60, GSL12_64
GSL12_9	Kadatua Island (West)	20	232.8 ± 23.8 *			MIS 7	GSL12_10
GSL12_11		20	230.5 ± 21.2 *				
GSL14_05	Kadatua Island (south)	26	212.7 ± 40.2 **			MIS7	GSL14_07
GSL14_06		26	229 ± 16 **				
GSL13_74	Ular Island (west)	0	193 ± 11.1 **			MIS 6e	GSL13_73
GSL14_13		0	184.7 ± 9				
GSL16_53		0	184.2 ± 5 **		49.5 ***		
GSL16_50		0	188.5 ± 5.6 **		>45.6 ***		
GSL16_59 Δ		0			49.3 ***		
GSL16_44 Δ	Ular Island (east)	0			0.745 ± 0.3	Late Holocene	GSL16_44
GSL16_48		0	7 ± 0.1 **			Mid. Holocene	
GSL13_10	Lakeba (Buton Island)	6	170.3 ± 7.1			MIS 6e	GSL13_09

* Corrected ages with Thompson Model
** Open system no corrected
*** Understimated, on the detection limit of radicarbon technique (50 Ka)
Δ = Tridacnidae/Bivalve shell

4.8. Conclusions

In this chapter is illustrated the complications of assessing reliable chronology for Tridacnidae fossil shells, for different reasons: a) the impossibility of directly dating the shells b) the complex formation and history of reef terraces in this area mediated by low uplift rates and/or erosion leading to polycyclic reef terraces c) the need of a large quantity samples in order to obtain accurate U/Th ages. However, information derived from the geomorphology of the study area has to be considered and enables to verify if the age is coherent with other records of relative sea level. Confronting all these sources of information, even the ages in open-system can be exploited because most open-system ages are close or equal to closed-system ages.

Using these sources of information, it has been possible to identify reef formations from the last interglacial periods (MIS-7 and early MIS-5), the Holocene and one interstadial (incomplete deglaciation period): MIS 6e. In general, here it is confirmed the low-uplift rates in the area, which give coherent relative SL when comparing with SL records from tectonically stable areas such Western Australia, or accurate SL constrains (e.g. Argentarola cave).

Petrography and XRD analysis are important tests to scan fossil material, but they are not concluding about the open/close system behaviour of U-series as it was found here. For future analyses, additional screening methods must be improved.

Further work in dating could also include taxonomy of coral samples and test using different parts of the skeleton in order to establish all possible relations. The sampling of isolated coral samples must be avoided. Target areas must be sampled with a large (representative) quantity of corals on the same presumed terrace and in a vertical axe (several terraces) on the same area, in order to detect complete age sequences, abrasion process and polycyclic origins, which may confuse age estimates, with samples from different interglacial in the same terrace.

Chapter V.

Climate reconstructions of past interglacials

Chapitre V. Présentation

Dans cette dernière partie, on utilise les différents proxys géochimiques testés dans le Chapitre III, et les informations concernant la datation et le niveau marin relatif (Chapitre IV), pour reconstruire des conditions climatiques au cours des deux dernières périodes interglaciaires. Deux fossiles appartenant à l'espèce *T. gigas*, échantillonnés sur la zone de Nirwana (Ile de Buton), ont étés utilisés pour reconstruire des variations climatiques pendant le début de la dernière période interglaciaire ou MIS-5. La transition (Termination II) entre la période glaciaire MIS-6 et celle de MIS-5 a été caractérisée par une remontée du niveau marin et des augmentations de CO_2 très rapides par rapport à la Termination I (après la dernière glaciation). Les forts changements de la Termination II ont donné lieu à un pic interglaciaire particulièrement accentué (MIS-5) pour lequel, différentes études ont estimé des températures moyennes plus élevés (~ 1°C) qu'aujourd'hui, et un niveau marin également très élevé, autour de 5 mètres en moyenne. Cette période peut être vue comme un cas d'évolution analogue à une situation courante de réchauffement climatique. Raison pour laquelle cette période du MIS-5 suscite un très grand intérêt scientifique.

L'avant-dernière période interglaciaire ou MIS-7 a été peu étudiée. Cependant une chute du niveau marin très importante, jusqu'aux conditions glaciaires, s'est produite juste après le début de l'interglaciaire (MIS-7e). Par la suite, dans un intervalle de temps assez court, le niveau marin est revenu aux conditions interglaciaires de la période MIS-7d. Pour cette période on a utilisé également deux bénitiers de *T. gigas* échantillonnées sur l'ile de Muna.

On montrera dans ce chapitre comment les variations de niveau marin au cours du Pléistocène ont eu une forte répercussion sur le cycle hydrologique dans cette région. Des reconstructions de la variabilité saisonnière à partir des isotopiques stables ($\delta^{18}O$ and $\delta^{13}C$) sont comparées entre les bénitiers fossiles et les bénitiers modernes. Des différences importantes entre chaque période étudiée sont expliquées à partir de l'état climatique et océanographique actuel sur la zone d'étude, les résultats de la calibration (Chapitre III) et d'autres recherches sur des régions proches de l'ile de Sulawesi. Avec les rapports isotopiques du $\delta^{18}O$, il a été aussi possible d'analyser la variation interannuelle du système océan-atmosphère, laquelle est attribuée en partie au phénomène ENSO. Le signal fossile a donc permis de constater l'existence de ce phénomène pendant les périodes interglaciaires étudiées et mettre en évidence des différences d'amplitude par rapport à la période actuelle. Les analyses des éléments traces sur les bénitiers fossiles sont aussi décrites, mais avec des résultats plus hétérogènes et une influence qui semble liée à la taxonomie.

Chapter V. Climate reconstructions of past interglacials

5.1. Introduction

The Indo-Pacific warm pool (IPWP) has had a major role in global climate change due to the important source of water vapor (greenhouse gas) to the atmosphere and the influence on the Walker circulation which contributes to transfer heat to extra-topical regions (Cane and Clement, 1999; Lea et al., 2000; Visser et al., 2003; Kawamura et al., 2006; Partin et al., 2007). In this thermodynamic motor there are three main parameters which contribute to the exchange of energy and modulate local and global climatic conditions: 1) high SST (> 28°C) of the IPWP 2) The conveyor belt connection between the Pacific and Indian Ocean: the Indonesian Throughflow (ITF) and 3) the bi-annual latitudinal shifts of the Inter-Tropical Convergence Zone (ITCZ). Over past glacial-interglacial variations these parameters have changed (Fig. 5.1) with profound impact on the dynamics of climate system, oceanographic circulation and finally, ecosystem shifts.

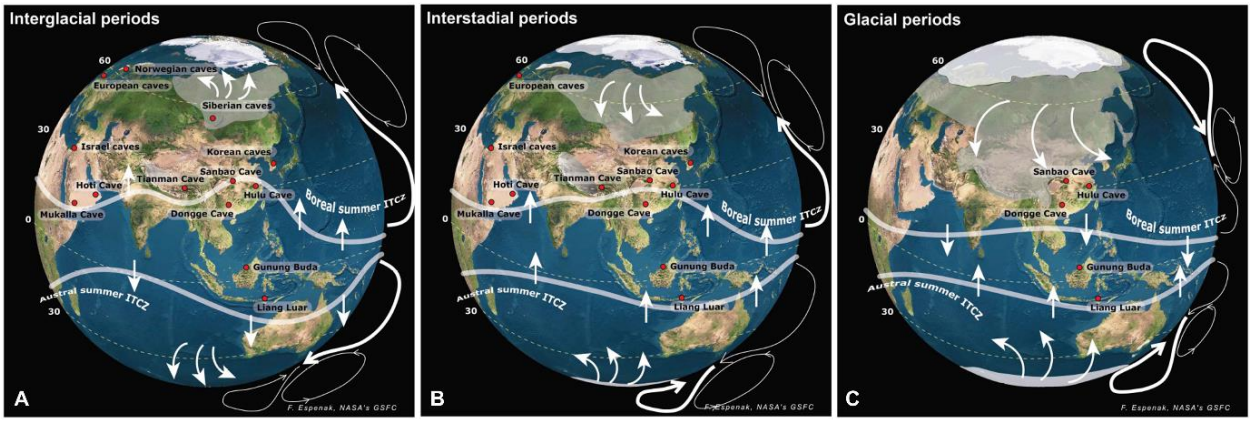

Fig. 5.1. Scenario of palaeoclimate changes linked with the interhemispheric hydrologic seesaw **A)** Peak interglacial periods are characterized by large geographic variations in the seasonal ITCZ and strong atmospheric meridional overturning circulations **B)** Interstadial periods show intermediate climatic conditions between those of peak interglacial and full glacial periods **C)** Full glacial periods are characterized by small geographic variations in the seasonal ITCZ and weak atmospheric meridional overturning circulations. Modified from Jo et al. (2014).

In paleo-reconstructions, high resolution records are of special interest because they allow the assessment of seasonal to interannual sea-surface temperature (SST) variability, like ENSO or monsoon-related changes in SST (e. g. Tudhope et al., 2001; Driscoll et al., 2014; Warter et al.,

2015). Such results are used in climate models to better constrain hypothetic scenarios for the future climate change (e.g. Emile Geay et al., 2015; Kopp et al., 2016).

In this chapter, reconstructions from the two past interglacial periods are derived from shells of fossil giant clams collected in the heart of the WPWP. Two *T. gigas* fossil samples from Nirwana are used for proxy reconstructions of the period corresponding to transition between Termination II and early MIS 5. For the previous interglacial, MIS 7, two *T. gigas* fossil are used, these samples come from Rahia (Muna Island). The results are compared between them, to other available high resolution records from the same periods, and finally to the modern conditions in the study area.

5.1.1. Mean climate state during T-II/MIS-5 Interglacial

The marine transgression (T-II) and posterior events during MIS-5 (Fig. 4.16 in Chapter IV) were accompanied by considerable ice volume changes, oceanographic reorganization and global circulation shifts, and then, provide a point of comparison or scenario for a greenhouse world (Hearty et al., 2007). Making this interval appropriate for testing models of the response of sea level to climate forcing (Dutton et al., 2015). In the last 800 ka, Termination II present the largest glacial–interglacial temperature increase in records from Antarctica (Broecker and Henderson, 1998; Masson-Delmotte et al., 2010). The maximum δD (deuterium) in Antartica Dome C (ice core) is reached ~129 ka BP, at the end of Termination II and the onset of last interglacial (LIG) (Masson-Delmotte et al., 2010).

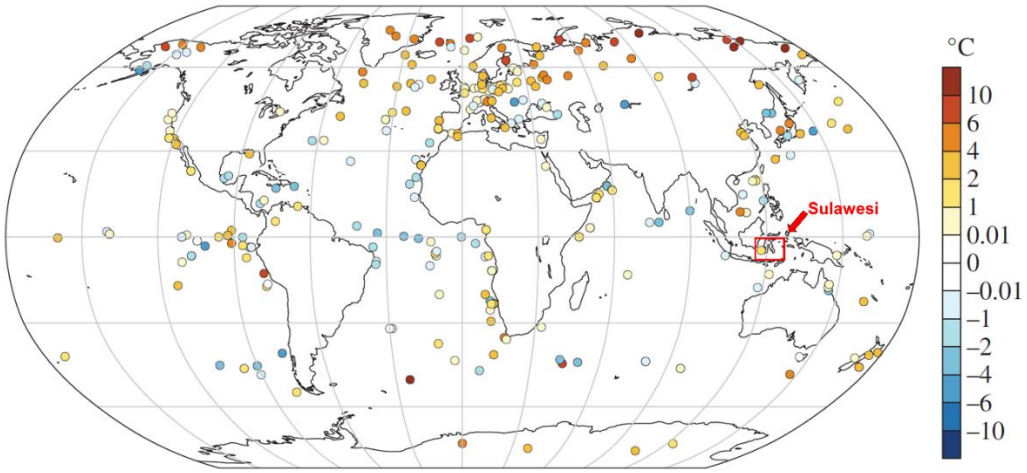

Fig. 5.2. Available temperature records for MIS-5 in the world. The nearest record to our study area is that of Visser et al. (2003) from the Makassar straight. Modified from Otto-Bliesner et al. (2017).

In Fig. 5.2 are plotted all records around the world, from which MIS 5e or LIG temperature is reconstructed. The global mean SST was around 1°C warmer during the LIG compared to modern present interglacial (Otto-Bliesner et al., 2006; Rohling et al., 2007; McCulloch and Mortimer, 2008). Paleontological studies (fossil assemblages) also argued for a LIG warmer than today, based on the occurrence of fossils of extant thermophilous plant and animal species in MIS 5, which are intolerant to the current climate (Kendrick et al., 1991; Muhs et al., 2002; Candi et al., 2016). The sea level during MIS-5e highstand has been estimated from different records around the world, average value is ~5 m above modern SL (e. g. Lambeck and Nakada, 1992; Blanchon et al., 2009; Dutton and Lambeck, 2012).

During the T-II and MIS-5 the West Antarctica ice sheet (WAIS) and Greenland ice sheet (GIS) experienced significant mass loss (Blanchon et al., 2009; Kopp et al., 2010; Dutton and Lambeck, 2012; Raymo and Mitrovica, 2012; O'Leary et al., 2013; Hay et al., 2014). Different records show that warming in Antarctic and tropical Pacific starts before the melting of Northern Hemisphere ice sheets and cannot be explained directly by the common North Atlantic Hemisphere Insolation (Broecker and Henderson, 1998; Gallup et al., 2002; Visser et al., 2003; Drysdale et al., 2009; Thomas et al., 2009; Masson-Delmotte et al., 2010). Drysdale et al. (2009) provide evidence that T-I and T-II started at near-identical obliquity phases.

Compared to T-I (Last glacial maximum-Holocene transition), T-II is marked by a constant pulse of melt water and faster global SL rising (Broecker and Henderson, 1998; Stirling et al., 1998; Esat et al., 1999; Gallup et al., 2002). The research about these last transgression periods conclude that the reason is a stronger insolation and CO_2 forcing earlier in T-II, resulting in different ice-volume and atmospheric changes (moisture increase) compared to T-I (Broecker and Henderson, 1998; Visser et al., 2003; Siddal et al., 2006). Marino et al. (2015) show that Heinrich Stadial 11 (massive iceberg discharge in the North Atlantic) cold episode occurred between 135±1 and 130±2 ka and is linked with rapid SL rise during T-II. This occurrence is also supported by Masson-Delmotte et al. (2010), reflecting a bipolar seesaw linked with changes in the Atlantic meridional overturning circulation (EPICA Community Members, 2006).

5.1.2. MIS-7

The penultimate interglacial MIS-7 (see Fig. 4.19 in Chapter IV) has not been a major topic of scientific interest compared to MIS-5 and consequently fewer records (including high-resolution) are available for this period. The best chronology of sea level highstands during this interglacial comes from the Argentarola Cave (Bard et al., 2002; Dutton et al., 2009) and provides precise and accurate ages that are critical benchmarks: from ~190-245 ka to 235 ka BP, and highstands with a maximum of 9 m below modern SL and minimum at -20 m. Hearty and Kindler (1995) consider that sea level was within -5m (maximum) of present SL in one or more stages of MIS-7. In other records (Imbrie et al., 1984; Martinson et al., 1987; Shackleton et al., 2000; Siddall et al., 2003), MIS-7 is globally recognized as a period of lower SL relative to current interglacial.

MIS-7 was also characterized by a period of unstable sea level, since an important reversal in sea level is observed after the beginning of this interglacial corresponding to MIS-7e (see Fig. 4.19, Chapter IV). The preceding sea level lowstand (MIS-7d) has been associated with cold temperatures and ice volumes that approach the full glacial conditions of MIS-8 (e.g., Roucoux et al., 2006; Jouzel et al., 2007; Martrat et al., 2007). This lowstand had a short duration (~10 ka) before reaching again the MIS-7c highstand (Fig. 4.19). These two warmer intervals (7e and 7c) separated by a cooling (7d) are also observed in palynological records from Europe (Desprat et al., 2006; Roucoux et al., 2008) and Nord-Pacific region (Razjigaeva et al., 2015), with coniferous species gaining in importance during cooling and retreating during the warm intervals/higstands.

The succession of diatom assemblages in Tanfiliev Island (Nord-Pacific, Russia) gives an indication of changes in the sedimentation environments and water column depth, which corresponded to two transgressive phases (Razjigaeva et al., 2015). Desprat et al. (2006) found that MIS-7 is characterized by a similar climatic variability in two sediment core records from north-western Iberia and in northern North Atlantic. These authors argued that the good correlation between these two sediment cores also showed that most of the cold periods during MIS 7 are associated with icebergs discharges in the North Atlantic Ocean.

5.2. Methodology

5.2.1 Study areas (description)

Nirwana is situated in the SW of the Buton Island (Fig. 5.3-A). Here, it is possible to observe multiple terrace sequences (Fig. 5.3-B). The number of terraces increases from Lakeba to the southernmost point (Fig. 5.3-B, up black arrows) and from the south of Nirwana to the point of the silo (Fig. 5.3-B, bottom black arrows). These two areas, are in the prolongation of two anticlines, which meet on the coast. Added to the lateral dip of the terraces, vertical velocity increases according to the same trend as the number of terraces. These terraces are below the red terrace (in red on the map). In a few kilometers, on the scale of the overall morphology, at the bottom of the sequence, one passes from a wide flat terrace, which falls directly into the sea, to a series of little-terraces more or less well marked (sampling area). The sampling zone is located on the yellow sequence (Fig. 5.3B), in a private terrain under construction (see Fig. 4.8, Chapter IV). Due to the presence of faults between Lakeba and Niwana (Fig. 5.3B), it is not possible to laterally follow the yellow sequence (in Fig. 5.3-B) of Lakeba to reach Nirwana.

Muna Island is a monotonous limestone plateau (Fig. 5.3-A) gently sloping up toward the southeast, where the highest elevations are around 400 m (Satyana and Purwaningsih, 2011). Steep, narrow ridges along much of the east coast may mark the site of a former barrier reef complex (Ali et al., 1996; Satyana and Purwaningsih, 2011). The limestones generally are considered to be of Quaternary and have been correlated with the Wapulaka Formation of Buton (Ali et al., 1996). The sampling area is placed in the north face of the Rahia village (Fig. 4.10, Chapter IV).

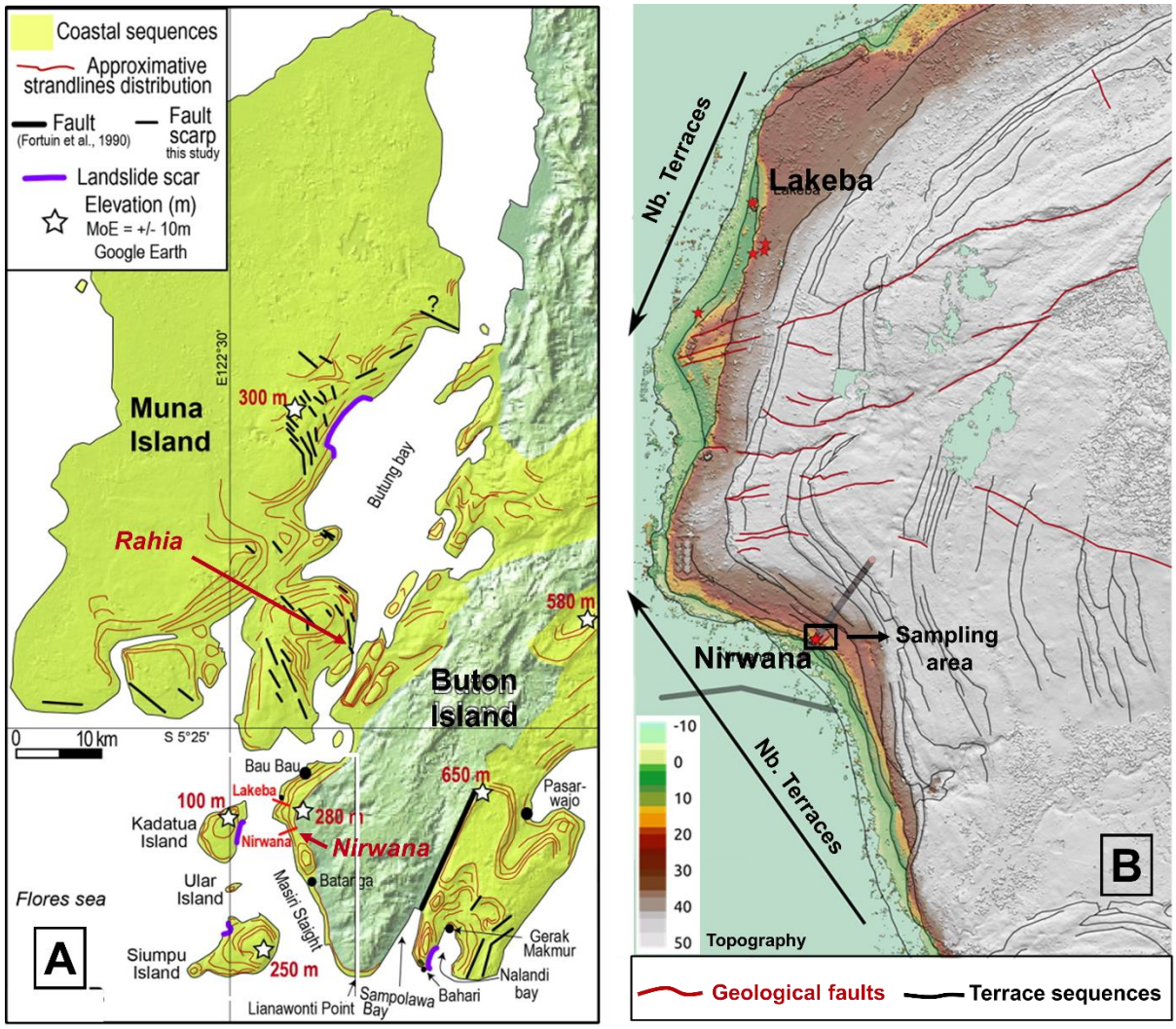

Fig. 5.3. Studied zones. Sequences of marine and coral reef terraces, active faults and landslides on Muna and south central Buton **A)** General distribution. **B)** Sequence of coral reef terrace on SW Buton. Modified from Pedoja et al. (submitted) and Pastier et al. (in prep).

5.2.2. Sample description

This chapter is focused on geochemical reconstructions derived from 26 fossil giant clam shells (see Table 5.1). Bulk $\delta^{18}O$ and seasonally resolved profiles of trace elements have been measured on all samples and seasonally resolved $\delta^{18}O$ profiles have been measured on 4 fossil *T. gigas* samples (Figures 5.4 to 5.7). *T. gigas* is the largest species of Tridacnidae family, it may grows to more than 1 m and weigh up to 300 kg (Lukas, 1988), and is the best preserved Tridacnine fossil in the field. *T. gigas* is found in many habitats, whether lagoons, fringing reefs, and even

exposed in the interstadial zone (Munro, 1989; Lucas, 1989), however they are more common subtidal species (5 to 15 m depth) on offshore reefs (Klump and Griffiths, 1994).

T. gigas is an obligate phototroph with survival rate decreasing when light is deficient (Copland and Lucas, 1988), as long as there is lots of sunlight, the clams require no additional food (Hawkins and Klumpp, 1995).

Seasonally resolved isotopic and trace elements profiles were derived from two fossil *T. gigas* samples from Nirwana, GSL12_80 and GSL12_81 (Fig. 5.4 and Fig. 5.5), and two fossil *T. gigas* from Rahia, GSL12_64 and GSL12_60 (Fig. 5.6 and Fig. 5.7).

Carbonate isotopic micro-sampling was performed only in one portion (adulthood) of the shells. No entire inner layer area was sampled in reason of time and coust of the analyses. Further analysis must be provided the complete resolved record for the life period of every sample.

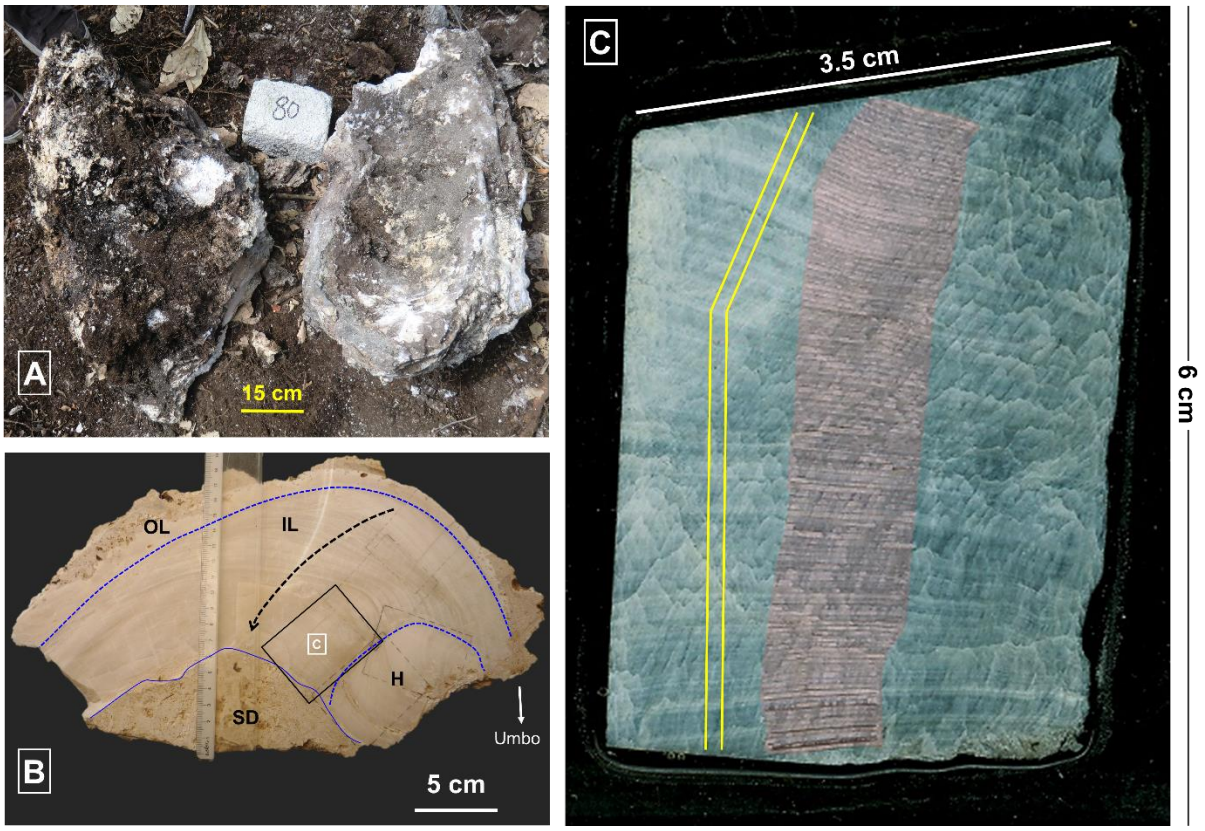

Fig. 5.4. GSL12_80 sample (*T. gigas*), Nirwana **A)** Field picture of fossil sample **B)** Sectioned valve, pallial line in blue **C)** Thick section with Micro-drill marks highlighted with a red shadow, yellow lines indicates the laser ablation tracks. OL= outer layer, IL= Inner layer, H= Hinge, SD= Sediment deposition. Black dash arrows indicated the growth direction from young depositions to old (more recent) deposition.

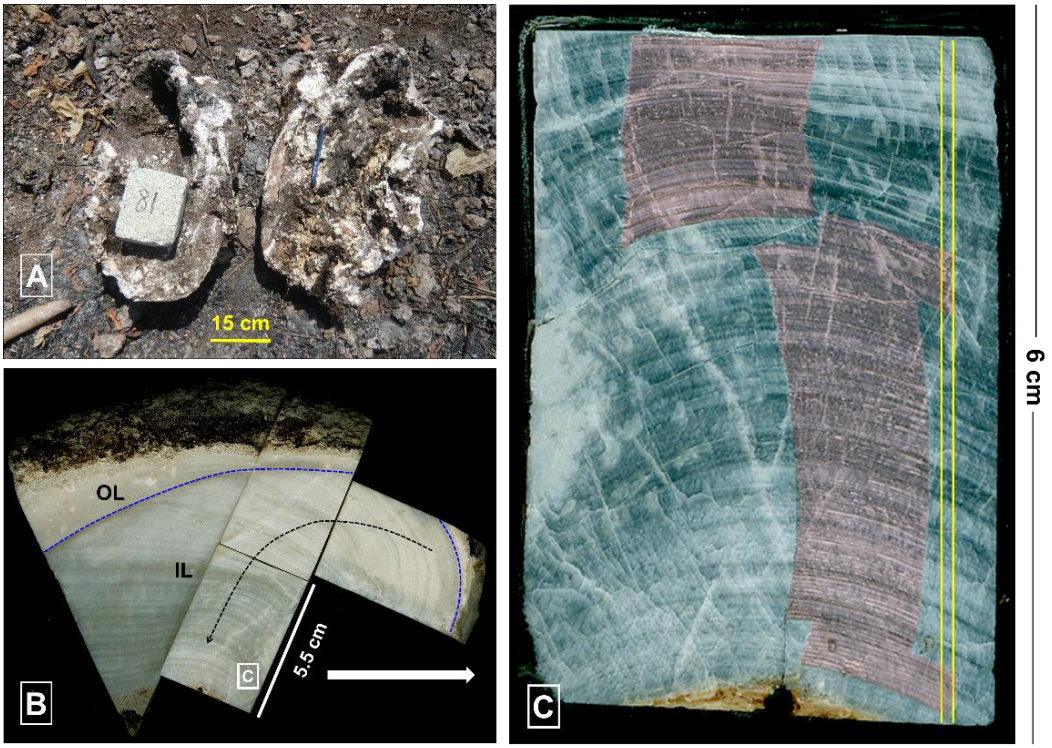

Fig. 5.5. GSL12_81 sample (*T. gigas*) **A)** Field picture of fossil sample **B)** Sectioned valve, pallial line in blue **C)** Thick section with Micro-drill marks highlighted with a red shadow, yellow lines indicates the laser ablation tracks.

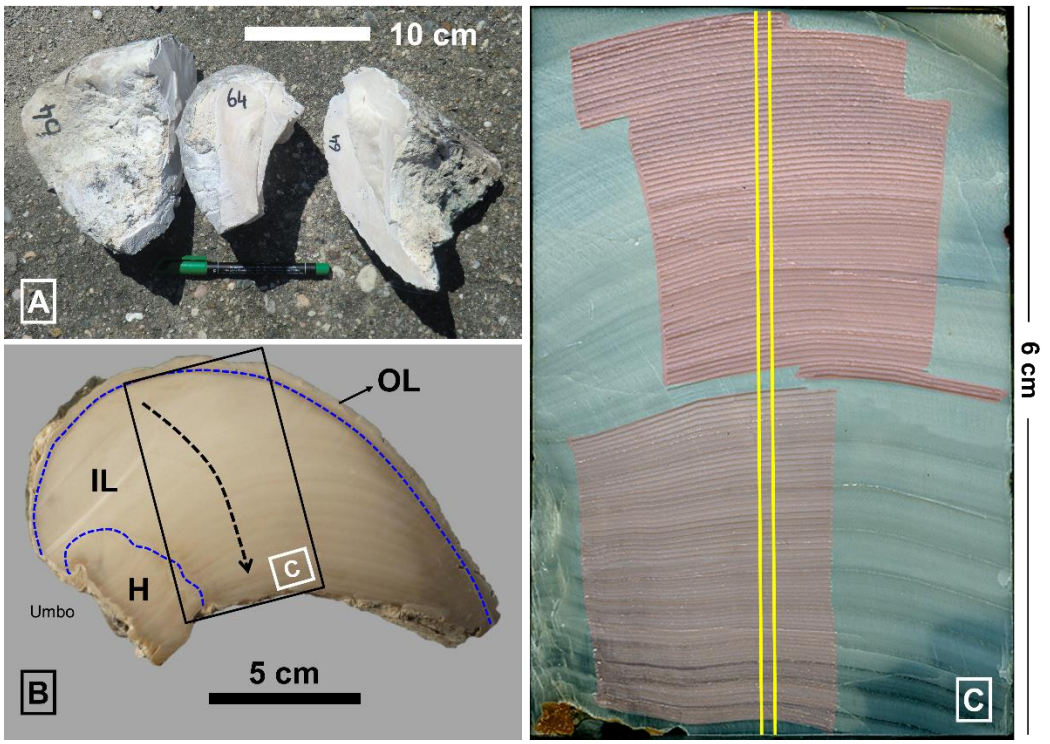

Fig. 5.6. GSL12_64 sample (*T. gigas*), Rahia (Muna) **A)** Field picture of fossil sample **B)** Sectioned valve, pallial line in blue **C)** Thick section with Micro-drill marks highlighted with a red shadow, yellow lines indicates the laser ablation tracks.

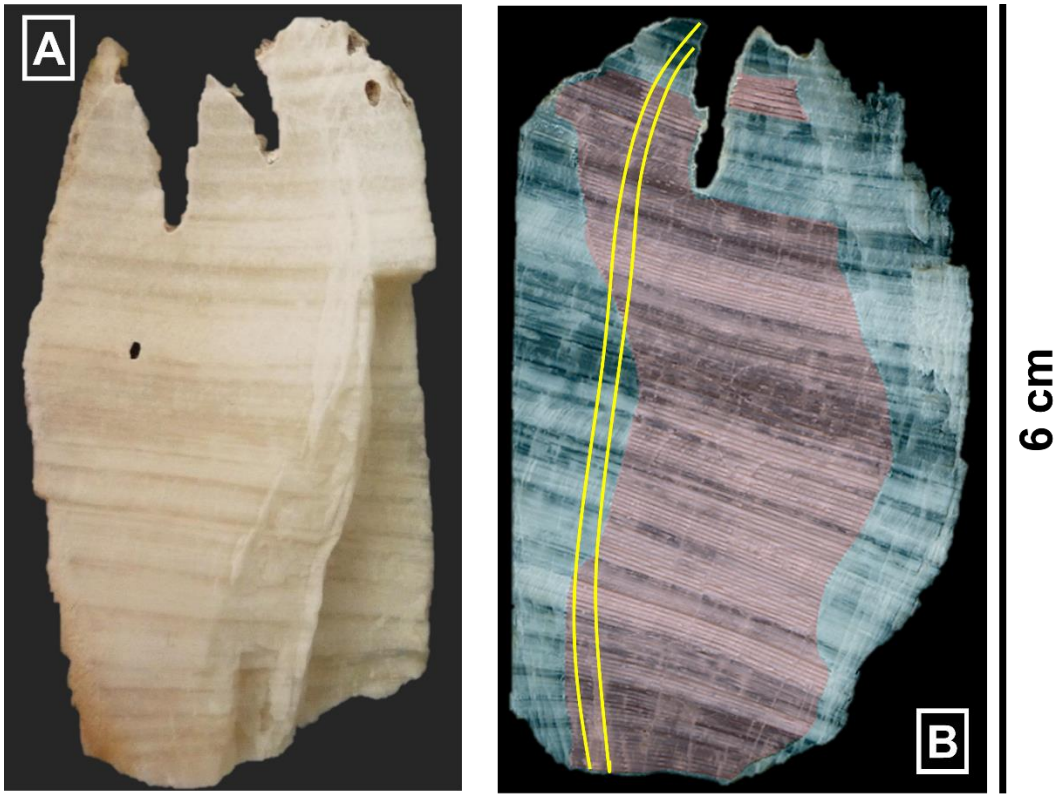

Fig. 5.7. GSL12_60 sample (*T. gigas*), Rahia (Muna) **A)** Core fragment of the inner layer shell **B)** Thick section with Micro-drill marks highlighted with a red shadow, yellow lines indicates the laser ablation tracks.

5.2.3. Geochemical analyses

Fossil shells were first scanned for diagenesis trough XRD analyses. Refers to Chapter II for technical details. No scanning electron microscopy (SEM) or cathodoluninescence (CL) imaging were improved in this study inreason of time. The chronology for these samples was established using U-series dating on coral fossil sampled around fossil clams (see U-series dating in Chapter IV).

For the whole fossil collection stable isotope analyses ($\delta^{18}O$ and $\delta^{13}C$) were obtained from bulk material (inner layer powders). Only for the four samples described above, powder micro-sampling using Microdrill system was performed for isotopic reconstructions (see Chapter II for detail). The sea level component of the $\delta^{18}O$ was subtracted based on the age and SL estimates for that period (see Chapter IV). For samples with unknown ages it was not possible to subtract sea level component.

LA-ICP-MS was performed on the entire fossil collection for trace element analyses, but in this chapter the same samples chosen for isotopic reconstructions will be primarily discussed. The trace element results of whole collection are provided in Appendix 3. See Chapter II for description of LA-ICP-MS analyses. Two parallel laser ablations were always performed to verify reproducibility. The position of laser ablation tracks and $\delta^{18}O$ micro-sampling can be observed for every sample: GSL12_80 (Fig. 5.4), GSL12_81 (Fig. 5.5), GSL12_60 (Fig. 5.6) and GSL12_64 (Fig. 5.7). Both laser ablations and micro-powder sampling were performed on the thick sections from the inner layer area of the shells (Fig. 5.4 to Fig. 5.7).

5.3. Results

5.3.1. XRD and bulk/mean isotopic signature ($\delta^{18}O$ and $\delta^{13}C$)

Bulk $\delta^{18}O$ and XRD scanning analyses were performed on every Tridacnidae sample (Table 5.1). XRD analyses reveals more than 98% of aragonite composition for the most part of the shells and considered unaltered, i.e. the geochemical profiles are preserved and not affected by diagenesis (Table 5.1). Only 4 samples present less than 98% of aragonite, the minimal aragonite composition was 89% for GSL12_78 (Table 5.1). Calcite recrystallization represents a loss of information and reveals structural differences in density for Tridacnidae shells. Aragonite appears to be composed of small precipitates organized in a fibrous structure while calcite is a compact grain (Fig. 2.9, Chapter II). The former is much more porous than the second, hence the difference in density.
In general Tridacnidae fossil shells are well preserved as demonstrated in other studies (e.g. Ayiling et al., 2015; Wartr et al., 2015).
The selected samples for proxy reconstructions (GSL12_80, GSL12_81, GSL12_60 and GSL12_64), presents more than 98% in aragonite content (Table 5.1).

Bulk isotope measures represents a mean value for the inner layer in every Tridacnidae sample. Bulk $\delta^{18}O$ values range from -0.2‰ to -1.6‰ values are systematically more positive when compared to modern (Figure 5.8-A). Similarly, $\delta^{13}C$ values range from 1.8 ‰ to 3.2 ‰ are systematically higher than modern values (Figure 5.8-B). In most cases, more negative $\delta^{18}O$ values are associated with lower $\delta^{13}C$ values (Table 5.1). In the discussion section, the dated samples are

corrected for sea level component $\delta^{18}O$ in order to compare with the modern record from the studied area.

Bulk $\delta^{18}O$ results are compared to expected ranges for an interglacial and a glacial period (Fig. 5.8-A). These ranges were calculated from the modern samples, and for a glacial period it was used the relationship between sea level change and mean oceanic $\delta^{18}O$ enrichment of 0.010 ± 0.001 ‰ m^{-1} from Adkins et al. (2002). This comparison helps to constrain the period (warm or cold) at which shells grew.

Table 5.1. Bulk isotopic results ($\delta^{18}O$ and $\delta^{13}C$) of Tridacnidae shell collection. Bulk material from the inner layer growth zone.

ID. Sample	Classification	Location	Aragonite (%)	$\delta^{13}C$ Bulk (‰)	$\delta^{18}O$ Bulk (‰)
GSL12_10	*Tridacna sp.*	Kadatua Island	99,4	3,110	-0,19
GSL12_18	*T. gigas*	Nirwana (Buton Island)	99,7	1,956	-1,19
GSL12_19	*T. gigas*	Nirwana (Buton Island)	95,8	2,539	-1,12
GSL12_56	*Tridacna sp.*	Muna Island	99,4	2,267	-1,39
GSL12_60	*T. gigas*	Muna Island	99,1	2,904	-0,89
GSL12_64	*Tridacna sp.*	Muna Island	99,4	2,465	-0,87
GSL12_78	*T. gigas*	Nirwana (Buton Island)	88,9	2,148	-1,57
GSL12_79	*T. gigas*	Nirwana (Buton Island)	99,4	2,527	-1,13
GSL12_80	*T. gigas*	Nirwana (Buton Island)	98,2	2,118	-1,14
GSL12_81	*T. gigas*	Nirwana (Buton Island)	99,8	1,779	-1,19
GSL12_82	*T. gigas*	Nirwana (Buton Island)	98,4	2,381	-1,04
GSL12_83	*T. gigas*	Nirwana (Buton Island)	98,3	2,149	-1,39
GSL13_01	*Tridacna sp.*	Buton Island	98,08	2,58	-0,20
GSL13_09	*T. gigas*	Lakeba (Buton Island)	98,66	2,35	-0,31
GSL13_56	*T. gigas*	Wangi-wangi	97,54	2,55	-1,18
GSL13_57	*T. gigas*	Lakeba (Buton Island)	97,61	1,95	-1,34
GSL13_73	*T. gigas*	Ular Island	98,7	2,67	-0,21
GSL13_75	*T. gigas*	Buton Island	99,18	2,87	-0,17
GSL14_07	*Tridacna sp.*	Kadatua South	98,81	2,41	-0,27
GSL14_12	*T. gigas*	Bahari (Buton Island)	99	2,62	-1,28
GSL14_15	*Tridacna sp.*	Kadatua South	98,66	1,93	-1,13
GSL14_19	*T. squamosa*	Kabaena Island	99,14	1,26	-1,70
GSL14_20	*Hippopus hippopus*	Kadatua South	98,64	1,34	-1,87
GSL14_21	*Tridacna sp.*	Ular Island	98,31	2,49	-1,26
GSL14_22	*Tridacna maxima*	Ular Island	98,25	2,50	-1,54
GSL14_23	*Hippopus hippopus*	Kadatua South	98,36	1,46	-1,84

In red, thes most altered sample material.

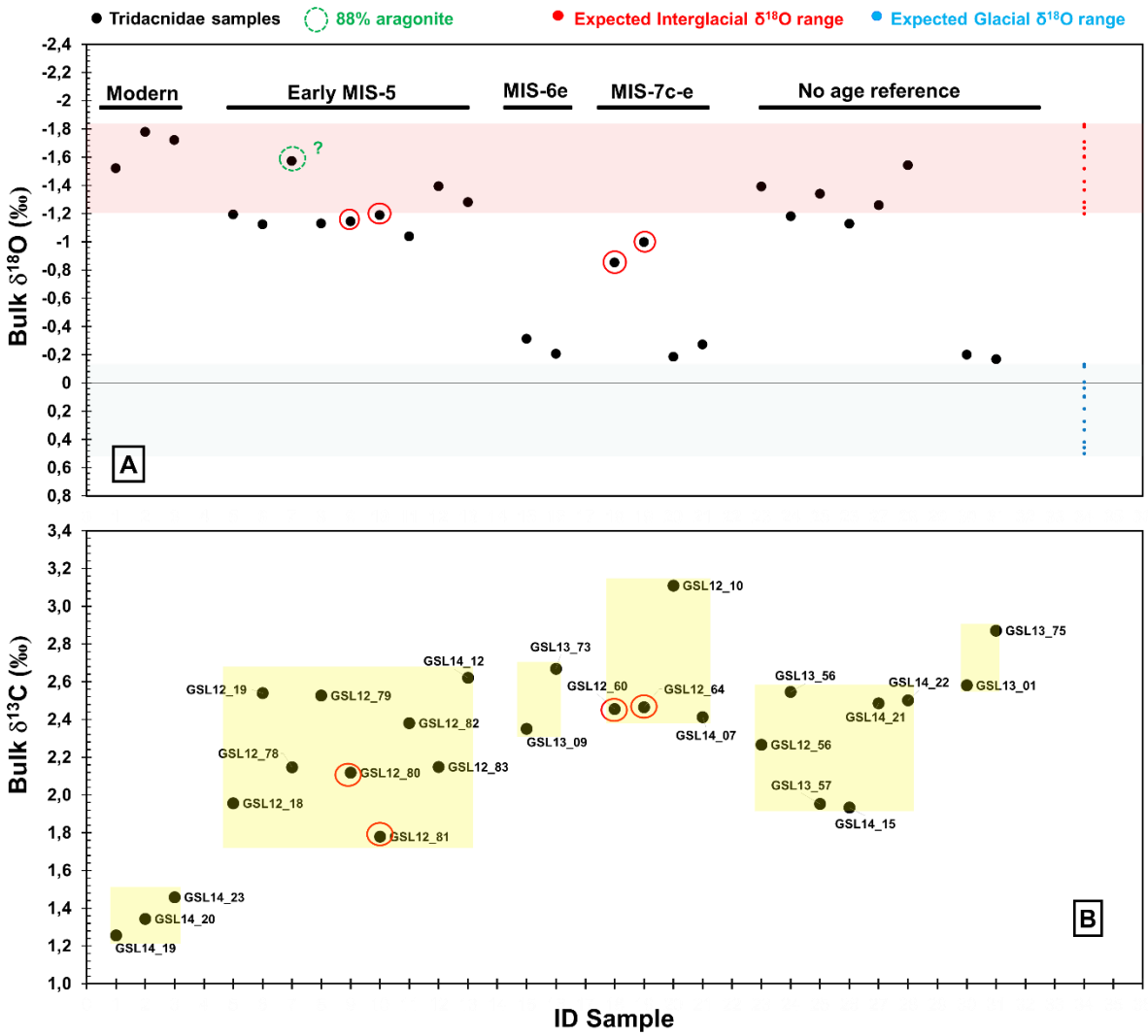

Fig. 5.8. Bulk isotopic results for the entire Tridacnidae shell collection **A)** Bulk $\delta^{18}O$ values **B)** Bulk $\delta^{13}C$ values. Samples are arranged in the same order for both figures A and B. Samples used for high resolution reconstructions in this chapter are bounded in red: GSL12_80, GSL12_81, GSL12_60 and GSL12_64.

5.3.2. Seasonal profiles of stable isotopes ($\delta^{18}O$ and $\delta^{13}C$)

The $\delta^{18}O$ values of GSL12_81 (Fig. 5.9-A) range from -1.63 to -0.75 ‰ with a mean of -1.16 ‰ (n = 181 micro-samplings), $\delta^{13}C$ values range from 1.72 to 2.20 ‰ with a mean value of 1.95 ‰. In $\delta^{18}O$ profile is possib1e to identify around 14 seasonal cycles, which confirm last 14 years of life of this clam (growth rate model, Appendix 5). $\delta^{13}C$ profile (Fig. 5.9-B) present less uniform variation that $\delta^{18}O$ profile, however in most part of the record, high values of $\delta^{13}C$ are associated with more positive values of $\delta^{18}O$, or during cold/dry season, and lowest values of $\delta^{13}C$ occurs during the more negative ratios of $\delta^{18}O$.

Stable isotopes profiles derived from sample GSL12_80 comes from the last 37 mm of the inner layer, or the last 13 year of life of the clam (growth rate model, Appendix 5). The $\delta^{18}O$ values of GSL12_80 (Fig. 5.9-C) range from -2.04 to -0.55 ‰ with a mean value of -1.15 ‰ (n = 79). The $\delta^{18}O$ profile shows around 13 seasonal cycles, which correspond to the last 13 years of life. $\delta^{13}C$ values (Fig. 5.9-C) range from 1.65 to 2.38 ‰ with a mean of 2.15 ‰ (Fig. 5.9-D). The variation in $\delta^{13}C$ is similar to that of GSL12_81, in most part of the record with low values during warm/wet seasons and high values during dry/cold season.

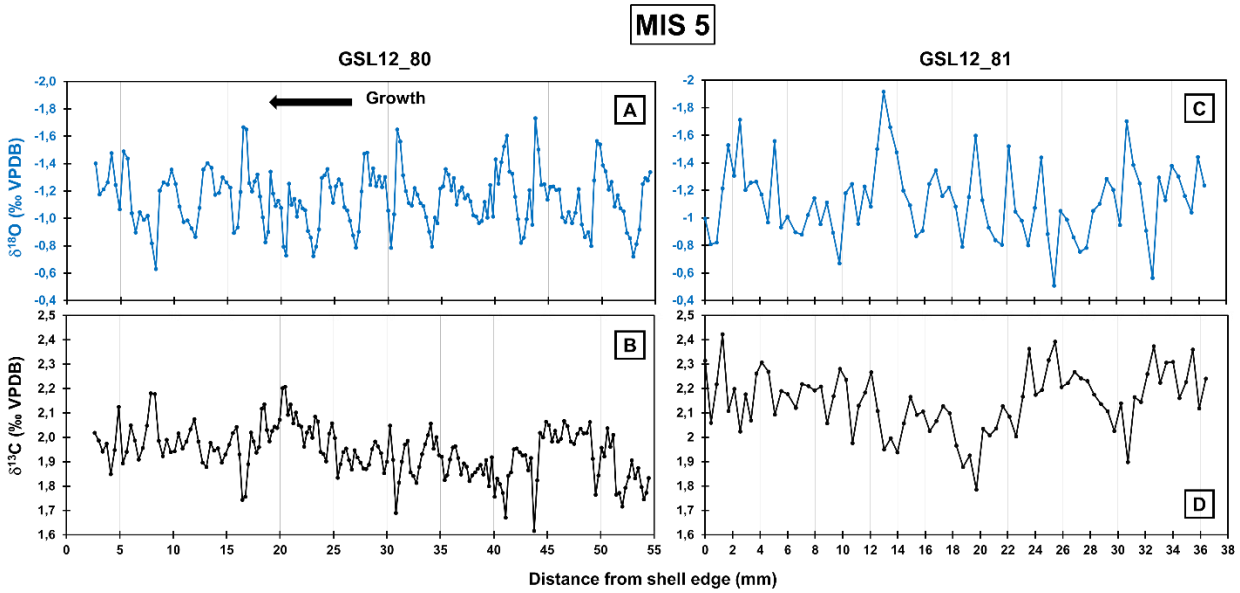

Fig. 5.9. Stable isotope reconstructions from Nirwana samples **A)** GSL12_81 (*T. gigas* fossil) $\delta^{18}O$ record **B)** GSL12_81 (*T. gigas* fossil) $\delta^{13}C$ record **C)** GSL12_80 (*T. gigas* fossil) $\delta^{18}O$ record **D)** GSL12_81 (*T. gigas* fossil) $\delta^{18}O$ record.

The $\delta^{18}O$ values of GSL12_60 (Fig. 5.10-A) ranges from -1.24 to -0.52 ‰ with a mean value of -1.24 ‰ (n = 150 micro-samplings). The $\delta^{18}O$ profile shows around 13 seasonal cycles, which correspond to ~13 years of life (Appendix 5). $\delta^{13}C$ values (Fig. 5.10-B) range from 1.85 to 2.62 ‰ with a mean of 2.24 ‰. In most part of the record low $\delta^{13}C$ values occurs during warm/wet seasons and high values during dry/cold season.

The $\delta^{18}O$ values derived from GSL12_64 (Fig. 5.10-C) range from -1.28 to -0.77 ‰ with a mean value of -1.0 ‰ (n = 159). Growth model indicate (Appendix 5) ~ 13 years of life,

nevertheless these $\delta^{18}O$ cycles are not well defined in the profile. The amplitude of the seasonal variation is reduced relative to GSL12_60 $\delta^{18}O$ profile. $\delta^{13}C$ values (Fig. 5.10-D) range from 1.89 to 2.86 ‰ with a mean of 2.24 ‰. In most part of the record low $\delta^{13}C$ values occurs also during warm/wet seasons and high values during dry/cold season, but also with reduced variation relative to GSL12_60.

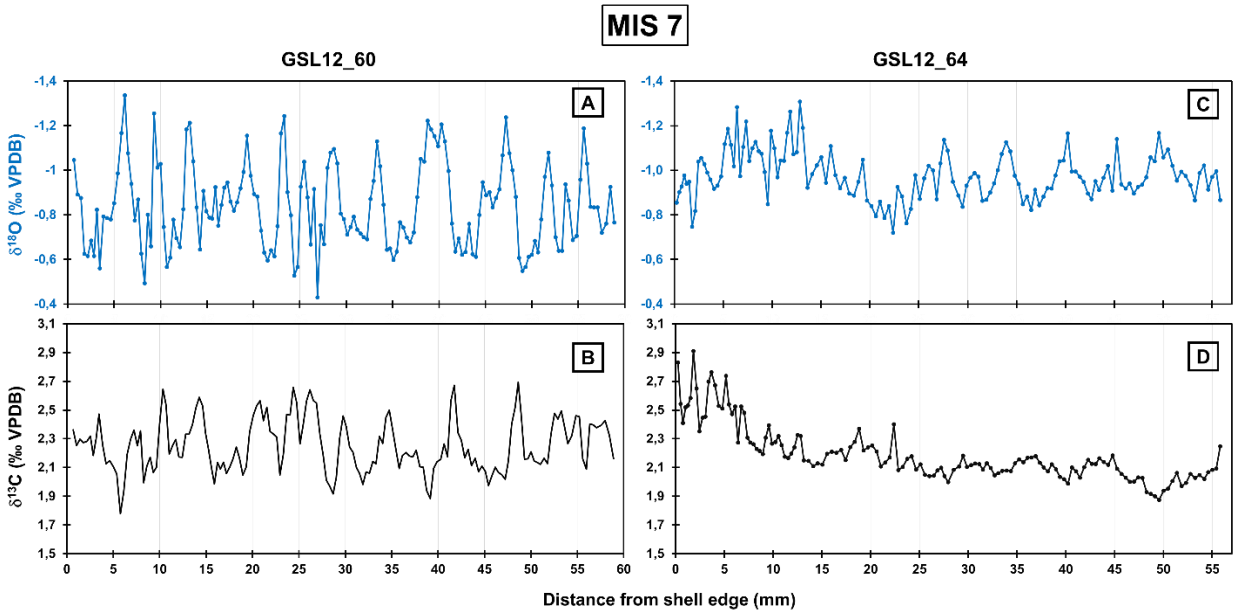

Fig. 5.10. Stable isotope reconstructions from Rahia (Muna) samples **A)** GSL12_60 (*T. gigas* fossil) $\delta^{18}O$ record **B)** GSL12_60 (*T. gigas* fossil) $\delta^{13}C$ record **C)** GSL12_64 (*T. gigas* fossil) $\delta^{18}O$ record **D)** GSL12_64 (*T. gigas* fossil) $\delta^{18}O$ record.

5.3.3. Trace elements reconstructions (Mg/Ca, Ba/Ca and Sr/Ca)

The following results (data and profiles) correspond to the laser ablations on the same thick sections used for stable isotopes micro-sampling for GSl12_80, GSL12_81, GSl12_60 and GSl12_64. The results from the entire lifespan of these samples, as the results for the entire fossil collection are presented in Appendix 4.

In GSL12_80 (n = 2 laser ablation tracks), Mg/Ca ranges from 0.71 to 2.96 mmol/mol with a mean value of 1.1 ± 0.1 mmol/mol (Fig. 5.11-A). Ba/Ca ranges from 1.62 to 6.70 µmol/mol with

a mean value of 3.1 ± 0.4 µmol/mol (Fig. 5.11-B). Sr/Ca ranges from 1.08 to 1.60 mmol/mol with a mean value of 1.3 ± 0.1 mmol/mol (Fig. 5.11-C).

In GSL12_81 (n = 2 laser ablations), Mg/Ca ranges from 0.97 to 2.86 mmol/mol with a mean value of 1.74 ± 0.1 mmol/mol (Fig. 5.11-D). Ba/Ca ranges from 3.12 to 12.7 µmol/mol with a mean value of 5.6 ± 0.9 µmol/mol (Fig. 5.11-E). Sr/Ca ranges from 1.27 to 1.64 mmol/mol with a mean value of 1.43 ± 0.1 mmol/mol (Fig. 5.11-F).

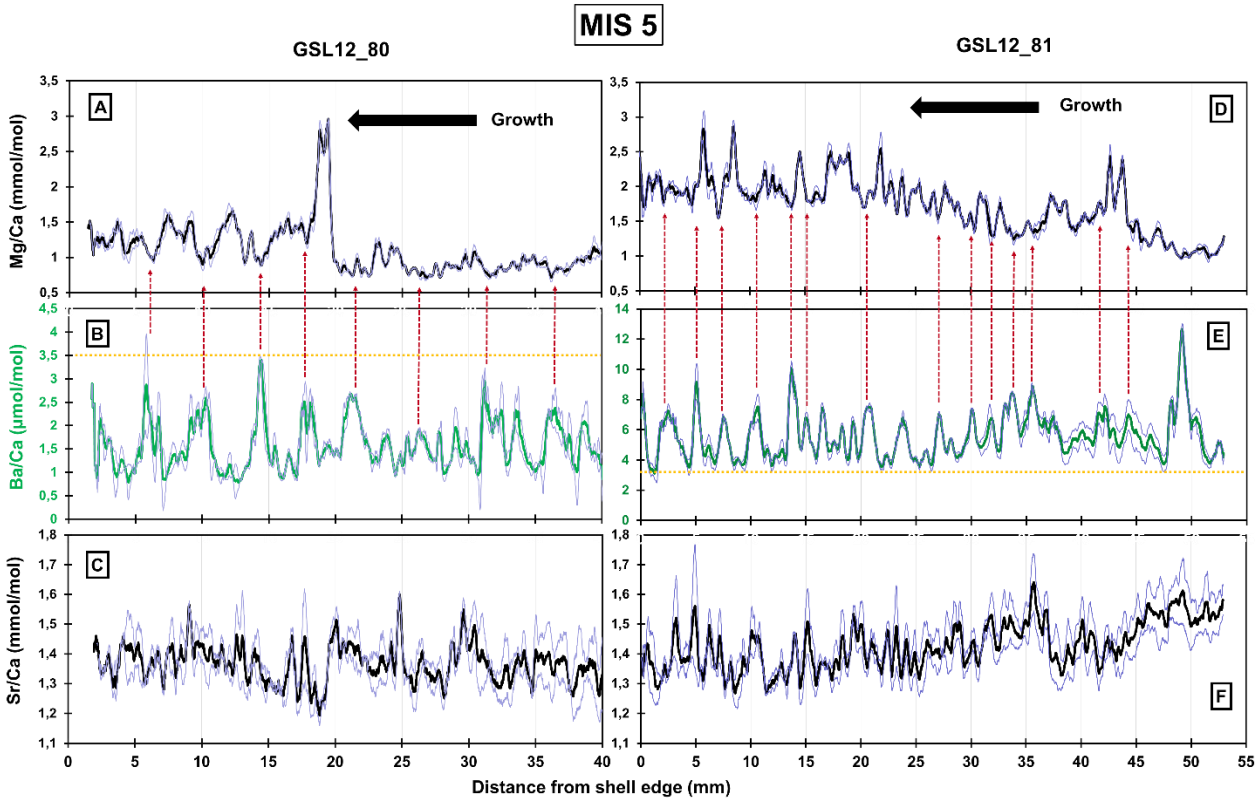

Fig. 5.11. Trace elements reconstructions from Nirwana samples **A)** GSL12_80 Mg/Ca **B)** GSL12_80 Ba/Ca **C)** GSL12_80 Sr/Ca. **D)** GSL12_81 Mg/Ca **E)** GSL12_81 Ba/Ca **F)** GSL12_81 Sr/Ca. Red arrows relate peaks of Ba/Ca with min values of Mg/Ca assumed as dry seasons.

In GSL12_60, Mg/Ca profile (n = 2 laser ablations) ranges from 0.50 to 2.06 mmol/mol avec a mean value of 0.91 ± 0.06 mmol/mol (Fig. 5.12-A). Ba/Ca Ca ranges from 0.38 to 3.56 µmol/mol with a mean value of 1.0 ± 0.1 µmol/mol (Fig. 5.12-B). Sr/Ca ranges from 1.34 to 1.98 mmol/mol with a mean value of 1.56 ± 0.06 mmol/mol (Fig. 5.12-C).

In GSL12_64, Mg/Ca (n = 2 laser ablations) ranges from 0.24 to 1.0 mmol/mol avec a mean value of 0.4 ± 0.04 mmol/mol (Fig. 5.12-D). Ba/Ca Ca ranges from 1.07 to 8.15 µmol/mol with a mean value of 2.87 ± 0.2 µmol/mol (Fig. 5.12-E). Sr/Ca ranges from 1.25 to 1.89 mmol/mol with a mean value of 1.42 ± 0.2 mmol/mol (Fig. 5.12-F).

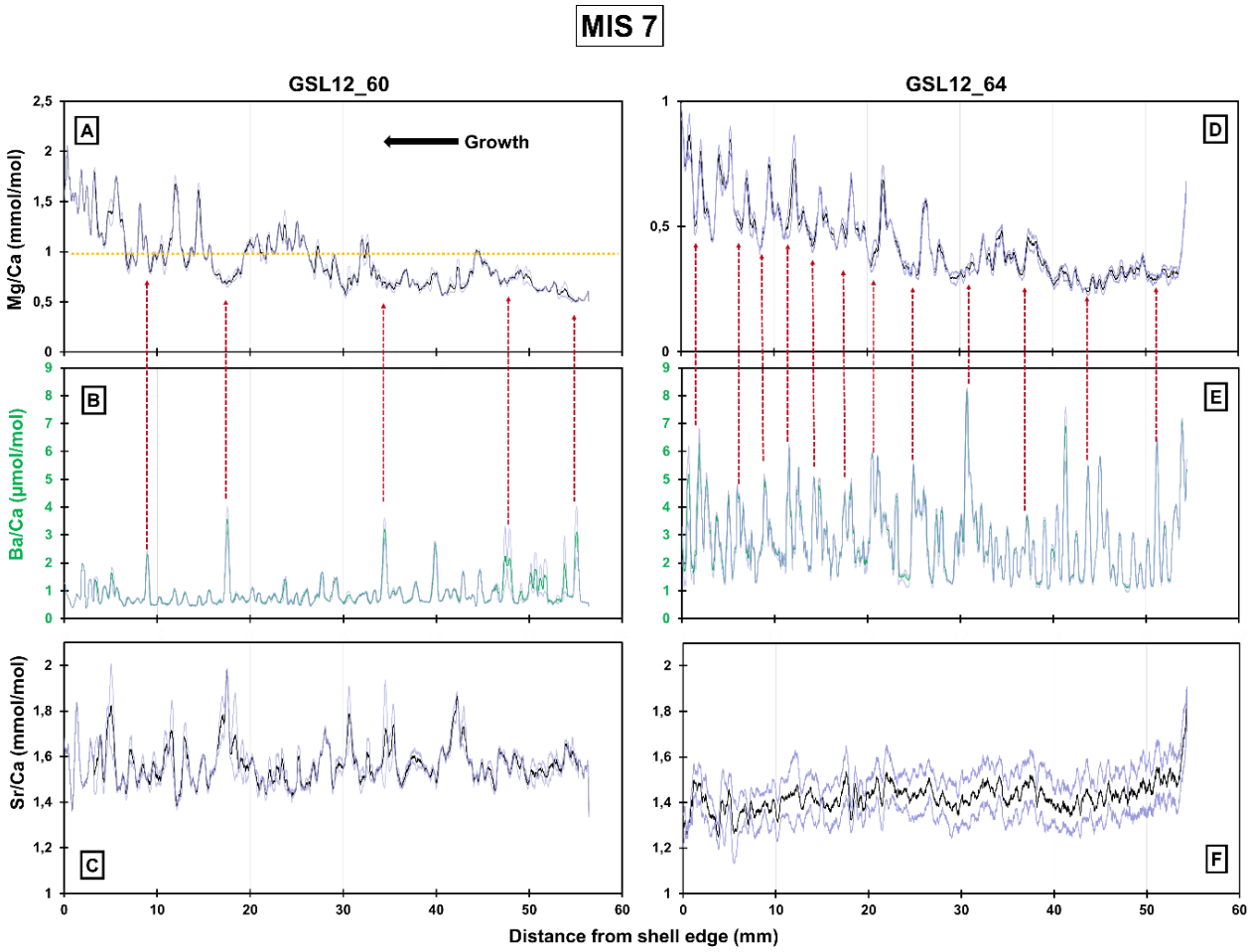

Fig. 5.12. Trace elements reconstructions from Rahia samples **A)** GSL12_60 Mg/Ca **B)** GSL12_60 Ba/Ca **C)** GSL12_60 Sr/Ca **D)** GSL12_64 Mg/Ca **E)** GSL12_64 Ba/Ca **F)** GSL12_64 Sr/Ca. Red arrows relate peaks of Ba/Ca with min values of Mg/Ca assumed as dry seasons. Mg/Ca profiles are not plotted in the same scale, yellow dashed line in Mg/Ca from GSL12_60 (A) represents the highest values of GSL12_64 (B)

5.4. Discussion

5.4.1. Isotopic comparison between fossil data

Bulk $\delta^{18}O$ results form Table 5.1 are plotted in Fig. 5.13 and arranged as a function of age (the 8 undated samples have been excluded from this figure). The dated samples where corrected for SL. Yokoyama et al. (2000) calculated a relationship between sea level and $\delta^{18}O_{water}$ from which a change in 0.0085 ± 0.015 ‰ m^{-1} is equivalent to 1 m sea level change. Adkins et al. (2002) provides new values on the same range, with a relationship between sea level change and mean oceanic $\delta^{18}O$ enrichment/decrease of 0.010 ± 0.001 ‰ m^{-1}. This last relation was used to correct SL. The corrected bulk results are compared to the modern bulk values. On this figure, the mean range of seasonal variation of modern samples (red box) represents a mean state for an interglacial period. The global average of glacial period (blue box) effect on $\delta^{18}O_{water}$ was estimated at approximately 1.0 ‰ for the 120 m sea-level change associated with the ice sheet build-up/melting (Schrag et al., 2002).

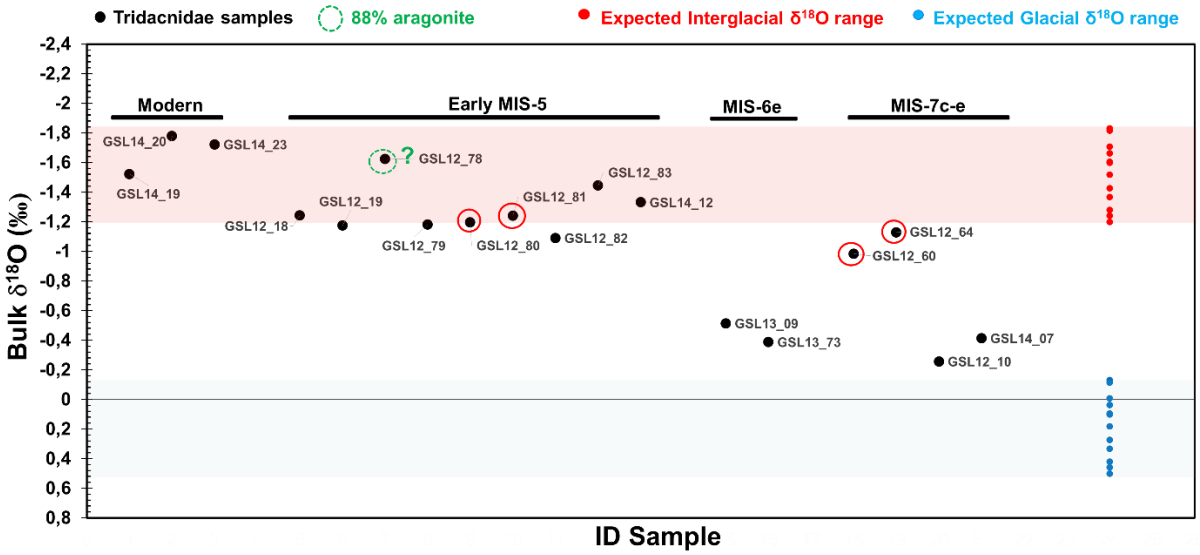

Fig. 5.13. Bulk isotopic results corrected for SL component. Samples used for reconstructions in this chapter are bounded in red: GSL12_80, GSL12_81, GSL12_60 and GSL12_64.

Most bulk $\delta^{18}O$ values derived from fossil samples are close the modern $\delta^{18}O$ range (Fig. 5.13). Principally, the samples collected at the Nirwana site are inside this range. Even the undated

samples for which we are unable to correct for SL also have bulk $\delta^{18}O$ values within interglacial signatures (See Fig. 5.8-A), and could come effectively from past interglacial reefs.

The selected samples from Nirwana (GSL18_80 and GSL12_81) are close to the upper range of modern $\delta^{18}O$ values (Fig. 5.13). The age of the site is early MIS-5 is discussed in Chapter IV. The samples from Rahia (MIS-7) are relatively close to the modern interglacial range, it is important to note that MIS-7 was a period below modern SL. The interstadial (MIS-6e) dated samples (GSL13_09 and GSL13_73) have more positive values (between -0.5 to -0.4‰) compared to modern. Another two samples (GSL12_10 and GSL14_07) have a reference age from MIS-7 with similar values from those of MIS-6e. The SL estimations in MIS-6e and MIS-7 highstands presents large uncertainties, with ~ 20 m below modern SL in common for both periods (Fig. 4.19-F, Chapter IV), consequently MIS-6e and MIS-7 (at least in some sub-stages) could had presented similar conditions.

To summarize the findings, 9 fossil samples have similar $\delta^{18}O$ compared to modern reflecting similar temperature/salinity conditions to present. Six other samples have bulk $\delta^{18}O$ values significantly more positive tan today, reflecting colder/drier environment relative to modern interglacial. No samples have values more negative than modern, indicating that this modern day conditions could reflect an optimal warm interglacial state in the region, during the past 250ka. MIS-7 however appears to be characterized by significantly different conditions, with coldest temperatures.

The bulk $\delta^{13}C$ results show that modern Tridacnidae samples have lowest values (around +1.2 to 1.5‰) compared to all fossil records (+1.8 to 3‰) (Fig. 5.8-B). This is a significant offset. The bulk $\delta^{13}C$ derived from Nirwana fossils range from 1.8 and 2.6 ‰. The rest of the fossils are in this range, except 2 samples, which presents the highest $\delta^{13}C$ values: 2.9 and 3.1 ‰). From which, one fossil (GSL12_10) is dated at MIS-7 and the other one (GSL12_75) have no age reference, but probably comes from the same period or MIS-6e at the same SL, as indicated by its $\delta^{18}O$ bulk signature (Fig. 5.8-A).

A wide variety of factors control $\delta^{13}C$ in bivalves, from biological effects to water $\delta^{13}C$ dissolved inorganic carbon (Chapter III), making it often difficult to identify any independent effect and provide a robust interpretation of the shell $\delta^{13}C$ signals (Lorrain et al. 2004; Titschack et al., 2010; Lartaud et al., 2010). However, in this study reproducible $\delta^{13}C$ signal from *T. squamosa* and *H. hippopus* have been observed (Chapter III). High $\delta^{13}C$ values appear related to dry/cold seasons characterized by high salinity and high productivity. Bulk $\delta^{13}C$ signal derived from fossil samples could thus reflect enhanced productivity/salinity, because highest bulk $\delta^{13}C$ values are often associated with more positive bulk $\delta^{18}O$ signal. Previous studies in this area have shown that primary productivity was enhanced during cold periods (Beaufort et al., 2003; Holbourn et al., 2005; Kawamura et al., 2006) and salinity was also higher (Stott et al., 2004). It is possible that the samples with higher $\delta^{13}C$ values reflect colder and drier periods, which would agree with the more positive bulk $\delta^{18}O$ values observed. Further analyses must be conducted on modern *T. gigas* and other Tirdacnidae species from the study area to understand the factors controlling shell $\delta^{13}C$, and verify the hypothesis of a potential paleo-productivity/salinity proxy.

5.4.2. Seasonally resolved record of past interglacials

5.4.2.1. Mean temperature difference during past interglacials MIS5 and MIS7

The isotopic profiles ($\delta^{18}O$ and $\delta^{13}C$) derived from 4 fossil samples (GSL12_80, GSL12_81, GSL12_60 and GSL12_64) provide information on the seasonality during these periods. Raw $\delta^{18}O$ and $\delta^{13}C$ profiles were resampled with a monthly resolution to obtain a monthly mean profile, and compare these data with modern records (Fig. 5.14). Fossil $\delta^{18}O$ records were corrected for SL effect in both cases, early MIS-5 samples (correction of 5m or 0.05 ‰) and MIS-7 samples (correction of 13.5 m or 0.13 ‰).

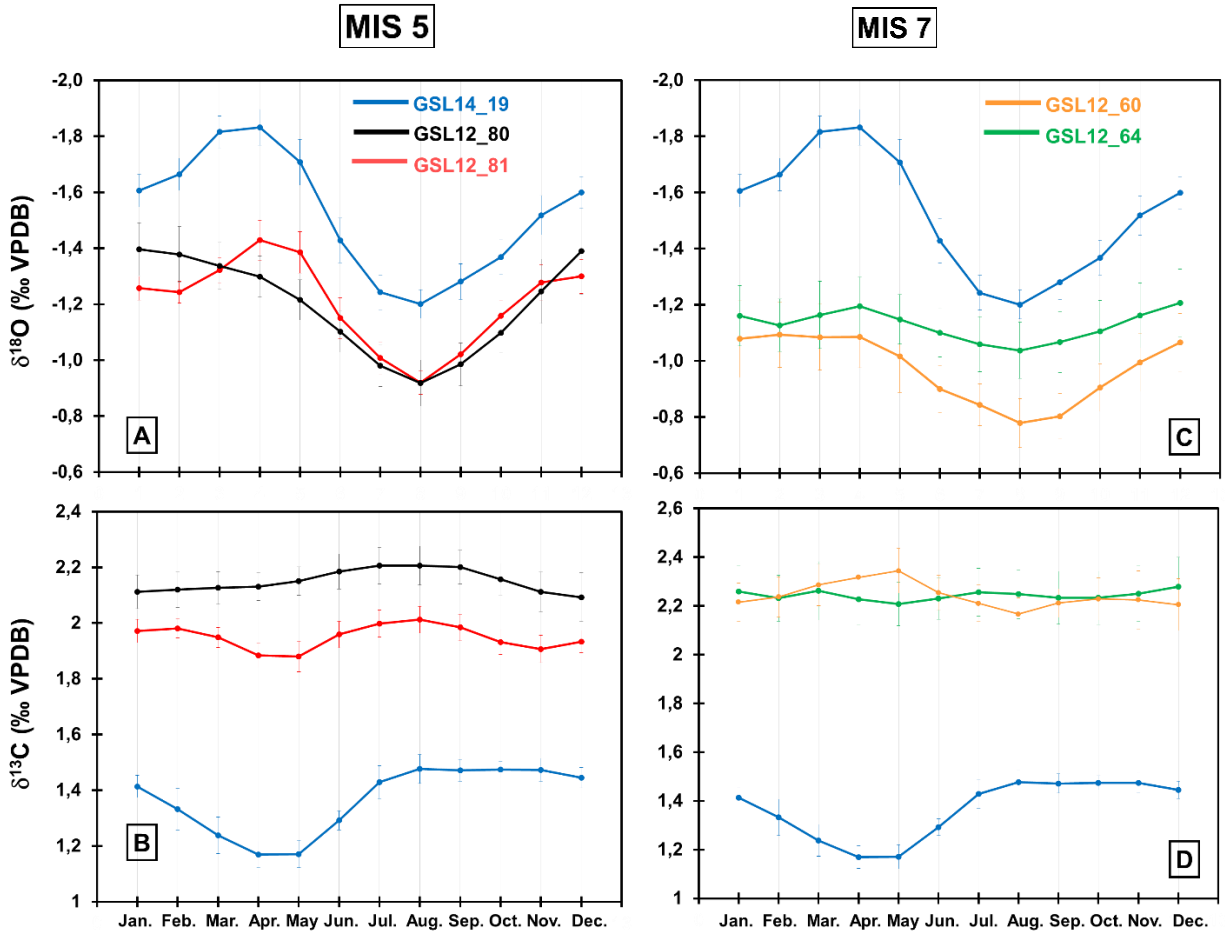

Fig. 5.14. Monthly mean isotopic records from Nirwana and Rahia fossils, compared to modern conditions (GSL14_19) **A)** $\delta^{18}O$ mean monthly profiles of GSL12_80 and GSL12_81 **B)** $\delta^{13}C$ mean monthly profiles of GSL2_80 and GSL12_81 **C)** $\delta^{18}O$ mean monthly profiles of GSL12_60 and GSL12_64 **D)** $\delta^{13}C$ mean monthly profiles of GSL12_60 and GSL12_64. $\delta^{18}O$ are corrected from SL effect.

When comparing early MIS-5 samples with modern record clear differences are observed (Fig. 5.14-A-B). Compared to $\delta^{18}O$ modern profiles, MIS-5 samples exhibit more positive values with a mean difference of 0.31 ‰. If a change of 1°C is equivalent to 0.2 ‰ (Grossman and Ku 1987), this translates into a mean 1.4 °C colder SST during early MIS-5 compared to current interglacial period. The mean SST today in the studied area is 29 ± 0.3 °C (data set IGOSS), so the mean SST at early MIS-5 would be around ~27.6 °C.

The comparison of $\delta^{18}O$ records between the Nirwana samples GSL12_80 and GSL12_81 shows no significant differences (Fig. 5.14-A), both records present the same mean value (-1.15 ‰), and the similar seasonal ranges: 0.49 ± 0.1 ‰ and 0.51± 0.1 ‰ respectively. However, the

profile of GSL12_81 presents the characteristic double peak during the summer season (Fig. 5.9-A), whereas in GSL12_80 profile the double summer peak is not observed (Fig. 5.9-B).

The closest SST reconstructions to SE Sulawesi comes from the sediment core MD9821-62, sampled in the Makassar strait (Visser et al. 2003), the derived SST show that SST was ~ 27 °C around 133 ka (Fig. 5.15-B) in agreement with this scenario. This record also suggests that Holocene SST and modern SST are colder than the highest MIS-5e temperatures (~31° C) (Fig. 5.15). When comparing T-II and T-I our SST record would reflect conditions equivalent to early Holocene SST's in this area (Fig. 5.15-A).

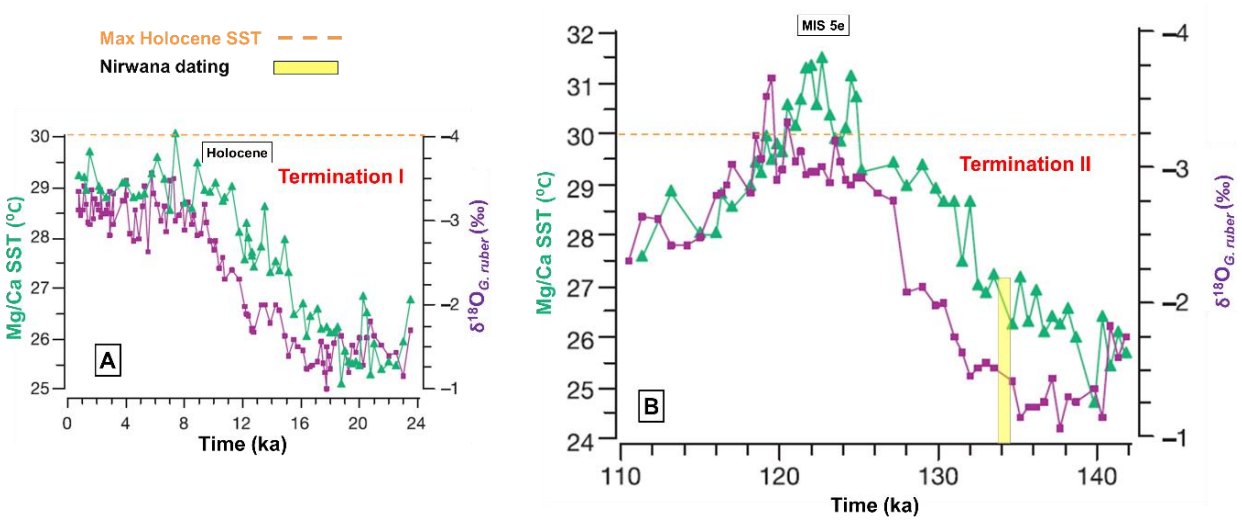

Fig. 5.15. SST and $\delta^{18}O$ records for core MD9821-62, Makassar Strait **A)** MIS 1 and 2 (Termination I) and **B)** MIS 5e and 6 (Termination II). *G. ruber* oxygen isotope (purple curve) and Mg/Ca SST (green curve). For both terminations, the surface temperature warming occurs several thousand years before the decrease in ice volume reflected by the $\delta^{18}O$ record. The yellow rectangle on Termination-II represents our fossil dating from Nirwana. Modified from Visser et al. (2003).

Similarly, another sediment core from the Western Pacific Warm Pool (S06B record from Lea et al. (2000)) also shows SST ~27 °C around 133 ka. The results derived from the *T. gigas* fossils collected in Nirwana site are thus coherent with regional patterns of SST during this period.

Table 5.2. Mean $\delta^{18}O$ and equivalent temperature differences between fossil samples relative to modern conditions.

Sample	Period	Mean difference in respect to modern conditions	
		$\delta^{18}O$ (‰)	Temp. (°C)
GSL12_81	T-II/MIS 5	0.31	1.4
GSL12_80		0.32	1.4
GSL12_60	MIS 7	0.68	3.1
GSL12-64		0.55	2.4

The mean seasonal profiles derived from the 2 fossil samples collected in the Rahia site (MIS-7) have a mean $\delta^{18}O$ offset around 0.15 ‰ (Fig. 5.14-C), with more positive values for GSL12_60 (-0.84 ‰) than GSL12_64 (-1.0 ‰). This translates into a temperature difference of 0.75 °C. This is close to the uncertainties of the method and this difference is not statistically significant. Although these exhibit similar mean $\delta^{18}O$ profiles, we cannot exclude that they come from different MIS7 sub-stage sea level highstands (Fig. 4.19, Chapter IV).

When comparing fossil with modern $\delta^{18}O$ record, the mean differences is: 0.55 ‰ more positive for GSL12_60 relative to modern $\delta^{18}O$, and 0.68 ‰ more positive for GSL12_64. This translates into a mean temperature difference of 2.7 °C colder during the MIS-7 (Table 5.2) compared to the current interglacial. If we consider that the $\delta^{18}O$ shift is only related to temperature the resultant mean SST for this period would be around ~26 °C.

For the penultimate interglacial MIS-7, there are no SST reconstructions close to the study area and in general there are not enough information around the world. However, if sea level was ~13 m below modern SL for this area (Chapter IV), it is coherent to find colder temperatures. It is also coherent when compared MIS-7 results with the MIS-5, the difference is ~0.7 °C.

In the Maritime continent (Indonesia, Malesia, northern Australia and New Guinea), when SL drops, an important shelf area is exposed , resulting in a contraction of the IPWP, contraction in the ITCZ latitudinal migration, reduced ITF transport and drier conditions (Denniston et al., 2013; Jo et al., 2014; Huang et al., 2015; Denniston et al., 2016; Di Nezio et al., 2016). The contraction of the IPWP and exposure of continental shelf in the region influences the contraction and

southward shift of the ITCZ in boreal winter during glacial periods (Denniston et al., 2013; Xu et al., 2006; Di Nezio et al., 2016). The displacement of the ITCZ is associated with relatively dry climatic conditions in our studied area. The decrease in moisture and convective activity is also attributed to the lowered sea-level (De Deckker et al., 2002; Griffiths et al., 2009). Although no data is available for MIS7 or MIS5 salinity in this area, sea surface salinity during glacial times has been shown to be ~2 PSU higher than the present (Stott et al., 2004), due to reduced monsoon (precipitation) activity, generating a column water destabilization with a final increase in primary productivity (Beaufort et al., 2003; Holbourn et al., 2005; Kawamura et al., 2006; Huang et al., 2015). Today the low salinity layer on the IPWP plays as barrier and stabilize column water (Kawmura et al., 2006). During glacials in the Indo-Australian region, primary productivity was higher even on terrestrial ecosystems, with cover vegetation on shelf exposed areas, by grass, sedges and eolian dunes (van der Kaars, 1991).

The inferred differences in temperature between MIS7 and modern, suggests that even a small reduction in SL change has an important impact in the hydrological cycle in SE Sulawesi, because SST and monsoon rainfall are correlated along seasonal and interannual variation (Chapters II and III).

5.4.2.2. Changes in $\delta^{18}O$ seasonality during MIS5 and MIS7

Additional and important information is provided by the mean seasonal profiles of the fossil records. In the modern conditions (Fig. 5.14-A) the $\delta^{18}O$ seasonal range is 0.66 ± 0.2 ‰ or 3 ± 1 °C of SST change between the wet and the dry season (Table 5.3). In the fossil record of early MIS-5, the mean $\delta^{18}O$ seasonal range is 0.49 ± 0.17 ‰, which translates into a 2.2 ± 0.7 °C of SST change (Table 5.3). For MIS-7 samples the seasonal range is 0.31 ± 0.1 ‰ (1.4 ± 0.6 °C) for GSL12_60 and 0.17 ‰ (1.4 ± 0.6 °C) for GSL12_64. We cannot exclude that changes in salinity induced by changes in seasonal rainfall are also associated with these shifts in seasonal $\delta^{18}O$ profiles. However, in the tropical areas high temperature and high precipitation are correlated thus these estimated SST ranges can be considered as a minimal SST range. Today modern $\delta^{18}O$ record is related to 72 % of contribution from SST and 28 % from salinity (Chapter III). If salinity increase in coldest periods (e. g. Stott et al., 2000), its contribution in fossil signal must be higher than in the current record.

Table 5.3. $\delta^{18}O$ seasonal range comparison and equivalence in temperature range differences between fossils and modern shell samples.

Sample	Time (yr)	Period	Mean seasonal range		(%)	Decrease (%)	Decrease (°C)
			$\delta^{18}O$ (‰)	Temp. (°C)			
Data set	30	Today	0.69 ± 0.2	X= 0.66 ± 0.2	3 ± 1	100	
GSL14_19	6		0.63 ± 0.2				
GSL14_20	1,8		0.74 ± 0.03				
GSL14_23	4		0.59 ± 0.2				
GSL12_81	14	T-II/MIS 5	0.51 ± 0.15		2.3 ± 0.7	81	-19	-0,7
GSL12_80	13		0.48 ± 0.18		2.2 ± 0.8	76	-24	-0,8
GSL12_60	14	MIS 7	0.31 ± 0.13		1.4 ± 0.6	49,2	-51	-1,6
GSL12-64	14		0.17 ± 0.08		0.8 ± 0.3	27	-73	-2,2

The higher seasonality today in SE Sulawesi relative to past interglacial records (Table 5.3), could be explained by more intense NW monsoon than presently. The influence of summer (NW) monsoon intensity on salinity and surface water $\delta^{18}O$ is marked by a large-scale redistribution of depleted $\delta^{18}O$ (rainfall amount) from land to sea when the monsoon initiates during deglaciations (Xu et al., 2006). The isotopic signal from early MIS-5 fossils should reflect the resumption of monsoon activity from glacial to interglacial conditions, with a moisture inception in the atmosphere. Whereas MIS-7 lowest seasonality is related to lowest SL and driest conditions. These Paleoclimate reconstructions highlight the sensibility of the study area to changes in ocean atmosphere interactions.

In the Huon Peninsula (Papua New Guinea), Welsh (2008) and Driscoll et al. (2014) also studied past climate conditions from giant clams and obtained information on past seasonality. Driscoll (2014b) found that the mean annual amplitude in 6 Tridacnidae fossils from MIS 3 was reduced compared to a modern *T. gigas* (MT-7). MIS-3 is considered an intermediate interstadial period with mean climatic conditions between full Glacial and full Interglacial conditions (Tzedackis et al., 2017). The seasonal amplitude during this period (MIS-3) was ~ 30 % reduced compared to modern, with maximum reductions of 45 % relative to modern conditions (Driscoll, 2014b). The mean seasonal cycle derived from Early Holocene (7–9 ka) fossil samples from the same study is also inferior (~36 %) than modern, reflecting colder winters in early Holocene (Driscoll et al., 2014a-b). In this study, a 22% reduction in seasonality with respect to modern conditions is also observed during early MIS-5 (Nirwana site) (Table 5.4).

McCulloch et al. (1999) found that seasonal variation was similar between Termination-II, MIS-5e and modern interglacial from fossil corals in Huon Peninsula. With a seasonal range of ~ 0.6 °C in T-II/early MIS-5, and 0.5 °C for MIS-5e and modern period. These seasonal temperature range is significantly smaller compared to our results for modern and early MIS-5 (Table 5.4). This difference could be explained by the different climatic settings between the Huon Peninsula and SE Sulawesi during this period of time. SE Sulawesi is located in a region with strong seasonal changes (Aldrian and Susanto, 2003; Chapter II). These contrasting results highlight the need to derive more records of past seasonality. For MIS-7c-e, actually there is no available high resolution records to compare our results.

5.4.2.3. Changes in $\delta^{13}C$ seasonality during MIS5 and MIS7

Regarding seasonality of $\delta^{13}C$, some variation is observed in both profiles of MIS-5 fossils (GSL12_80 and GSL12_81), but the mean amplitude (~ 0.12 ‰) is smaller compared to $\delta^{13}C$ modern samples (0.31 ‰) (Fig. 5.14-B). Resulting in a decrease of ~ 60 % in early MIS-5 relative to modern $\delta^{13}C$ amplitude (Table 5.4). For MIS-7 fossils, mean seasonal range for GSL12_60 is 0.18 ‰, and 0.04 ‰ for GSL12_64. Which means a reduction of 43 and 88 % respectively for GSL12_60 and GSL12_64, in respect to modern range (Table 5.4).

Table 5.4. $\delta^{13}C$ mean values and seasonal range comparison between fossils and modern sample

ID Sample	Period	$\delta^{13}C$ comparison		Reduction in seasonality (%)
		Mean (‰)	Seasonal range (‰)	
GSL14_19	Modern	1,4	0,31	
GSL12_81	Early-MIS 5	2	0,13	57
GSL12_80		2,1	0,11	63
GSL12_60	MIS 7	2,2	0,18	43
GSL12-64		2,2	0,04	88

Despite $\delta^{13}C$ record presents a reduction in seasonality for both last interglacials relative to modern records (Table 5.4), mean $\delta^{13}C$ values are higher in fossils (Fig. 5.14-B-D, Table 5.4). In $\delta^{13}C$ reconstructions for early MIS-5 (Fig. 5.9-B-D) and MIS-7 (Fig. 5.10-B-D), high values appear associated with more positive $\delta^{18}O$ characteristic of the dry/cold seasons. For *T. squamosa and H.*

hippopus (Chapter III), $\delta^{13}C$ seasonality is well defined with increases during the dry season and low values in wet season. If same cyclicity is observed in the fossil samples, the same parameters that control modern shells $\delta^{13}C$ could also explain fossil shell $\delta^{13}C$ seasonality. So, parameters driving $\delta^{13}C$ in fossil shells were higher in magnitude and persistent in time (constant inputs), reflecting less contrasted seasonal changes at these periods (early MIS-5 and MIS-7). As discussed before, these parameters could be salinity and productivity.

5.4.2.4. Interannual variation

In the next section a comparison of modern interannual climate variability between modern and fossil shell data is discussed. For every fossil record, a mean seasonal value was estimated, and then, subtracted from the record, the residual values reflects anomaly values. These new records (Fig. 5.16-C-F) can provide information on past interannual climate change (e.g. Cobb et al., 2007; Driscoll et al., 2014; Emile- Geay et al., 2015).

Firstly, theoretical $\delta^{18}O$ inter-annual variability is obtained from historical SST and SSS data (Fig. 5.16-B). The residual $\delta^{18}O$ record (Fig. 5.16 C-F) reflects SST and SSS anomalies in the study area for the past 35 years. Values range from + 0.4 to - 0.4 ‰ reflecting both changes in temperature and water $\delta^{18}O$ (salinity). In the modern record decadal (instrumental) trends can be observed with a marked difference between the 80-90's compare to 2000-2015. With the short records that have been derived in this work, such decadal trends are difficult to reproduce, this would require multi-decadal records.

However, fossil data from early MIS-5 (Fig. 5.16-C-D) suggest similar amplitudes of interannual climate variability relative to modern days whereas the fossil records derived from MIS-7 (Fig. 5.16-E-F) exhibit apparent interannual variation reduced when compared to both MIS-5 and the present, with maximum amplitude around 0.2 and -0.2.

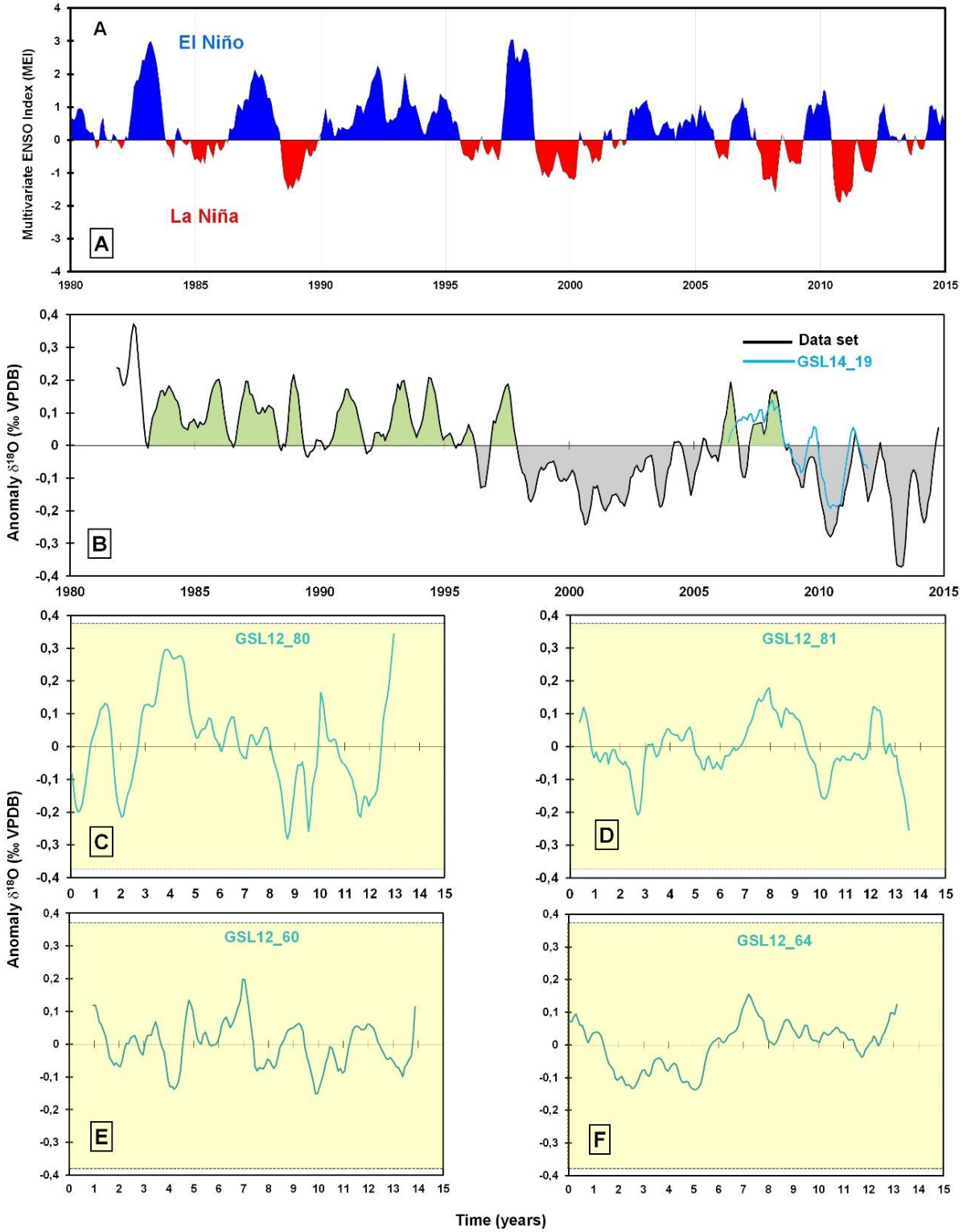

Fig. 5.16. $\delta^{18}O$ anomalies related to interannual variation derived from **A)** MEI Index **B)** Data set modern conditions and GSL14_19 record (*T. squamosa*). Positive/cold anomaliesin green, negative/warm anomalies in grey **C)** GSL12_80 (*T. gigas*) fossil **D)** GSL12_81 (*T. gigas*) fossil **E)** GSL12_60 (*T. gigas*) fossil **E)** GSL12_64 (*T. gigas*) fossil. Yellow box on fossil records represents the range of modern conditions (A).

In the tropical Western Pacific, interannual atmospheric at oceanographic variations comes mainly from ENSO (Nicholls, 1983; McBride et al., 2003; D'Arrigo et al., 2006; Emile-Geay et al., 2015). Using fossil corals, Tudhope et al. (2001) found that ENSO during the 20th century has been strong compared to previous glacial and interglacial periods. However similar magnitude of ENSO events (in fossil records) have rarely been found during the Holocene relative to our industrial times (Corrège et al., 2000; McGregor and Gagan, 2004; Carré et al., 2014) and during glacial periods (Driscoll et al., 2014). Most of these records are derived from areas closer to the center of action of modern day ENSO whereas in the SE Sulawesi ENSO variance is not the dominating source of interannual variability, as observed when comparing MEI Index and $\delta^{18}O$ anomalies (Fig.5.16-A-B). This mode of climate variability does not explain all the SST and SSS anomalies in the studied area. The records derived here suggest that interannual climate variability, which is partly driven by ENSO today, during the warm phases of the late Pleistocene could be similar or reduced but does not exceed modern conditions.

To obtain more robust evaluation of interannual variability and the frequency of ENSO in the studied area more seasonally resolved records will be necessary. However, this study illustrates that it is possible to assess this mode of climate variability during MIS-5 which apparently had similar behavior in magnitude relative to modern times, whereas in MIS-7 interannual variability was reduced by around 50 % compared to modern conditions.

5.4.3. Trace elements variation

Most profiles of trace elements exhibit some seasonality as seen for the modern *T. squamosa* (Arias-Ruiz et al., 2017). In most Tridacnidae species, as for many carbonate secreting organisms (e. g. foraminifera and corals) Mg/Ca has been shown to be positively correlated to water temperature. However, in *T. gigas* there is an increase in Mg/Ca during the lifespan which translates into varying temperature/Mg/Ca relationship (Elliot et al., 2009; Batenbourg et al., 2011; Warter et al., 2015). This biological effect seems to reflect an aging effect characteristic of this species which is not observed in *T. squamosa* (Arias-Ruiz et al., 2017). However, maxima (minima) Mg/Ca values correspond to warm/wet (dry/cold) season and inversely. The 4 seasonally resolved Mg/Ca profiles in fossils show some of these features: increase Mg/Ca with age, however the seasonal

Mg/Ca patterns are not always very clear in these fossil samples (FIG. 5.11-A-D and Fig. 5.12-A-D). The $\delta^{18}O$ and the trace element profiles are plotted on different distance scales and small offsets are difficult to avoid. As a result, these data is shown on independent plots. However, it is apparent that there are not the same number of Mg/Ca cycles of similar amplitude associated with each seasonal cycle of $\delta^{18}O$ unlike previous observations (Elliot et al., 2009). One possible explanation is that these samples are from Tropical areas where the seasonal amplitude is smaller and the amplitude of Mg/Ca is smaller.

Profiles of Ba/Ca in modern samples presents a characteristic pattern with low background values punctuated by sharp peaks (Chapter III). In the fossil samples, Ba/Ca have a more varied profiles. In MIS-5 samples Ba/Ca have a more cyclic seasonal signal (Fig. 5.11-B-E) than modern record (Chapter III). However GSL12_81 (Fig. 5.11-E) have higher values than GSL12_80 (Fig. 5.11-B). Between samples from MIS-7 there are more variability (Fig. 5.12-B-E).

In all cases the Ba/Ca profiles are very reproducible and the peaks in Ba/Ca occur in main part of the records during periods of low Mg/Ca, with the exception of GSL12_60 which present only some sporadic spikes (Fig. 5.12-B). The relationship between Ba/Ca and Mg/Ca in modern *T. gigas* has been shown to be variable and site dependent (Elliot et al., 2009). In SE Sulawesi modern samples, the Ba/Ca peaks occur during each cold/dry season except during years with particularly high rainfall, when they also occur during the warm/wet season. In the fossil samples, high Ba/Ca always seem associated with low Mg/Ca and thus occur during the cold/dry season (as seen today). In the modern *T. squamosa* sample (Chapter II), only 3 Ba/Ca peaks were attributed to abnormally enhanced rainfall during the wet seasons increasing nutrient runoff from the continent and increasing coastal primary productivity (PP). If the fossil Ba/Ca peaks are mainly related to dry seasons potentially reflecting upwelling events bringing nutrients into the surface waters increasing PP as seen today. This information would confirm drier conditions during early MIS-5 compared to today, with more regular profiles of Ba/Ca variation (Fig. 5.11-B-E).

The Ba/Ca profiles derived from fossil samples from both MIS5 and MIS-7 exhibit significant variability in both the background values and the frequency and amplitude of the peaks. Such results could reflect a more variable conditions during these periods which would require further analyses to constrain more precisely. All trace element profiles measured on dated fossil samples

are presented in the supplementary figures (Appendix 3). In this section only box plots of dated samples are shown as easier to compare between fossil and modern samples (Fig 5.17 and 5.18). These plots enable to assess if a coherent pattern of variability appears between different periods characterized by different SL, as seen in the stable isotopic results.

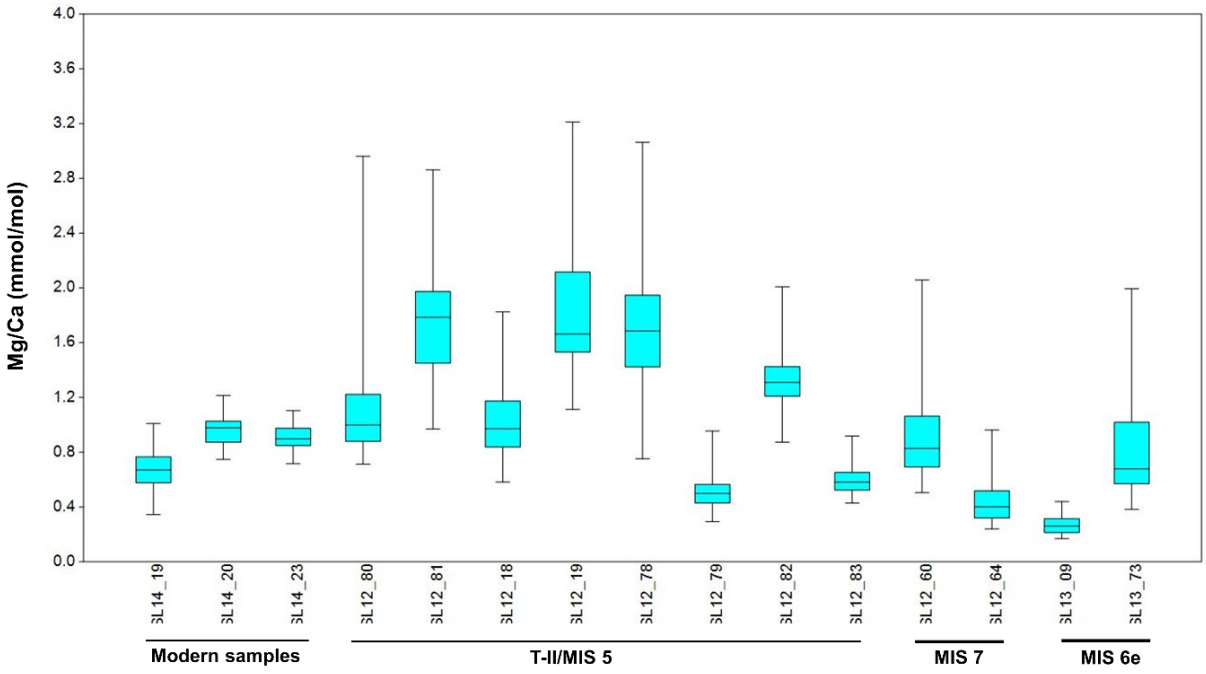

Fig. 5.17. Boxplot for Mg/Ca records from modern and dated fossil clams. Modern samples correspond to *T. squamosa* (GSL14_19) and *H. hippopus* (GSL14_20 and GSL14_23), the others were identified as *T. gigas*.

However, no clear pattern is identified. Fossil samples from Nirwana (early MIS-5) presents at the same time mean higher and lowest Mg/Ca values compared with modern samples (Fig. 5.17). From MIS-7 samples Mg/Ca values are similar for GSL12_64 but higher for GSL12_60. From interstadial MIS-6e one sample are higher (GSL13_73) and the other (GSL13_09) lower relative to modern samples. If mean Mg/Ca values reflect mean temperatures, fossil samples from MIS7 should reflect colder conditions i.e. lower values compared to modern values.

One possible explanation for this variation is the well-known and described taxonomic influence on trace elements incorporation for marine bivalves (e. g. Carré et al., 2006; Tynan et al., 2016), with the particular effect of growth rate in *T. gigas*, identified for Mg/Ca incorporation along growth development (Elliot et al., 2009; Batenbourg et al., 2011; Warter et al., 2015). In

Tridacnidae species, *T. gigas* presents the highest growth rates and is considered the faster growing bivalve ever to have existed (Griffits and Klumpp, 1996). The higher growth rate of this specific species could partly explain the higher values in fossils of Mg/Ca relative to the modern sample *T. squamosa*, however in respect to *H. hippopus*, similar growth rates are observed. Even *H. hippopus* presents high mean values (see the boxplot grow rate comparison in Appendix 5).

In modern *T. gigas* from different localities in the WPWP, mean Mg/Ca values are between 1-2 mmol/mol in young fast growing section of the shell's inner layer, and 4-6 mmol/mol in the adult slow growing zone zone (Elliot et al., 2009). Even the concentrations in the young *T. gigas* from Elliot et al. (2009) are higher than the results in the modern *T. squamosa* (mean= 0.67 ± 0.08 mmol/mol) and *H. hippopus* (mean = 0.93 ± 0.07 mmol/mol) from this study. And the Mg/Ca values of modern T. gigas e.g. (Elliot et al., 2009) are also higher than that observed in Nirwana fossil samples.

Further studies are required to assess the influence of growth on shell Mg/Ca. *T. squamosa* Mg/Ca-SST shows a good correlation with SST (r = 0.8, Chapter III). One possible avenue to explore would be to extract the growth rate influence from Mg/Ca in fossils and apply the equation performed for *T. squamosa*. Another possibility would be to perform aquaculture experiments with *T. gigas*, as this species is threatened and sampling live specimen is not possible (Neo et al., 2015).

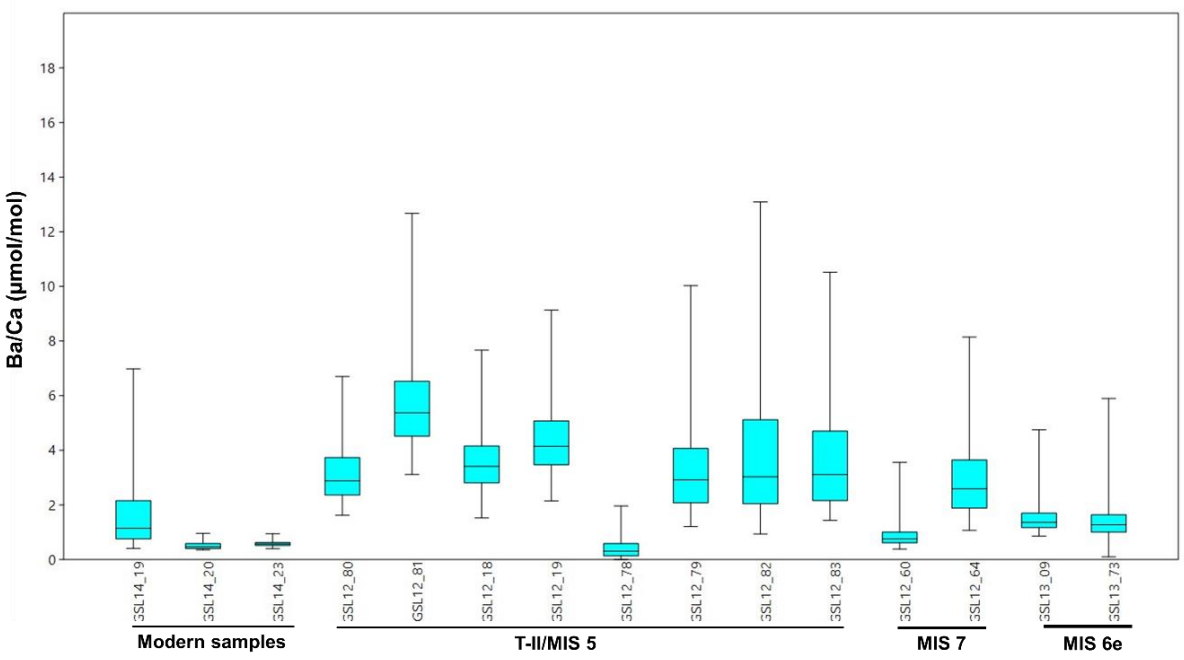

Fig. 5.18. Boxplot for Ba/Ca records from modern and dated fossil clams. Modern samples correspond to *T. squamosa* (GSL14_19) and *H. hippopus* (GSL14_20 and GSL14_23), the others were identified as *T. gigas*.

The shell Ba/Ca profiles not seem to reflect any clear pattern. Fossil samples particularly those from the Nirwana site have significantly higher peak values and background values compared to modern samples (Fig. 5.18). This could reflect higher productivity due to increased Ba and nutrients via coastal upwellings during this period. This would be in agreement with higher salinity. MIS-7 Ba/Ca records exhibit similar or lower values than during MIS-5 and modern samples. If productivity is enhanced in coldest periods, MIS-6e samples should present the higher Ba/Ca concentrations, but they have similar, even low values than modern samples (Fig. 5.18). Another actually unknown mechanisms should be involved in Ba/Ca acquisition for giant clams, or also taxonomic influence.

The trace element analysis shows some signals that deserve clarification at least for Mg/Ca and Ba/Ca. As concluded in Chapter III, *in situ* and/or controlled experiences are needed to understand the environmental versus the biological factors controlling trace element uptake in giant clam shells.

5.5. Conclusions

Stable isotope analysis of fossil samples reveals important differences in mean conditions and the seasonal cycles during modern conditions, early MIS-5 (analogue to early Holocene) and MIS-7c-e. For the studied periods, SL was estimated to be below modern highstand. Reduced sea level in the Indonesia region exposes large areas of the continental shelf and coastal zones. These changes in sea level appear associated with latitudinal migration of the ITCZ, decrease in NW monsoon reflected by drier climatic conditions. These modifications also affect local coastal oceanographic settings and contract the WPWP warm waters. Mean temperatures inferred from differences in $\delta^{18}O$ between past and present, shows a mean SST of 27.5 °C during early MIS-5, which is in agreement with SST reconstructions from the Makassar Straight (Visser et al., 2003) for the same period (~133 ka) and from WPWP (Lea et al., 2000). The amplitude of seasonal variations for early MIS-5 is also reduced by around ~20 % compared to modern seasonal range, confirming a reduced rainfall and moisture supply to the region during this early interglacial. It is interesting to note that results from early Holocene in Papua-New Guinea (Driscoll et al., 2014) also reflect drier conditions with a decrease in seasonal amplitude compared to modern conditions. Suggesting a pattern for early interglacial conditions.

MIS-7 fossil samples $\delta^{18}O$ values reflect colder SST/drier conditions with a maximum cooling of around ~2.8 °C compared to modern conditions. A reduction in seasonality of ~ 60 % is also observed during this period, suggesting even drier conditions and increased salinity associated with lower SL, around 15-20 m below modern SL. These results illustrate important environmental shifts in SE Sulawesi associated with past changes in SL and ice-volume. These results also illustrate the sensibility of the region to SL changes.

The analyses of trace elements on the same set of fossil samples reveals more complex results with possible influence growth rates which are specific to each species. The Mg/Ca values for *T. gigas* which have the highest growth rates are associated with the highest values of Mg/Ca. No clear patterns is observed for Sr/Ca. Finally, Ba/Ca profiles in the fossil samples presents seasonal peaks which occur principally during the low Mg/Ca values, or during the cold/dry season. Increases in PP during the cold season would be primarily associated with coastal upwelling bringing Ba and other nutrients into surface waters. Mean Ba/Ca values derived from fossil samples are also higher compared to modern samples from the same locality.

Chapter VI.

Conclusions and prospects

Chapter VI. Conclusions and prospects

This PhD research is one component of a larger project which aims to study different aspects of the Indonesian region evolution from geomorphology (Pedoja et al., submitted), coastal uplift (Pastier et al., in prep), links between carbonate production and sea level (Husson et al., submitted) and finally the links between biodiversity and changes in the land bridges in the Indonesian area (Sarr et al., submitted). This work focuses on paleoclimatic reconstructions at high resolution (seasonal to interannual) timescales using geochemical proxies on the modern and fossil giant clam family (Tridacnidae) from SE Sulawesi through an advantageous archive to study.

CALIBRATION

The calibration of modern specimen enabled to verify that shells of Tridacnidae record local environmental variables. These organisms precipitate their aragonitic shells in isotopic ($\delta^{18}O$) with surrounding sea water. $\delta^{18}O$ profiles derived from modern specimen reflect the strong importance influence of precipitations on water $\delta^{18}O$ values which is linearly related to salinity. Therefore, the modern $\delta^{18}O$ signal is composed of ~ 70 % from SST, and 30 % from SSS variations. The influence of ENSO variability on coastal hydrography was also demonstrated with a negative $\delta^{18}O$ anomaly, related to the warm and wet conditions that prevailed during the 2010 La Niña event.

Similar analyses were performed on *H. Hippopus* species. This is the first time that geochemical profiles are compared between two Tridacnidae species, enabling to test reproducibility and the links between environmental processes and shell geochemistry. The comparison between this species and *T. squamosa* confirms the reproducibility of $\delta^{18}O$ and influence of La Niña. However, an offset of 0.2 ‰ (1 °C of difference) was identified, and interpreted as a depth habitat differentiation, based on ecological information from literature. For trace elements, a high correlation ($r^2 = 0.8$) was found between Mg/Ca and SST for *T. squamosa* and a linear relationship proposed (Arias-Ruiz et al., 2017). The same relation was applied on the Mg/Ca profiles of *H. hippopus* to test the SST estimates. The results exhibit a difference of 1.1 °C between *T. squamosa* and *H. hippopus*, with warmer conditions for *H. hippopus*, preferentially inter-tidal species, relative to sub-littoral *T. squamosa*.

Although Sr/Ca covaries with Mg/Ca in *T. squamosa*, the relation with SST is less robust (r^2 = 0.6), and presents heterogeneous results when comparing with *H. hippopus* species. In previous studies, Sr/Ca profiles derived from giant clams also appeared to have less coherent variability.

Finally, the Ba/ca in *T. squamosa* was interpreted as response to Ba inputs from deeper waters through local coastal upwelling events increasing local primary productivity. These increases in PP occur mainly during dry seasons. The Ba/Ca records also seems to record continental runoff events, as the Ba/Ca peaks are associated with enhanced precipitation as for example during La Niña years. These Ba/Ca records are highly reproducible in modern *T. squamosa* and *T. gigas*, however, the signal is not reproducible in *H. hippopus*.

Profiles of $\delta^{13}C$ exhibit a clear seasonal pattern observed in both species with the same amplitude. High value of $\delta^{13}C$ occurs during the dry season, when salinity and primary productivity are higher. This relation argued for $\delta^{13}C$ as salinity/productivity proxy fro the region, however it need to be verified in other giant clamspecies.

CHRONOLOGY

Assessing a chronology of the past periods appears as a challenge and an effort, from the sampling in the field to the analytical procedures in the laboratory process, in order to obtain coherent and reproducible results. Chronology is the backbone of all paleoclimate research, however in this study, chronology uncertainties became crucial for the interpretation of paleo reef terraces. In this study tests were done to directly date the fossil Tridacnae. However, giant clam shells presents very low Uranium concentrations and heterogeneous ages were obtained on the same sample reflecting no equilibrium process with sea water.

Fossil corals have been successfully dated using U-series, and from these ages past sea level was estimated. However, unlike giant clams, corals are prone to diagenetic alteration due to the more porous structure. For this first reason, multiple samples are needed in order to obtain robust and reproducible results. This sampling strategy is also necessary in coastal areas with low uplift rates were polycyclic terraces exists, where more than one period can be identified in the same reef unit or sequence.

Another complication encountered was when a sample has an estimated 100 % of aragonite content (well preserved fossil) does not ensure a result in closed-system evolution with sea water. However, open-system age results presented same age result than closed-system, for this reason we use some open-system ages as reference.

From this process it was possible to identify different periods: the early MIS-5 (last interglacial), the MIS-7 (penultimate interglacial) and the MIS-6e interstadial. At the same time relative sea level was estimated for this periods, and used it to extract the sea level component of $\delta^{18}O$ in Tridacnidae fossils. The Holocene was also identified, but there not still reconstructions for giant clam shells of this period on the studied area.

Additional stratigraphy and sequential dating in following a vertical profile in a same area will be necessary in SE Sulawesi in order to identify the MIS-5e highstand interglacial, and obtain seasonal records for this period. But also other past interglacials (MIS-9 and 11). It could be interesting to apply in the future other dating techniques on shells and corals as ^{231}Pa (protactinium), electron spin resonance and complementary scanning test as the amino acid racemization.

PALEOCLIMATE RECONSTRUCTIONS

To summarize the fossil results from the last two interglacial (MIS-5 and 7) reconstructions, important modifications in the hydrological cycle have been identified, with important differences in mean temperature and seasonal changes. The monsoon activity is expected to be affected by changes in sea level. In this study, the early MIS-5 and the MIS-7 presents lower sea levels, relative to the modern level. Mean climatic conditions for both past periods appears cold and drier in respect to modern conditions. The amplitude of the seasonal cycle is also reduced during these periods, reflecting weakened monsoon activity. Interannual variation was also compared between fossil and modern conditions with similar amplitudes in the early MIS-5 and reduced variation in the MIS 7.

Although ENSO impacts the study area and is responsible for interannual variation in the WPWP region, it does not seem to explain the entire interannual variation observed in the SST/SSS anomalies on the studied area. Which are recorded in the $\delta^{18}O$ signal for the last 35 years. To better

constrain and quantify ENSO frequencies on past periods, more high resolution and interannual fossil records will be necessary to provide a representative time window.

The trace element results, Mg/Ca derived from fossil samples exhibit taxonomic effects, which are commonly observed in studies on other bivalve species. The longer lived *T. gigas* seems to be associated with higher shell Mg/Ca during the later adult slow growing part of the shell. A pattern is emerging where there seems to be a relationship between growth and Mg/Ca which should be explored further in the future. A possibility for future research will be to remove the growth effect on *T. gigas* species for example, and to test the equation calibrated in the modern *T. squamosa*. Shell Ba/Ca seem less affected by biological and species effects, higher Ba/Ca values are recorded in fossil samples compared to modern and may be reflected an increase in productivity, because in the region coastal upwelling and primary productivity is higher during colder/driest season.

The $\delta^{13}C$ signal appears also as a possible indirect proxy for salinity and/or primary productivity in this area, because the signal in fossils, as in modern samples, present high values during the dry season, and mean fossil $\delta^{13}C$ is higher than modern values.

Supplementary *in situ* and/or laboratory experiments will be necessary to advance in the interpretation and application of these proxies in paleo-environmental reconstructions. Perform biochemical analyses of live specimen to better understand the geochemical results and reconstruct the environment in Tridacnidae and other species of marine bivalve's shells.

This work represents a starting point to enlarge the study of late Pleistocene with high resolution information for SE Sulawesi, because older highstands have been identified in this area. And it could be considered as one of the most complete Quaternary reef sequences in world.

References

Accordi, G., Brilli, M., Carbone, F., Voltaggio, M., 2010. The raised coral reef complex of the Kenyan coast: *Tridacna gigas* U-series dates and geological implications. Journal of African Earth Sciences, 58, 97-114.

Adams, T., Dalzell, P., Ledua, E., 1999. Ocean resources. In M. Rapaport (Ed.), The Pacific Islands: Environment and society (pp. 366–381). Honolulu: Bess Press.

Adkins, J. F., McIntyre, K., Schrag, D. P., 2002. The salinity, temperature and $\delta^{18}O$ of the glacial deep ocean. Science 298, 1769-1773.

Aharon, P., 1983. 40,000-Yr Isotope climatic record from raised coral reefs in New Guinea. Nature, 304, 720-723.

Aharon, P., Chappell, J., 1986. Oxygen isotopes, sea level changes and the temperature history of a coral reef environment in New Guinea over the last 105 years. Palaeogeogr. Palaeoclimatol. Palaeoecol., 56, 337-379.

Aldrian, E., Susanto, R., 2003. Identification of three dominant rainfall regions within Indonesia and their relationship to sea surface temperature. Int. J. Climatol. 23, 1435-1452.

Ali, J., J. Milsom, E. Finch, and B. Mubroto., 1996. SE Sundaland accretion: palaeomagnetic evidence of large Plio-Pleistocene thin-skin rotations in Buton. Geological Society, London, Special Publications, 106, 431-443.

Ali, J.R., Hall, R., 1995. Evolution of the boundary between the Philippine Sea Plate and Australia: palaeomagnetic evidence from eastern Indonesia. Tectonophysics 251, 251-275.

Andersen, M. B., Stirling, C. H., Potter, E.-K., Halliday, A. N., Blake, S. G., McCulloch, M. T., Ayling, B. F., O'Leary, M. J., 2008. High-precision U-series measurements of more than 500,000 year old fossil corals. Earth Planet. Sci. Lett. 265, 229-245.

Andersen, M. B., Stirling, C. H., Potter, E.-K., Halliday, A. N., Blake, S. G., McCulloch, M. T., Ayling, B. F., O'Leary, M. J., 2010. The timing of sea-level high-stands during Marine Isotope Stages 7.5 and 9: constraints from the uranium-series dating of fossil corals from Henderson Island. Geochim. Cosmochim. Acta 74, 3598-3620.

As-syakur, A. R., Adnyana, I-W. S., Mahendra, M. S., Arthana, I-W., Merit I-N., Kasa I-W., Ekayanti N. W., Nuarsa I-W., Sunarta, I-N., 2014. Observation of spatial patterns on the rainfall response to ENSO and IOD over Indonesia using TRMM Multisatellite Precipitation Analysis (TMPA). Int. J. Climatol. DOI: 10.1002/joc.3939.

Aubert, A., Lazareth, C., Cabioch, G., Boucher, H., Yamada, T., Iryu, Y., Farman, R., 2009. The tropical giant clam Hippopus hippopus shell, a new archive of environmental conditions as revealed by sclerochronological and δ18O profiles. Coral Reefs, 28, 989-998.

Audley-Charles, M.G., Ballantyne, P.D., Hall, R., 1988. Mesozoic-Cenozoic rift-drift sequence of Asian fragments from Gondwanaland. Tectonophysics155, 317-330.

Australian government bureau of meteorology. http://www.bom.gov.au/?ref=logo

Ayling, B., Chappell, J., Gagan, M., McCulloch, M., 2015. ENSO variability during MIS 11 (424–374 ka) from *Tridacna gigas* at Huon Peninsula, Papua New Guinea. Earth and Planetary Science Letters, 431, 236-246.

Ayling, B., Eggins, S., McCulloch, M., Chappell, J., Grün, R., Mortimer, G., 2017. Uranium uptake history, open-system behaviour and uranium-series ages of fossil *Tridacna gigas* from Huon Peninsula, Papua New Guinea. Geochimica Et Cosmochimica Acta. In press.

Banner, J.L., Wasserburg, G.J., Chen, J.H. and Humphrey, J.D., 1991. Uranium-series evidence on diagenesis and hydrology in Pleistocene carbonates on Barbados, West Indies. Earth Planet. Sci. Lett. 107, 129-137.

Barber, A.J., Crow, M.J., 2003. An evaluation of plate tectonic models for the development of Sumatra. Gondwana Research 6, 1-28.

Bard, E., Antonioli, F., Silenzi, S., 2002. Sea-level during the penultimate interglacial period based on submerged stalagmite from Argentarola Cave (Italy). Earth and Planetary Science Letters 196, 135–146.

Bard, E., Fairbanks, R.G., Hamelin, B., Zindler, A., Hoang, C.T., 1991. Uranium-234 anomalies in corals older than 150,000 years. Geochim. Cosmochim. Acta 55, 2385-2390.

Bard, E., Hamelin, B., Fairbanks, R. G., 1990. U–Th ages obtained by mass spectrometry in corals from Barbados: sea level during the past 130,000 years. Nature 346, 456-458.

Bard, E., Jouannic, C., Hamelin, B., Pirazzoli, P., Arnold, M., Faure, G., Sumosusastro, Syaefudin, P., 1996. Pleistocene sea levels and tectonic uplift based on dating of corals from Sumba Island, Indonesia. Geophysical Research Letters, 23, 1473-1476.

Bar-Matthews, M., Wasserburg, G. J., Chen, J. H., 199. Diagenesis of fossil coral skeletons: correlation between trace elements, textures, and $^{234}U/^{238}U$. Geochim. Cosmochim. Acta 57, 257-276.

Batenburg, S.J., Reichart, G.-J., Jilbert T., Janse M., Wesselingh F.P., Renema, W., 2011. Interannual climate variability in the Miocene: high resolution trace element and stable isotope ratios in giant clams. Palaeogeogr. Palaeoclimatol. Palaeoecol., 306 (1-2), 75-81.

Beaufort, L., de Garidel-Thoron, T., Linsley Braddock, K., Oppo, D.W., Buchet, N., 2003. Biomass burning and oceanic primary production estimates in the Sulu Sea area over the last 380 kyr and the East Asian monsoon dynamics. Marine Geology 201, 53– 65.

Berger, A., Loutre, M.F., Gallée, H., 1998. Sensitivity of the LLN climate model to the astronomical and CO2 forcings over the last 200 ky. Clim. Dyn., 14, 615-629.

Berger, W., 1981. Oxygen and carbon isotopes in foraminifera: An introduction. Palaeogeography, Palaeoclimatology, Palaeoecology, 33, 3-7.

bin Othman, A.S., Goh, G.H.S., Todd, P.A., 2010. The distribution and status of giant clams (family Tridacnidae) – a short review. Raffles Bull. Zool., 58, 103-111.

Bintanja, R., van de Wal, R. S. W., Oerlemans, J., 2005. Modelled atmospheric temperatures and global sea levels over the past million years. Nature 437, 125-128.

Bjerknes, J., 1969. Atmospheric teleconnections from the equatorial Pacific. Monthly Weather Review 97, 163-172.

Blanchon, P., Eisenhauer, A., Fietzke, J., Liebetrau, V., 2009. Rapid sea-level rise and reef back-stepping at the close of the last interglacial highstand. Nature, 458, 881-884.

Boening, C., Willis, J. K., Landerer, F. W., Nerem, R. S., Fasullo, J., 2012. The 2011 La Niña: So strong, the oceans fell. Geophys. Res. Lett. 39, L19602.

Bond, G., Lotti, R., 1995. Iceberg Discharges into the North Atlantic on Millennial Time Scales During the Last Glaciation. Science, 267:1005-1010.

Bourdon, B., Turner, S.P., Henderson, G.M., Lundstrom, C.C., 2003. Introduction to U-Series Geochemistry. In: Bourdon, B., Henderson, G.M., Lundstrom, C.C. & Turner, S.P. (Eds.): Uranium-series Geochemistry: 1-21; Washington, DC (Mineralogical Society of America).

Broecker, W., Henderson, G., 1998. The sequence of events surrounding Termination II and their implications for the cause of glacial-interglacial CO_2 changes. Paleoceanography, 13, 352-364.

Cabioch, G., 2011. In: David Hopley (ed.). Encyclopedia of Modern Coral Reefs, 373-378. DOI 10.1007/978-90-481-2639-2.

Cai, W., Wang, G., Santoso, A., McPhaden, M., Wu, L., Jin, F., Timmermann, A., Collins, M., Vecchi, G., Lengaigne, M., England, M., Dommenget, D., Takahashi, K., Guilyardi, E., 2015.

Increased frequency of extreme La Niña events under greenhouse warming. Nature Clim. Change. 5 (2), 132-137.

Cal-Pal software: http://www.calpal-online.de/

Calvert, S.J., 2000. The Cenozoic evolution of the Lariang and Karama basins, Sulawesi. Proceedings Indonesian Petroleum Association, 27th Annual Convention, pp. 505-511.

Candy, I., White, T., Elias, S., 2016. How warm was Britain during the Last Interglacial? A critical review of Ipswichian (MIS 5e) palaeotemperature reconstructions. Journal of Quaternary Science, 31, 2910.

Cane, M. & Clement, A., 1999. Mechanisms of Global Climate Change at Millennial Time Scales, AGU Geophysical Monograph 112 (eds Clark, P., Webb, R. & Keigwin, L.) 373–383 (American Geophysical Union, Washington DC,).

Carré, M., Bentaleb, I., Bruguier, O., Ordinola, E., Barrett, N., Fontugne, M., 2006. Calcification rate influence on trace element concentrations in aragonitic bivalve shells: Evidences and mechanisms. Geochim. Cosmochim. Ac. 70, 4906-4920.

Carré, M., Sachs, J., Purca, S., Schauer, A., Braconnot, P., Falcon, R., Julien, M., Lavallee, D., 2014. Holocene history of ENSO variance and asymmetry in the eastern tropical Pacific. Science, 345, 1045-1048.

Cathles, L.M., 1975. The Viscosity of the Earth's Mantle. Princeton University Press, Princeton, NJ, 386pp. In: Lambeck, K., Purcell, A., Johnston, P., Nakada, M., and Yokoyama, Y. 2003. Water-load definition in the glacio-hydro-isostatic sea-level equation. Quaternary Science Reviews, 22: 309-318.

Chappell, J., Ota, Y., Berryman, K., 1996. Late quaternary coseismic uplift history of Huon Peninsula, Papua New Guinea. Quaternary Science Reviews, 15, 7-22.

Chappell, J., Shackleton, N.J., 1986. Oxygen isotopes and sea level. Nature 324, 137-140.

Chen, J.H., Curran, H.A., White, B. & Wasserburg, G.J., 1991. Precise chronology of the last interglacial period: ^{234}U-^{230}Th data from fossil coral reefs in the Bahamas. GSA Bulletin, 103, 82-97.

Chen, J.H., Edwards, R.L., Wasserburg, G.J., 1986. ^{238}U-^{234}U-^{232}Th in seawater. – Earth and Planetary Science Letters, 80, 241-251.

Cheng, H., Edwards, R.L., Hoff, J., Gallup, C.D., Richards, D.A., Asmerom, Y., 2000. The halflives of uranium-234 and thorium-230. – Chemical Geology, 169, 17-33.

Cheng, R.L., Edwards, M.T., Murrell, T.M. Benjamin, 1998. Uranium–thorium– protactinium dating systematics, Geochim. Cosmochim. Acta 62, 3437-3452.

Clement, A.C., Hall, A., Broccoli, A.J., 2004. The importance of precessional signals in the tropical climate. Clim. Dyn. 22, 327-341.

Cloern, J., Foster, S., Kleckner, A., 2014. Phytoplankton primary production in the world's estuarine-coastal ecosystems. Biogeosciences 11, 2477-2501.

Cobb, K., J. Adkins, J. Partin, and B. Clark. 2007. Regional-scale climate influences on temporal variations of rainwater and cave dripwater oxygen isotopes in northern Borneo. Earth And Planetary Science Letters, 263:207-220.

Cobb, K.M., Charles, C.D., Cheng, H., Kastner, M., Edwards, R.L., 2003. U/Th-dating living and young fossil corals from the central tropical Pacific. Earth and Planetary Science Letters, 210: 91-103.

Collins, M., 2000. The El Niño–Southern Oscillation in the Second Hadley Centre Coupled Model and Its Response to Greenhouse Warming. J. Climate., 13, 1299-1312.

Conroy, J., Noone, D., Cobb, K., Moerman, J., Konecky, B., 2016. Paired stable isotopologues in precipitation and vapor: A case study of the amount effect within western tropical Pacific storms. J. Geophys. Res. Atmos. 121, 3290-3303.

Copland, J .W., Lucas, J.S., 1988. Giant clams in Asia and the Pacific. ACIAR Monograph No. 9, 274 p.

Corrège, T., Delcroix, T., Rècy, J., Beck, W., Cabioch, G., Le Cornec, F., 2000. Evidence for stronger El Niño-Southern Oscillation (ENSO) events in a Mid-Holocene massive coral. Paleoceanography 15, 465-470.

Cross, T.S., Cross, B.W., 1983. U, Sr and Mg in Holocene and Pleistocene corals *A. palmata* and *M. annularis*. Journal of Sedimentary Petrology, 53, 587-594.

Dang, H., Jian, Z., Kissel, C., Bassinot, F., 2015. Precessional changes in the western equatorial Pacific Hydroclimate: A 240 kyr marine record from the Halmahera Sea, East Indonesia. Geochemistry, Geophysics, Geosystems, 16, 148-164.

Dansgaard, W., 1964. Stable isotopes in precipitation. Tellusa.

D'Arrigo, R., Wilson, R., Palmer, J., Krusic, P., Curtis, A., Sakulich, J., Bijaksana, S., Zulaikah, S., Ngkoimani, L. O., Tudhope, A., 2006. The reconstructed Indonesian warm pool sea surface temperatures from tree rings and corals: Linkages to Asian monsoon drought and El Niño–Southern Oscillation. Paleoceanography, 21, PA3005.

D'Arrigo, R., Wilson, R., Palmer, J., Krusic, P., Curtis, A., Sakulich, J., Bijaksana, S., Zulaikah, S., Ngkoimani, L. O., Tudhope, A., 2006. The reconstructed Indonesian warm pool sea surface temperatures from tree rings and corals: Linkages to Asian monsoon drought and El Niño–Southern Oscillation. Paleoceanography, 21, PA3005.

Davidson, J.W., 1991. The geology and prospectivity of Buton Island, S.E. Sulawesi, Indonesia, Proceedings of Indonesian Petroleum Association, 20th Annual Convention, 209-233.

de Boer, B., van de Wal, R., Lourens, L., Bintanja, R., 2012. Transient nature of the Earth's climate and the implications for the interpretation of benthic records. Palaeogeography, Palaeoclimatology, Palaeoecology, 335-336, 4-11.

De Deckker, P., Tapper, N. J., van der Kaars, S., 2002. The status of the Indo-Pacific Warm Pool and adjacent land at the Last Glacial Maximum. Global Planet. Change, 35, 25-35.

De Smet, M.E.M., Fortuin, A.R., Tjokrosapoetro, S., J.E. Van Hinte., 1989. Late Cenozoic Vertical Movement of Non-volcanic Islands in the Banda-Arc Area, Netherlands Journal of Sea Research, 24(2/3), 263-275.

Delanghe, D., Bard, E., Hamelin, B., 2002. New TIMS constraints on the uranium-238 and uranium- 234 in seawaters from the main ocean basins and the Mediterranean Sea. – Marine Chemistry, 80, 79-93.

Delaygue, G., Bard, E., Rollion, C., Jouzel, J., Stiévenard, M., Duplessy, J., Ganssen, G., 2001. Oxygen isotope/salinity relationship in the northern Indian Ocean. J. Geophys. Res. Oceans. 106:4565-4574.

Denniston, R., C. Ummenhofer, A. Wanamaker, M. Lachniet, G. Villarini, Y. Asmerom, V. Polyak, K. Passaro, J. Cugley, D. Woods, W. Humphreys., 2016. Expansion and Contraction of the Indo-Pacific Tropical Rain Belt over the Last Three Millennia. Scientific Reports, 6.

Denniston, R., Wyrwoll, K., Asmerom, Y., Polyak, V., Humphreys, W., Cugley, J., Woods, D., LaPointe, Z. Peota, J., Greaves, E., 2013. North Atlantic forcing of millennial-scale Indo-Australian monsoon dynamics during the Last Glacial period. Quaternary Science Reviews, 72, 159-168.

Desprat, S., Sánchez Goñi, M., Turon, J., Duprat, J., Malaizé, B., Peypouquet, J., 2006. Climatic variability of Marine Isotope Stage 7: direct land–sea–ice correlation from a multiproxy analysis of a north-western Iberian margin deep-sea core. Quaternary Science Reviews, 25, 1010-1026.

Di Nezio, P. N., Timmermann, A., Tierney, J. E., Jin, F.-F., Otto-Bliesner, B., Rosenbloom, N., Mapes, B., Neale, R., Ivanovic, R. F., Montenegro., A., 2016. The climate response of the Indo-Pacific warm pool to glacial sea level. Paleoceanography, 31, 866-894.

Dodd, J. R., 1967. Magnesium and Strontium in Calcareous Skeletons: A Review Journal of Paleontology., 41(6), 1313-1329.

Douville, E., Sallé, E., Frank, N., Eisele, M., Pons-Branchu, E., Ayrault, S.., 2010. Rapid and accurate U-Th dating of ancient carbonates using inductively coupled plasma-quadrupole mass spectrometry. Chemical Geology 272(1-4), 1-11.

Driscoll, R., 2014b. Paleo ENSO reconstructions of the Holocene and Last Glacial Period. PhD Thesis.

Driscoll, R., Elliot, M., Russon, T., Welsh, K., Yokoyama, Y., Tudhope, A., 2014. ENSO reconstructions over the past 60 ka using giant clams (*Tridacna* sp.) from Papua New Guinea. Geophys. Res. Lett. 41 (19), 6819-6825.

Drysdale, R., Hellstrom, J., Zanchetta, G., Fallick, A., Sanchez Goni, M., Couchoud, I., McDonald, J. et al., 2009. Evidence for Obliquity Forcing of Glacial Termination II. Science, 325, 1527-1531.

Dumoulin, J-P., Comby-Zerbino, C., Delqué-Količ, E., Moreau, C., Caffy, I., Hain, S., Perron, M., Thellier, B., Setti, V., Berthier, B., Beck, L., 2017. Status report on sample preparation protocols developed at the LMC14 Laboratory, Saclay, France: from sample collection to ^{14}C AMS measurement. Radiocarbon, 1-14.

Dutton, A., Carlson, A. E., Long, A. J., Milne, G. A., Clark, P. U., DeConto, R., Horton, B. P., Rahmstorf, S., Raymo, M. E., 2015. Sea-level rise due to polar ice-sheet mass loss during past warm periods. Science, 349, 6244.

Dutton, A., Carlson, A. E., Long, A. J., Milne, G. A., Clark, P. U., DeConto, R., Horton, B. P., Rahmstorf, S., Raymo, M. E., 2015. Sea-level rise due to polar ice-sheet mass loss during past warm periods. Science 349, 6244.

Dutton, A., E. Bard, F. Antonioli, T. Esat, K. Lambeck, M. McCulloch., 2009. Phasing and amplitude of sea-level and climate change during the penultimate interglacial. Nature Geoscience, 2:355-359.

Dutton, A., Lambeck, K., 2012. Ice Volume and Sea Level During the Last Interglacial. Science, 337, 216-219.

Dutton, A., Webster, J., Zwartz, D., Lambeck, K., Wohlfarth, B., 2015. Tropical tales of polar ice: evidence of Last Interglacial polar ice sheet retreat recorded by fossil reefs of the granitic Seychelles islands. Quaternary Science Reviews, 107, 182-196.

Eagle, R. A., Eiler, J. M., Tripati, A. K., Ries, J. B., Freitas, P. S., Hiebenthal, C., Wanamaker Jr., A. D., Taviani, M., Elliot, M., Marenssi, S., Nakamura, K., Ramirez, P., and Roy, K., 2013. The influence of temperature and seawater carbonate saturation state on 13C–18O bond ordering in bivalve mollusks, Biogeosciences, 10, 4591-4606.

Edwards, R.L., Chen, J.H., Wasserburg, G.J., 1986. ^{238}U-^{234}U-^{230}Th-^{232}Th systematics and the precise measurement of time over the past 500,000 years. – Earth and Planetary Science Letters, 81, 175-192.

Elliot, M., Welsh, K., Chilcott, C., McCulloch, M., Chappell, J., Ayling, B., 2009. Profiles of trace elements and stable isotopes derived from giant long-lived *Tridacna gigas* bivalves: Potential applications in paleoclimate studies. Palaeogeogr. Palaeoclimatol. Palaeoecol. 280 (1-2), 132-142.

Emile-Geay, J., K. Cobb, M. Carré, P. Braconnot, J. Leloup, Y. Zhou, S. Harrison, T. Corrège, H. McGregor, M. Collins, R. Driscoll, M. Elliot, B. Schneider, A. Tudhope., 2015. Links between tropical Pacific seasonal, interannual and orbital variability during the Holocene. Nature Geoscience, 9, 168-173.

Emiliani, C., 1955. Pleistocene temperatures. Journal of Geology, 63, 538-578.

EPICA community members (2006) One-to-one coupling of glacial climate variability in Greenland and Antarctica. Nature 444:195–198

Esat, T., 1999. Rapid Fluctuations in Sea Level Recorded at Huon Peninsula During the Penultimate Deglaciation. Science, 283, 197-201.

Esat, T.M., Yokoyama, Y., 2006. Variability in the uranium isotopic composition of the oceans over glacial-interglacial timescales. Geochimica et Cosmochimica Acta, 70, 4140-4150.

Fairbanks, R., Evans, M., Rubenstone, J., Mortlock, R., Broad, K., Moore, M., Charles, C., 1997. Evaluating climate indices and their geochemical proxies measured in corals. Coral Reefs 16, 93-100.

Feng, M., Benthuysen, J., Zhang, N., Slawinski, D., 2015. Freshening anomalies in the Indonesian throughflow and impacts on the Leeuwin Current during 2010–2011. Geophys. Res. Lett. 42, 8555-8562.

Ffield, A., Vranes, K., Gordon, A., Dwi Susanto, R., Garzoli, S., 2000. Temperature variability within Makassar Strait. Geophys. Res. Lett. 27, 237-240.

Fortuin, A. R., De Smet, M.E.M., Hadiwasastra, S., van Marle, L.J., Toelstra, S.R., Tjokrosapoetro, S., 1990. Late Cenozoic sedimentary and tectonic history of south Buton, Indonesia. Journal of Southeast Asian Earth Science. 4, 107-124.

Fowell, S., Sandford, K., Stewart, J., Castillo, K., Ries, J., Foster, G., 2016. Intrareef variations in Li/Mg and Sr/Ca sea surface temperature proxies in the Caribbean reef-building coral *Siderastrea siderea*. Paleoceanography, 31, 1315-1329.

Freitas, P., Clarke, L., Kennedy, H., Richardson, C.A., Abrantes, F., 2005. Mg/Ca, Sr/Ca and stable-isotope ($\delta^{18}O$ and $\delta^{13}C$) ratio profiles from the fan mussel *Pinna nobilis*: seasonal records and temperature relationships. Geochem. Geophys. Geosyst. 6 (4), Q04D14. doi:10.1029/2004GC000872.

Friedrich, T., Timmermann, A., Tigchelaar, M., Elison Timm, O., Ganopolski, A., 2016. Nonlinear climate sensitivity and its implications for future greenhouse warming. Science Advances, 2, e1501923-e1501923.

Gallup, C., 2002. Direct Determination of the Timing of Sea Level Change During Termination II. Science, 295, 310-313.

Gertisser, R., Keller, J., 2003. Trace Element and Sr, Nd, Pb and O Isotope Variations in Medium-K and High-K Volcanic Rocks from Merapi Volcano, Central Java, Indonesia: Evidence for the Involvement of Subducted Sediments in Sunda Arc Magma Genesis. J. Petrology 44 (3), 457-489.

Gieskes, W., Kraay, G., Nontji, A., Setiapermana, D., Sutomo., 1990. Monsoonal differences in primary production in the eastern Banda Sea (Indonesia). Neth. J. Sea Res. 25 (4), 473-483.

Gillikin, D. P., Lorrain, A., Paulet, Y.-M., André, L., Dehairs, F., 2008. Synchronous barium peaks in high-resolution profiles of calcite and aragonite marine bivalve shells. Geo-Mar. Lett., 28, 351-358.

Gillikin, D., Dehairs, F., Lorrain, A., Steenmans, D., Baeyens, W., André, L., 2006. Barium uptake into the shells of the common mussel (*Mytilus edulis*) and the potential for estuarine paleo-chemistry reconstruction. Geochim. Cosmochim. Acta 70, 395-407.

Gillikin, D., Lorrain, A., Navez, J., Taylor, J., André, L., Keppens, E., Baeyens, W., Dehairs, F., 2005. Strong biological controls on Sr/Ca ratios in aragonitic marine bivalve shells. Geochem. Geophys. Geosyst. 6, Q05009. doi:10.1029/2004GC000874.

Godfrey, J. S., 1996. The effect of the Indonesian Throughflow on ocean circulation and heat exchange with the atmosphere: A review, J. Geophys. Res., 101(C5), 12,217-12,237.

Gomez, N., Mitrovica, J.X., Tamisiea, M.E., Clark, P.U., 2010. A new projection of sea level change in response to collapse of marine sectors of the Antarctic Ice Sheet. Geophys. J. Int. 180, 623-634.

Gordon, A. L., Susanto, R. D., Vranes, K., 2003. Cool Indonesian Throughflow as a consequence of restricted surface layer flow, Nature, 425, 824-828.

Griffiths, C. L., Klump, D. W., 1996. Relationships between size, mantle area and zooxanthellae numbers in five species of giant clam (Tridacnidae). Mar. Ecol. Prog. Ser. 137, 139-147.

Griffiths, M., R. Drysdale, M. Gagan, J. Zhao, L. Ayliffe, J. Hellstrom, W. Hantoro, S. Frisia, Y. Feng, I. Cartwright, E. Pierre, M. Fischer, B. Suwargadi., 2009. Increasing Australian–Indonesian monsoon rainfall linked to early Holocene sea-level rise. Nature Geoscience, 2, 636-639.

Grossman, E.L., Ku T-L., 1986. Oxygen and carbon isotope fractionation in biogenic aragonite: Temperature effects. Chem. Geol. Isot. Geosci. Sect. 59, 59-74.

Gutman, G., Csiszar, I., Romanov, P., 2000. Using NOAA/AVHRR Products to Monitor El Niño Impacts: Focus on Indonesia in 1997–98. Bull. Amer. Meteor. Soc., 81(6), 1189-1206.

Habibi, A., Setiawan, R.Y., Zuhdy, A.Y., 2010. Wind-driven coastal upwelling along south of Sulawesi island. Indonesian journal of marine sciences 15 (2), 113-118.

Haile, N.S., 1978. Reconnaissance palaeomagnetic results from Sulawesi Indonesia, and their bearing on palaeogeographic reconstruction. Tectonophysics, 46, 77–85.

Hall, R., 2002. Cenozoic geological and plate tectonic evolution of SE Asia and the SW Pacific: computer-based reconstructions, model and animations. J Asian Earth Sci., 20 (4), 353-431.

Hall, R., and Wilson, M.E.J., 2000. Neogene sutures in eastern Indonesia. Journal of Asian Earth Sciences, 18, 781-808.

Ham, Y., Jeong, Y. And Kug, J., 2015. Changes in Independency between Two Types of El Niño Events under a Greenhouse Warming Scenario in CMIP5 Models. Journal of Climate, 28, 7561-7575.

Hamada, J., Yamanaka, M. D., Matsumoto, J., Fukao, S., Winarso, P. A., Sribimawati, T., 2002. Spatial and Temporal Variations of the Rainy Season over Indonesia and their Link to ENSO. J. Meteor. Soc. Japan. 80 (2), 285- 310.

Hamelin, B., Bard, E., Zindler A., Fairbanks, R. G., 1991. $^{234}U/^{238}U$ mass spectrometry of corals: how accurate is the U–Th age of the last interglacial period? Earth Planet. Sci. Lett. 106, 169-180.

Hamilton, W., 1979. Tectonics of the Indonesian region. U.S.G.S. Prof. Paper, 1078, 345pp.

Hammer, Ø., Harper, D.A.T., and P. D. Ryan, 2001. PAST: Paleontological Statistics Software Package for Education and Data Analysis. Palaeontol. Electronica 4(1), 9.

Harzhauser, M., Mandic, O., Piller, W. E., Reuther, M., Kroh, A., 2008. Tracing back the origin of the Indo-Pacific mollusc fauna: Basal Tridacninae from the Oligocene and Miocene of the Sultanate of Oman. Palaeontology, 51 (1), 199-213.

Hatch, M. B. A., Schellenberg, S. A., Carter, M. L., 2012. Ba/Ca variations in the modern intertidal bean clam *Donax gouldii*: an upwelling proxy? Palaeogeogr. Palaeoclimatol. Palaeoecol. 373, 98-107.

Hawkins, A., D. Klumpp., 1995. Nutrition of the giant clam *Tridacna gigas* (L.). II. Relative contributions of filter-feeding and the ammonium-nitrogen acquired and recycled by symbiotic alga towards total nitrogen requirements for tissue growth and metabolism. Journal Of Experimental Marine Biology And Ecology, 190, 263-290.

Hay, C., Mitrovica, J., Gomez, N., Creveling, J., Austermann, J. And E. Kopp, R., 2014. The sea-level fingerprints of ice-sheet collapse during interglacial periods. Quaternary Science Reviews, 87, 60-69.

Hay, C., Morrow, E., Kopp, R., Mitrovica, J., 2013. Estimating the sources of global sea level rise with data assimilation techniques. Proceedings Of The National Academy Of Sciences, 110, 3692-3699.

Haylock, M., McBride, J., 2001. Spatial coherence and predictability of indonesian wet season rainfall. J. Clim. 14, 3882-3887.

Hays, J.D., Imbrie, J., Shackleton, N.J., 1976. Variations in the earth's orbit: pacemaker of the ice ages. Science 194, 1121-1132.

Hearty, P., Hollin, J., Neumann, A., O'Leary, M., McCulloch, M., 2007. Global sea-level fluctuations during the Last Interglaciation (MIS 5e). Quaternary Science Reviews, 26, 2090-2112.

Helmle, K. P., Dodge, R. E., 2011. In: David Hopley (ed.). Encyclopedia of Modern Coral Reefs, 958-966. DOI 10.1007/978-90-481-2639-2.

Henderson, G.M., 2002. Seawater ($_{234}U/_{238}U$) during the last 800 thousand years. Earth and Planetary Science Letters, 199: 97-110.

Henderson, G.M., 2006. Caving in to new chronologies. Science 313, 620-622.

Hendon, H., 2003. Indonesian rainfall variability: Impacts of ENSO and Local Air-Sea Interaction. J. Clim. 16 (11), 1775-1790.

Hendon, H., Lim, E., Arblaster, J., Anderson, D., 2014. Causes and predictability of the record wet east Australian spring 2010. Clim. Dyn. 42, 1155-1174.

Hernawan, U., 2012. Taxonomy of Indonesian giant clams (Cardiidae, Tridacninae). Biodiversitas 13 (3), 118-123.

Higuera-Ruiz, R., Elorza, J., 2009. Biometric, microstructural, and high-resolution trace element studies in *Crassostrea gigas* of Cantabria (Bay of Biscay, Spain): Anthropogenic and seasonal influence. Estuar. Coast. Shelf Sci. 82, 201-213.

Hirose, E., Iwai K., Maruyama, T., 2006. Establishment of the photosymbiosis in the early ontogeny of three giant clams. Mar. Biol., 148, 551-558.

Holbourn, A., Kuhnt, W., Kawamura, H., Jian, Z., Grootes, P., Erlenkeuser, H., Xu, J., 2005. Orbitally-paced paleoproductivity variations in the Timor Sea and Indonesian Throughflow variability during the last 460-ky. Paleoceanography 20, PA3002. doi:10.1029/2004PA001094.

Holden, N.E., 1990. Total half-lives for selected nuclides. Pure & Applied Chemistry, 62: 941-958.

Hori, M., Sano, Y., Ishida, A., Takahata, N., Shirai, K. And Watanabe, T., 2015. Middle Holocene daily light cycle reconstructed from the strontium/calcium ratios of a fossil giant clam shell. Scientific Reports, 5.

Huang, E., Tian, J., Liu, J., 2015. Dynamics of the Australian–Indonesian monsoon across Termination II: Implications of molecular-biomarker reconstructions from the Timor Sea. Palaeogeography, Palaeoclimatology, Palaeoecology, 423, 32-43.

Hudson, H., Shinn, E. A., Halley, R. B., Lidz, B., 1976. Sclerochronology: a tool for interpreting past environments. Geology, 4, 361–364.

Hwang, Y.-T., Frierson, D. M. W., 2013. Link between the double-Intertropical Convergence Zone problem and cloud biases over the Southern Ocean. Proc. Natl. Acad. Sci. U.S.A. 110 (13), 4935-4940.

Imbrie, John D; Hays, James D; Martinson, Douglas G; McIntyre, Andrew; Mix, Alan C; Morley, Joseph J; Pisias, Nicklas G; Prell, Warren L; Shackleton, Nicholas J., 1984. The orbital theory

of Pleistocene climate: support from a revised chronology of the marine d18O record. In: Berger, A L, et al. (eds.), Milankovitch and Climate. 1: Dordrecht (D. Reidel Publishing Company), 269-305,

International Union for Conservation of Nature (IUCN), 2017. Red List of Threatened Species. http://www.iucnredlist.org/details/22140/0

IUPAC. Compendium of Chemical Terminology, 2nd ed. (the "Gold Book"). Compiled by A. D. McNaught and A. Wilkinson. Blackwell Scientific Publications, Oxford (1997). XML on-line corrected version: http://goldbook.iupac.org (2006) created by M. Nic, J. Jirat, B. Kosata; updates compiled by A. Jenkins. ISBN 0-9678550-9-8. https://doi.org/10.1351/goldbook.

Ivanova, E., Beaufort, L., Vidal, L., Kucera, M., 2012. Precession forcing of productivity in the Eastern Equatorial Pacific during the last glacial cycle. Quaternary Science Reviews, 40, 64-77.

Jaffey, A.H., Flynn, K.F., Glendenin, L.E., Bentley, W.C., Essling, A.M., 1971. Precision Measurement of Half-Lives and Specific Activities of 235U and 238U. Physical Reviews, C4, 1889-1906.

Jameson, S. C., 1976. Early Life History of the Giant Clams *Tridacna crocea* Lamarck, *Tridacna maxima* (Röding), and *Hippopus hippopus* (Linnaeus). Pacific Science 30 (3), 219-233.

Jian, Z., Huang, B., Kuhnt, W., Lin, H., 2001. Late Quaternary Upwelling Intensity and East Asian Monsoon Forcing in the South China Sea. Quaternary Research, 55: 363-370.

Jo, K., Woo, K., Yi, S., Yang, D., Lim, H., Wang, Y., Cheng, H., Edwards, R., 2014. Mid-latitude interhemispheric hydrologic seesaw over the past 550,000 years. Nature, 508, 378-382.

Jochum, K.P., Scholz, D., Stoll B., Weis, U., Wilson, S.A., Yang, Q., Schwalb, A., Börner, N., Jacob, D.E., Andreae., M.O., 2012. Accurate trace element analysis of speleothems and biogenic calcium carbonates by LA-ICP-MS. Chem. Geol. 318, 31-44.

Jones, D., Williams, D., Romanek, C., 1986. Life History of Symbiont-Bearing Giant Clams from Stable Isotope Profiles. Science 231, 46-48.

Jouzel, J. et al., 2007. Orbital and millennial Antarctic climate variability over the past 800,000 years. Science 317, 793-797.

Kach, D.J., Ward, J.E., 2008. The role of marine aggregates in the ingestion of picoplanktonsize particles by suspension-feeding molluscs. Mar. Biol. 153, 797-805.

Kaufman, A., Broecker, W.S., Ku, T.L., Thurber, D.L., 1971. The status of U-series methods of mollusk dating. Geochim. Cosmochim. Acta 35, 1155-1183.

Kaufman, A., Ghaleb, B., Wehmiller, J.F., Hillaire-Marcel, C., 1996. Uranium concentration and isotope ratio profiles within Mercenaria shells: geochronological implications. Geochim. Cosmochim. Acta 60 (19).

Kawamura, H., Holbourn, A., Kuhnt, W., 2006. Climate variability and land–ocean interactions in the Indo Pacific Warm Pool: A 460-ka palynological and organic geochemical record from the Timor Sea. Mar. Micropaleontol. 59, 1-14.

Kendrick, G.W., Wyrwoll, K-H., Szabo, B.J., 1991. Pliocene–Pleistocene coastal events and history along the western margin of Australia. Quaternary Science Reviews 10, 419–439.

Kirby, M. X., 2000. Paleoecological differences between Tertiary and Quaternary *Crassostrea* oysters, as revealed by stable isotope sclerochronology. Palaios 15, 132-141.

Klumpp D. W., Lukas, J. S. 1994. Nutritional ecology of the giant clams *Tridacna tevoroa* and *T. derasa* from Tonga: influence of light on filter-feeding and photosynthesis. Mar. Ecol. Prog. Ser., 107, 147-157.

Klumpp, D., Bayne, B., Hawkins, A., 1992. Nutrition of the giant clam *Tridacna gigas* (L.) I. Contribution of filter feeding and photosynthates to respiration and growth. J. Exp. Mar. Biol. Ecol., 155, 105-122.

Klumpp, D., C. Griffiths., 1994. Contributions of phototrophic and heterotrophic nutrition to the metabolic and growth requirements of four species of giant clam (Tridacnidae). Marine Ecology Progress Series, 115, 103-115.

Kopp, R. E., Kemp, A. C., Bittermann, K., Horton, B. P., Donnelly, J. P., Gehrels, W. R., Hay, C. C., Mitrovica, J. X., Morrowa, E. D., Rahmstor, S., 2016. Temperature-driven global sea-level variability in the Common Era. Proceedings of the National Academy of Sciences, 113, E5694-E5696.

Kopp, R.E., Mitrovica, J.X., Griffies, S.M., Yin, J., Hay, C.C., Stouffer, R.J., 2010. The impact of Greenland melt on local sea levels: a partially coupled analysis of dynamic and static equilibrium effects in idealized water-hosing experiments. Clim. Change 103, 619-625.

Koutavas, A., Lynch-Stieglitz, J., Marchitto Jr., T. M., Sachs, J. P., 2002. El Niño-like pattern in ice age tropical Pacific sea surface temperature. Science, 297, 226-230.

Kreeger, D.A., Newell, R.I.E., 1996. Ingestion and assimilation of carbon from cellulolytic bacteria and heterotrophic flagellates by the mussels *Geukensia demissa* and *Mytilus edulis* (Bivalvia, Mollusca). Aquat. Microb. Ecol. 11, 205-214.

Kuenen, P. H., 1933. The formation of the atolls in the Toekang-Besi-group by subsidence. Proceedings of the Koninklijke Nederlandse Akademie van Wetenschappen Amsterdam 36, 331-336.

Lambeck, K., Esat, T., Potter, E., 2002. Links between climate and sea levels for the past three million years. Nature, 419, 199-206.

Lambeck, K., Nakada, M., 1992. Constraints on the age and duration of the last interglacial period and on sea-level variations. Nature, 357, 125-128.

Lancrenon, E., Zanette, D., 2011. *Tridacna gigas*, objets de prestige en Mélanésie de la période Lapita aux chasseurs de tête. Vent des Iles editeurs.

Lang, N., Wolff, E. W., 2011. Interglacial and glacial variability from the last 800 ka in marine, ice and terrestrial archives. Clim. Past, 7, 361-380.

Lartaud, F., Emmanuel, L., De Rafelis, M., Pouvreau, S., Renard, M., 2010. Influence of food supply on the $\delta^{13}C$ signature of mollusc shells: implications for palaeoenvironmental reconstructions. Geo-Mar Lett 30, 23-34.

Latif, M., Anderson, D., Barnett, T., Cane, M., Kleeman, R., Leetmaa, A., O'Brien, J., Rosati, A., Schneider, E., 1998. A review of the predictability and prediction of ENSO. J. Geophys. Res. 103, 14.375-14.393.

Latif, M., Keenlyside, N. S., 2009. El Niño/Southern Oscillation response to global warming. Proc. Natl. Acad. Sci. U. S. A. 106 (49), 20578-20583.

Lau, K., Wu, H., Bony, S., 1997. The role of large-scale atmospheric circulation in the relationship between tropical convection and sea surface temperature. J. Clim. 10, 381-392.

Lau, K., Wu, H., Bony, S., 1997. The role of large-scale atmospheric circulation in the relationship between tropical convection and sea surface temperature. J. Clim. 10, 381-392.

Lazareth, C., Putten, E., André, L., Dehairs, F., 2003. High-resolution trace element profiles in shells of the mangrove bivalve *Isognomon ephippium*: a record of environmental spatio-temporal variations? Estuar. Coast. Shelf. S. 57, 1103-1114.

Lea, D. W., Pak, D. K., Spero, H. J., 2000. Climate impact of late Quaternary equatorial Pacific sea surface temperature variations. Science, 289, 1719-1724.

Leggat, W., Buck, B. H., Grice, A. M., Yellowlees, D., 2003. The impact of bleaching on the metabolic contribution of dinoflagellate symbionts to their giant clam host. Plant Cell and Environment, 26, 1951-61.

LeGrande, A., Schmidt, G., 2006. Global gridded data set of the oxygen isotopic composition in seawater. Geophys. Res. Lett. 33.

Li, J., S. Xie, E. Cook, G. Huang, R. D'Arrigo, F. Liu, J. Ma, and X. Zheng. 2011. Interdecadal modulation of El Niño amplitude during the past millennium. Nature Climate Change, 1:114-118.

Liu, Z., Lu, Z., Wen, X., Otto-Bliesner, B., Timmermann, A., Cobb, K., 2014. Evolution and forcing mechanisms of El Niño over the past 21,000 years. Nature, 515, 550-553.

Lorrain, A., Paulet, Y-M., Chauvaud, L., Dunbar, R., Mucciarone, D., Fontugne, M., 2004. $\delta^{13}C$ variations in scallop shells: Increasing metabolic carbon contribution with body size? Geochim. Cosmochim. Acta 68, 3509-3519.

Lucas, J. S., Nash, W. J., Crawford, C. M., Braley, R. D., 1989. Environmental Influences on Growth and Survival During the Ocean-Nursery Rearing of Giant Clams, *Tridacna gigas* (L.). Aquaculture 80, 45-61.

Lucia software, Laboratory Imaging s.r.o., © 2016. http://www.lucia.cz/

Madkour, H. A., 2005. Distribution and relationships of heavy metals in the giant clam Tridacna maxima and associated sediments from different sites in the Egyptian Red Sea coast. Egyptian Journal of Aquatic Research, 31(2), 45-59.

Mangum, C. P., Johansen, K., 1982. The influence of symbiotic dinoflagellates on respiratory processes in the giant clam *Tridacna squamosa*. Pac. Sci., 36 (3), 295-401.

Marino, G., Rohling, E., Rodríguez-Sanz, L., Grant, K., Heslop, D., Roberts, A., and Stanford, J. et al., 2015. Bipolar seesaw control on last interglacial sea level. Nature, 522, 197-201.

Martinson, D.G., Pisias, N.G., Hays, J.D., Imbrie, J., Moore, T.C., Shackleton, N.J., 1987. Age dating and the orbital theory of the ice ages: development of a high-resolution 0 to 300,000-year chronostratigraphy, Quat. Res. 27, 1-29.

Martrat, B., Grimalt, J.O., Shackleton, N.J., de Abreu, L., Hutterli, M.A., Stocker, T.F., 2007. Four climate cycles of recurring deep and surface water destabilizations on the Iberian margin. Science 317, 502–507.

Masson-Delmotte, V., Stenni, B., Blunier, T., Cattani, O., Chappellaz, J., Cheng, H., and Dreyfus, G. et al., 2010. Abrupt change of Antarctic moisture origin at the end of Termination II. Proceedings of the National Academy of Sciences, 107, 12091-12094.

McBride, J., Haylock, M., Nicholls, N., 2003. Relationships between the Maritime Continent Heat Source and the El Niño–Southern Oscillation Phenomenon. J. Clim. 16, 2905-2914.

McConnaughey, T., Gillikin, D. P., 2008. Carbon isotopes in mollusk shell carbonates. Geo-Mar. Lett. 28, 287-299.

McCulloch, M., 1999. Coral Record of Equatorial Sea-Surface Temperatures during the Penultimate Deglaciation at Huon Peninsula. Science, 283, 202-204.

McCulloch, M., T. Esat., 2000. The coral record of last interglacial sea levels and sea surface temperatures. Chemical Geology, 169:107-129.

McCulloch, M.T., Mortimer, G., 2008. Applications of the 238U-230Th decay series to dating of fossil and modern corals using MC-ICPMS. Aus. J. Earth Sci. 55, 955-965.

McGregor, H.V., Gagan, M.K., 2004. Western Pacific coral $\delta^{18}O$ records of anomalous Holocene variability in the El Niño-Southern Oscillation. Geophys. Res. Lett. 31, L11204.

Measey, M., 2010. Indonesia: A Vulnerable Country in the Face of Climate Change. Global Majority E-Journal. 1 (1), 31-45.

Medina-Elizalde, M., Lea D. W., 2005. The mid-Pleistocene transition in the tropical Pacific. Science, 310, 1009-1012.

Milankovitch, M., 1941. Kanon der Erdbestrahlung (Canon of insolation and the ice age problem), Sect. Math. Nat. Sci. 33, 132 (English translation by Israel Program for Scientific Translations, Jerusalem, 1969).

Milsom, J., 2000. Stratigraphic constraints on suture models for eastern Indonesia. J. Asian Earth Sci. 18, 761-779.

Min, G.R., Edwards, R.L., Taylor, F.W., Recy, J., Gallup, C.D., Beck, J.W., 1995. Annual cycles of U/Ca in coral skeletons and U/Ca thermometry. Geochimica et Cosmochimica Acta, 59, 2025-2042.

Mitrovica, J., Tamisiea, M., Davis, J., Milne, G., 2001. Recent mass balance of polar ice sheets inferred from patterns of global sea-level change. Nature, 409, 1026-1029.

Mitrovica, J.X., Peltier, W.R., 1991. On postglacial geoid subsidence over the equatorial oceans. J. Geophys. Res. 96, 20053–20071.

Moore, D. M., Reynolds, R. C., Jr., 1997. X-Ray Diffraction and the Identification and Analysis of Clay Minerals, 2nd ed. xviii + 378 pp. Oxford, New York: Oxford University Press.

Moore, M., Kuang, Z., Blossey, P., 2014. A moisture budget perspective of the amount effect. Geophys. Res. Lett. 41, 1329-1335.

Moreno, A., Sancho, C., Bartolomé, M., Oliva-Urcia, B., Delgado-Huertas, A., Estrela, M., Corell D., López-Moreno, J., Cacho, I., 2014. Climate controls on rainfall isotopes and their effects

on cave drip water and speleothem growth: the case of Molinos cave (Teruel, NE Spain). Clim. Dyn. 43, 221-241.

Muhs, D.R., Szabo, B.J., 1994. New uranium-series ages of the Waimanalo Limstone, Oahu, Hawaii: Implications for sea level during the Last Interglacial period. Marine Geology 118, 315–326.

Müller, A., Opdyke, B., 2000. Glacial-interglacial changes in nutrient utilization and paleoproductivity in the Indonesian Throughflow sensitive Timor Trough, easternmost Indian Ocean. Paleoceanography, 15, 85-94.

Munro, J.L., 1989. Fisheries for giant clams (Tridacnidae: Bivalvia) and prospects for stock enhancement. In: Caddy, J.F. (Ed.), Marine Invertebrate Fisheries: Their Assessment and Management. John Wiley and Sons Inc., New York, 541-558.

NASA, 2016. Ice sheets in northern hemisphere. http://sites.gsu.edu/geog1112/global-surface-temperature/

Neo, M., Eckman, W., Vicentuan, K., Teo, S., Todd, P., 2015. The ecological significance of giant clams in coral reef ecosystems. Biological Conservation, 181, 111-123.

Neo, M.L., Todd, P.A., 2013. Conservation status reassessment of giant clams (Mollusca: Bivalvia: Tridacninae) in Singapore. Nat. Singapore 6, 125-133.

Nerot, C., Lorrain, A., Grall, J., Gillikin, D., Munaron, J., Le Bris, H., and Paulet, Y., 2012. Stable isotope variations in benthic filter feeders across a large depth gradient on the continental shelf. Estuar. Coast. Shelf. Sci. 96, 228-235.

Nicholls, N., 1981. Air–sea interaction and the possibility of long-range weather prediction in the Indonesian Archipelago. Mon. Wea. Rev. 109, 2435-2443.

Nicholls, N., 1983. The Southern Oscillation and Indonesian Sea Surface Temperature. Monthly Weather Review, 112, 424-432.

Nicholls, N., 2011. What caused the eastern Australia heavy rains and floods of 2010/11? Bull. Aust. Meteorol. Oceanogr. Soc. 24, 33-34.

Norton, J. H., Prior, H. C., Baillie, B. K., Yellowlees, D., 1995. Atrophy of the zooxanthellal tubular system in bleached giant clams *Tridacna gigas*. Journal of Invertebrate Pathology, 66, 307-310.

O'Leary, M., Hearty, P., Thompson, W., Raymo, M., Mitrovica, J., Webster, J., 2013. Ice sheet collapse following a prolonged period of stable sea level during the last interglacial. Nature Geoscience, 6, 796-800.

O'Neil JR, Clayton, R. N., Mayeda, T. K., 1969. Oxygen isotope fractionation on divalent metal carbonates. Journal of Chemical Physics 51, 5547-5558.

Obert, J., Scholz, D., Felis, T., Brocas, W., Jochum, K., Andreae, M., 2016. ^{230}Th/U dating of Last Interglacial brain corals from Bonaire (southern Caribbean) using bulk and theca wall material. Geochimica et Cosmochimica Acta, 178, 20-40.

Ota, Y., Chappell, J., Kelley, R., Yonekura, N., Matsumoto, E., Nishimura, T., Head, J., 1993. Holocene coral reef terraces and coseismic uplift of Huon Peninsula. Quat. Res. 40, 177-188.

Otto-Bliesner et al., 2006;

Paillard, D., Laberyrie, L., Yiou, P., 1996. Macintosh program performs time-series analysis, Eos Trans. AGU, 77, 39.

Paillard, D., Laberyrie, L., Yiou, P., 1996. Macintosh program performs time-series analysis, Eos Trans. AGU, 77, 39.

Pandolfi, J. M., Best, M. M. R., Murray, S. P., 1994. Coseismic event of May 15, 1992, Huon Peninsula, Papua New Guinea: Comparison with Quaternary tectonic history. Geology 22, 239-242.

Partin, J., K. Cobb, J. Adkins, B. Clark, and D. Fernandez. 2007. Millennial-scale trends in west Pacific warm pool hydrology since the Last Glacial Maximum. Nature, 459:736-736.

Pastier, A.M., et al., 2017. Model simulations of Quaternary reef terraces evolution in southeast Sulawesi (East Indonesia). In prep.

Pätzold, J., Heinrichs, J.P., Wolschendorf, K., Wefer, G., 1991. Correlation of stable oxygen isotope temperature record with light attenuation profiles in reef-dwelling Tridacna shells. Coral Reefs, 10, 65-69.

Pedoja et al. (submitted). On the well preserved long-lasting sequences of marine and coral reef terraces from SE Sulawesi (Indonesia).

Pedoja, K., Husson, L., Johnson, M., Melnick D., Witt, C., Pochat, S., Nexer, M., Delcaillau, B., Pinegina, T., Poprawski, Y., Authemayou, C., Elliot, M., Regard, V., Garestier, F., 2014. Coastal staircase sequences reflecting sea-level oscillations and tectonic uplift during the Quaternary and Neogene. Earth Sci. Rev., 132, 13-38.

Philander, S. G. H., 1983. El Niño Southern Oscillation phenomena. Nature, 302, 295-301.

Pirazzoli, P., Radtke, U., Hantoro, W., Jouannic, C., Hoang, C., Causse, C., Best. M., 1991. Quaternary Raised Coral-Reef Terraces on Sumba Island, Indonesia. Science, 252, 1834-1836.

Pons-Branchu, E., Douville, E., Roy-Barman, M., Dumont, E., Branchu, P., Thil, F., Frank, N. et al., 2014. A geochemical perspective on Parisian urban history based on U–Th dating, laminae counting and yttrium and REE concentrations of recent carbonates in underground aqueducts. Quaternary Geochronology, 24, 44-53.

Potter, E., Esat, T., Schellmann, G., Radtke, U., Lambeck, K., Mcculloch, M., 2004. Suborbital-period sea-level oscillations during marine isotope substages 5a and 5c. Earth and Planetary Science Letters, 225, 191-204.

Potter, E.K., Lambeck, K., 2003. Reconciliation of sea-level observations in the Western North Atlantic during the last glacial cycle. Earth and Planetary Science Letters, 217, 171-181.

Poulain, C., Gillikin, D., Thébault, J., Munaron, J., Bohn, M., Robert, R., Paulet, Y., Lorrain, A., 2015. An evaluation of Mg/Ca, Sr/Ca, and Ba/Ca ratios as environmental proxies in aragonite bivalve shells. Chem. Geo. 396, 42-50.

Prell, W.L., Kutzbach, J., 1987. Monsoon variability over the past 150.000 years. Journal of Geophysical Research 92, 8411 – 8425.

Radtke, U., Schellmann, G., 2006. Uplift History along the Clermont Nose Traverse on the West Coast of Barbados during the Last 500,000 Years-Implications for Paleo–Sea Level Reconstructions. Journal Of Coastal Research, 222, 350-356.

Raymo, M., Mitrovica, J.X., 2012. Collapse of polar ice sheets during the stage 11 interglacial. Nature 483, 453-456.

Raymo, M.E., Mitrovica, J.X., O'Leary, M.J., Deconto, R.M., Hearty, P.J., 2011. Departures from eustasy in Pliocene sea-level records. Nat. Geosci. 4, 328-332.

Razjigaeva et al., 2015

Riera, P., Richard, P., 1997. Temporal variation of δ13C in particulate organic matter and oyster *Crassostrea gigas* in Marennes-Oleron Bay (France): effect of freshwater inflow. Mar. Ecol. Prog. Ser. 147, 105-115.

Robinson, L.F., Belshaw, N., Henderson, G.M., 2004. U and Th concentrations and isotope ratios in modern carbonates and waters from the Bahamas. Geochimica et Cosmochimica Acta, 68, 1777-1789.

Rohling, E. J., 2013. Oxygen Isotope Composition of Seawater. In: Elias S.A. (ed.) The Encyclopedia of Quaternary Science, vol. 2, pp. 915-922. Amsterdam: Elsevier.

Rohling, E., Grant, K., Hemleben, C., Siddall, M., Hoogakker, B., Bolshaw, M. And Kucera, M., 2007. High rates of sea-level rise during the last interglacial period. Nature Geoscience, 1, 38-42.

Romanek, C. S., Grossman, E. L., Morse, J. W., 1992. Carbon isotopic fractionation in synthetic aragonite and calcite—Effects of temperature and precipitation rate. Geochim Cosmochim Acta 56, 419-430.

Romanek, C. S., Jones, D. S., Williams, D. F., Krantz, D. E., Radtke, R., 1987. Stable isotopic investigation of physiological and environmental changes recorded in shell carbonate from the giant clam Tridacna maxima. Mar. Bio. 94, 385-393.

Romanek, C.S., Grossman, E.L., 1989. Stable Isotope Profiles of *Tridacna maxima* as Environmental Indicators. Palaios, 4 (5), 402-413.

Rosewater, J., 1965. The family Tridacnidae in the Indo-Pacific. Indo-Pacific Mollusca, 1, 347-396.

Roucoux K.H., Tzedakis P.C., Frogley M.R., Lawson I.T., Preece R.C., 2008. Vegetation history of the marine isotope stage 7 interglacial complex at Ioannina, NW Greece. Quaternary Science Reviews 27, 1378– 1395.

Sano, Y., Kobayashi, S., Shirai, K., Takahata, N., Matsumoto, K., Watanabe, T., Sowa, K., Iwai, K., 2012. Past daily light cycle recorded in the strontium/calcium ratios of giant clam shells. Nat. Commun. 3, 761.

Sarr, A.-C., L. Husson, P. Sepulchre, A-M. Pastier, A.F. Holt, K. Pedoja, M. Elliot, C. Arias-Ruiz, T. Solihuddin, S. Aribowo, (Submited) Subsiding Sundaland as an early open route for biotic dispersal in Southeast Asia.

Sasajima, S., Nishimura, S., Hirooka, K., Otofuji, Y.E.A., 1980. Palaeomagnetic studies combined with fission-track datings on the western arc of Sulawesi, East Indonesia. Tectonophysics 64, 163–172.

Satyana, A.H., Purwaningsih, M.E.M., 2011. Collision of micro-continents with eastern Sulawesi: records from uplifted reef terraces and proven-potential petroleum plays. Proceedings, Indonesian Petroleum Association.

Schiller, A., Godfrey, J., McIntosh, P., Meyers, G., Wijffels, S., 1998. Seasonal Near-Surface Dynamics and Thermodynamics of the Indian Ocean and Indonesian Throughflow in a Global Ocean General Circulation Model. Journal of Physical Oceanography, 28: 2288-2312.

Schiller, A., Wijffels, S., Sprintall, J., Molcard, R., Oke, P., 2010. Pathways of intraseasonal variability in the Indonesian Throughflow region. Dyn. Atmos. Oceans. 50, 174-200.

Schneider, J. 1998. Phylogeny of the Cardiidae (Bivalvia): phylogenetic relationships and morphological evolution within the subfamilies Clinocardiinae, Lymnocardiinae, Fraginae and Tridacninae. Malacologia, 40, 321-373.

Schneider, J. and Foighil, D., 1999. Phylogeny of Giant Clams (Cardiidae: Tridacninae) Based on Partial Mitochondrial 16S rDNA Gene Sequences. Mol. Phylogenet. Evol., 13, 59-66.

Schneider, T., Bischoff, T., Haug, G. H., 2014. Migrations and dynamics of the intertropical convergence zone. Nature 513, 45-53.

Scholz, D. and Mangini, A., 2007. How precise are U-series coral ages? Geochimica et Cosmochimica Acta 71, 1935-1948.

Scholz, D., Hoffmann D. L., 2008. 230Th/U-dating of fossil corals and speleothems. Quat. Sci. J. 57, 52-76.

Scholz, D., Mangini, A., Felis, T., 2004. U-series dating of diagenetically altered fossil reef corals. Earth Planet. Sci. Lett. 218, 163-178.

Schöne, B., Lega, J., W. Flessa, K., Goodwin, D. And Dettman, D., 2002. Reconstructing daily temperatures from growth rates of the intertidal bivalve mollusk Chione cortezi (northern Gulf of California, Mexico). Palaeogeogr. Palaeoclimatol. Palaeoecol. 184, 131-146.

Schrag, D.P., Adkins, J.F., McIntyre, K., Alexander, J.L., Hodell, D.A., Charles, C.D., McManus, J.F., 2002. The oxygen isotopic composition of seawater during the Last Glacial Maximum. Quaternary Science Reviews 21, 331–342.

Seeto, J., Nunn, P., and Sanjana, S., 2012. Human-Mediated Prehistoric Marine Extinction in the Tropical Pacific? Understanding the Presence of *Hippopus hippopus* (Linn. 1758) in Ancient Shell Middens on the Rove Peninsula, Southwest Viti Levu Island, Fiji. Geoarchaeology 27, 2-17.

Shackleton, N., Sánchez-Goñi, M., Pailler, D. And Lancelot, Y., 2003. Marine Isotope Substage 5e and the Eemian Interglacial. Global and Planetary Change, 36, 151-155.

Shackleton, N.J., 1967. Oxygen isotope analyses and Pleistocene temperatures re-assessed. Nature, 215, 15-17.

Shackleton, N.J., 1987. Oxygen isotopes, ice volume and sea level. Quaternary Science Reviews, 6(3-4), 183-190.

Shackleton, N.J., 2000. The 100,000-year ice-age cycle identified and found to lag temperature, carbon dioxide, and orbital eccentricity, Science 289, 1897-1902.

Shen, G.T., Dunbar, R.B., 1995. Environmental controls on uranium in reef corals. Geochimica et Cosmochimica Acta, 59, 2009-2024.

Siddall, M., Bard, E., Rohling, E., and Hemleben, C., 2006. Sea-level reversal during Termination II. Geology, 34, 817.

Siddall, M., Chappell, J., Potter, E.-K., 2006. Eustatic Sea Level During Past Interglacials. In The Climate Of Past Interglacials. Elsevier, Amsterdam.

Silver, E.A., McCaffrey, R., Smith, R.B., 1983. Collision, rotation, and the initiation of subduction in the evolution of Sulawesi, Indonesia. Journal of Geophysical Research, 88, 9407-9418.

Sinclair, D., Mcculloch, M., 2004. Corals Record Low Mobile Barium Concentrations in the Burdekin River during the 1974 flood: evidence for limited Ba supply to rivers? Palaeogeogr. Palaeoclimatol. Palaeoecol. 214, 155-174.

Smith, R.B., Silver, E.A., 1991. Geology of a Miocene collision complex, Buton, eastern Indonesia. Geological Society of America Bulletin, 103(5), 660–678.

Sprintall, J., Gordon, A., Koch-Larrouy, A., Lee, T., Potemra, J., Pujiana, K., Wijffels, S., 2014. The Indonesian seas and their role in the coupled ocean–climate system. Nature Geosci. 7, 487-492.

Sprintall, J., Wijffels, S., Molcard, R., Jaya, I., 2009. Direct estimates of the Indonesian Throughflow entering the Indian Ocean: 2004–2006. J. Geophys. Res., 114.

Stanford, J., Rohling, E., Hunter, S., Roberts, A., Rasmussen, S., Bard, E., Mcmanus, J., Fairbanks, R., 2006. Timing of meltwater pulse 1a and climate responses to meltwater injections. Paleoceanography, 21.

Stasek, C. R., 1962. The form, growth, and evolution of the Tridacnidae (giant clams). Archives de Zoologie Expérimentale et Générale, 101, 1-40.

Stein, M., G.J. Wasserburg, P. Aharon, J.H. Chen, Z.R. Zhu, A. Bloom, J. Chappell, 1993. TIMS U-series dating and stable isotopes of the last interglacial event in Papua New Guinea, Geochim. Cosmochim. Acta 57, 2541–2554.

Stirling, C. H., Andersen, M. B., 2009. Uranium-series dating of fossil coral reefs: extending the sea-level record beyond the last glacial cycle. Earth Planet. Sci. Lett. 284 (3–4), 269–283.

Stirling, C. H., Esat T. M., McCulloch, M. T., Lambeck, K., 1995. High-precision U-series dating of corals from Western Australia and implications for the timing and duration of the Last Interglacial. Earth Planet. Sci. Lett. 135, 115–130.

Stirling, C. H., Esat, T. M., Lambeck, K., McCulloch, M. T., 1998. Timing and duration of the Last Interglacial: evidence for a restricted interval of widespread coral reef growth. Earth Planet. Sci. Lett. 160, 745-762.

Stott, L., K. Cannariato, R. Thunell, G. Haug, A. Koutavas, and S. Lund. 2004. Decline of surface temperature and salinity in the western tropical Pacific Ocean in the Holocene epoch. Nature, 431:56-59.

Surge, D., Lohmann, K., 2008. Evaluating Mg/Ca ratios as a temperature proxy in the estuarine oyster, *Crassostrea virginica*. J. Geophys. Res. 113, G02001 2156-2202.

Susanto, R., Gordon, A., Zheng. Q., 2001. Upwelling along the coasts of Java and Sumatra and its relation to ENSO. Geophysical Research Letters, 28, 1599-1602.

Swart, P.K., Hubbard, J.A.E.B., 1982. Uranium in scleractinian coral skeletons. Coral Reefs, 1, 13-19.

Tachikawa, K., Cartapanis, O., Vidal, L., Beaufort, L., Barlyaeva, T., Bard, E., 2011. The precession phase of hydrological variability in the Western Pacific Warm Pool during the past 400 ka. Quaternary Science Reviews, 30, 3716-3727.

Tapper, N., 2002. Climate, climatic variability and atmospheric circulation patterns in the maritime continent region, in Bridging Wallace's Line: The Environmental and Cultural History and Dynamics of the SE-Asian-Australian Region, edited by P. Kershaw et al., Adv. Geoecol., 34, 5-38.

Taylor, R.E.,1987. Radiocarbon Dating. London: Academic Press. ISBN 0-12-433663-9.

Thébault, J., Chauvaud, L., L'Helguen, S., Clavier, J., Barats, A., Jacquet, S., Pécheyran, C., Amouroux, D., 2009. Barium and molybdenum records in bivalve shells: Geochemical proxies for phytoplankton dynamics in coastal environments? Limnol. Oceanogr. 54, 1002-1014.

Thomas, A., Henderson, G., Deschamps, P., Yokoyama, Y., Mason, A., Bard, E., Hamelin, B., et al., 2009. Penultimate Deglacial Sea-Level Timing from Uranium/Thorium Dating of Tahitian Corals. Science, 324, 1186-1189.

Thomas, F.R., 2007. The behavioral ecology of shellfish gathering in western Kiribati, Micronesia 1: Prey choice. Hum. Ecol., 35, 179-194.

Thompson, W. G., Goldstein, S. L., 20015. Open-system coral ages reveal persistent suborbital sea-level cycles. Science 308, 401-404.

Thompson, W.G., Spiegelman, M.W., Goldstein, S.L., Speed, R.C., 2003. An open-system model for U-series age determinations of fossil corals. Earth Planet. Sci. Lett. 210, 365-381.

Timmermann A., 2001. Changes of ENSO stability due to greenhouse warming. Geophysical Research Letters, 28 (10), 2061-2064.

Timmermann, A., Latif, M., Bacher, A., Oberhuber, J., Roeckner, E., 1999. Increased El Niño frequency in a climate model forced by future greenhouse warming. Nature 398, 694-696.

Timmermann, A., Lorenz, S., An, S., Clement, A., Xie, S., 2007. The Effect of Orbital Forcing on the Mean Climate and Variability of the Tropical Pacific. Journal of Climate, 20, 4147-4159.

Timmermann, A., M. Latif, A., Bacher, J., Oberhuber, E. Roeckner., 1999. Increased El Niño frequency in a climate model forced by future greenhouse warming. Nature, 398, 694-696.

Titschack, J., M. Zuschin, C. Spötl, C., Baal., 2010. The giant oyster Hyotissa hyotis from the northern Red Sea as a decadal-scale archive for seasonal environmental fluctuations in coral reef habitats. Coral Reefs, 29, 1061-1075.

Tjia, H. D., S. Fujii, K. Kigoshi and A. Sugimura (1974). "Late Quaternary uplift in eastern Indonesia." Tectonophysics 23(4): 427-433.

Tomiak, P., M., Andersen, E., Hendy, E., Potter, K., Johnson, K. Penkman., 2016. The role of skeletal micro-architecture in diagenesis and dating of *Acropora palmata*. Geochim. Cosmochim. Acta, 183,153-175.

Tudhope, A., Chilcott, C., McCulloch, M., Cook, E., Chappell J., Ellam R., Lea D., Lough, J., Shimmield, G., 2001. Variability in the El Niño Southern Oscillation through a Glacial-Interglacial Cycle. Science 291, 1511-1517.

Tynan, S., Opdyke, B., Walczak, M., Eggins, S., Dutton, A., 2017. Assessment of Mg/Ca in Saccostrea glomerata (the Sydney rock oyster) shell as a potential temperature record. Palaeogeogr. Palaeoclimatol. Palaeoecol. 484, 79–88.

Tzedakis, P., Crucifix, M., Mitsui, T., Wolff, E., 2017. A simple rule to determine which insolation cycles lead to interglacials. Nature, 542, 427-432.

van der Kaars, W.A., 1991. Palynology of eastern Indonesian marine piston-cores: a Late Quaternary vegetational and climatic record for Australasia. Palaeogeogr. Palaeoclimatol. Palaeoecol. 85, 239–302.

Vander Putten, E., Dehairs, F., Keppens, E., Baeyens, W., 2000. High resolution distribution of trace elements in the calcite shell layer of modern *Mytilus edulis*: Environmental and biological controls. Geochim. Cosmochim. Acta 64 (6), 997-1011.

Vander Zanden, M., and Rasmussen, J., 1999. Primary consumer $\delta^{13}C$ and $\delta^{15}N$ and the trophic position of aquatic consumers. Ecology, 80: 1395-1404.

Verbeek, R. D. M. (1908). Rapport sur les Moluques: Reconnaissances géologiques dans la partie orientale de l'Archipel des Indes Orientales Néerlandaises. Batavia, Imprimerie de l'état.

Villemant, B., Feuillet, N., 2003. Dating open systems by the ^{238}U-^{234}U-^{230}Th method: application to Quarternary reef terraces. Earth Planet. Sci. Lett. 210, 105-118.

Villeneuve, M., Cornée, J.J., Gunawan, W., Janin, M.C., Butterlin, J., Saint-Marc, P., Samodra, H., 2000. Continental block collision in the eastern arm of Sulawesi (Indonesia). Structure and geodynamic interpretation. Comptes Rendus de l'Académie des Sciences, Paris 330, 371-378.

Villeneuve, M., Martini, R., Bellon, H., Réhault, J.P., Cornée, J.J., Bellier, O., Burhannuddin, S., Hinschberger, F., Honthaas, C., Monnier, C., 2010. Deciphering of six blocks of Gondwanan origin within Eastern Indonesia (South East Asia). Gondwana Research 18, 420-437.

Visser, K., Thunell, R., Stott, L., 2003. Magnitude and timing of temperature change in the Indo-Pacific warm pool during deglaciation. Nature, 421, 152-155.

Waelbroeck, C., L. Labeyrie, E. Michel, J. Duplessy, J. McManus, K. Lambeck, E. Balbon, and M. Labracherie. 2002. Sea-level and deep water temperature changes derived from benthic foraminifera isotopic records. Quaternary Science Reviews, 21:295-305.

Waliser, D. E., Gautier, C., 1993. A satellite-derived climatology of the ITCZ. J. Clim., 6, 2162-2174.

Wanamaker, A., Kreutz, K., Wilson, T., Borns, H., Introne, D., Feindel, S., 2008. Experimentally determined Mg/Ca and Sr/Ca ratios in juvenile bivalve calcite for *Mytilus edulis*: implications for paleotemperature reconstructions. Geo-Mar. Lett. 28, 359-368.

Warter, V., Müller, W., 2017. Daily growth and tidal rhythms in Miocene and modern giant clams revealed via ultra-high resolution LA-ICPMS analysis — A novel methodological approach towards improved sclerochemistry. Palaeogeogr. Palaeoclimatol. Palaeoecol., 362-375.

Warter, V., Müller, W., Wesselingh, F.P., Todd, J.A., Renema, W., 2015. Late Miocene seasonal to sub-decadal climate variability in the Indo-West Pacific (East Kalimantan, Indonesia) preserved in giant clams. Palaios 30, 66-82.

Watanabe, T., Oba, T., 1999. Daily reconstruction of water temperature from oxygen isotopic ratios of a modern Tridacna shell using a freezing microtome sampling technique. J. Geophys. Res., 104 (C9), 20667-20674.

Watanabe, T., Suzuki, A., Kawahata, H., Kan, H., Ogawa, S., 2004. A 60-year isotopic record from a mid-Holocene fossil giant clam (Tridacna gigas) in the Ryukyu Islands: physiological and paleoclimatic implications. Palaeogeography, Palaeoclimatology, Palaeoecology, 212: 343-354.

Welsh, K., 2008. Reconstructing the climate of the Western Warm Pool of the tropical Pacific using oxygen isotopes from the long-lived bivalves, Tridacna sp. PhD.

Welsh, K., Elliot, M., Tudhope, A., Ayling, B., Chappell, J., 2011. Giant bivalves (*Tridacna gigas*) as recorders of ENSO variability. Earth Planet. Sci. Lett., 307 (3-4), 266-270.

Wilson, M.E.J., Bosence, D.W.J., Limbong, A., 2000. Tertiary syntectonic carbonate platform development in Indinesia. Sedimentology, 47, 395-419.

Wolter, K., Timlin, M.S., 2011. El Niño/Southern Oscillation behaviour since 1871 as diagnosed in an extended multivariate ENSO index (MEI.ext). Int. J. Climatol., 31, 1074-1087.

Xu, J., Holbourn, A., Kuhnt, W., Jian, Z., Kawamura, H., 2008. Changes in the thermocline structure of the Indonesian outflow during Terminations I and II. Earth and Planetary Science Letters, 273 (1–2), 152-162.

Xu, J., Kuhnt, W., Holbourn, A., Andersen, N., Bartoli, G., 2006. Changes in the vertical profile of the Indonesian Throughflow during Termination II: Evidence from the Timor Sea. Paleoceanography, 21. PA4202.

Yan, H., Liu, C., Zhang, W., Li, M., Zheng, X., Wei, G., Xie, L., Deng, W., Sun, L., 2016. ENSO variability around 2000 years ago recorded by *Tridacna gigas* $\delta^{18}O$ from the South China Sea. Quaternary International.

Yan, H., Shao, D., Wang, Y., Sun, L., 2013. Sr/Ca profile of long-lived *Tridacna gigas* bivalves from South China Sea: a new high-resolution SST proxy. Geochim. Cosmochim. Acta, 112, 52-65.

Yan, H., Sun, L., Shao, D., Wang, Y., 2015. Seawater temperature seasonality in the South China Sea during the late Holocene derived from high-resolution Sr/Ca ratios of *Tridacna gigas*. Quat. Res. 83, 298-306.

Yokoyama, Y., Esat, T., and Lambeck, K. 2001. Coupled climate and sea-level changes deduced from Huon Peninsula coral terraces of the last ice age. Earth and Planetary Science Letters, 193, 579-587.

Yonge, C. M., 1981. Functional morphology and evolution in the Tridacnidae (Mollusca: Bivalvia: Cardiacea). Rec. Aust. Mus., 33: 735-777.

Zhu, Z.R., Wyrwoll, K.-H., Collins, L.B., Chen, J.H., Wasserburg, G.J. & Eisenhauer, A., 1993. High-precision U-series dating of Last Interglacial events by mass spectrometry: Houtman Abrolhos Islands, Western Australia. Earth and Planetary Science Letters, 118, 281-293.

List of Figures

Chapter I.

Fig. 1.1. Quaternary evolution……20
Fig. 1.2. Glacial-Interglacial changes……..23
Fig. 1.3. ENSO phases over the Pacific Ocean……...26
Fig. 1.4. Schematic coastal Paleo-reef sequences……...28
Fig. 1.5. *Tridacna gigas* shell, Tridacnidae family……..28
Fig. 1.6. Evolution and stratigraphic description of Tridacnidae family……..29
Fig. 1.7. Modern distribution of Tridacnide family……30

Chapter II.

Fig. 2.1. Geological setting of SE Sulawesi……39
Fig. 2.2. The studied area: SE Sulawesi……..40
Fig. 2.3. Paleo-reef sequences……41
Fig. 2.4. The three climate regions in Indonesia……43
Fig. 2.5. Sea surface temperature (SST) distribution in the western Pacific Ocean……45
Fig. 2.6. Mean monthly climatological and oceanographic data for south Sulawesi……..46
Fig. 2.7. Field work, Tridacnidae shell extraction……...47
Fig. 2.8. Recrystallization from aragonite (up) into calcite (down)……50
Fig. 2.9. Left valve of a *T. squamosa* specimen (GSL14_19)……51
Fig. 2.10. Manufactured shell sections on glass slides……52
Fig. 2.11. *T. gigas* sectioned shell (sample GSL14_12)……..52
Fig. 2.12. Transversal cut of a giant clam Shell (simple GSL12_64)……53
Fig. 2.13. Laser ablation……..57

Chapter III.

Fig. 3.1. Study areas……66
Fig. 3.2. *H. hippopus* shells……82
Fig. 3.3. Isotopic results from *H. hippopus* shells……...83
Fig. 3.4. Trace elements comparison in *H. Hippopus* samples……...84
Fig. 3.5. $\delta^{18}O$ profile of GLS14_23 sample compared to SST……85
Fig. 3.6. Intra-species comparison for Trace elements ……...86
Fig. 3.7. Inter-species growth rate comparison……...88
Fig. 3.8. Isotopic inter-species comparison……89
Fig. 3.9. Interannual mean comparisons……..90
Fig. 3.10. Habitat differentiation……91

Fig. 3.11. Inter-species comparison for trace elements……...94
Fig. 3.12. SST derived from Mg/Ca ratios in *H. hippopus*……..95

Chapter IV.

Fig. 4.1. Map of Indonesia……103
Fig. 4.2. Drilling on a paleo coral reef terrace from Buton Island……104
Fig. 4.3. Studied Reef terrace in Nirwana locality (Buton Island)……105
Fig. 4.4. Transversal cut of coral sample GSL13_74……105
Fig. 4.5. Schematic drawing of the ^{238}U, ^{235}U and ^{232}Th decay chains……..107
Fig. 4.6. Seawater evolution curve ($^{234}U/^{238}U$ vs. $^{230}Th/^{238}U$ diagram)……109
Fig. 4.7. SE Sulawesi map……110
Fig. 4.8. Nirwana studied zone……..114
Fig. 4.9. Bahari village (Sampolawa Peninsula, Buton Island)……115
Fig. 4.10. Rahia village, Muna Island……116
Fig. 4.11. Kadatua samples……117
Fig. 4.12. Ular Island dating map……..118
Fig. 4.13. Control sample (GSL12_14) results in different analytical sessions (years)……119
Fig. 4.14. *T. gigas* U-Th test……..122
Fig. 4.15. U-series results from selected corals……124
Fig. 4.16. U-Th dating results relative to the last glacial-interglacial periods……..127
Fig. 4.17. Relative Sea Level (RSL) during the LIG……129
Fig. 4.18. Simplified model for SL evolution in Nirwana zone……....130
Fig. 4.19. RSL during the penultimate interglacial (MIS 7)……..131

Chapter V.

Fig. 5.1. Scenario of palaeoclimate changes linked with the interhemispheric hydrologic seesaw……..140
Fig. 5.2. Available temperature records for MIS-5 in the world……...141
Fig. 5.3. Studied zones……...145
Fig. 5.4. GSL12_80 sample (*T. gigas*), Nirwana……...146
Fig. 5.5. GSL12_81 sample (*T. gigas*)……..147
Fig. 5.6. GSL12_64 sample (*T. gigas*), Rahia (Muna)……..147
Fig. 5.7. GSL12_60 sample (*T. gigas*), Rahia (Muna)……..148
Fig. 5.8. Bulk isotopic results for the entire Tridacnidae shell collection……151
Fig. 5.9. Stable isotope reconstructions from Nirwana samples……...152
Fig. 5.10. Stable isotope reconstructions from Rahia (Muna) samples……153
Fig. 5.11. Trace elements reconstructions from Nirwana samples……154
Fig. 5.12. Trace elements reconstructions from Rahia samples……155
Fig. 5.13. Bulk isotopic results corrected for SL component……156

Fig. 5.14. Monthly mean isotopic records from Nirwana and Rahia fossils…….159
Fig. 5.15. SST and $\delta^{18}O$ records for core MD9821-62, Makassar Strait……...160
Fig. 5.16. $\delta^{18}O$ anomalies related to interannual variation……166
Fig. 5.17. Boxplot for Mg/Ca records from modern and dated fossil clams…….169
Fig. 5.18. Boxplot for Ba/Ca records from modern and dated fossil clams……..170

List of Tables

Chapter II.

Table 2.1. Sample information of Tridacnidae shell collection used in this work……49

Chapter III.

Table 3.1. Seasonal range comparison between all modern sells……..92

Chapter IV.

Table 4.1. Fossil coral samples information……111

Table 4.2. Fossil Shells information……112

Table 4.3. U-Th test results from GSL14_12 shell……..112

Table 4.4. U-series results from selected corals……...113

Table 4.5. Control sample (GSL12_14) results……...118

Table 4.6. Comparison between U-Th and ^{14}C ages……120

Table 4.7. Sea level reconstruction for MIS 5e and T-II……128

Table 4.8. Final chronology……133

Chapter V.

Table 5.1. Bulk isotopic results ($\delta^{18}O$ and $\delta^{13}C$) of Tridacnidae shell collection……....150

Table 5.2. Mean $\delta^{18}O$ and equivalent temperature differences……161

Table 5.3. $\delta^{18}O$ seasonal range comparison and equivalence in temperature……..163

Table 5.4. $\delta^{13}C$ mean values and seasonal range comparison……..164

Appendix 1. Shell Sample collection

GSL12_10 sectioned shell



Tridacna sp.

GSL12_18 sectioned shell

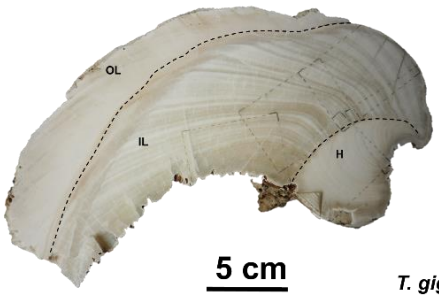

T. gigas

GSL12_19 sectioned shell

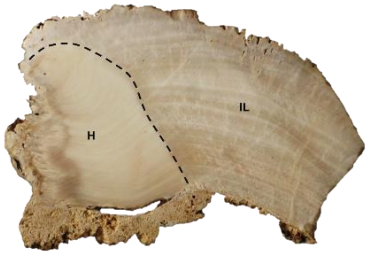

T. gigas

GSL12_56 sectioned shell

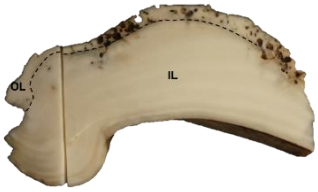

Tridacna sp.

GSL12_60 Inner layer core



T. gigas

GSL12_64 sectioned shell

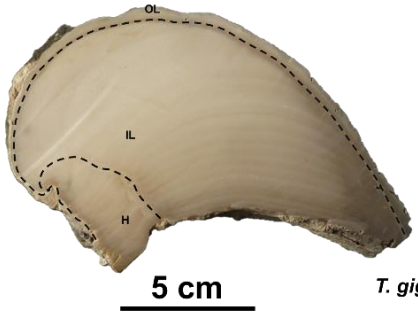

T. gigas


GSL12_78
Inner layer core
Recrystallization (calcite)
5 cm
T. gigas
GSL12_79
sectioned shell
Recrystallization (calcite)
5 cm
T. gigas
GSL12_80
sectioned shell
OL
IL
H
5 cm
T. gigas
GSL12_81
sectioned shell
OL
IL
H
5 cm
T. gigas
GSL12_82
sectioned shell
OL
IL
H
5 cm
T. gigas
GSL12_83
Inner layer core
5 cm
T. gigas

GSL13_01 sectioned shell

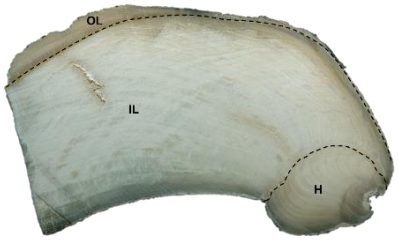

5 cm

Tridacna sp.

GSL13_09 Inner layer core



5 cm

Tridacna sp.

GSL13_56 Inner layer core



5 cm

T. gigas

GSL13_57 Inner layer core



5 cm

T. gigas

GSL13_73 Inner layer core



5 cm

T. gigas

GSL13_75 Inner layer core



5 cm

T. gigas

GSL14_7 sectioned shell

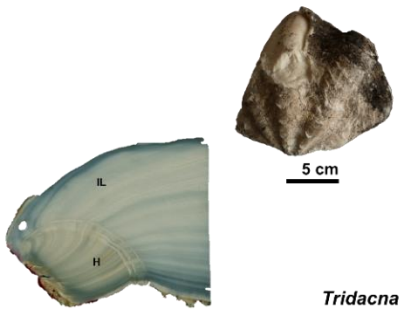

Tridacna sp.

GSL14_12 sectioned shell

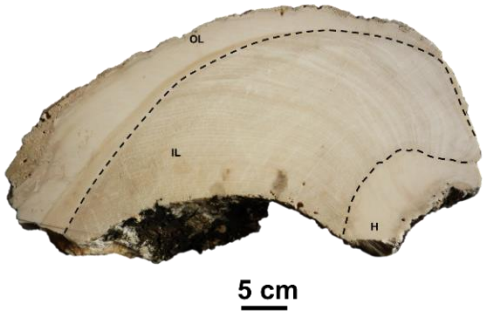

T. gigas

GSL14_15 sectioned shell

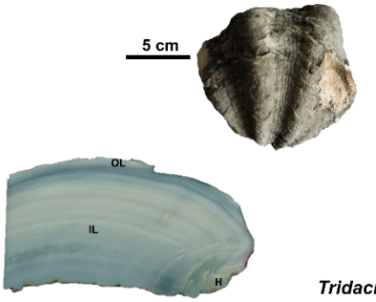

Tridacna sp.

GSL14_19 sectioned shell

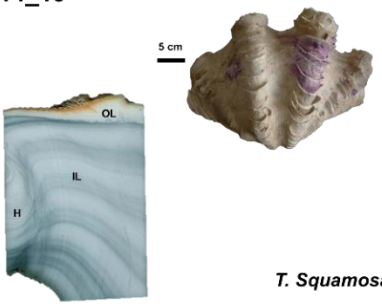

T. Squamosa

GSL14_20 sectioned shell

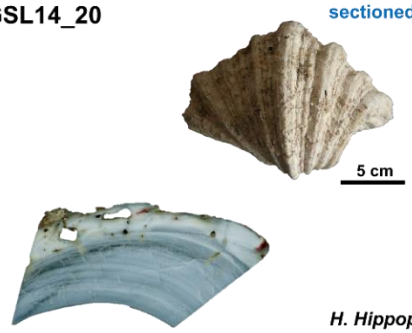

H. Hippopus

GSL14_21 sectioned shell

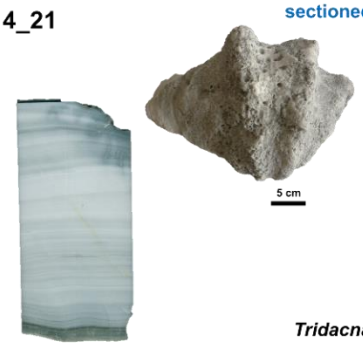

Tridacna sp.

GSL14_22 sectioned shell

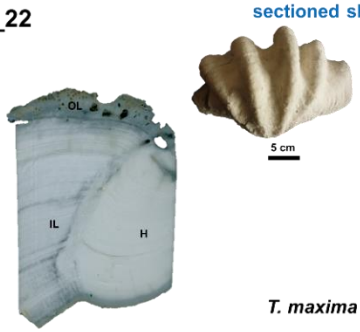

T. maxima

GSL14_23 sectioned shell

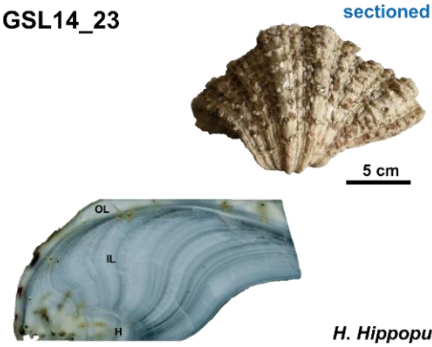

H. Hippopus

Appendix 2. ICP-MS Standards fiability

Comparison between the standards measured here Vs. the international Standards references (GEOREM and Jochum et al., 2012) for geochemical analyses in trace elements.

MACS 3 (Synthetic Calcium Carbonate)

Run or analytical sessions = 4

Total trucks or laser ablations (n) = 18

Element ratio	Measured (mmol/mol)		Recomended (mmol/mol) GEOREM 2017		Jochum et al. (2012)	
	Mean	Std. Dev.	Mean	Std. Dev.	Mean	Std. Dev.
Li(7)/Ca(43)	1,19	0,087	0,95	0,064		
B(11)/Ca(43)	0,11	0,029	0,06	0,005	0,058	0,000
Mg(24)/Ca(43)	7,97	0,471	7,68	0,595	8,224	0,306
Mg(25)/Ca(43)	7,75	0,492	7,68	0,595	8,224	0,306
Mg(26)/Ca(43)	8,29	0,500	7,68	0,595	8,224	0,306
Mn(55)/Ca(43)	1,15	0,056	1,04	0,054	1,030	0,045
Sr(88)/Ca(43)	7,30	0,471	8,20	0,425	7,974	0,206
Ba(135)/Ca(43)	0,06	0,006	0,05	0,002	0,046	0,001
Ba(137)/Ca(43)	0,06	0,006	0,05	0,002	0,046	0,001

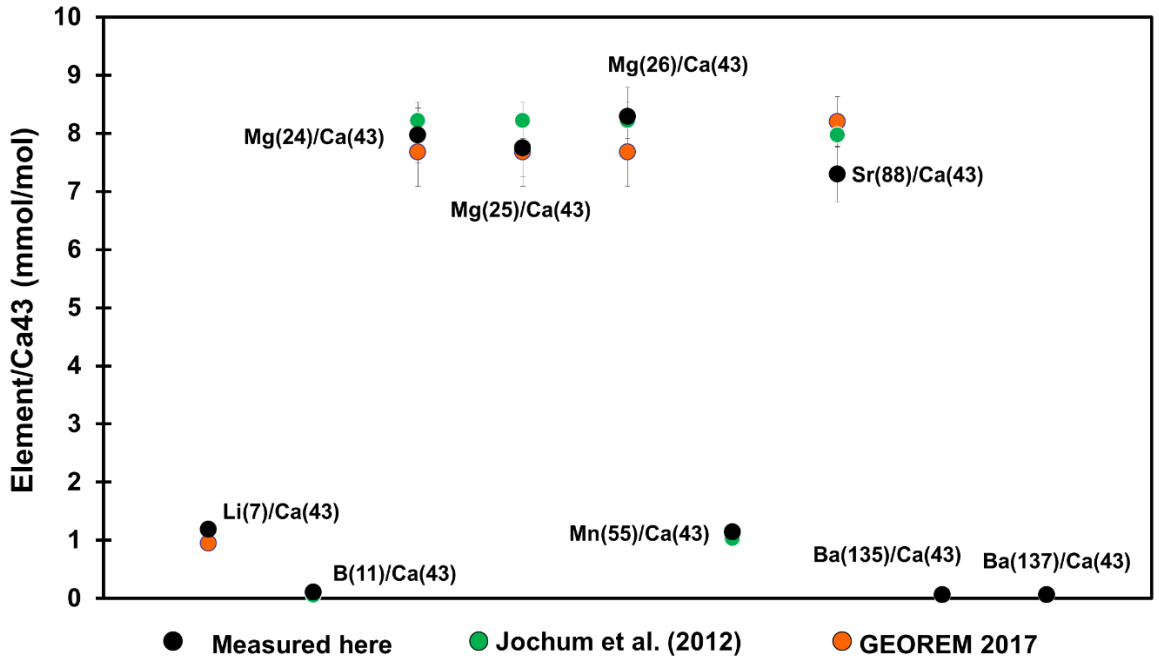

NIST-610 (analysis for trace elements in glass)

National Institute of Standards & Technology (NIST). Standard Reference Material (SRM) 610.

Run or analytical sessions = 6

Total trucks or laser ablations (n) = 39

Element ratio	Measured (mmol/mol)		Recomended (mmol/mol) GEOREM 2017		Jochum et al. (2012)	
	Mean	Std. Dev.	Mean	Std. Dev.	Mean	Std. Dev.
Li(7)/Ca(43)	32,85	2,99	33,34	1,71	33,98	2,21
B(11)/Ca(43)	15,62	1,53	16,01	2,56	15,91	2,88
Mg(24)/Ca(43)	10,24	0,96	9,47	0,54	9,13	0,92
Mg(25)/Ca(43)	10,33	1,03	9,47	0,54	9,13	0,92
Mg(26)/Ca(43)	10,53	1,02	9,47	0,54	9,13	0,92
P(31)/Ca(43)	7,35	0,70	5,47	0,85	6,70	0,91
Mn(55)/Ca(43)	3,94	0,37	3,90	0,29	4,05	0,13
Sr(88)/Ca(43)	2,89	0,28	2,81	0,10	2,86	0,24
Ba(135)/Ca(43)	1,59	0,14	1,53	0,11	1,62	0,08
Ba(137)/Ca(43)	1,60	0,14	1,53	0,11	1,62	0,08
Pb(208)/Ca(43)	1,01	0,09	0,99	0,04	0,99	0,09

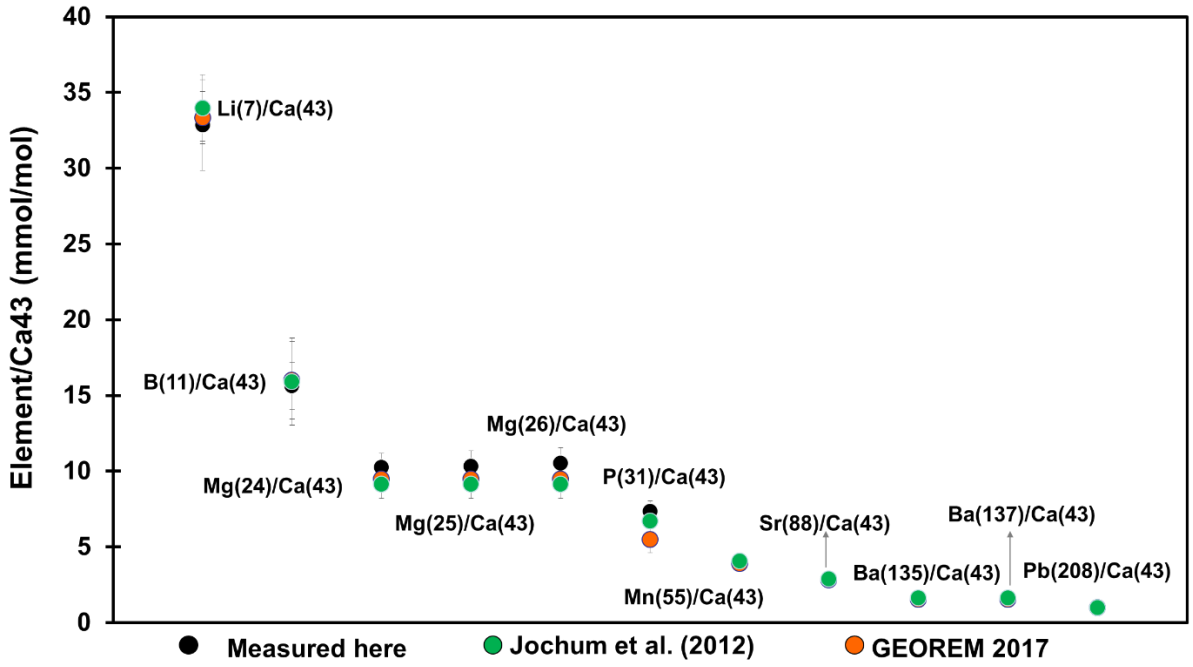

NIST-612 (analysis for trace elements in glass)

National Institute of Standards & Technology (NIST). Standard Reference Material (SRM) 612.

Run or analytical sessions = 6

Total trucks or laser ablations (n) = 40

Element ratio	Measured (mmol/mol)		Recomended (mmol/mol) GEOREM 2017		Jochum et al. (2012)	
	Mean	Std. Dev.	Mean	Std. Dev.	Mean	Std. Dev.
Li(7)/Ca(43)	2,75	0,16	2,88	0,199	2,78	0,14
B(11)/Ca(43)	1,48	0,15	1,55	0,143	1,56	0,13
Mg(24)/Ca(43)	1,17	0,07	1,35	0,101	1,35	0,14
Mg(25)/Ca(43)	1,15	0,09	1,35	0,101	1,35	0,14
Mg(26)/Ca(43)	1,15	0,09	1,35	0,101	1,35	0,14
P(31)/Ca(43)	0,71	0,13	0,71	0,124	0,78	0,11
Mn(55)/Ca(43)	0,34	0,02	0,34	0,009	0,33	0,02
Sr(88)/Ca(43)	0,40	0,03	0,42	0,013	0,42	0,02
Ba(135)/Ca(43)	0,11	0,01	0,13	0,004	0,14	0,01
Ba(137)/Ca(43)	0,10	0,02	0,13	0,004	0,14	0,01
Pb(208)/Ca(43)	0,07	0,01	0,09	0,004	0,09	0,01

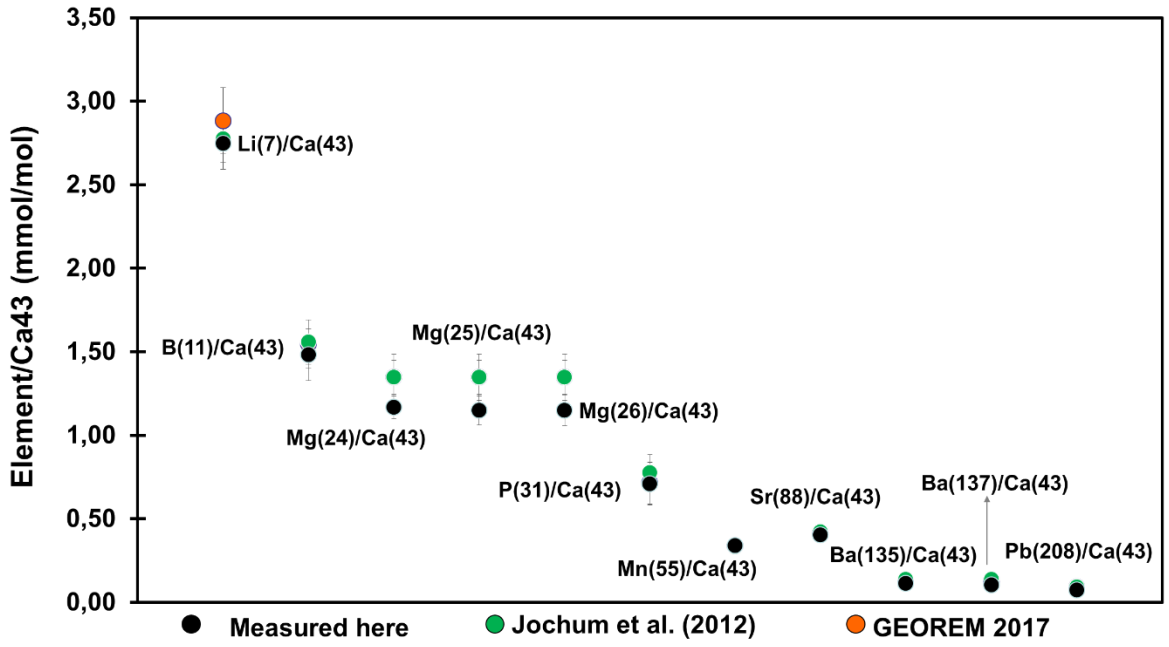

Appendix 3. Trace elements profiles

(Li/Ca – B/Ca – Sr/Ca – Mg/Ca – Ba/Ca)

Nirwana Samples

GSL12_18

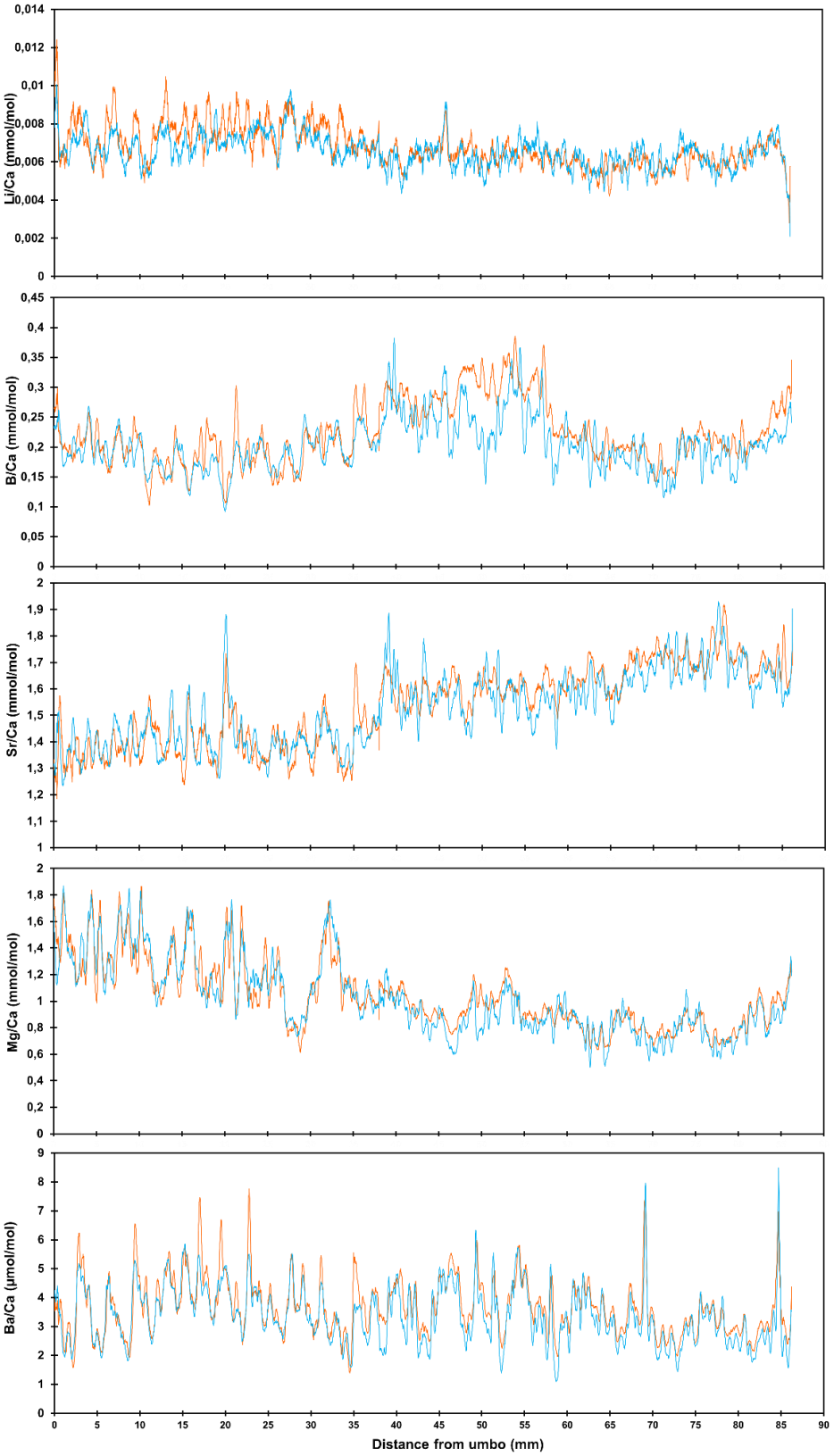

GSL12_19

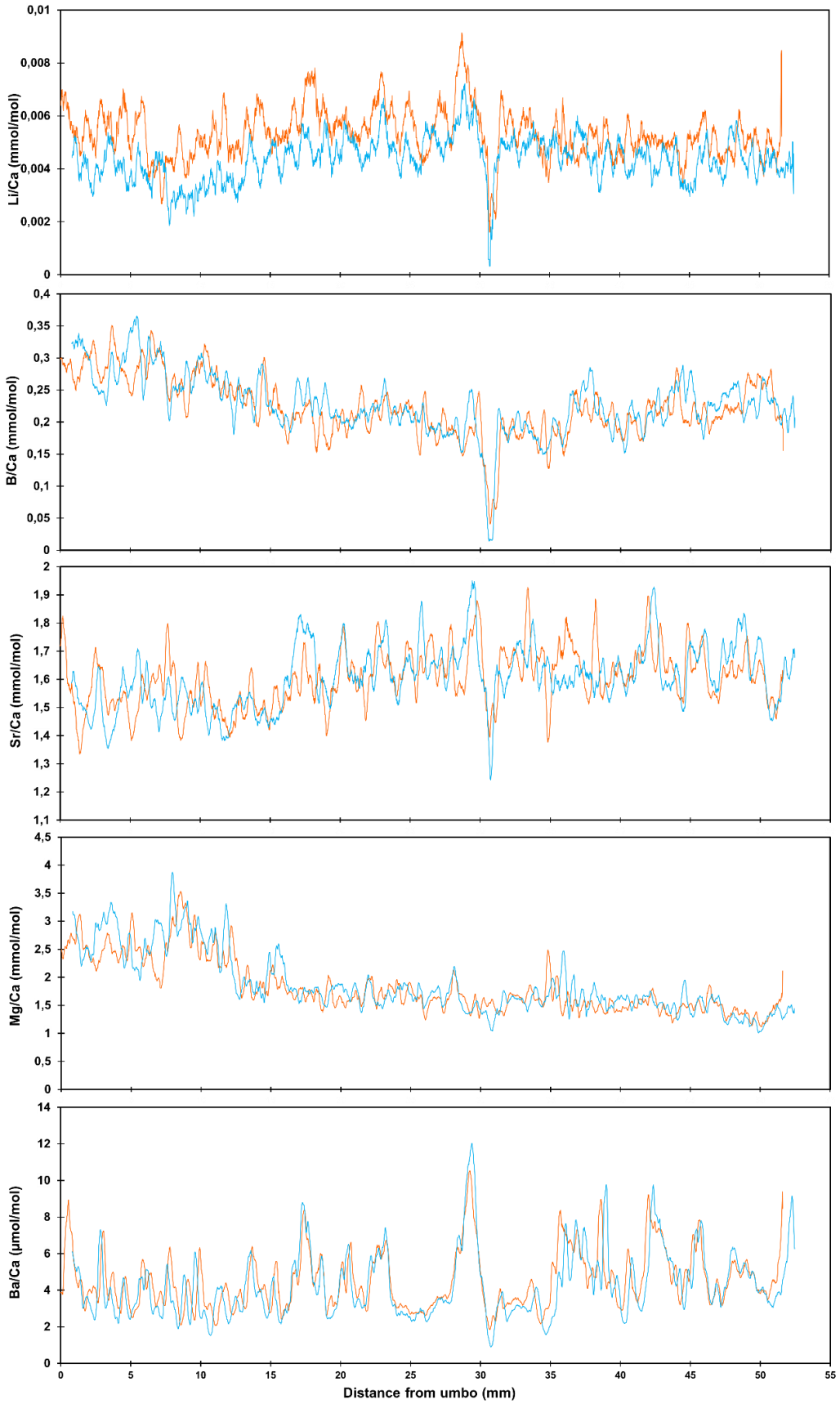
Li/Ca (mmol/mol)
0,01
0,008
0,006
0,004
0,002
0
B/Ca (mmol/mol)
0,4
0,35
0,3
0,25
0,2
0,15
0,1
0,05
0
Sr/Ca (mmol/mol)
2
1,9
1,8
1,7
1,6
1,5
1,4
1,3
1,2
1,1
Mg/Ca (mmol/mol)
4,5
4
3,5
3
2,5
2
1,5
1
0,5
0
Ba/Ca (µmol/mol)
14
12
10
8
6
4
2
0
0
5
10
15
20
25
30
35
40
45
50
55
Distance from umbo (mm)

GSL12_78

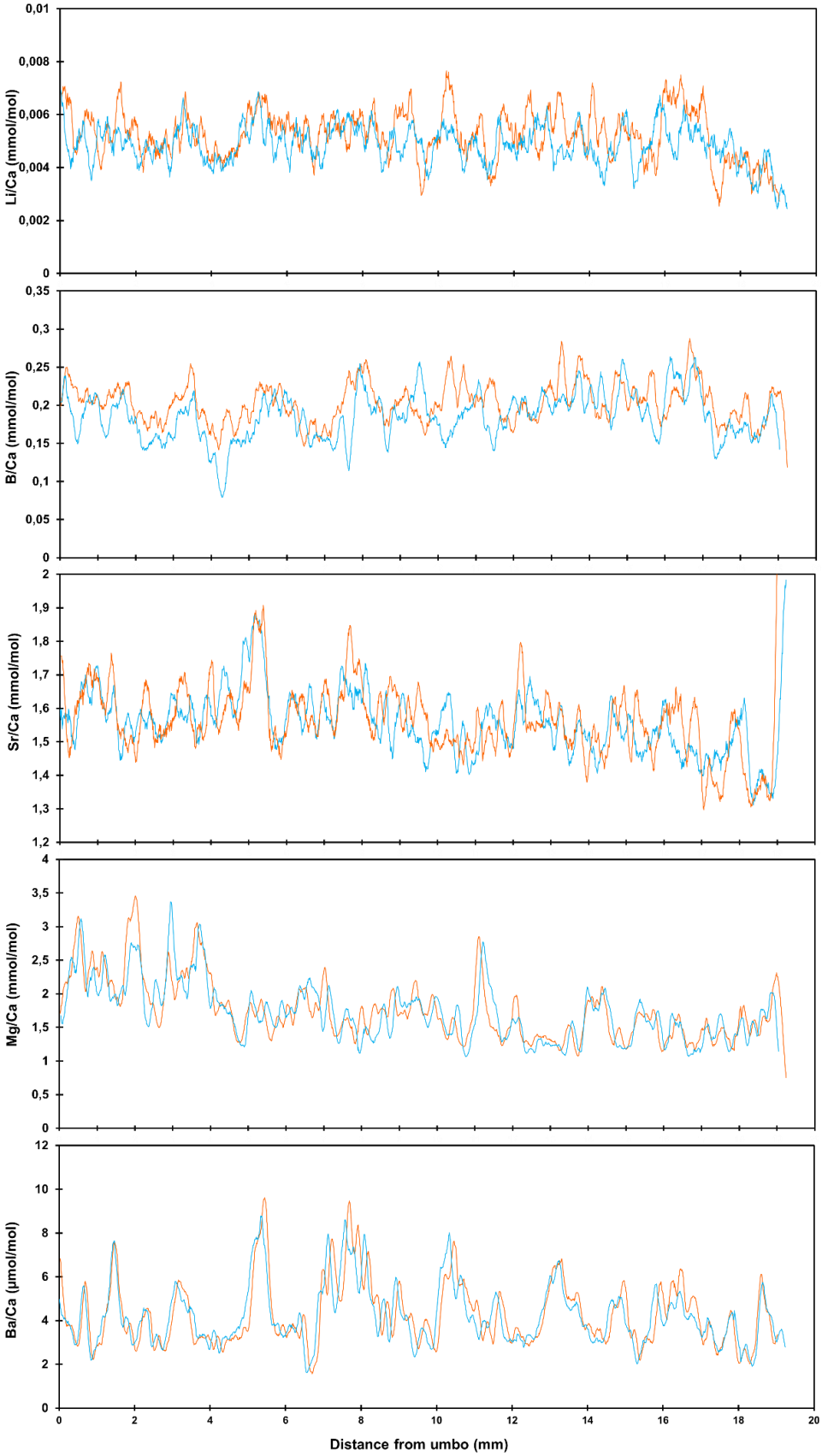
Li/Ca (mmol/mol)
0,01
0,008
0,006
0,004
0,002
0
B/Ca (mmol/mol)
0,35
0,3
0,25
0,2
0,15
0,1
0,05
0
Sr/Ca (mmol/mol)
2
1,9
1,8
1,7
1,6
1,5
1,4
1,3
1,2
Mg/Ca (mmol/mol)
4
3,5
3
2,5
2
1,5
1
0,5
0
Ba/Ca (µmol/mol)
12
10
8
6
4
2
0
0
2
4
6
8
10
12
14
16
18
20
Distance from umbo (mm)

GSL12_79

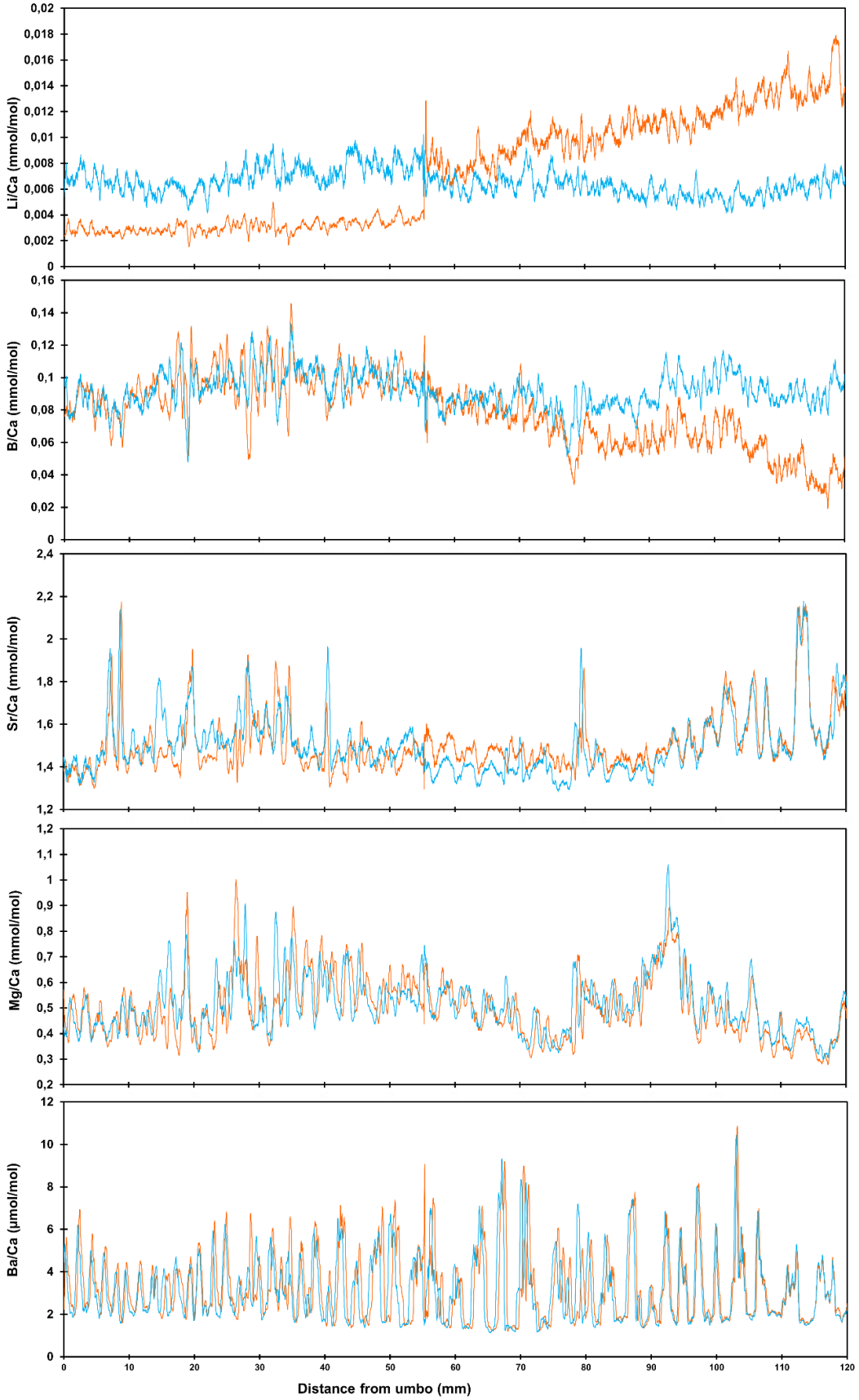
Li/Ca (mmol/mol)
B/Ca (mmol/mol)
Sr/Ca (mmol/mol)
Mg/Ca (mmol/mol)
Ba/Ca (µmol/mol)
Distance from umbo (mm)

GSL12_81

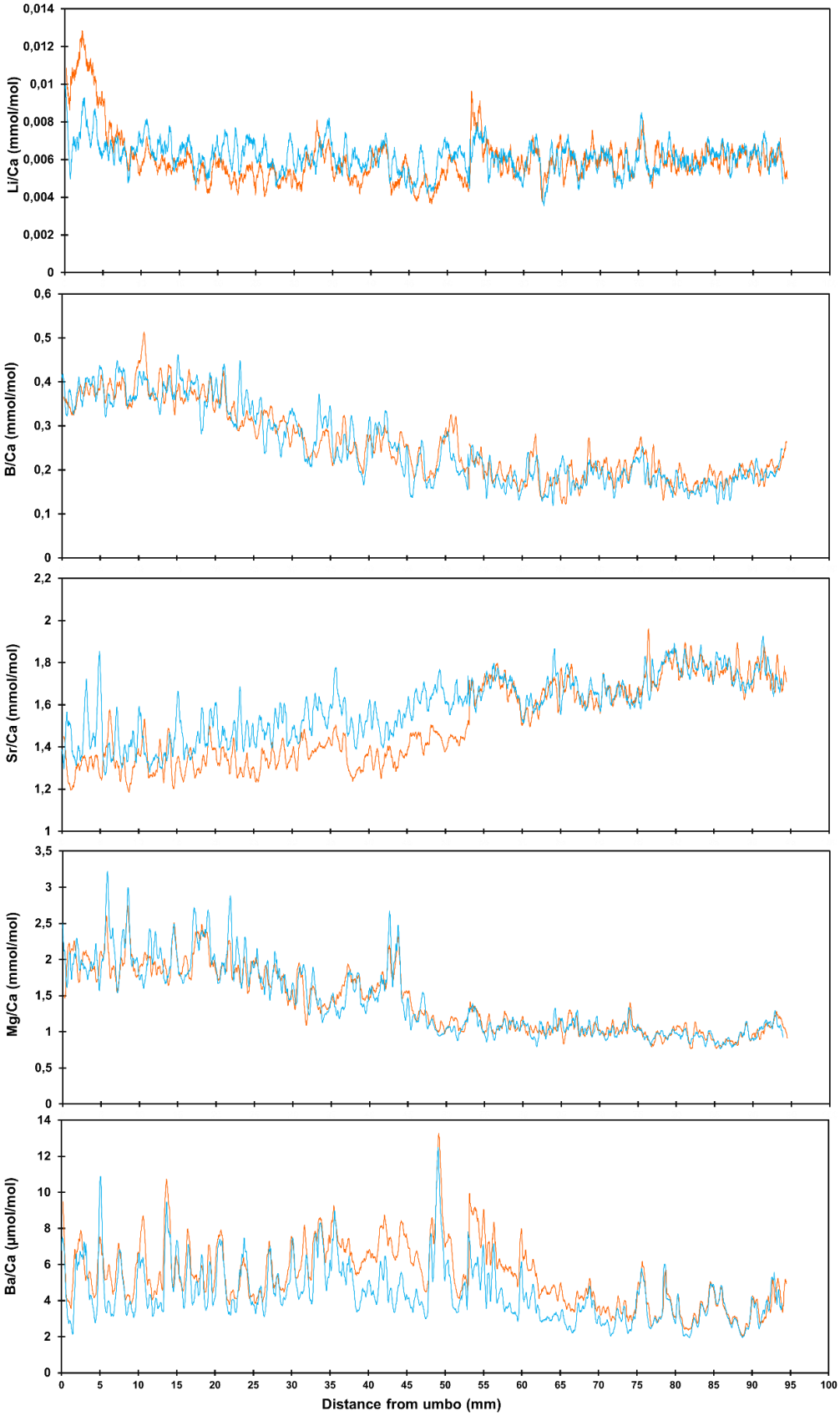
Li/Ca (mmol/mol)
0,014
0,012
0,01
0,008
0,006
0,004
0,002
0
B/Ca (mmol/mol)
0,6
0,5
0,4
0,3
0,2
0,1
0
Sr/Ca (mmol/mol)
2,2
2
1,8
1,6
1,4
1,2
1
Mg/Ca (mmol/mol)
3,5
3
2,5
2
1,5
1
0,5
0
Ba/Ca (µmol/mol)
14
12
10
8
6
4
2
0
0 5 10 15 20 25 30 35 40 45 50 55 60 65 70 75 80 85 90 95 100
Distance from umbo (mm)

GSL12_82

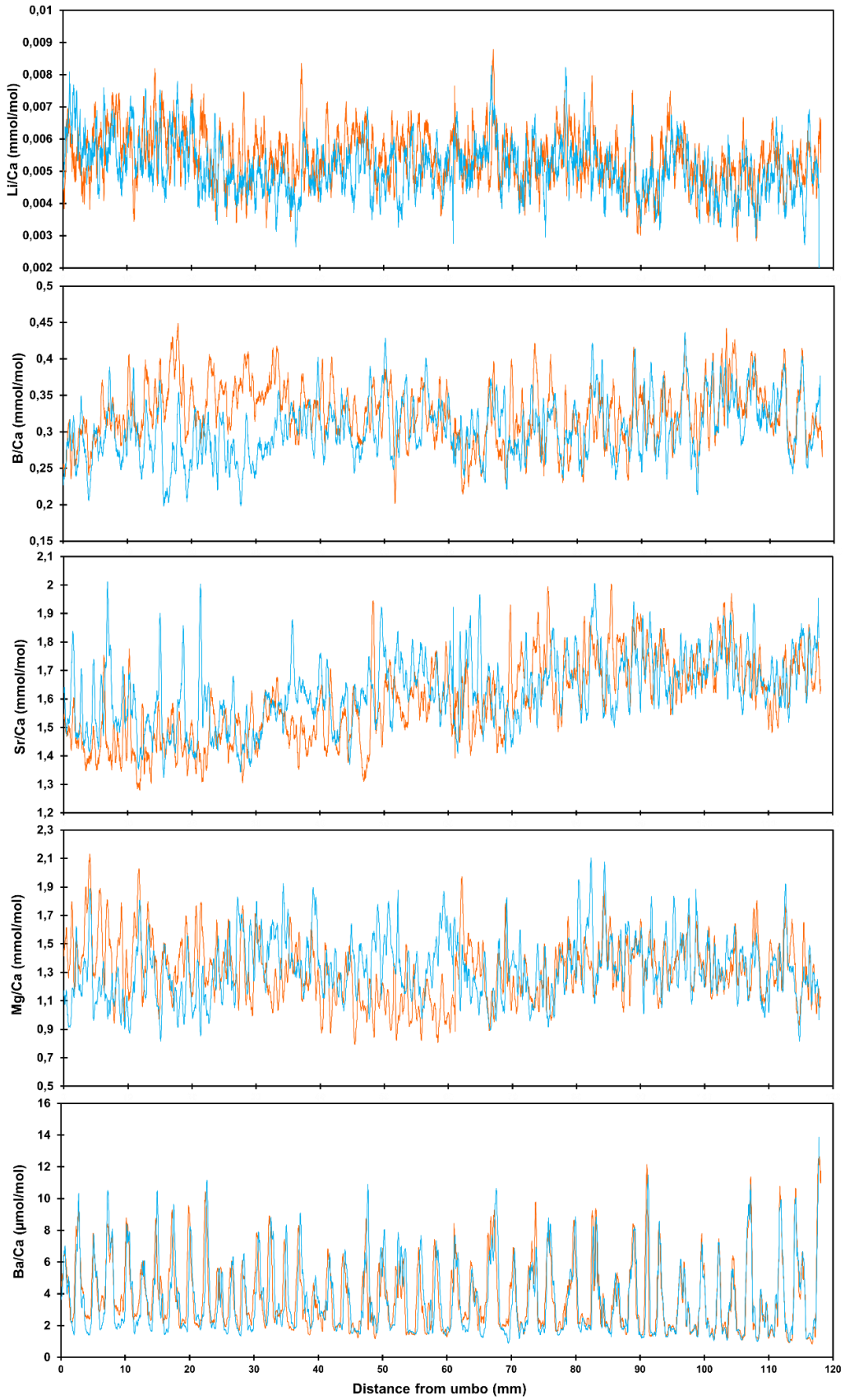
Li/Ca (mmol/mol)
B/Ca (mmol/mol)
Sr/Ca (mmol/mol)
Mg/Ca (mmol/mol)
Ba/Ca (µmol/mol)
Distance from umbo (mm)

GSL12_83

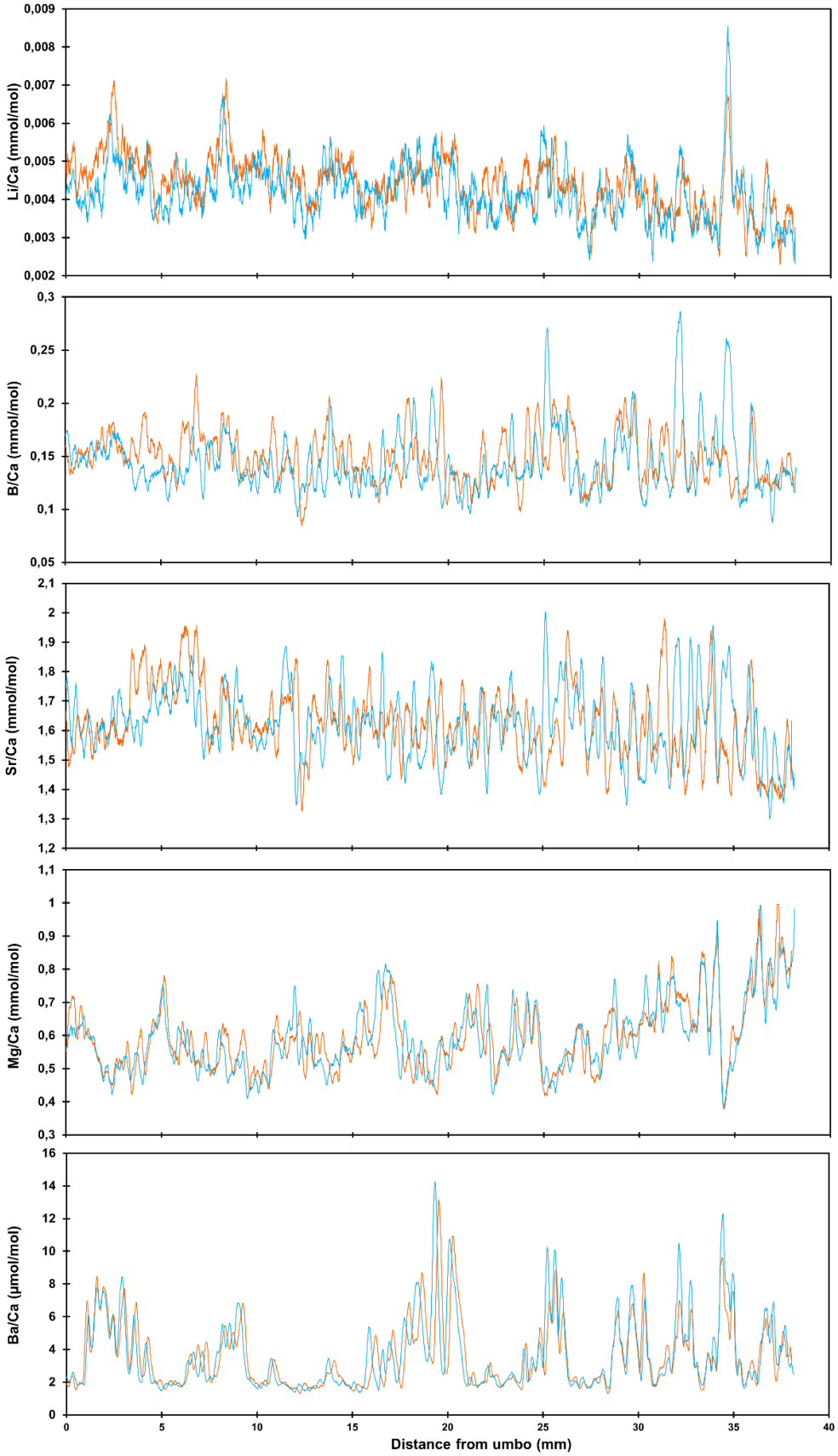
Li/Ca (mmol/mol)
0,009
0,008
0,007
0,006
0,005
0,004
0,003
0,002
B/Ca (mmol/mol)
0,3
0,25
0,2
0,15
0,1
0,05
Sr/Ca (mmol/mol)
2,1
2
1,9
1,8
1,7
1,6
1,5
1,4
1,3
1,2
Mg/Ca (mmol/mol)
1,1
1
0,9
0,8
0,7
0,6
0,5
0,4
0,3
Ba/Ca (µmol/mol)
16
14
12
10
8
6
4
2
0
0
5
10
15
20
25
30
35
40
Distance from umbo (mm)

Rahia (Muna) samples

GSL12_60

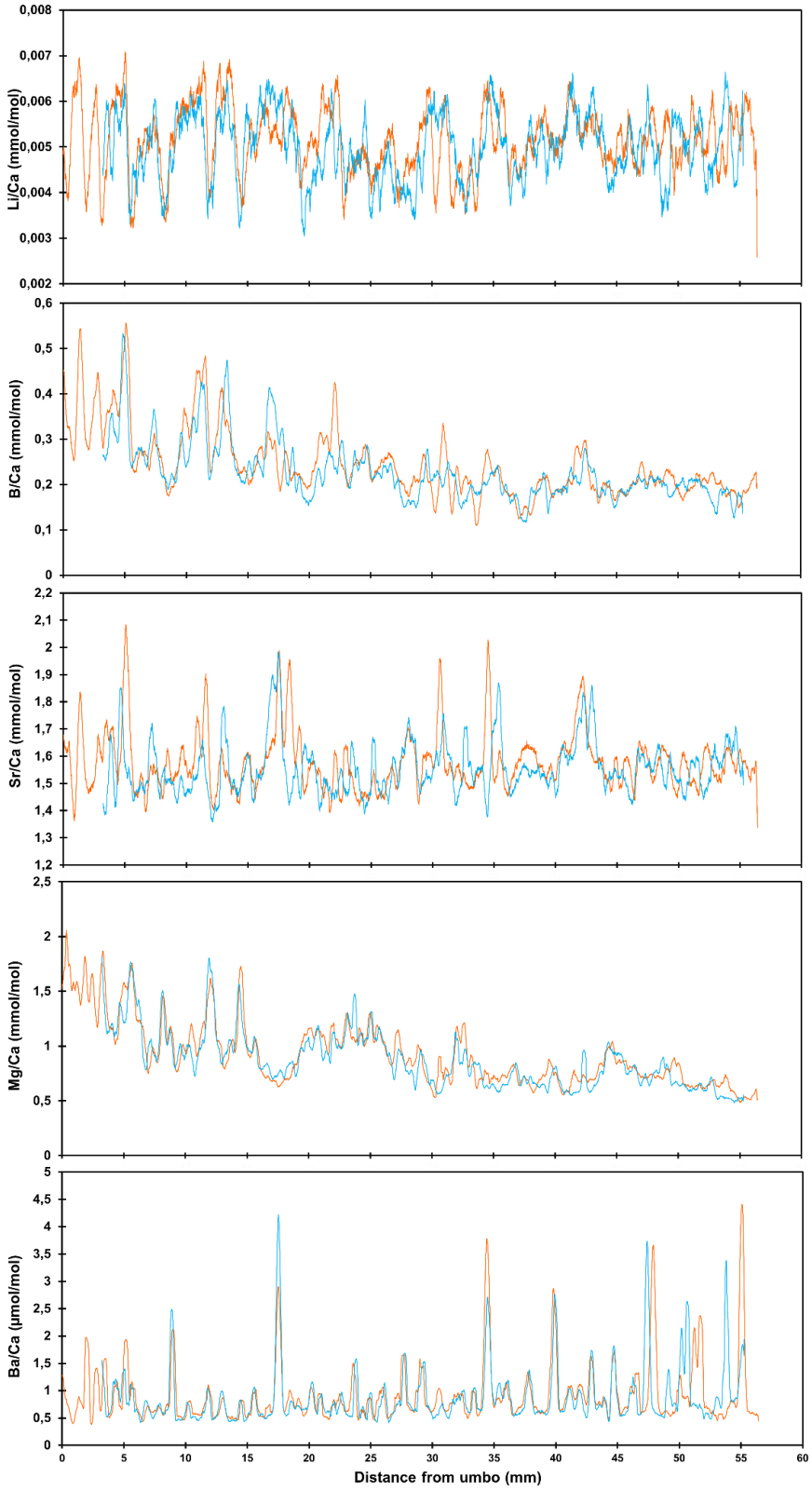

GSL12_64

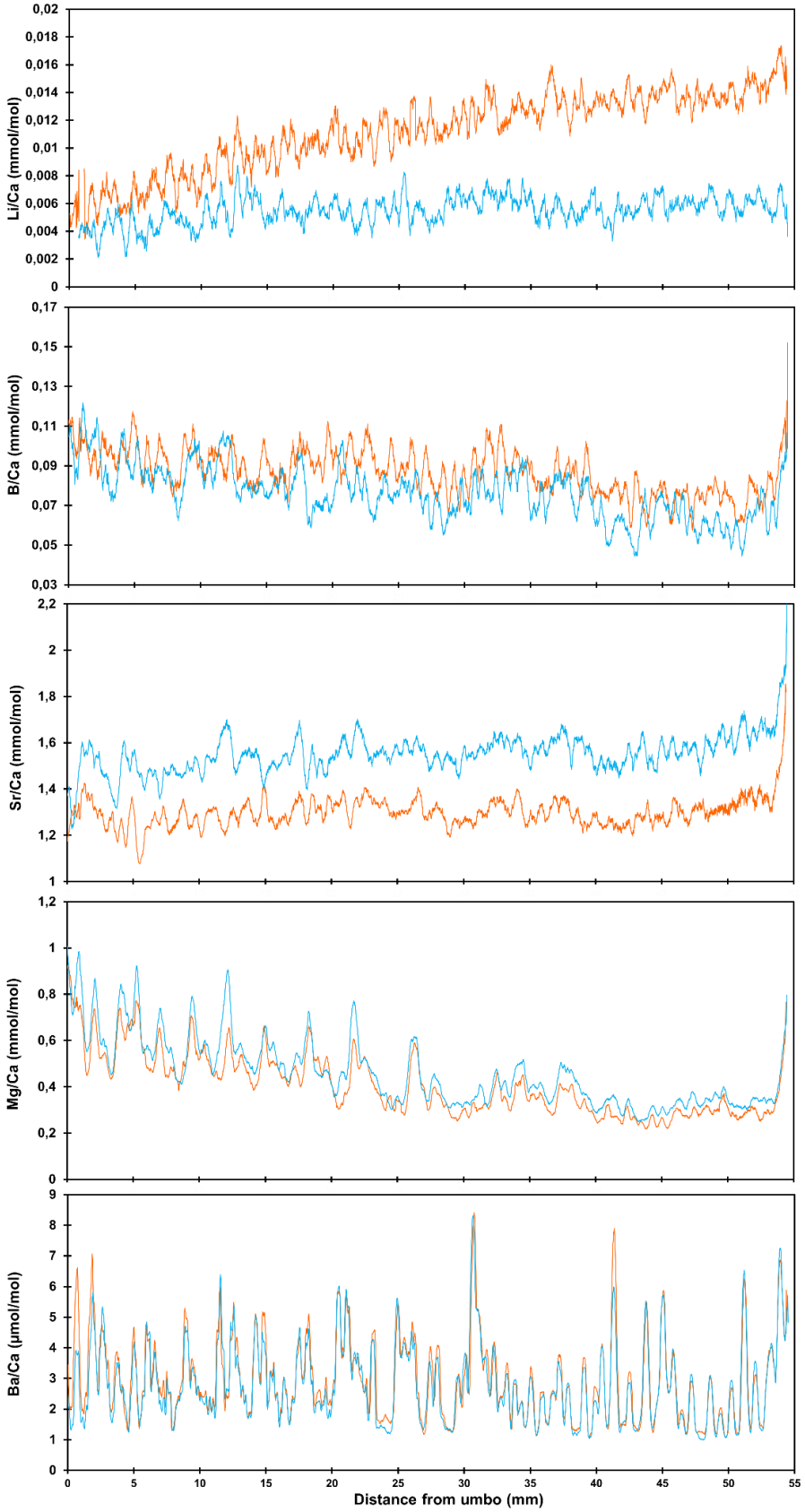
Li/Ca (mmol/mol)
B/Ca (mmol/mol)
Sr/Ca (mmol/mol)
Mg/Ca (mmol/mol)
Ba/Ca (µmol/mol)
Distance from umbo (mm)

No age reference

GSL12_56

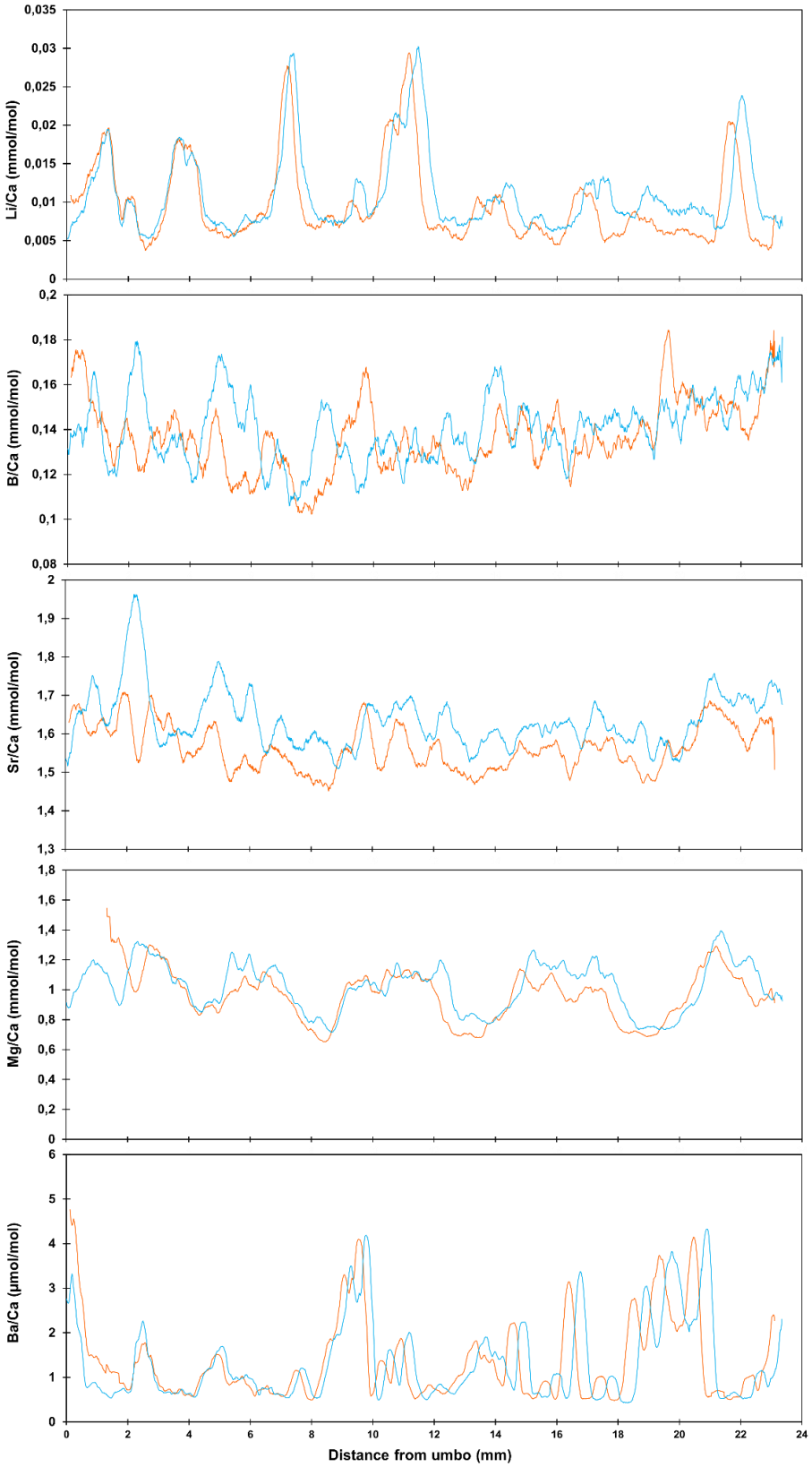

GSL13_56

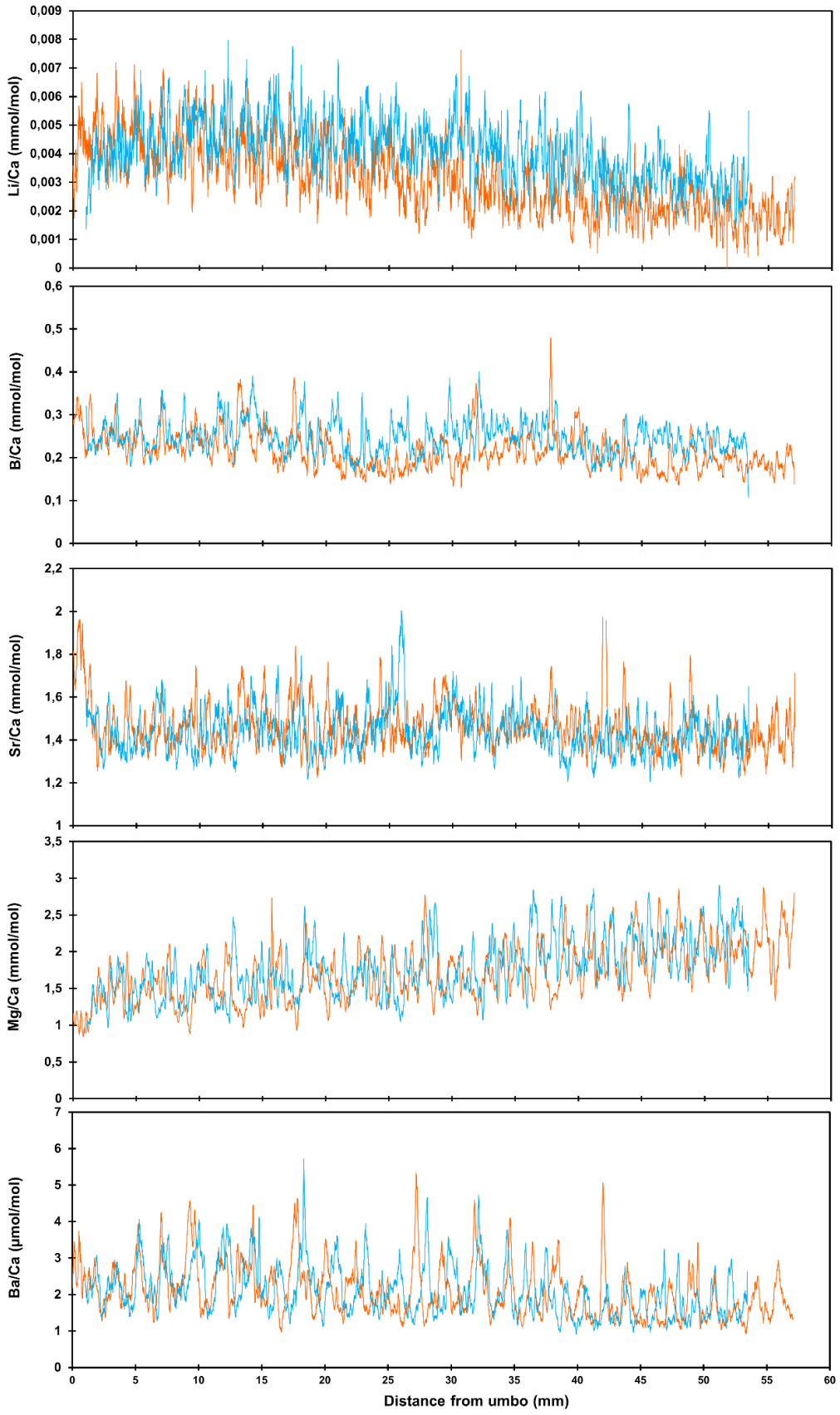
Li/Ca (mmol/mol)
0,009
0,008
0,007
0,006
0,005
0,004
0,003
0,002
0,001
0
B/Ca (mmol/mol)
0,6
0,5
0,4
0,3
0,2
0,1
0
Sr/Ca (mmol/mol)
2,2
2
1,8
1,6
1,4
1,2
1
Mg/Ca (mmol/mol)
3,5
3
2,5
2
1,5
1
0,5
0
Ba/Ca (µmol/mol)
7
6
5
4
3
2
1
0
0
5
10
15
20
25
30
35
40
45
50
55
60
Distance from umbo (mm)

GSL13_57

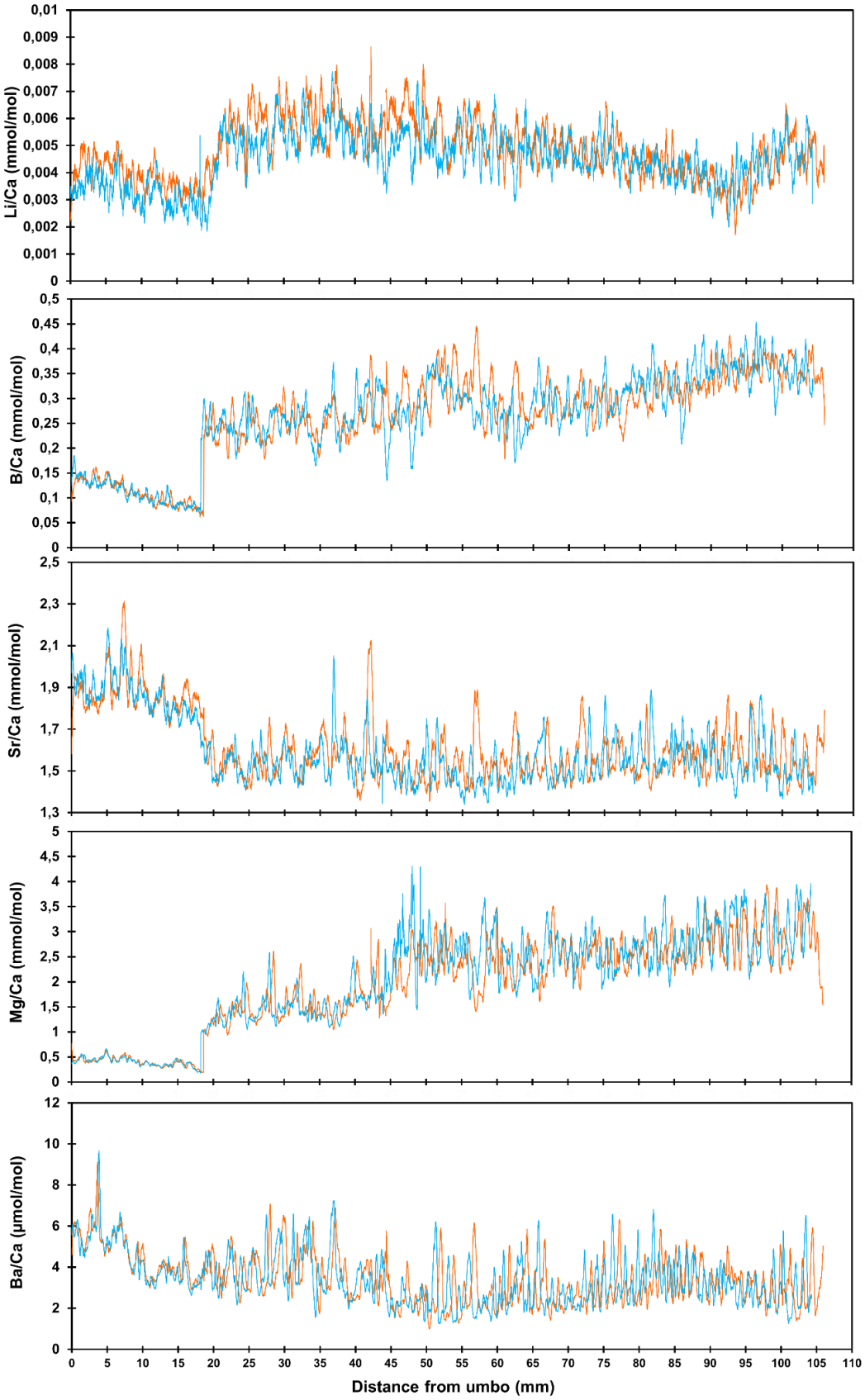
Li/Ca (mmol/mol)
B/Ca (mmol/mol)
Sr/Ca (mmol/mol)
Mg/Ca (mmol/mol)
Ba/Ca (µmol/mol)
Distance from umbo (mm)

GSL14_15

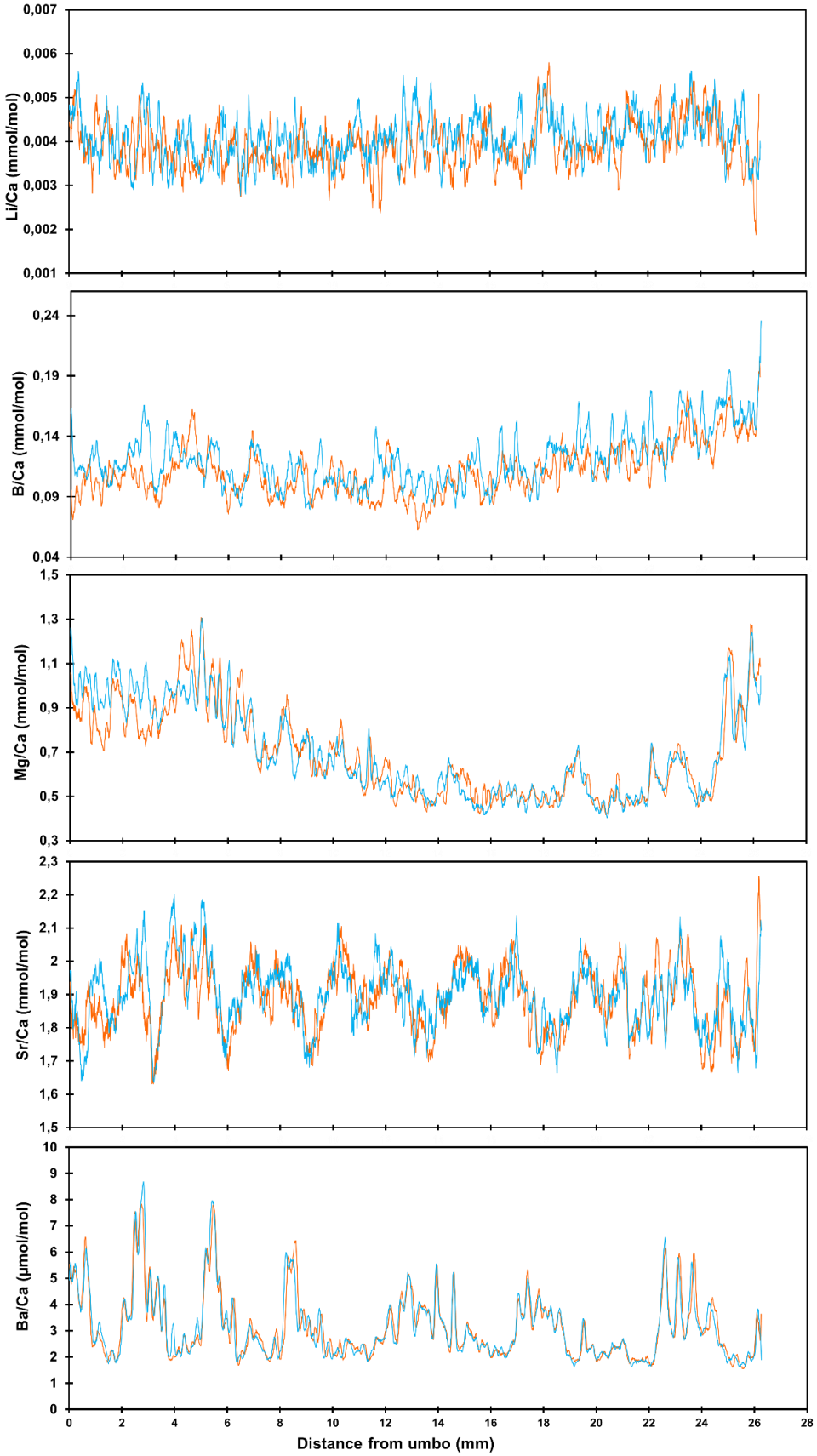
Li/Ca (mmol/mol)
0,007
0,006
0,005
0,004
0,003
0,002
0,001
B/Ca (mmol/mol)
0,24
0,19
0,14
0,09
0,04
Mg/Ca (mmol/mol)
1,5
1,3
1,1
0,9
0,7
0,5
0,3
Sr/Ca (mmol/mol)
2,3
2,2
2,1
2
1,9
1,8
1,7
1,6
1,5
Ba/Ca (µmol/mol)
10
9
8
7
6
5
4
3
2
1
0
0
2
4
6
8
10
12
14
16
18
20
22
24
26
28
Distance from umbo (mm)

GSL14_21

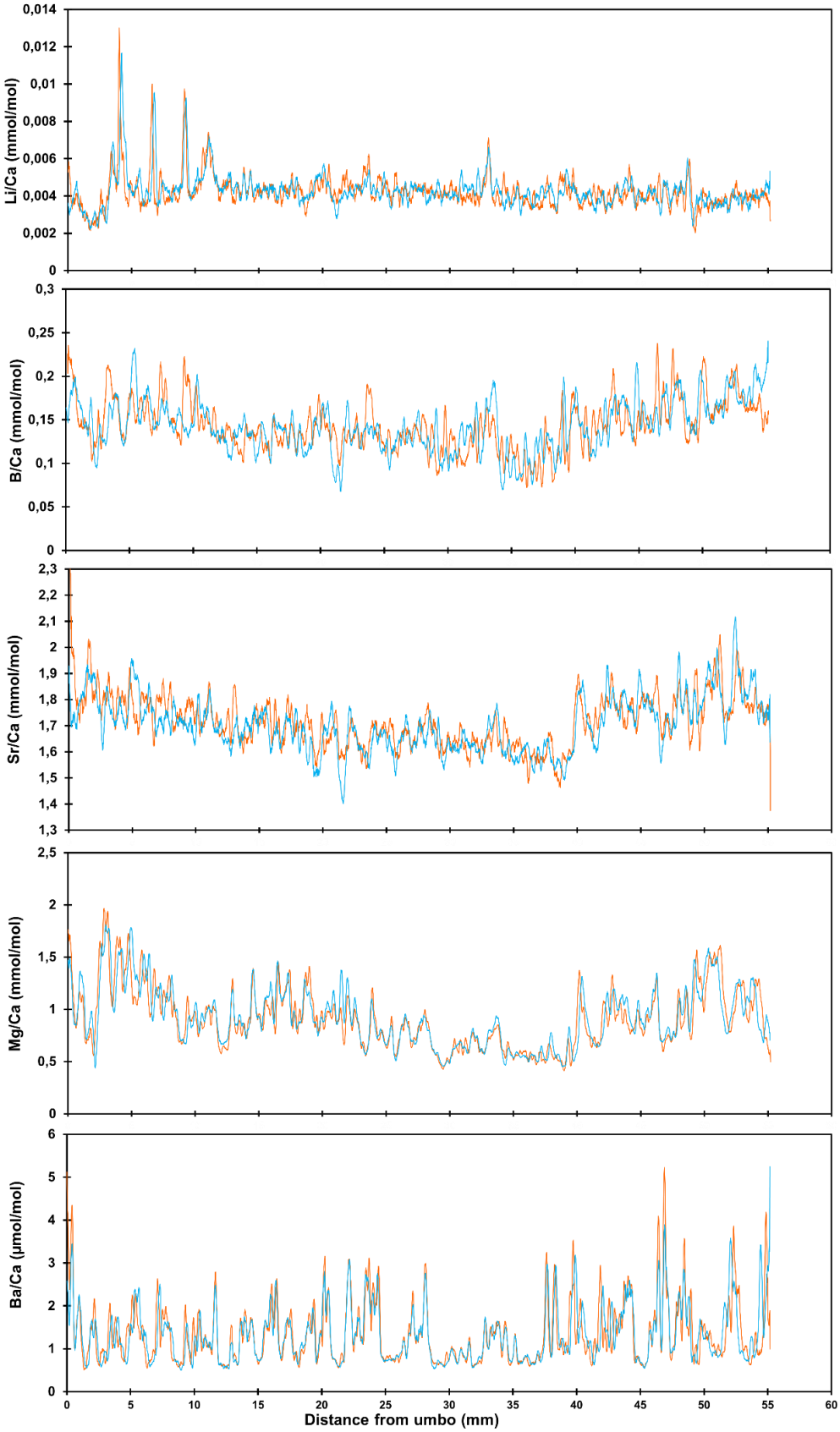
Li/Ca (mmol/mol)
0,014
0,012
0,01
0,008
0,006
0,004
0,002
0
B/Ca (mmol/mol)
0,3
0,25
0,2
0,15
0,1
0,05
0
Sr/Ca (mmol/mol)
2,3
2,2
2,1
2
1,9
1,8
1,7
1,6
1,5
1,4
1,3
Mg/Ca (mmol/mol)
2,5
2
1,5
1
0,5
0
Ba/Ca (µmol/mol)
6
5
4
3
2
1
0
0
5
10
15
20
25
30
35
40
45
50
55
60
Distance from umbo (mm)

GSL14_22

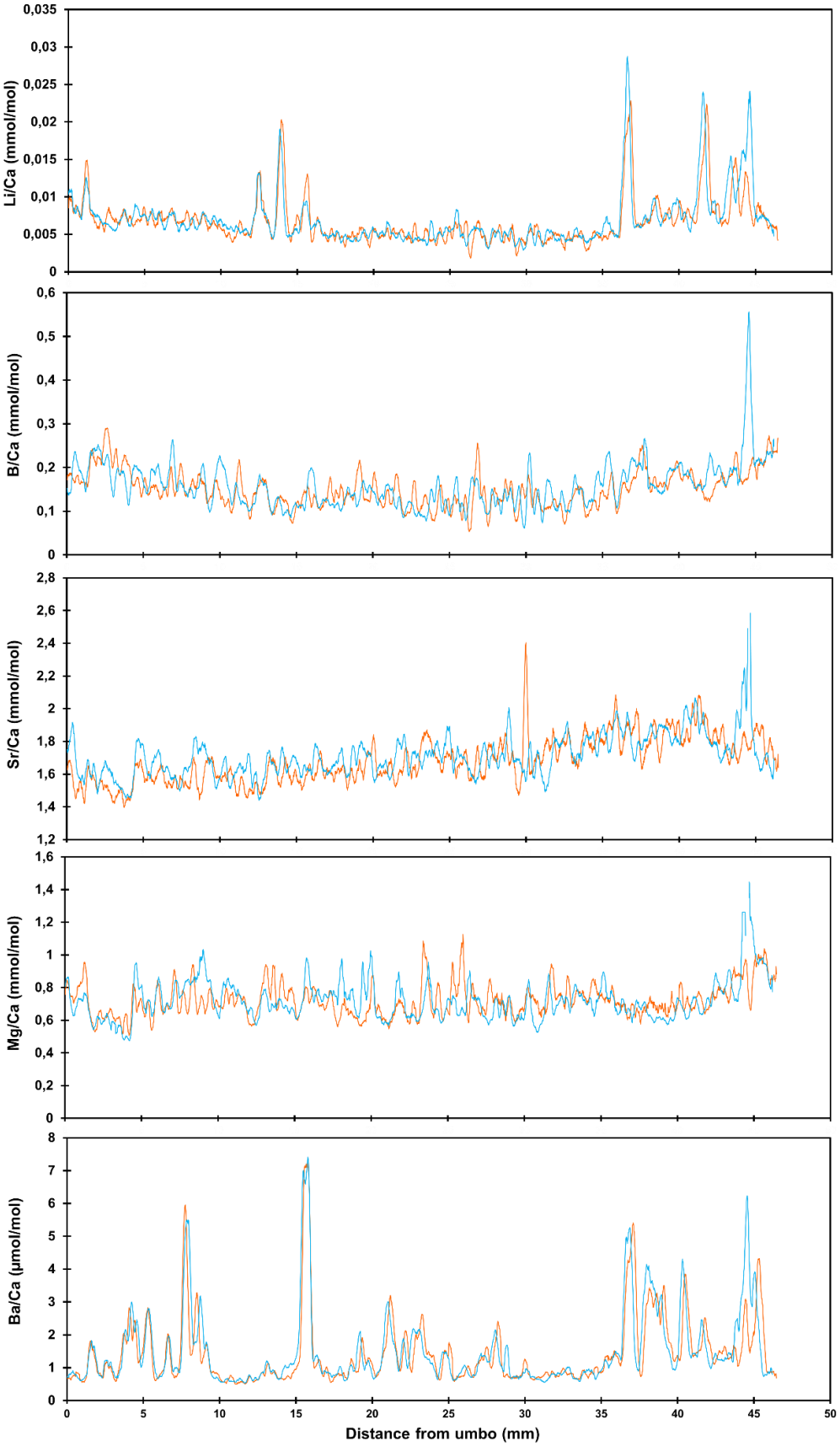
Li/Ca (mmol/mol)
0,035
0,03
0,025
0,02
0,015
0,01
0,005
0
B/Ca (mmol/mol)
0,6
0,5
0,4
0,3
0,2
0,1
0
Sr/Ca (mmol/mol)
2,8
2,6
2,4
2,2
2
1,8
1,6
1,4
1,2
Mg/Ca (mmol/mol)
1,6
1,4
1,2
1
0,8
0,6
0,4
0,2
0
Ba/Ca (µmol/mol)
8
7
6
5
4
3
2
1
0
0
5
10
15
20
25
30
35
40
45
50
Distance from umbo (mm)

Interstadial

GSL12_10

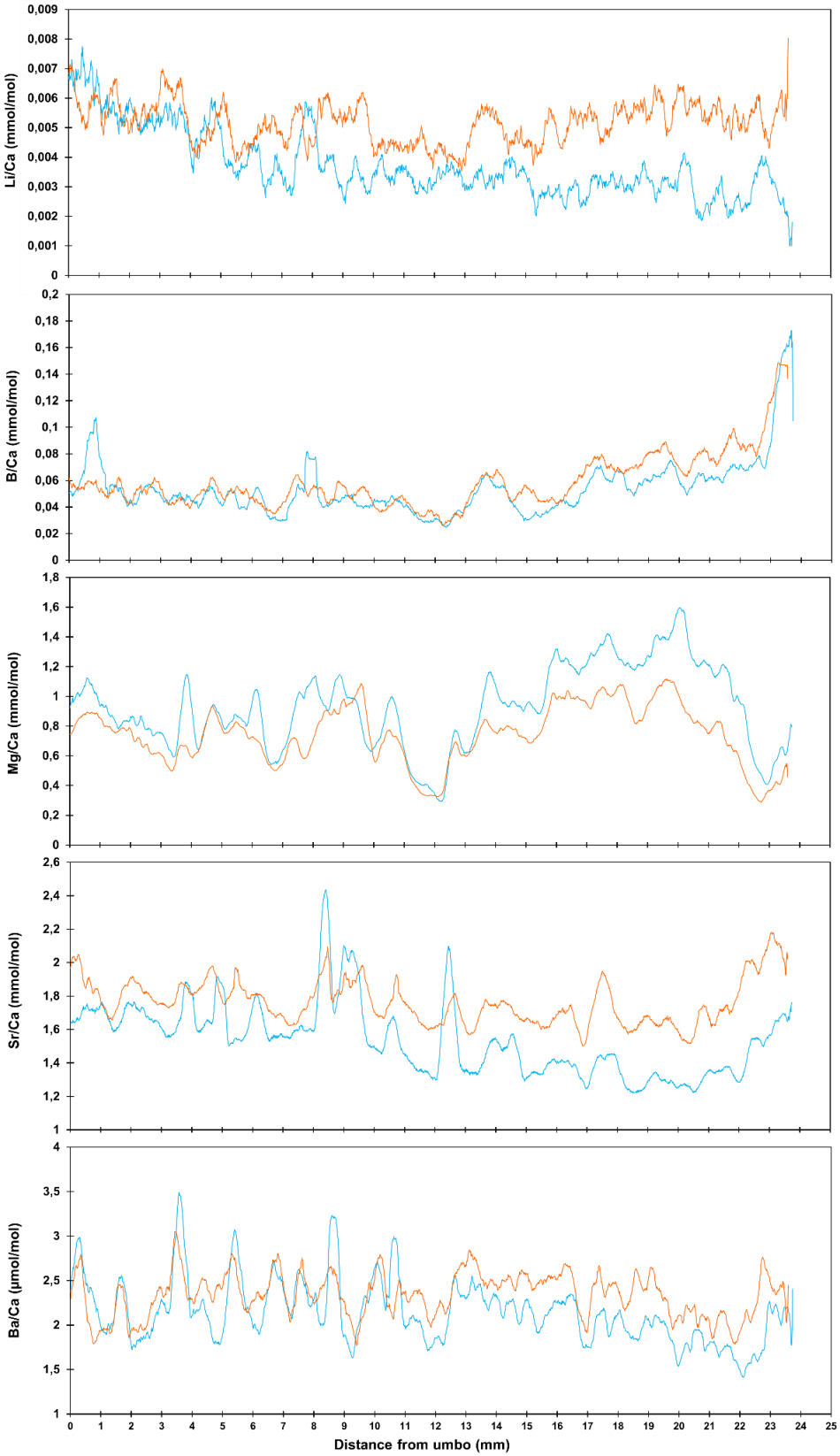

GSL13_01

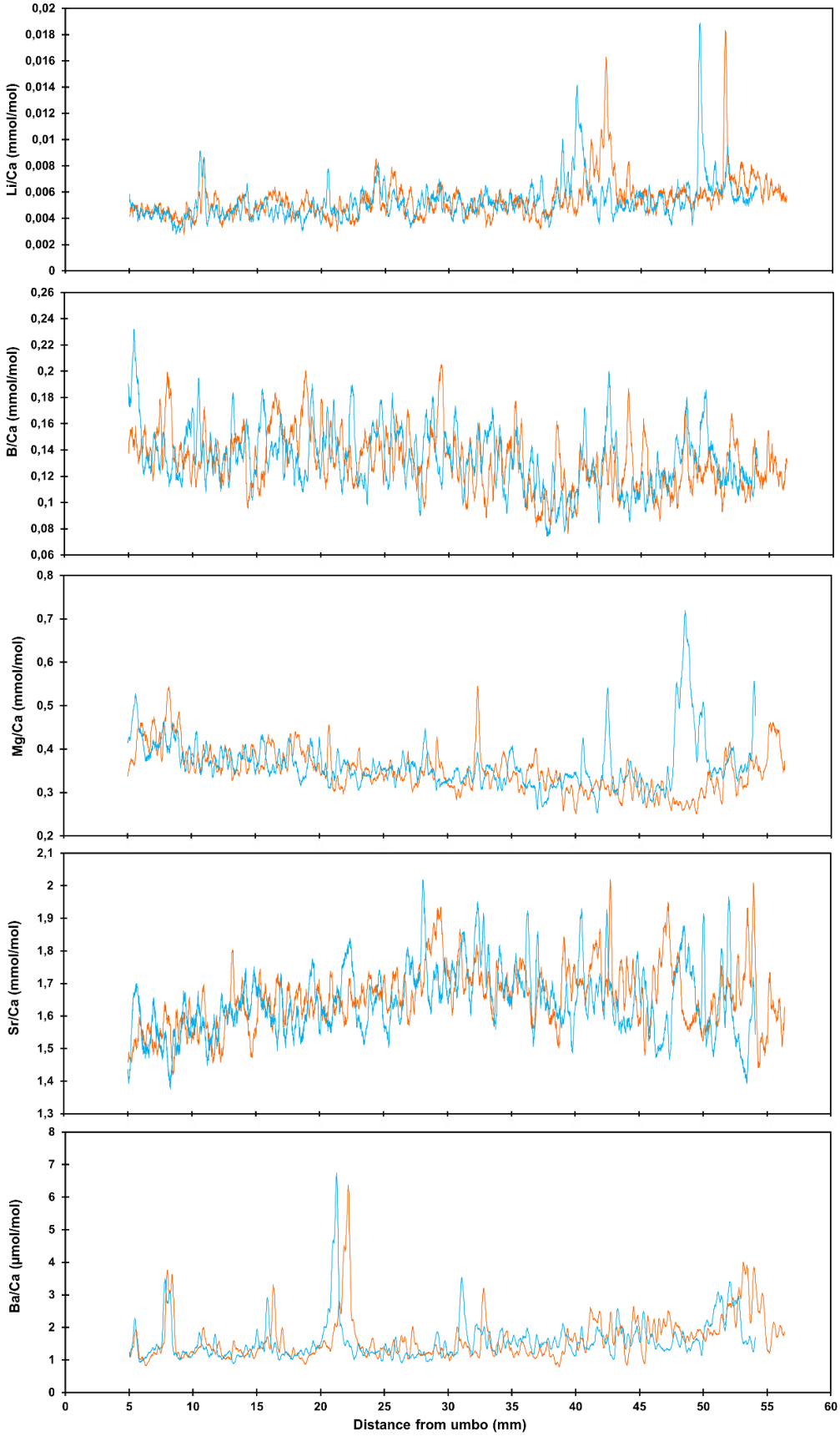
Li/Ca (mmol/mol)
B/Ca (mmol/mol)
Mg/Ca (mmol/mol)
Sr/Ca (mmol/mol)
Ba/Ca (µmol/mol)
Distance from umbo (mm)

GSL13_09

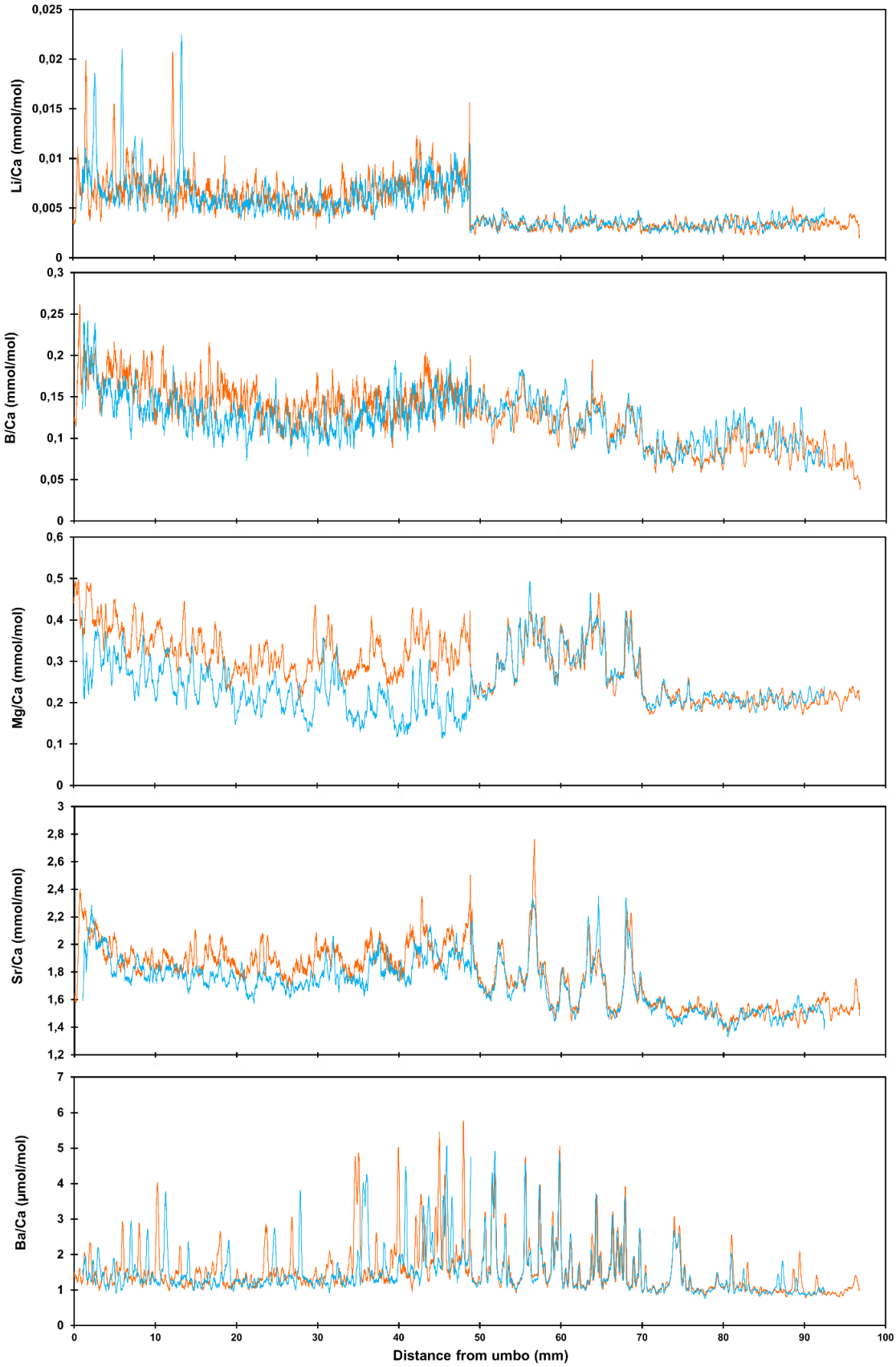
Li/Ca (mmol/mol)
0,025
0,02
0,015
0,01
0,005
0
B/Ca (mmol/mol)
0,3
0,25
0,2
0,15
0,1
0,05
0
Mg/Ca (mmol/mol)
0,6
0,5
0,4
0,3
0,2
0,1
0
Sr/Ca (mmol/mol)
3
2,8
2,6
2,4
2,2
2
1,8
1,6
1,4
1,2
Ba/Ca (µmol/mol)
7
6
5
4
3
2
1
0
0
10
20
30
40
50
60
70
80
90
100
Distance from umbo (mm)

GSL13_73

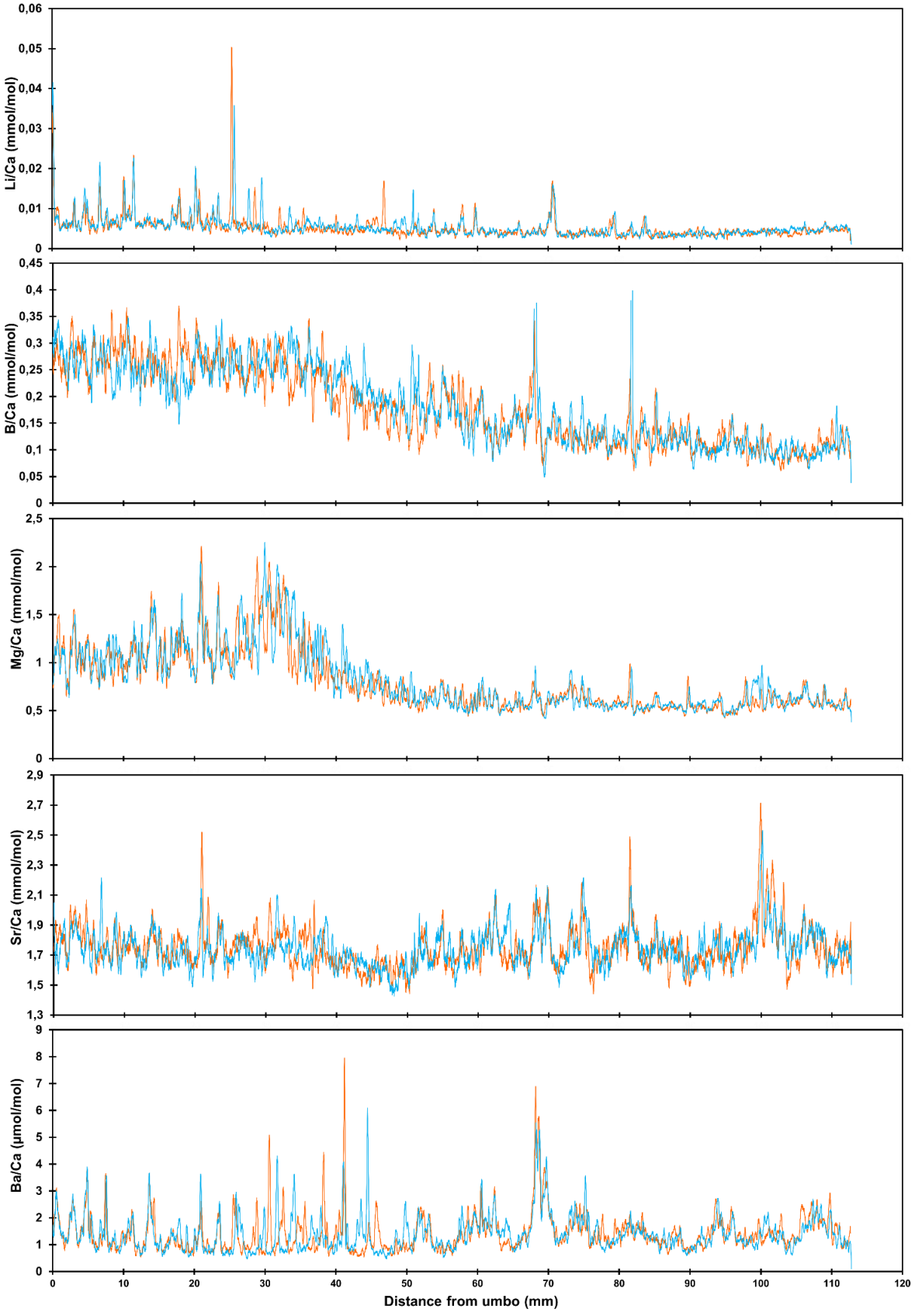
Li/Ca (mmol/mol)
0,06
0,05
0,04
0,03
0,02
0,01
0
B/Ca (mmol/mol)
0,45
0,4
0,35
0,3
0,25
0,2
0,15
0,1
0,05
0
Mg/Ca (mmol/mol)
2,5
2
1,5
1
0,5
0
Sr/Ca (mmol/mol)
2,9
2,7
2,5
2,3
2,1
1,9
1,7
1,5
1,3
Ba/Ca (µmol/mol)
9
8
7
6
5
4
3
2
1
0
0
10
20
30
40
50
60
70
80
90
100
110
120
Distance from umbo (mm)

GSL14_07

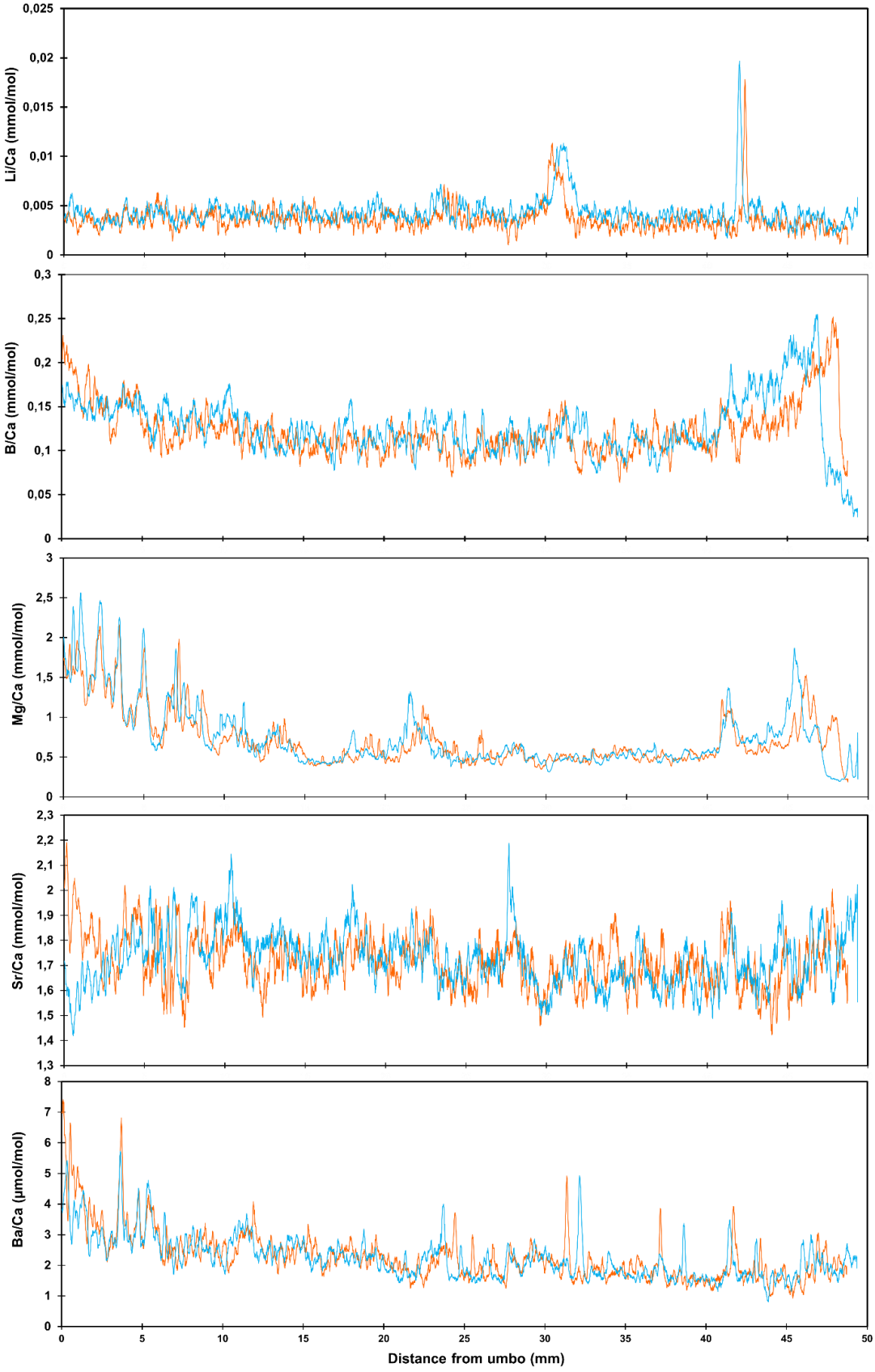
Li/Ca (mmol/mol)
0,025
0,02
0,015
0,01
0,005
0
B/Ca (mmol/mol)
0,3
0,25
0,2
0,15
0,1
0,05
0
Mg/Ca (mmol/mol)
3
2,5
2
1,5
1
0,5
0
Sr/Ca (mmol/mol)
2,3
2,2
2,1
2
1,9
1,8
1,7
1,6
1,5
1,4
1,3
Ba/Ca (µmol/mol)
8
7
6
5
4
3
2
1
0
0
5
10
15
20
25
30
35
40
45
50
Distance from umbo (mm)

Appendix 4. ^{14}C dating

^{14}C age results using bivalve shells and corals from Ular Island (SE Sulawesi) and Belitung (west Indonesia).

Id. Sample	Localilty	Nature	C (mg)	$\delta^{13}C$	pMC	Age BP (Ka)
GSL16_44	Ular	*Tridacna sp.*	1,46	0,4	91.12 ± 0.21	0.745 ± 0.3
GSL16_59	Ular	*Tridacna sp.*	1,18	-5,2	0.21 ± 0.1	49.3 ± 3.4
GSL16_50	Ular	Corail	0,54	-0,3	0.21 ± 0.1	49.5 ± 3.6
GSL16_53	Ular	Corail	1,52	-2,1	0.34*	>45.600
BEL15_3A	Belitung	Veneridae (Bivalve)	1,38	-2,6	42.56 ± 0.15	6.86 ± 0.3
BEL16_05	Belitung	Corail	1,25	-2,5	45.7 ± 0.18	6.29 ± 0.3
BEL16_08	Belitung	Corail	1,4	-2,5	46.8 ± 0.17	6.1 ± 0.3
BEL15_04	Belitung	*T. squamosa*	1,05	0,8	47.9 ± 0.16	5.9 ± 0.3

*sans blanc soustrait

pMC stands for "Percent Modern Carbon" as calculated against a reference sample of ^{14}C activity from a known standard. With modern or present defined as 1950 of our era.

Plateforme Nationale LMC14

CEA Saclay - Bât. 450 - Porte 4E - 91191 GIF sur YVETTE Cedex

Chimie des carbonates

Les échantillons de foraminifères sont traités dans 2 ml d'acide nitrique 0.01 M pendant 15 minutes. Les échantillons de coquilles sont traités (après sablage) dans 2 ml d'acide nitrique 0.01 M pendant 15 minutes. Le carbone est extrait sous forme de CO2 en attaquant les carbonates par l'acide orthophosphorique déshydraté à 60°C jusqu'à ce qu'il n'y ait plus de dégagement gazeux. Une quantité suffisante de chaque échantillon a été prélevée afin de produire un volume de CO2 contenant environ 1 mg de C.

Protocole de réduction en graphite

Le CO2 est réduit par hydrogène en présence de poudre de fer à 600°C. La masse de fer est égale à 3 fois la masse de carbone avec une valeur minimale de 1,5 mg et une valeur maximale de 4 mg. Le carbone se dépose sur la poudre de fer et l'ensemble est ensuite pressé dans un support pour la mesure par SMA.

Protocole de Mesure et d'Analyse

L'activité en 14C de l'échantillon est calculée en comparant les intensités mesurées séquentiellement des faisceaux de 14C, 13C et 12C de chaque échantillon avec ceux de standards de CO2 préparés à partir de l'acide oxalique de référence HOxII. Elle est exprimée en pMC (percent Modern Carbon) normalisé à un deltaC13 de -25 pour mille.

Les âges radiocarbone sont calculés selon Mook et Van der Plicht (Radiocarbon 41 (1999) p.227) en corrigeant le fractionnement avec le delta C13 calculé à partir du rapport 13C/12C mesuré sur ARTEMIS.

Le delta C13 utilisé inclut le fractionnement survenant aussi bien pendant la préparation des échantillons que pendant la mesure SMA. Il est également dépendant de la transmission de l'installation, à savoir la valeur 13C/12C mesurée en sortie du spectromètre de masse ARTEMIS par rapport à la valeur de 13C/12C en sortie de source. Ces valeurs dépendent du faisceau à l'injection, courant et emittance. Le delta C13 mesuré par ARTEMIS ne peut donc pas être comparé au delta C13 mesuré sur un spectromètre de masse. Les valeurs de delta C13 étant corrigées par rapport à un standard, elles n'influent pas sur la mesure de l'âge 14C.

Appendix 5. Growth rate comparison in fossils

Early MIS-5 Fossils from Nirwana (GSL12_80 and GSL12_81):

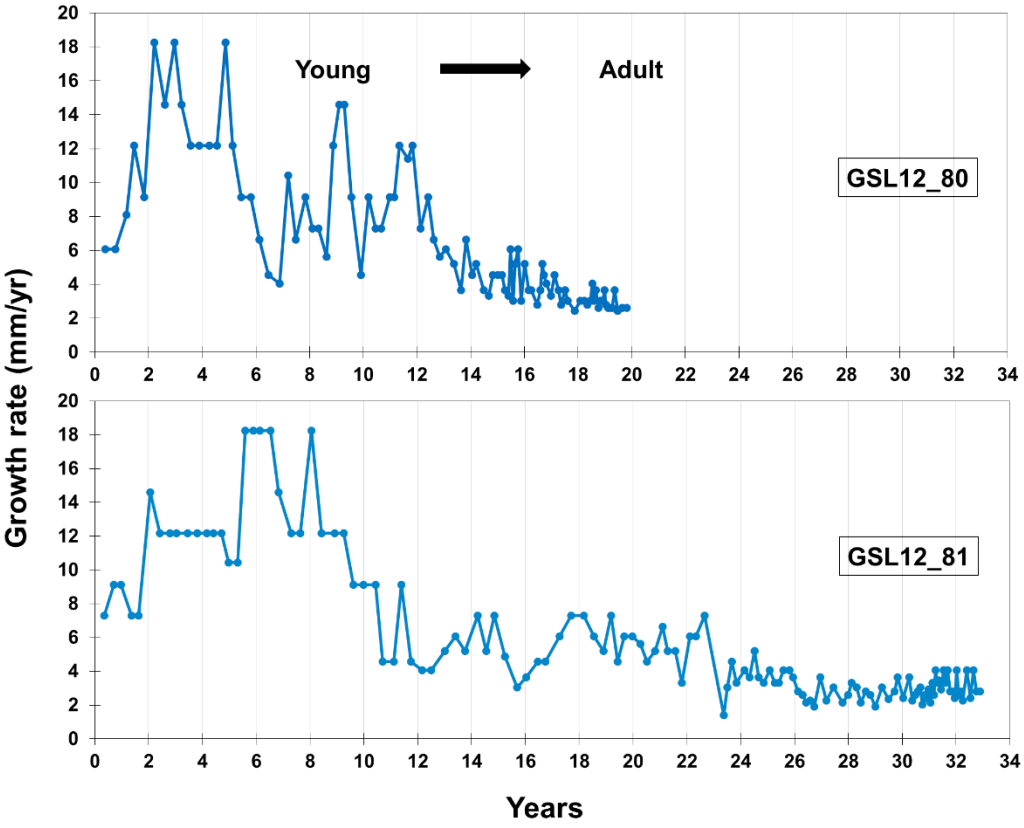

MIS-7-c-e Fossils from Muna (GSL12_60 and GSL12_64):

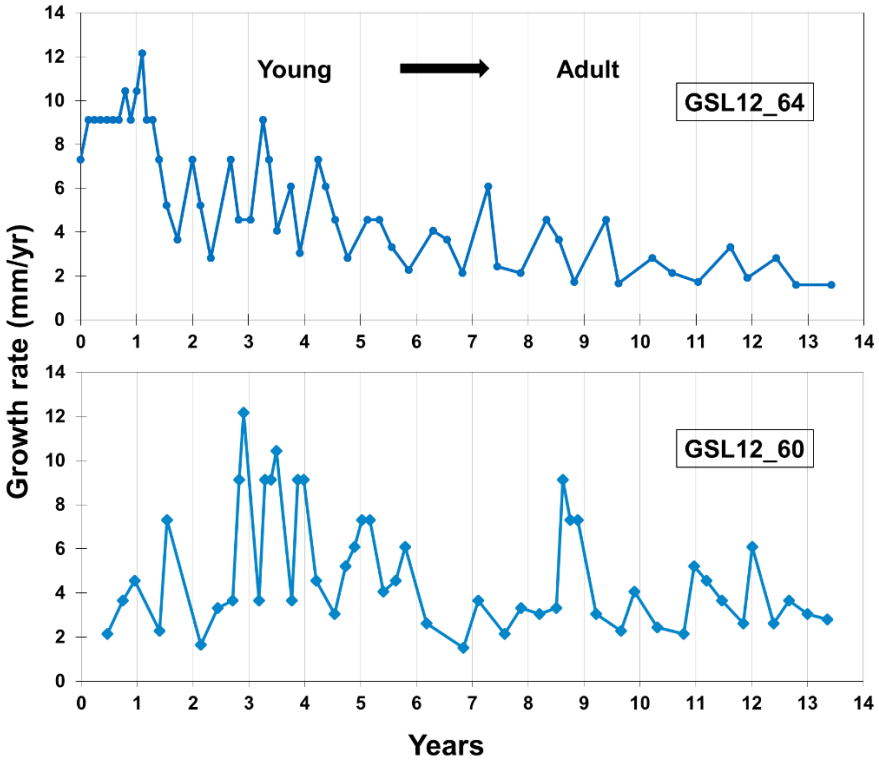

Boxplot comparison of dated fossils from past interglacials and modern samples:

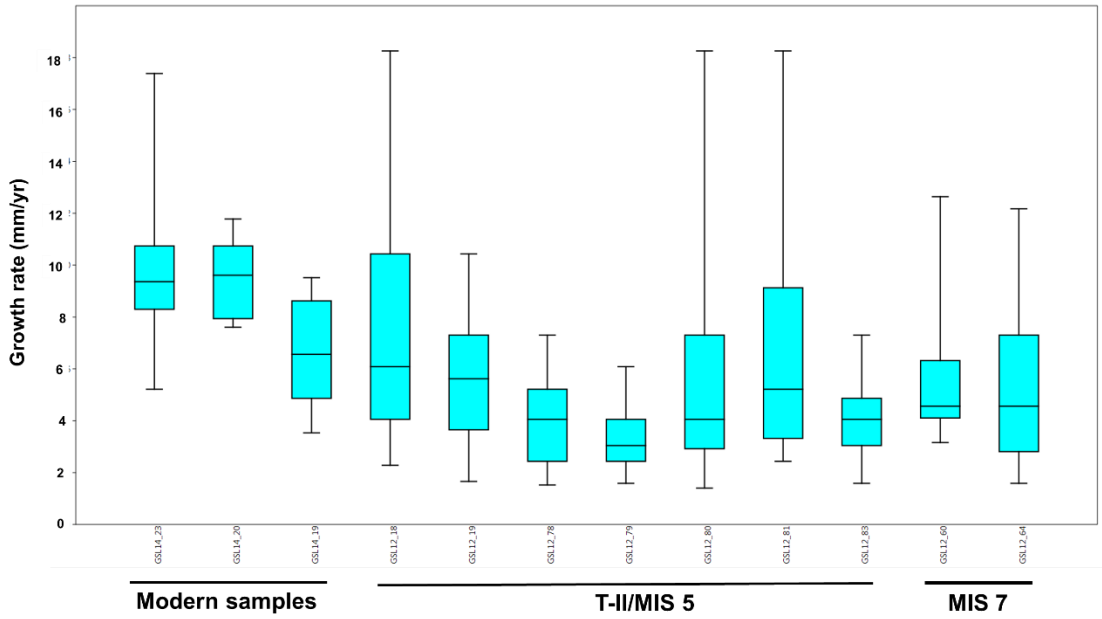

In this graphic samples GSL14_20 and GSL14_23 are *H. hippopus*. GSL14_19 is a *T. squamosal* and the rest fossil samples are *T. gigas.*

UNIVERSITE BRETAGNE LOIRE

UNIVERSITÉ DE NANTES

Thèse de Doctorat

Camilo ARIAS RUIZ

Reconstructions climatiques à haute résolution à partir de bénitiers géants sur l'île de Sulawesi (Indonésie) au cours du Pléistocène.

High resolution climate records from modern and last interglacial periods derived from giant clam shells (Tridacnidae) in Sulawesi, Indonesia.

Résumé

Des coquilles de bénitiers géants (Famille Tridacnidae) ont étés utilisées pour reconstruire des conditions climatiques au cours des dernières périodes interglaciaires dans l'île de Sulawesi, en Indonésie. Des analyses géochimiques sur des coquilles modernes, ont montré que ces organismes enregistrent effectivement la variation de l'environnement dans lequel ils habitent, en termes de : température, salinité, précipitations et apports en nutriments. Les résultats principaux ont été la reproductibilité du signal géochimique ($\delta^{18}O$, $\delta^{13}C$ et Mg/Ca) dans deux espèces différentes et l'enregistrement des anomalies climatiques liées au phénomène La Niña en 2010. La datation à travers l'Uranium-Thorium a mis en évidence des récifs formés lors du début de la dernière période interglaciaire (MIS-5) et de l'avant dernière interglaciaire ou MIS-7. La comparaison entre reconstructions modernes et fossiles a donné comme résultats: 1) des conditions de température en moyenne plus froides et avec une saisonnalité réduite pour ce deux périodes (début du MIS-5 et MIS-7), liée à des conditions plus sèches. 2) Ces paramètres répondent systématiquement aux variations du niveau marin et témoignent la forte interaction entre la circulation atmosphérique et océanique dans la région. 3) La variabilité interannuelle SST/SSS présente des oscillations dans la même amplitude qu'aujourd'hui pour la période du MIS-5, cependant pour le MIS 7, ces oscillations sont réduites autour de 50 % par rapport à l'actuelle. 4) Le Mg/Ca présente une forte variation taxonomique, des études complémentaires sont nécessaires pour enlever le facteur biologique du signal géochimique. 5) Le Ba/Ca et le $\delta^{13}C$ sont potentiellement liées aux processus d'upwelling et/ou variations de salinité.

Mots clés
SE Sulawesi, Tridacnidae**,** Traceurs environnementales, terrasses récifales, niveau marin, Pléistocène tardif.

Abstract

Giant clam shells (Tridacnidae family) were used to reconstruct climatic conditions during the last interglacial periods in Indonesia's Sulawesi Island. Geochemical analyzes on modern shells have shown that these organisms actually record the variation of the environment in which they live, in terms of: temperature, salinity, precipitation and nutrient inputs.
The main results were the reproducibility of the geochemical signal ($\delta^{18}O$, $\delta^{13}C$ and Mg/Ca) in two different species, as well as the recording of the climatic anomalies related to the La Niña phenomenon in 2010.
Uranium-series dating revealed reefs formed at the beginning of the last interglacial period (MIS-5) and the penultimate interglacial or MIS-7.
The comparison between modern and fossil reconstructions gave the following main results: 1) colder average temperature conditions with reduced seasonality for both periods (beginning of MIS-5 and MIS-7) due to drier conditions. 2) These parameters respond systematically to a decrease / increase of the sea level and testify the strong interaction between the atmospheric and ocean circulation in the region 3) The interannual variability of SST / SSS presents oscillations in the same amplitude as today for the MIS-5 period, however for MIS 7, these oscillations are reduced around 50% compared to the current interglacial 4) The Mg/Ca ratio has a strong taxonomic variation, additional studies are needed to remove the biological factor related to geochemical signal. 5) Ba/Ca and $\delta^{13}C$ present a potential use as tracers of upwelling processes and/or variations in salinity.

Key Words
SE Sulawesi, Tridacnidae, geochemical proxies, paleo-reef terraces, sea level evolution, late Pleistocene.